Novel techniques for the measurement of atmospheric organic aerosol physiochemical properties

Submitted in partial fulfillment of the requirements for

the degree of

Doctor of Philosophy

in

Chemical Engineering

Kerrigan P. Cain

B.S., Chemical Engineering, Case Western Reserve University

Carnegie Mellon University
Pittsburgh, PA

May 2020

To my family and friends

Acknowledgements

This achievement (and my ability to get to this point) would not have been possible without the guidance, help, and support of many people. It is true that it takes a village to raise a child (or, in this case, a Ph.D. student) and my village is full of people that are smart, supportive, and many other endearing qualities that would take several pages to finish. I am forever grateful to everyone that has influenced my life and cannot thank each person enough, let alone try to summarize it in a few short paragraphs.

This work and my growth as an individual over the past five years have been greatly influenced by my advisor, Dr. Spyros Pandis. Under his guidance, I have learned to navigate the challenging scientific world as an independent researcher with integrity and confidence. I have also learned how to improve my approach of complex problems with creative solutions. I am sincerely grateful for Dr. Pandis's invaluable input and help with this work and for giving me the opportunities to attend and present at scientific conferences and the ability to participate in an international field campaign. I am very lucky to have been able to learn from such a great role model.

I also am very thankful for my wife, Serafina, because, without her, I am not sure how I would have gotten to or through this process. She has been my steady, supportive, and loving rock to lean on for the past 13 years and continues to encourage me every day. She has voluntarily listened to countless practice presentations and me talking about my research so much that she could give an excellent summary of this work. Her endless amounts of support and encouragement continue to amaze me and I cannot thank her enough for everything she has done for me and our family. This achievement is as much hers as it is mine because she has been here every step of the way.

Also incredibly important for my journey to this point is my family. My parents, Brian and Carol, created a loving and supporting family environment that allowed myself and my siblings, Aaron and Colleen, to thrive. Their success as parents made my journey a reality and I am deeply grateful for all of the opportunities they provided me along the way. I also want to thank my second family (legally my in-laws, but they are actually family to me), Joe, Karen, Anthony, Carol, Gabriel, Emilia, Brenna, Michael, Francesca, Lucia, and Dominic, for their unwavering support in my endeavors.

I have also been supported greatly by my friends, both new and old, to get to where I am today. Specifically, my friends in CAPS and the department of chemical engineering have helped me work through challenging problems and been there to celebrate. I would like to specifically acknowledge the Pandis research group, Dr. Antonios Tasoglou, Dr. Ningxin Wang, Dr. Eleni Karnezi, Dr. Christos Kaltsonoudis, Dr. Pablo Garcia, Aikaterini Liangou, Spiro Jorga, Brian Dinkelacker, and Dontavious Sippial, for helping form me into the researcher I have become.

I would like to thank my committee members, Dr. Peter Adams, Dr. Neil Donahue, Dr. Andrew Gellman, and Dr. Ryan Sullivan, for reading my proposal and thesis, sharing their wisdom and expertise, and providing excellent advice and suggestions to improve this work. It has been a pleasure getting to learn from and work with these talented researchers.

Finally, I would like to thank and acknowledge the funding support for this work. This research would not have been possible without funding from the National Science Foundation grant 1455244, the Carnegie Mellon University Steinbrenner Institute Robert W. Dunlap Fellowship, and the Center for Air, Climate, and Energy Solutions.

Abstract

Atmospheric aerosols significantly impact both human health, as they increase the frequency of cardiovascular and respiratory diseases, and climate change, as they affect the Earth's energy balance. Organic aerosol (OA) comprises a substantial fraction of atmospheric aerosol, but there is limited knowledge about its sources, chemical evolution, and physical properties, leading to considerable uncertainty in atmospheric chemical transport model predictions. The magnitude of the impact of OA on human health and climate change is strongly dependent on an improved understanding of the evolution of organic compounds in the atmosphere.

Hygroscopicity, oxidation level, and volatility are three of the most crucial properties of OA because they control its atmospheric fate and climate relevance. Hygroscopicity is a measure of a compound's ability to interact with and absorb water. The oxidation level is a useful surrogate for changes in chemical composition since the atmosphere is an oxidizing environment. Volatility determines, to a large extent, the partitioning of compounds between the particulate and vapor-phases. This work develops and tests novel techniques that can be used to measure these critical properties of OA and provide a foundation to update these properties in atmospheric models.

The first part of this work describes the development and testing of a technique that quantitatively relates the hygroscopicity and oxidation level of OA components to their volatility. The technique utilizes a thermodenuder (TD) along with aerosol mass spectrometry and size-resolved cloud condensation nuclei measurements to separate the OA by volatility and characterize its hygroscopicity and oxidation level. The technique was tested with secondary OA (SOA) from the ozonolysis of α-pinene and the results indicated that the least volatile components in this SOA system were the least hygroscopic and least oxidized.

The second part of this work improves the characterization of the volatility distribution of OA by combining TD and isothermal dilution measurements. The technique was tested with SOA from the ozonolysis of α-pinene and cyclohexene. The results from this work demonstrated the challenges that arise in estimating the volatility distributions of OA using thermal evaporation techniques and the benefits of combining techniques to measure properties of OA.

The third part of this work combines the techniques from the first and second parts of this thesis and applies them to SOA from the ozonolysis of α-pinene, limonene, and cyclohexene. The results suggested that some OA systems have a more complex relationship between these properties than originally thought. Use of the techniques developed in this thesis to different OA, both laboratory and ambient, can supply needed parameters that can be incorporated in atmospheric models.

Table of contents

List of tables

List of figures

List of acronyms

1D-VBS	One-dimensional volatility basis set
2D-VBS	Two-dimensional volatility basis set
AMS	Aerosol mass spectrometer
AQL	Air quality laboratory
BBA	Biomass-burning aerosol
BBOA	Biomass-burning organic aerosol
BP	By-pass
CCN	Cloud condensation nuclei
CCNC	Cloud condensation nuclei counter
CIMS	Chemical ionization mass spectrometer
CN	Condensation nuclei
CPC	Condensation particle counter
CTMs	Chemical transport models
DMA	Differential mobility analyzer
ELVOCs	Extremely low volatility organic compounds
FIGAERO	Filter inlet for gases and aerosols
H-TDMA	Hygroscopicity tandem differential mobility analyzer
HEPA	High-efficiency particulate air
HGF	Hygroscopic growth factor
HR-ToF-AMS	High-resolution time-of-flight aerosol mass spectrometer
IVOCs	Intermediate volatility organic compounds
LVOCs	Low volatility organic compounds
MFR	Mass fraction remaining
OA	Organic aerosol
PM	Particulate matter
$PM_{0.1}$	Particulate matter with a diameter less than 0.1 μm
$PM_{2.5}$	Particulate matter with a diameter less than 2.5 μm
PMF	Positive matrix factorization
POA	Primary organic aerosol
PTR-MS	Proton transfer reaction mass spectrometer
RH	Relative humidity
SMCA	Scanning mobility cloud condensation nuclei analysis
SMPS	Scanning mobility particle sizer
SOA	Secondary organic aerosol
SP-AMS	Soot particle aerosol mass spectrometer
SS	Supersaturation
SVOCs	Semi-volatile organic compounds
TD	Thermodenuder
V-TDMA	Volatility tandem differential mobility analyzer
V/H-TDMA	Volatility and hygroscopicity tandem differential mobility analyzer
VOCs	Volatile organic compounds

Chapter 1

Introduction

1.1 Atmospheric aerosols

Atmospheric aerosols, also known as particulate matter (PM), are solid or liquid particles suspended in the atmosphere with sizes ranging from a few nanometers to around 100 μm. These particles are classified by their size into two groups: fine PM, particles with diameters less than 2.5 μm ($PM_{2.5}$), and coarse PM, particles with diameters larger than 2.5 μm. Ultrafine PM is a subset of $PM_{2.5}$ and defined as particles with diameters less than 0.1 μm ($PM_{0.1}$). PM and its precursors can be emitted from a variety of sources, but it is usually separated into two main categories: anthropogenic (e.g., combustion, cooking, transportation, and other human activities) and biogenic (e.g., vegetation emissions, volcanic eruptions, wildfires, and other natural sources). $PM_{2.5}$ includes organic compounds, sulfates, nitrates, ammonium, black carbon, and a number of combustion-related trace metals while dust and sea-salt dominate the coarse PM composition (Zhang et al., 2007; Jimenez et al., 2009; Seinfeld and Pandis, 2016).

PM is associated with many adverse health effects. A series of epidemiological studies have shown that $PM_{2.5}$ can deposit deep in the lungs and induce oxidative stress, cardiovascular and respiratory diseases, and even premature death (Dockery et al., 1993; Pope et al., 2015; Du et al., 2016; Cohen et al., 2017; Shiraiwa et al., 2017; Burnett et al., 2018). Global mortality rates related to $PM_{2.5}$ exposure are estimated at around 5 million deaths per year (Cohen et al., 2017; Burnett et al., 2018). These effects have resulted in regulations of ambient PM mass concentrations.

PM also impacts the Earth's climate because it can absorb and scatter radiation (direct effect) and influence cloud properties and lifetime (indirect effect) by serving as cloud condensation nuclei (CCN) or ice nuclei (Boucher et al., 2013). PM currently represents the largest source of uncertainty in the Earth's energy budget due to complex interactions with radiation and

clouds (Boucher et al., 2013). In general, PM exerts a cooling effect on the Earth's climate, but energy absorbing components, such as black and brown carbon, can provide a warming effect (Boucher et al., 2013; Tsigaridis and Kanakidou, 2018).

1.2 Organic aerosol

Organic aerosol (OA) is a complex mixture of organic compounds and represents a substantial fraction (20–90%) of submicron PM depending on location (Kanakidou et al., 2005; Zhang et al., 2007; Jimenez et al., 2009). Primary OA (POA) is organic matter emitted directly in the particulate-phase, while secondary OA (SOA) is produced by the vapor-phase oxidation of volatile (VOCs), intermediate volatility (IVOCs), and semi-volatile (SVOCs) organic compounds (Robinson et al., 2007; Hallquist et al., 2009). SOA precursors and POA can be emitted from multiple anthropogenic and biogenic sources, such as combustion, cooking, and vegetation. OA components continuously evolve in the atmosphere due to reactions with the hydroxyl radical, ozone, nitrate radical, and other oxidants. Uncertainties surrounding the sources and evolution of OA enhance the difficulty in elucidating its physiochemical properties (Jimenez et al., 2009; Ditto et al., 2018).

OA, being a large fraction of PM, has a substantial impact on the Earth's climate through both the direct and indirect effects (Seinfeld et al., 2016; Tsigaridis and Kanakidou, 2018). Quantifying the effect of OA changes on present and future climate is one of the most uncertain aspects of global climate predictions (Carslaw et al., 2017; Shrivastava et al., 2017). The magnitude of these effects is strongly dependent on understanding the abundance and properties of OA, both in the preindustrial and current atmospheres (Carslaw et al., 2017).

1.3 Physiochemical properties of OA

Hygroscopicity is a measure of a compound's ability to interact with and absorb water and is often parameterized by the dimensionless hygroscopicity parameter, κ (Petters and Kreidenweis, 2007). κ is calculated as a sum of the volume-weighted hygroscopicity of all components that constitute the total PM volume. Since OA can be a considerable fraction of PM, understanding the influence of OA as CCN is key to understanding aerosol-cloud interactions (Shrivastava et al., 2017). The hygroscopicity of OA, κ_{org}, is relatively low when compared to the hygroscopicity of inorganic PM components, such as sulfate and nitrate, and κ_{org} is not expected to exceed 0.3 in the atmosphere (Nakao, 2017). However, the CCN concentration can be very sensitive to the OA fraction in environments where organics dominate the volume fraction of PM (Mei et al., 2013; Ruehl et al., 2012) or when the organic and inorganic components are not present in the same particles (i.e., external mixing). Furthermore, condensation of organic compounds is crucial to the growth of ultrafine particles to CCN sizes (Riipinen et al., 2011). Therefore, the composition of OA as a function of size and its impact on κ_{org} need to be better understood in order to fully represent aerosol-cloud interactions in climate models (Shrivastava et al., 2017).

Currently, it is impossible to quantify the composition of OA on the molecular level due to its chemical complexity and sheer magnitude of organic compounds present in the atmosphere. Multiple reaction pathways and an increasing number of possible isomers as carbon number increases make it difficult to track the evolution of OA in the atmosphere (Goldstein and Galbally, 2007; Kroll et al., 2011). Therefore, it is useful to track changes in the composition of OA with surrogates, such as the oxidation level. Since the atmosphere is an oxidizing environment, the oxidation level provides information about the atmospheric age of organic compounds. The oxidation level of OA can be determined from high-resolution mass spectrometry and is usually

expressed by the atomic oxygen-to-carbon ratio (O:C) or average carbon oxidation state (OS_C). The O:C characterizes the extent of oxygenation and is useful in possibly predicting other OA properties, including hygroscopicity and volatility (Jimenez et al., 2009; Massoli et al., 2010; Donahue et al., 2011; Rickards et al., 2013).

Volatility is one of the most important physical properties of OA because it determines, to a large extent, the partitioning of organic compounds between the particulate and vapor-phases. A compound's saturation concentration and the particulate-phase OA mass concentration drive vapor-to-particle partitioning. Due to the large range of saturation concentrations of atmospheric organic compounds, the one-dimensional volatility basis set (1D-VBS) has been proposed as a framework to describe the evolution of OA (Donahue et al., 2006). The 1D-VBS utilizes logarithmically spaced bins based on an effective saturation concentration at 298 K that attempts to collect organic compounds with similar volatility, albeit different structures (Donahue et al., 2011). OA volatility, specifically SOA volatility, has been characterized as one of the most important properties missing from climate models (Tsigaridis and Kanakidou, 2018) and models that do simulate OA often underestimate OA concentrations when compared to ambient measurements (Tsigaridis et al., 2014).

Together, hygroscopicity, oxidation level, and volatility are three of the most crucial properties of OA because they control their atmospheric fate and effect on climate (Shrivastava et al., 2017; Tsigaridis and Kanakidou, 2018). A growing body of literature (Jimenez et al., 2009; Poulain et al., 2010; Kuwata et al., 2011; Tritscher et al., 2011; Hong et al., 2014; Cerully et al., 2015; Hildebrandt Ruiz et al., 2015; Cain and Pandis, 2017; Nakao, 2017; Alroe et al., 2018; Kostenidou et al., 2018) has attempted to relate these three properties in order to develop parameterizations that can then be implemented in chemical transport models (CTMs), but a clear

relationship has yet to be established. This has hindered their description in CTMs, increasing the corresponding uncertainty of their predictions.

1.4 Thesis overview

In this thesis, novel experimental and analysis techniques are developed and tested that characterize the hygroscopicity, oxidation level, and volatility of OA. In Chapter 2, a technique that relates hygroscopicity and oxidation level as a function of volatility is developed. The technique separates OA by volatility with a thermodenuder (TD), observes the resulting hygroscopicity and oxidation level with a CCN counter and high-resolution time-of-flight aerosol mass spectrometer, and determines κ and O:C distributions as a function of volatility in the 1D-VBS. This technique is tested with SOA from the ozonolysis of α-pinene and can be used to provide valuable insights about the relationship between the hygroscopicity, oxidation level, and volatility of OA.

In Chapter 3, a technique that improves the estimation of the volatility distribution of OA by combining TD and isothermal dilution measurements is developed. This technique is tested with SOA from the ozonolysis of α-pinene and cyclohexene and demonstrates the importance of combining techniques to accurately estimate OA volatility. A method that provides information about vapor wall-losses in a Teflon atmospheric simulation chamber is also developed.

In Chapter 4, the techniques from Chapters 2 and 3 are combined to determine κ and O:C distributions over a larger range of volatility. This technique is tested with SOA from the ozonolysis of α-pinene, limonene, and cyclohexene. The results from this technique provide a foundation to understand when and why OA behave differently and how to implement them in CTMs.

Lastly, an application of the technique in Chapter 2 to emissions from biomass-burning is described in Appendix E.

1.5 References

Alroe, J., Cravigan, L. T., Mallet, M. D., Ristovski, Z. D., Miljevic, B., Osuagwu, C. G., & Johnson, G. R.: Determining the link between hygroscopicity and composition for semi-volatile aerosol species, Atmos. Meas. Tech., 11, 4361–4372, doi: 10.5194/amt-11-4361-2018, 2018.

Boucher, O., Randall, D., Artaxo, P., Bretherton, C., Feingold, G., Forster, P., Kerminen, V.-M., Kondo, Y., Liao, H., Lohmann, U., Rasch, P., Satheesh, S. K., Sherwood, S., Stevens, B., and Zhang, X. Y.: Clouds and aerosols, in: Climate Change 2013: The Physical Basis: Working Group I Contribution to the Fifth Assessment Report of the Intergovernmental Panel on Climate Change, edited by: Stoker, T. F., Qin, D., Plattner, G.-K., Tignor, M., Allen, S. K., Boschung, J., Nauels, A., Xia, Y., and Midgley, P. M., Cambridge University Press, Cambridge, United Kingdom, and New York, NY, USA, doi: 10.1017/CBO9781107415324.016, 2013.

Burnett, R., Chen, H., Szyszkowicz, M., Fann, N., Hubbell, B., Pope, C. A., Apte, J. S., Brauer, M., Cohen, A., Weichenthal, S., Coggins, J., Di, Q., Brunekreef, B., Frostad, J., Lim, S. S., Kan, H., Walker, K. D., Thurston, G. D., Hayes, R. B., Lim, C. C., Turner, M. C., Jerrett, M., Krewski, D., Gapstur, S. M., Diver, W. R., Ostro, B., Goldberg, D., Crouse, D. L., Martin, R. V., Peters, P., Pinault, L., Tjepkema, M., van Donkelaar, A., Villeneuve, P. J., Miller, A. B., Yin, P., Zhou, M., Wang, L., Janssen, N. A. H., Marra, M., Atkinson, R. W., Tsang, H., Thach, T. Q., Cannon, J. B., Allen, R. T., Hart, J. E., Laden, F., Cesaroni, G., Forastiere, F., Weinmayr, G., Jaensch, A., Nagel, G., Concin, H., and Spadaro, J. V.: Global estimates of mortality associated with long-term exposure to outdoor fine particulate matter, Proc. Natl. Acad. Sci., 115, 9592–9597, doi: 10.1073/pnas.1803222115, 2018.

Cain, K. P., and Pandis, S. N.: A technique for the measurement of organic aerosol hygroscopicity, oxidation level, and volatility distributions, Atmos. Meas. Tech., 10, 4865–4876, doi: 10.5194/amt-10-4865-2017, 2017.

Carslaw, K. S., Gordon, H., Hamilton, D. S., Johnson, J. S., Regayre, L. A., Yoshioka, M., and Pringle, K. J.: Aerosols in the pre-industrial atmosphere, Curr. Clim. Change Rep., 3, 1–15, doi: 10.1007/s40641-017-0061-2, 2017.

Cerully, K. M., Bougiatioti, A., Hite Jr., J. R., Guo, H., Xu, L., Ng, N. L., Weber, R., and Nenes, A.: On the link between hygroscopicity, volatility, and oxidation state of ambient and water-soluble aerosols in the southeastern United States, Atmos. Chem. Phys., 15, 8679–8694, doi: 10.5194/acp-15-8679-2015, 2015.

Cohen, A. J., Brauer, M., Burnett, R., Anderson, H. R., Frostad, J., Estep, K., Balakrishnan, K.,

Brunekreef, B., Dandona, L., Dandona, R., Feigin, V., Freedman, G., Hubbell, B., Jobling, A., Kan, H., Knibbs, L., Liu, Y., Martin, R., Morawska, L., Pope, C. A., Shin, H., Straif, K., Shaddick, G., Thomas, M., van Dingenen, R., van Donkelaar, A., Vos, T., Murray, C. J. L., and Forouzanfar, M. H.: Estimates and 25-year trends of the global burden of disease attributable to ambient air pollution: An analysis of data from the Global Burden of Diseases Study 2015, Lancet, 389, 1907–1918, doi: 10.1016/S0140-6736(17)30505-6, 2017.

Ditto, J. C., Barnes, E. B., Khare, P., Takeuchi, M., Joo, T., Bui, A. A. T., Lee-Taylor, J., Eris, G., Chen, Y., Aumont, B., Jimenez, J. L., Ng, N. L., Griffin, R. J., and Gentner, D. R.: An omnipresent diversity and variability in the chemical composition of atmospheric functionalized organic aerosol, Comm. Chem., 1, 75, doi: 10.1038/s42004-018-0074-3, 2018.

Dockery, D. W., Pope, C. A., Xu, X., Spengler, J. D., Ware, J. H., Fay, M. E., Ferris, B. G., and Speizer, F. E.: An association between air pollution and mortality in six U.S. cities, New Engl. J. Med., 329, 1753–1759, doi: 10.1056/NEJM199312093292401, 1993.

Donahue, N. M., Robinson, A. L., Stanier, C. O., and Pandis, S. N.: Coupled partitioning, dilution, and chemical aging of semivolatile organics, Environ. Sci. Technol., 40, 2635–2643, doi: 10.1021/es052297c, 2006.

Donahue, N. M., Epstein, S. A., Pandis, S. N., and Robinson, A. L.: A two-dimensional volatility basis set: 1. Organic-aerosol mixing thermodynamics, Atmos. Chem. Phys., 11, 3303–3318, doi: 10.5194/acp-11-3303-2011, 2011.

Du, Y., Xu, X., Chu, M., Guo, Y., and Wang, J.: Air particulate matter and cardiovascular disease: The epidemiological, biomedical and clinical evidence, J. Thorac. Dis., 8, E8–E19, doi: 10.3978/j.issn.2072-1439.2015.11.37, 2016.

Goldstein, A. H., and Galbally, I. E.: Known and unexplored organic constituents in the Earth's atmosphere, Environ. Sci. Technol., 41, 1514–1521, doi: 10.1021/es072476p, 2007.

Hallquist, M., Wenger, J. C., Baltensperger, U., Rudich, Y., Simpson, D., Claeys, M., Dommen, J., Donahue, N. M., George, C., Goldstein, A. H., Hamilton, J. F., Herrmann, H., Hoffmann, T., Iinuma, Y., Jang, M., Jenkin, M. E., Jimenez, J. L., Kiendler-Scharr, A., Maenhaut, W., McFiggans, G., Mentel, T. F., Monod, A., Prévôt, A. S. H., Seinfeld, J. H., Surratt, J. D., Szmigielski, R., and Wildt, J.: The formation, properties and impact of secondary organic aerosol: Current and emerging issues, Atmos. Chem. Phys., 9, 5155–5236, doi: 10.5194/acp-9-5155-2009, 2009.

Hildebrandt Ruiz, L., Paciga, A. L., Cerully, K. M., Nenes, A., Donahue, N. M., and Pandis, S. N.: Formation and aging of secondary organic aerosol from toluene: Changes in chemical composition, volatility, and hygroscopicity, Atmos. Chem. Phys., 15, 8301–8313, doi: 10.5194/acp-15-8301-2015, 2015.

Hong, J., Häkkinen, S. A. K., Paramonov, M., Äijälä, M., Hakala, J., Nieminen, T., Mikkilä, J., Prisle, N. L., Kulmala, M., Riipinen, I., Bilde, M., Kerminen, V.-M., and Petäjä, T.:

Hygroscopicity, CCN and volatility properties of submicron atmospheric aerosol in a boreal forest environment during the summer of 2010, Atmos. Chem. Phys., 14, 4733–4748, doi: 10.5194/acp-14-4733-2014, 2014.

Jimenez, J. L., Canagaratna, M. R., Donahue, N. M., Prévôt, A. S. H., Zhang, Q., Kroll, J. H., DeCarlo, P. F., Allan, J. D., Coe, H., Ng, N. L., Aiken, A. C., Docherty, K. S., Ulbrich, I. M., Grieshop, A. P., Robinson, A. L., Duplissy, J., Smith, J. D., Wilson, K. R., Lanz, V. A., Hueglin, C., Sun., Y. L., Tian, J., Laaksonen, A., Raatikainen, T., Rautiainen, J., Vaattovaara, P., Ehn, M., Kulmala, M., Tomlinson, J. M., Collins, D. R., Cubison, M. J., Dunlea, E., J., Huffman, J. A., Onasch, T. B., Alfarra, M. R., Williams, P. I., Bower, K., Kondo, Y., Schneider, J., Drewnick, F., Borrmann, S., Weimer, S., Demerjian, K., Salcedo, D., Cottrell, L., Griffin, R., Takami, A., Miyoshi, T., Hatakeyama, S., Shimono, A., Sun, J. Y, Zhang, Y. M., Dzepina, K., Kimmel, J. R., Sueper, D., Jayne, J. T., Herndon, S. C., Trimborn, A. M., Williams, L. R., Wood, E. C., Middlebrook, A. M., Kolb, C. E., Baltensperger, U., and Worsnop, D. R.: Evolution of organic aerosols in the atmosphere, Science, 326, 1525–1529, doi: 10.1126/science.1180353, 2009.

Kanakidou, M., Seinfeld, J. H., Pandis, S. N., Barnes, I., Dentener, F. J., Facchini, M. C., Van Dingenen, R., Ervens, B., Nenes, A., Nielsen, C. J., Swietlicki, E., Putaud, J. P., Balkanski, Y., Fuzzi, S., Horth, J., Moortgat, G. K., Winterhalter, R., Myhre, C. E. L., Tsigaridis, K., Vignati, E., Stephanou, E. G., and Wilson, J.: Organic aerosol and global climate modelling: a review, Atmos. Chem. Phys., 5, 1053–1123, doi: 10.5194/acp-5-1053-2005, 2005.

Kostenidou, E., Karnezi, E., Hite Jr., J. R., Bougiatioti, A., Cerully, K., Xu, L., Ng, N. L., Nenes, A., Pandis, S. N.: Organic aerosol in the summertime southeastern United States: Components and their link to volatility distribution, oxidation state and hygroscopicity, Atmos. Chem. Phys., 18, 5799–5819, doi: 10.5194/acp-18-5799-2018, 2018.

Kroll, J. H., Donahue, N. M., Jimenez, J. L., Kessler, S. H., Canagaratna, M. R., Wilson, K. R., Altieri, K. E., Mazzoleni, L. R., Wozniak, A. S., Bluhm, H., Mysak, E. R., Smith, J. D., Kolb, C. E., and Worsnop, D. R.: Carbon oxidation state as a metric for describing the chemistry of atmospheric organic aerosol, Nat. Chem., 3, 133–139, doi: 10.1038/nchem.948, 2011.

Kuwata, M., Chen, Q., and Martin, S. T.: Cloud condensation nuclei (CCN) activity and oxygen-to-carbon elemental ratios following thermodenuder treatment of organic particles grown by α-pinene ozonolysis, Phys. Chem. Chem. Phys., 13, 14571–14583, doi: 10.1039/c1cp20253g, 2011.

Massoli, P., Lambe, A. T., Ahern, A. T., Williams, L. R., Ehn, M., Mikkilä, J., Canagaratna, M. R., Brune, W. H., Onasch, T. B., Jayne, J. T., Petäjä, T., Kulmala, M., Laaksonen, A., Kolb, C. E., Davidovits, P., and Worsnop, D. R.: Relationship between aerosol oxidation level and hygroscopic properties of laboratory generated secondary organic aerosol (SOA) particles, Geophys. Res. Lett., 37, L24801, doi: 10.1029/2010GL045258, 2010.

Mei, F., Hayes, P. L., Ortega, A., Taylor, J. W., Allan, J. D., Gilman, J., Kuster, W., de Gouw, J., Jimenez, J. L., and Wang, J: Droplet activation properties of organic aerosols observed at an

urban site during CalNex-LA, J. Geophys. Res., 118, 2903–2917, doi: 10.1002/jgrd.50285, 2013.

Nakao, S.: Why would apparent κ linearly change with O/C? Assessing the role of volatility, solubility, and surface activity of organic aerosols, Aerosol Sci. Technol., 51, 1377–1388, doi: 10.1080/02786826.2017.1352082, 2017.

Petters, M. D., and Kreidenweis, S. M.: A single parameter representation of hygroscopic growth and cloud condensation nucleus activity, Atmos. Chem. Phys., 7, 1961–1971, doi: 10.5194/acp-7-1961-2007, 2007.

Poulain, L., Wu, Z., Petters, M. D., and Wex, H.: Towards closing the gap between hygroscopic growth and CCN activation for secondary organic aerosols – Part 3: Influence of the chemical composition on the hygroscopic properties of volatile fractions of aerosols, Atmos. Chem. Phys., 10, 3775–3785, doi: 10.5194/acp-10-3775-2010, 2010.

Pope, C. A., Turner, M. C., Burnett, R. T., Jerrett, M., Gapstur, S. M., Diver, W. R., Krewski, D., and Brook, R. D.: Relationships between fine particulate air pollution, cardiometabolic disorders, and cardiovascular mortality, Circ. Res., 116, 108–115, doi: 10.1161/CIRCRESAHA.116.305060, 2015.

Rickards, A. M. J., Miles, R. E. H., Davies, J. F., Marshall, F. H., and Reid, J. P.: Measurements of the sensitivity of aerosol hygroscopicity and the κ parameter to the O/C ratio, J. Phys. Chem., 117, 14120–14131, doi: 10.1021/jp407991n, 2013.

Riipinen, I., Pierce, J. R., Yli-Juuti, T., Nieminen, T., Häkkinen, S., Ehn, M., Junninen, H., Lehtipalo, K., Petäjä, T., Slowik, J., Chang, R., Shantz, N. C., Abbatt, J., Leaitch, W. R., Kerminen, V.-M., Worsnop, D. R., Pandis, S. N., Donahue, N. M., and Kulmala, M.: Organic condensation: A vital link connecting aerosol formation to cloud condensation nuclei (CCN) concentrations, Atmos. Chem. Phys., 11, 3865–3878, doi: 10.5194/acp-11-3865-2011, 2011.

Robinson, A. L., Donahue, N. M., Shrivastava, M. K., Weitkamp, E. A., Sage, A. M., Grieshop, A. P., Lane, T. E., Pierce, J. R., and Pandis, S. N.: Rethinking organic aerosols: Semivolatile emissions and photochemical aging, Science, 315, 1259–1262, doi: 10.1126/science.1133061, 2007.

Ruehl, C. R., Chuang, P. Y., Nenes, A., Cappa, C. D., Kolesar, K. R., & Goldstein, A. H.: Strong evidence of surface tension reduction in microscopic aqueous droplets, Geophys. Res. Lett., 39, L23801, doi: 10.1029/2012GL053706, 2012.

Seinfeld, J. H., Bretherton, C., Carslaw, K. S., Coe, H., DeMott, P. J., Dunlea, E. J., Feingold, G., Ghan, S., Guenther, A. B., Kahn, R., Kraucunas, I., Kreidenweis, S. M., Molina, M., J., Nenes, A., Penner, J. E., Prather, K. A., Ramanathan, V., Ramaswamy, V., Rasch, P. J., Ravishankara, A. R., Rosenfeld, D., Stephens, G., and Wood, R.: Improving our fundamental understanding of the role of aerosol-cloud interactions in the climate system, Proc. Natl. Acad. Sci., 113, 5781–5790, doi: 10.1073/pnas.1514043113, 2016.

Seinfeld, J. H., and Pandis, S. N.: Atmospheric Chemistry and Physics, 3rd ed, John Wiley & Sons, Inc, Hoboken, NJ, 2016.

Shiraiwa, M., Ueda, K., Pozzer, A., Lammel, G., Kampf, C. J., Fushimi, A., Enami, S., Arangio, A. M., Fröhlich-Nowoisky, J., Fujitani, Y., Furuyama, A., Lakey, P. S. J., Lelieveld, J., Lucas, K., Morino, Y., Pöschl, U., Takahama, S., Takami, A., Tong, H., Weber, B., Yoshino, A., and Sato, K.: Aerosol health effects from molecular to global scales, Environ. Sci. Technol., 51, 13545–13567, doi: 10.1021/acs.est.7b04417, 2017.

Shrivastava, M., Cappa, C. D., Fan, J., Goldstein, A. H., Guenther, A. B., Jimenez, J. L., Kuang, C., Laskin, A., Martin, S. T., Ng, N. L., Petäjä, T., Pierce, J. R., Rasch, P. J., Roldin, P., Seinfeld, J. H., Shilling, J., Smith, J. N., Thornton, J. A., Volkamer, R., Wang, J., Worsnop, D. R., Zaveri, R. A., Zelenyuk, A., and Zhang, Q.: Recent advances in understanding secondary organic aerosol: Implications for global climate forcing, Rev. Geophys., 55, 509–559, doi: 10.1002/2016RG000540, 2017.

Tritscher, T., Dommen, J., Decarlo, P. F., Gysel, M., Barmet, P. B., Praplan, A. P., Weingartner, E., Prévôt, A. S. H., Riipinen, I., Donahue, N. M., and Baltensperger, U.: Volatility and hygroscopicity of aging secondary organic aerosol in a smog chamber, Atmos. Chem. Phys., 11, 11477–11496, doi: 10.5194/acp-11-11477-2011, 2011.

Tsigaridis, K., Daskalakis, N., Kanakidou, M., Adams, P. J., Artaxo, P., Bahadur, R., Balkanski, Y., Bauer, S. E., Bellouin, N., Benedetti, A., Bergman, T., Berntsen, T. K., Beukes, J. P., Bian, H., Carslaw, K. S., Chin, M., Curci, G., Diehl, T., Easter, R. C., Ghan, S. J., Gong, S. L., Hodzic, A., Hoyle, C. R., Iversen, T., Jathar, S., Jimenez, J. L., Kaiser, J. W., Kirkevåg, A., Koch, D., Kokkola, H., Lee, Y. H., Lin, G., Liu, X., Luo, G., Ma, X., Mann, G. W., Mihalopoulos, N., Morcrette, J.-J., Müller, J.-F., Myhre G., Myriokefalitakis, S., Ng, N. L., O'Donnell, D., Penner, J. E., Pozzoli, L., Pringle, K. J., Russell, L. M., Schulz, M., Sciare, J., Seland, Ø., Shindell, D. T., Sillman, S., van Noije, T., van Zyl, P. G., von Salzen, K., Yu, F., Wang, Z., Wang., Z., Zaveri, R. A., Zhang, H., Zhang, K., Zhang, Q., and Zhang, X.: The AeroCom evaluation and intercomparison of organic aerosol in global models, Atmos. Chem. Phys., 14, 10845–10895, doi: 10.5194/acp-14-10845-2014, 2014.

Tsigaridis, K., and Kanakidou, M.: The present and future of secondary organic aerosol direct forcing on climate, Curr. Clim. Change Rep., 4, 84–98, doi: 10.1007/s40641-018-0092-3, 2018.

Zhang, Q., Jimenez, J. L., Canagaratna, M. R., Allan, J. D., Coe, H., Ulbrich, I., Alfarra, M. R., Takami, A., Middlebrook, A. M., Sun, Y. L., Dzepina, K., Dunlea, E., Docherty, K., DeCarlo, P. F., Salcedo, D., Onasch, T., Jayne, J. T., Miyoshi, T., Shimono, A., Hatakeyama, S., Takegawa, N., Kondo, Y., Schneider, J., Drewnick, F., Borrmann, S., Weimer, S., Demerjian, K., Williams, P., Bower, K., Bahreini, R., Cottrell, L., Griffin, R. J., Rautiainen, J., Sun, J. Y., Zhang, Y. M., and Worsnop, D. R.: Ubiquity and dominance of oxygenated species in organic aerosols in anthropogenically-influenced Northern Hemisphere midlatitudes, Geophys. Res. Lett., 34, L13801, doi: 10.1029/2007GL029979, 2007.

Chapter 2

A technique for the measurement of organic aerosol hygroscopicity, oxidation level, and volatility distributions[1]

[1] Published as: Cain, K. P. and Pandis, S. N.: A technique for the measurement of organic aerosol hygroscopicity, oxidation level, and volatility distributions, Atmos. Meas. Tech., 10, 4865–4676, doi: 10.5194/amt-10-4865-2017, 2017.

2.1 Abstract

Hygroscopicity, oxidation level, and volatility are three crucial properties of organic pollutants. This study assesses the feasibility of a novel measurement and analysis technique to determine these properties and establish their relationship. The proposed experimental setup utilizes a cloud condensation nuclei (CCN) counter to quantify hygroscopic activity, an aerosol mass spectrometer to measure the oxidation level, and a thermodenuder to evaluate the volatility. The setup was first tested with secondary organic aerosol (SOA) formed from the ozonolysis of α-pinene. The results of the first experiments indicated that, for this system, the less volatile SOA contained species that had on average lower O:C ratios and hygroscopicities. In this SOA system, both low and high volatility components can have comparable oxidation levels and hygroscopicities. The method developed here can be used to provide valuable insights about the relationships among organic aerosol hygroscopicity, oxidation level, and volatility.

2.2 Introduction

Anthropogenic activities, such as fuel combustion, as well as biogenic sources, such as emissions from vegetation, can introduce particles and particle precursors into the atmosphere. These airborne particles have been identified as a factor contributing to cardiovascular and respiratory diseases (Pope, 2000; van Eeden et al., 2005) and an increased risk for acute morbidity and mortality (Brook et al., 2010). In addition, atmospheric aerosols influence the Earth's radiation balance directly by scattering and absorbing solar radiation and indirectly by serving as cloud condensation nuclei (CCN). Despite their major role in the Earth's energy balance, their net effect on climate is one of the major uncertainties in the climate change problem (IPCC, 2013).

In most areas, organic compounds represent anywhere from 20–90% of the submicron aerosol mass (Murphy et al., 2006; Zhang et al., 2007). Organic aerosol (OA) is traditionally

classified either as primary (POA) or secondary (SOA). POA refers to organic compounds that are emitted to the atmosphere directly in the particulate phase. SOA refers to particulate matter produced by gas-to-particle conversion processes. In general, intermediate volatility, semi-volatile, and volatile organic compounds undergo oxidation in the atmosphere and form products that can produce new particles and condense on pre-existing particles.

Three of the most important properties regarding OA lifetime in the atmosphere are hygroscopicity, oxidation level, and volatility. Hygroscopicity, often quantified by the hygroscopicity parameter, κ (Petters and Kreidenweis, 2007), is a measure of the volume of water associated with a unit volume of solute. Oxidation level often provides an indication of the age of the OA in the atmosphere. It is expressed as the oxygen to carbon (O:C) ratio or, more accurately, the average carbon oxidation state (OS_C). Volatility determines the partitioning of organic compounds between the gas and particle phases. The one-dimensional volatility basis set (1D-VBS, Donahue et al., 2006) has been proposed as a framework for the description of the evolution of the OA volatility distribution using logarithmically spaced bins.

Several studies have shown that SOA from the ozonolysis of α-pinene is reasonable CCN material (VanReken et al., 2005; Huff Hartz et al., 2005; Prenni et al., 2007; King et al., 2007; Engelhart et al., 2008; King et al., 2009; Wex et al., 2009; Massoli et al., 2010; Kuwata et al., 2011; Frosch et al., 2011). These studies all reported similar κ values based on measurements at supersaturated conditions, ranging from 0.07–0.15. Huff-Hartz et al. (2005) found that SOA produced from monoterpenes was more hygroscopic than SOA from sesquiterpenes. Both King et al. (2007) and Kuwata et al. (2011) observed that the CCN behavior of α-pinene ozonolysis SOA was dependent on the OA mass concentration. Frosch et al. (2011) found that κ for α-pinene ozonolysis SOA increased with chemical aging.

Hygroscopic properties of α-pinene ozonolysis SOA have also been studied using subsaturated conditions (Prenni et al., 2007; Wex et al., 2009; Poulain et al., 2010; Massoli et al., 2010; Tritscher et al., 2011). These studies determined a hygroscopic growth factor (HGF) to estimate κ, reporting values from 0.01–0.08. Massoli et al. (2010) used both a hygroscopic tandem differential mobility analyzer (H-TDMA) and a CCN counter while studying SOA from the ozonolysis of α-pinene and found that the κ at subsaturated conditions (estimated from HGF measurements) was 20–50% lower than that based on CCN measurements at supersaturated conditions. A number of explanations have been proposed for this behavior including increasing dissolution of SOA components at supersaturated conditions, surface tension effects, etc. (Petters et al., 2009; Good et al., 2010).

The oxidation level of α-pinene ozonolysis SOA has mainly been studied through the use of high resolution mass spectrometry (Bahreini et al., 2005; Alfarra et al., 2006; Song et al., 2007; Shilling et al., 2009; Huffman et al., 2009; Poulain et al., 2010; Massoli et al., 2010; Kuwata et al., 2011; Tritscher et al., 2011; Frosch et al., 2011). These studies reported O:C ratios from around 0.3–1. The higher O:C ratios were determined by Massoli et al. (2010) for extended periods of chemical aging; most of the average O:C ratios ranged from 0.3 to 0.5. The use of the O:C ratio can allow for easier classification of OA into different classes using the two-dimensional volatility basis set (2D-VBS, Donahue et al., 2011). Poulain et al. (2010) observed that the most oxygenated compounds were less volatile than the less oxygenated ones, and Kuwata et al. (2011) found that the O:C ratio for α-pinene ozonolysis SOA depended on the mass concentration.

In addition to hygroscopicity and oxidation level, there have been a number of studies focusing on the volatility of SOA from the ozonolysis of α-pinene with either a thermodenuder (TD) (An et al., 2007; Kostenidou et al., 2009; Huffman et al., 2009; Poulain et al., 2010; Lee et

al., 2011; Cappa and Wilson, 2011; Kuwata et al., 2011) or a volatility tandem differential mobility analyzer (V-TDMA) (Stanier et al., 2007; Jonsson et al., 2007; Tritscher et al., 2011). The difficulty in comparing these volatility studies stems from different heating methods (TD, V-TDMA, etc.), residence times in heating sections, and temperatures. For example, Poulain et al. (2010) observed nearly all of the SOA evaporated at 200°C at a residence time of 9 s in the heating section of a TD, but Lee et al. (2011) reported that most of the SOA evaporated at around 90°C for a residence time of 16 s. The use of the 1D-VBS (Donahue et al., 2006) can help overcome this obstacle, making it easier to compare volatility distributions rather than thermograms, which express the mass fraction remaining (MFR) as a function of temperature and are influenced by several different experimental factors (particle size, residence time in heating section, OA concentration, etc.) (Cappa, 2010; Riipinen et al., 2010; Kuwata et al., 2011). Furthermore, the evolution of OA's volatility distribution can provide an indirect way to gain insights about the very difficult to measure chemical composition and evolution of these compounds (Donahue et al., 2011).

Several studies have attempted to relate two of the three properties, but few have attempted to relate all three. Jimenez et al. (2009) proposed that the hygroscopicity of OA generally increases with the oxidation level expressed by the O:C ratio and that there is also an inverse relationship between the O:C ratio and volatility. Tritscher et al. (2011) used a volatility and hygroscopicity tandem differential mobility analyzer (V/H-TDMA) and an Aerodyne High-Resolution Time-of-Flight Aerosol Mass Spectrometer (HR-ToF-AMS, hereafter AMS) during the chemical aging of α-pinene SOA and found that volatility decreased while hygroscopicity and the O:C ratio remained fairly constant. Cerully et al. (2015) used a TD followed by a CCN counter, a scanning mobility particle sizer (SMPS), and an AMS in parallel and observed small changes in hygroscopicity for

ambient OA components with dramatically different volatilities and concluded that the more volatile compounds were more hygroscopic than the remaining material. Several other studies (Poulain et al., 2010; Kuwata et al., 2011; Hong et al., 2014; Hildebrandt Ruiz et al., 2015) have investigated the effects of environmental parameters on one or all of these properties. However, these results are often inconclusive or even contradictory and the links among these three properties are yet to be elucidated.

A theoretical framework (Nakao, 2017) has attempted to relate these three properties using the 2D-VBS framework (Donahue et al., 2011). The approach utilized correlations between the O:C ratio, volatility, and hygroscopicity to predict lines of constant κ in the 2D-VBS. The study concluded that relatively volatile OA components with a low O:C ratio can have the same hygroscopicity as OA with lower volatility and a higher O:C ratio.

One major obstacle pertaining to an experimentally-determined relationship between these three properties for ambient aerosols is the often unknown or uncertain composition. The AMS can quantify the concentrations of the non-refractory inorganic aerosol components as well as the total organic aerosol concentration, with further separation of the OA into components provided by techniques like positive matrix factorization (PMF). However, the analysis of the combined measurements of all three properties remains challenging.

The purpose of this work is the development of a method for the synchronous measurement of OA hygroscopicity, oxidation level, and volatility. In the next section, we describe the technique that utilizes a suite of aerosol instrumentation to measure these properties. Then, the method is tested with α-pinene ozonolysis SOA. This SOA system has been studied extensively so it can be a useful first test for the proposed experimental approach. Our objective is not to perform a comprehensive study of the properties of this SOA (which depend on SOA levels, relative

humidity, etc.), but rather to use it as a pilot study. Finally, a data analysis technique is developed to interpret and synthesize the corresponding measurements.

2.3 Methodology

2.3.1 Instrument setup

A schematic of the experimental setup can be seen in Fig. 2.1. Particles are sampled through either a TD or a by-pass (BP) line via two three-way valves and then the sample stream is split using a T union between an AMS and a differential mobility analyzer (DMA, TSI, model 3081). The stream from the DMA is split again with a T union between a condensation particle counter (CPC, TSI, model 3010/72) and a CCN counter (CCNC, Droplet Measurement Technologies). In this study, the AMS used a flow rate of 0.1 L min^{-1} while the CPC and the CCNC used 0.3 and 0.5 L min^{-1} respectively. The sheath flow in the DMA was set to 8 L min^{-1} to allow for a 10:1 sheath to aerosol flow ratio as the particles were classified. The upscan of the DMA was set to 120 s and the downscan was set to 15 s.

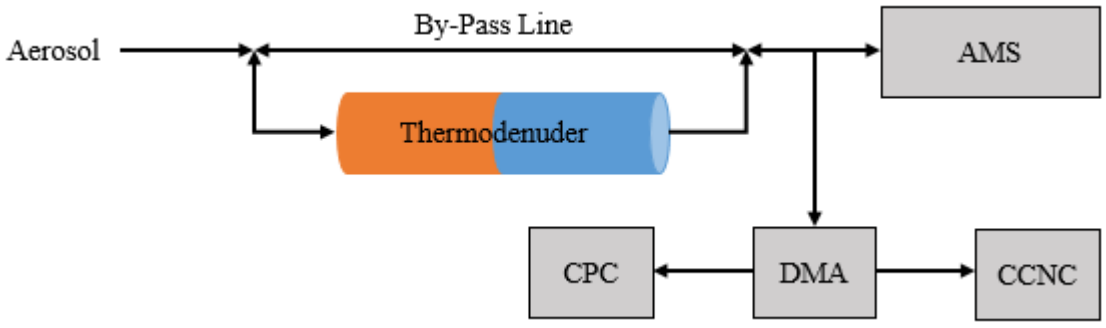

Figure 2.1. Schematic of the experimental setup for the hygroscopicity, oxidation level, and volatility measurements. The sampling technique employs a TD to measure volatility, an AMS to study the oxidation level, and a CCNC to determine hygroscopic activity.

In a typical experiment, once particles are ready for sampling, they pass through the TD at the first temperature set point for 15-25 min. Then, the particles are sent through the BP as the temperature of the TD increases (another 15-25 min). Once the TD reaches the next set point, the particles are directed through the TD for the same sampling period and this process is repeated until measurements at all desired temperatures have been obtained. Total sampling time for 4–5 temperature set points is around 2.5–3.5 hr. Set points for the TD start at the lowest temperature and always increase.

2.3.2 Hygroscopicity

Hygroscopicity measurements were made with a CCNC, which generates supersaturations by exploiting water's higher mass diffusivity than heat's thermal diffusivity in air (Roberts and Nenes, 2005). The CCNC's fast response time allows it to be coupled to an SMPS, a technique called Scanning Mobility CCN Analysis (SMCA, Moore et al., 2010). In our experiments, polydisperse aerosol was charged with a Po-210 neutralizer and then entered a DMA where the particles were classified by their electrical mobility and counted by a CPC and the CCNC as the DMA voltage was scanned. Particle number concentrations (CN) and size distributions were obtained from the SMPS using the AIM software. CCN concentrations and size distributions were obtained following the technique described in Moore et al. (2010). The SMPS and CCNC size distributions were aligned by matching the minimum in concentration that occurs during the transition between the DMA upscan and downscan. An activation curve was produced by dividing the CCN concentration by the CN concentration at each size. The activation diameter was calculated by fitting the activation curve to a sigmoidal function:

$$\frac{\mathrm{CCN}}{\mathrm{CN}} = \frac{B}{\left(1+\frac{D_d}{D_{p50}}\right)^c} \tag{2.1}$$

where CCN/CN is the fraction of activated particles, B and c describe the asymptote and slope of the sigmoid respectively, D_d is the dry diameter, and D_{p50} is the diameter at which 50% of the particles activate for a symmetric size distribution; this corresponds to the activation diameter.

The method to determine κ follows the analysis done by Petters and Kreidenweis (2007) and will be explained briefly here. The defining equation is known as the κ-Köhler equation:

$$S = \frac{D^3\text{-}D_d^3}{D^3\text{-}D_d^3(1\text{-}\kappa)} \exp\left(\frac{4\sigma M_w}{RT\rho_w D}\right) \tag{2.2}$$

where S is the saturation ratio, D is the wet particle diameter, D_d is the dry diameter, σ is the surface tension of the solution/air interface, M_w is the molecular weight of water, R is the universal gas constant, T is the temperature, and ρ_w is the density of water. For a selected D_d and κ, the critical supersaturation, S_c, can be computed from the maximum of Eq. (2.2). Then, lines of constant κ can be obtained by plotting $\log(S_c)$ as a function of $\log(D_d)$. To estimate κ, experimentally-determined activation diameters at different supersaturations were added to the $\log(S_c)$-$\log(D_d)$ plot and the κ was estimated by which isopleth fit the data.

2.3.3 Oxygen content

An AMS was used to monitor the aerosol's composition. In our experiments, the AMS was operated in the V-mode (DeCarlo et al., 2006) and used an averaging time of one minute. The data were analyzed in Igor Pro 6.22A (Wavemetrics) using "Squirrel" version 1.56D for unit mass resolution analysis and "Pika" version 1.15D for high resolution analysis. The O:C ratios reported here were calculated using the Canagaratna et al. (2015) method.

2.3.4 Volatility

Volatility measurements were made with the TD and the SMPS. These instruments were used to generate thermograms. To calculate the MFR, we divided the TD mass at each SMPS measurement by an interpolated BP mass using the BP measurements before and after the TD measurements. The MFR represents the fraction of particle mass that did not evaporate in the TD. The thermogram can be combined with a TD model (Riipinen et al., 2010), which describes the multicomponent OA evaporation to calculate the OA volatility distribution. The fitting algorithm has been described and evaluated by Karnezi et al. (2014). The 1D-VBS (Donahue et al., 2006) is used here, which discretizes the volatility distribution into logarithmically spaced bins based on an effective saturation concentration, C^*.

The TD used for this study consisted of two parts: a heating section and a cooling section. The heating section is 2 ft long and is surrounded by heating tape to control the temperature. The cooling section is also 2 ft long and contains activated carbon to avoid any recondensation while the aerosol returns to room temperature. Aerosol passes through the entire TD via 1.5 in. tubing. Therefore, after accounting for all of the flows, there will be laminar flow in the TD, resulting in a centerline residence time of 23 s at 298 K in the heating section, but the residence time will be shorter for the higher temperatures used in this study.

As particles pass through the TD, some of the mass will evaporate, but some particles will also be lost to the walls. To characterize these losses, NaCl particles were generated and passed through the BP and TD alternately for several temperatures. By comparing the size distributions through the BP and TD, the particle losses were quantified as a function of temperature and particle size for the flowrate used in our experiments (Fig. A.1). Particle losses increased with temperature

in the TD, but were fairly low (< 25% at 125°C) and roughly constant over the size range of interest in this study (50–250 nm).

2.3.5 Smog chamber setup

All experiments were conducted in the Carnegie Mellon University smog chamber, a 10 m^3 Teflon (Welch Fluorocarbons) reactor suspended in a temperature-controlled room (Pathak et al., 2007). Before each experiment, the chamber was flushed overnight with purified air under UV illumination (GE, model 10526 and 10244) to remove any potential contaminants. Purified air was generated by passing compressed air through a high-efficiency particulate air (HEPA) filter to remove any particles, an activated carbon filter to remove any vapors, and silica gel to maintain the relative humidity (RH) at less than 5%.

2.4 System test with ammonium sulfate aerosol

To determine whether the proposed and rather complex setup of several instruments operating together in series and in parallel was operating properly, a 1 g L^{-1} solution of ammonium sulfate was pumped through an atomizer (TSI, model 3075) at a constant rate of 90 mL h^{-1} using a constant output syringe pump (Braintree Scientific, model BS-300). Before entering the chamber, the resulting droplets passed through a silica gel dryer to produce dry particles. Ammonium sulfate particles have traditionally been used in TD and CCN tests because they are easy to produce and are relatively non-volatile at temperatures below approximately 100°C (Clarke, 1991; An et al., 2007). Furthermore, they are very hygroscopic with well-known properties. Their CCN activity has been shown to be consistent with Köhler theory (Cruz and Pandis, 1997). At different TD temperatures below 100°C, ammonium sulfate particles should behave the same hygroscopically as the particles passing through the BP.

The thermogram for the ammonium sulfate particles is shown in Fig. 2.2a. No aerosol mass evaporated at 50 and 100°C, but nearly all of the mass evaporated at 150°C. The remaining material at 150°C also included impurities in the ammonium sulfate solution that do not evaporate at that temperature. The measured activation diameter for the BP, two TD temperatures (50 and 100°C), and Köhler theory from this experiment is shown in Fig. 2.2b. The activation diameters at all supersaturations through the BP and the TD agreed with Köhler theory, confirming that our system operates properly for at least this simple model system.

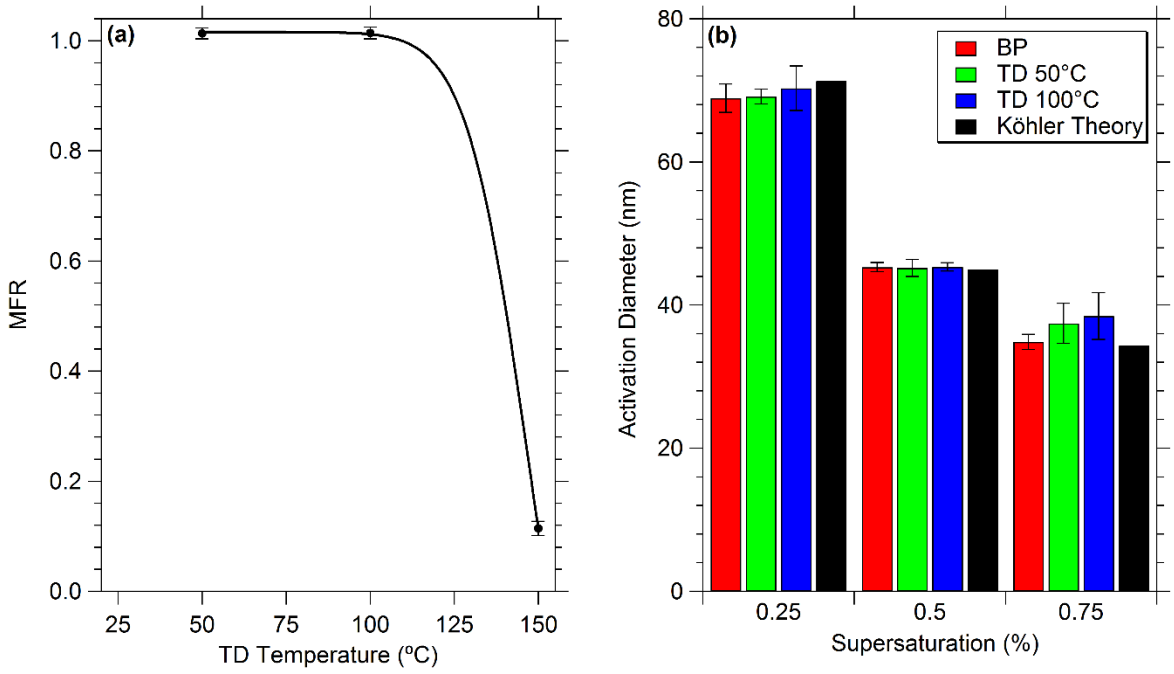

Figure 2.2. (a) The thermogram for ammonium sulfate aerosol. (b) The calculated activation diameter at three CCNC supersaturations for the BP (red), two TD temperatures (green and blue), and Köhler theory (black) for ammonium sulfate aerosol. The error bars represent one standard deviation of the mean.

2.5 Application to α-pinene ozonolysis SOA

The experimental approach was then applied to SOA. For these experiments, α-pinene (Sigma-Aldrich, ≥ 99%) was injected into the chamber using a heated septum injector with purified

air as carrier flow. Ozone was generated by an ozone generator (AZCO, model HTU-500ACPS) and injected into the chamber after the α-pinene injection. Table 2.1 displays the different experimental conditions examined in this pilot study. The initial ozone concentration and RH remained almost the same in all experiments, but the initial α-pinene concentration and water supersaturation in the CCNC were varied.

Table 2.1. Description of experimental conditions used in this study.

Exp.	α-Pinene (ppb)	Ozone (ppb)	RH (%)	Supersaturation (%)[a]	Max. OA (μg m^{-3})
1	100	~500	<15	0.20	108
2	50	~500	<15	0.30	35
3	50	~500	<15	0.25	39
4	50	~500	<15	0.27	46

[a]CCNC supersaturation was held constant during experiments in order to allow sufficient time for an average activation diameter to be measured at each TD temperature.

For Experiment 1, 100 ppb of α-pinene were injected into the chamber immediately followed by around 500 ppb of ozone. After one hour of reaction time, the ozonolysis was practically complete and particles were sampled through the TD and BP alternatively for five temperatures (25, 50, 75, 100, and 125°C). The SOA mass concentration, measured with the SMPS assuming a density of 1.4 g cm^{-3} (Kostenidou et al., 2007), increased immediately following the ozone injection and reached a maximum of around 108 μg m^{-3}. The SOA then began decreasing due to particles being lost to the chamber walls.

To check that the SOA sampled at the beginning of the experiment was similar to the SOA sampled at the end of the experiment, we compared the corresponding AMS mass spectra using the theta angle (θ) proposed by Kostenidou et al. (2009). The θ angle between the mass spectra of the BP at the beginning of the experiment and the BP before passing through the TD at 125°C was

2.4°, indicating that the change of the SOA's spectra during the experiment was minimal. The same behavior was observed in all other experiments in this study.

The thermogram, TD model prediction, and corresponding estimated volatility distribution, using the Karnezi et al. (2014) algorithm, for Experiment 1 are shown in Fig. 2.3. The TD model reproduced the MFR measurements well. For this experiment with OA around 100 μg m^{-3}, over two-thirds of the SOA had an effective saturation concentration (C^*) of 1 or 10 μg m^{-3}, 20% had a C^* = 0.1 μg m^{-3}, and 10% had a C^* = 0.01 μg m^{-3}. The C^* = 0.01 μg m^{-3} bin also includes compounds with even lower volatilities. An effective enthalpy of vaporization, ΔH_{vap}, equal to 65 kJ mol^{-1} was estimated assuming an accommodation coefficient equal to unity.

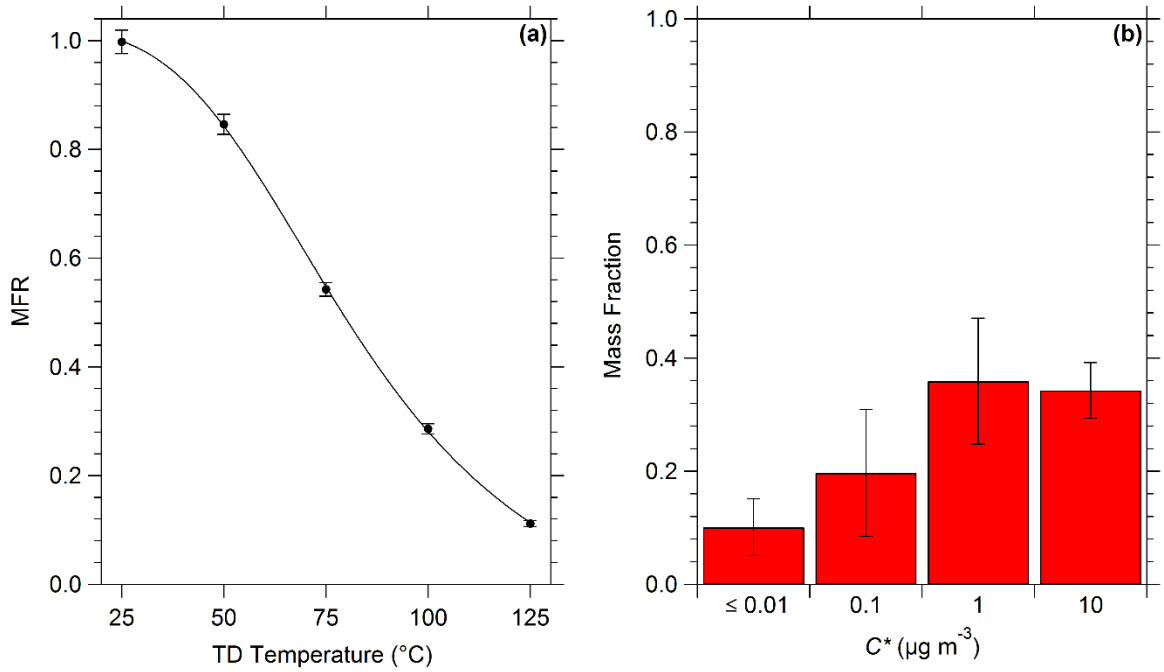

Figure 2.3. (a) Thermogram, corrected for losses in the TD, for Experiment 1 with the fit from the TD model (Riipinen et al., 2010; Karnezi et al., 2014). The error bars represent one standard deviation of the mean. (b) SOA volatility distribution for Experiment 1 using the 1D-VBS framework (Donahue et al., 2006). The error bars correspond to one standard deviation of the solution calculated by the model.

Our TD results are comparable to those in the literature for α-pinene ozonolysis SOA. At 100°C, the MFR for the SOA in Experiment 1 was 0.29 ± 0.01. Huffman et al. (2009) and Poulain et al. (2010) reported a MFR of around 0.35 at 100°C, but their SOA levels were several times larger (4–6) and their residence times were about half of the one used in this study. Kuwata et al. (2011) observed a MFR of 0.50 at a TD temperature of 100°C for lower SOA levels (25–37 μg m^{-3}) and a significantly shorter residence time (0.4 s). This further reiterates the difficulty in comparing volatility studies using different experimental methods, which is why our study uses the 1D-VBS, allowing for comparisons between studies, regardless of TD operating conditions.

In addition to volatility, the SOA's oxygen content was also measured. Figure 2.4 shows the average O:C ratio through the BP and TD at different temperatures for Experiment 1. The O:C ratio started around 0.49 and decreased at higher temperatures, ending at 0.39 while passing through the TD at 125°C. All of the O:C ratios at a TD temperature of 50°C and above were statistically lower than the O:C ratios through the BP and TD at 25°C (one-tailed *t*-test, $p < 0.0001$). The final O:C ratio of 0.39 corresponds to 11% of the least volatile SOA (Fig. 2.3a). When compared to an O:C ratio of 0.49 through the BP, an O:C ratio of 0.39 through the TD at 125°C indicates that the least volatile material in these experiments contained components that were not very oxidized at least on average.

Our O:C ratios fall into the reported range of O:C ratios in the literature for α-pinene ozonolysis SOA (Huffman et al., 2009; Massoli et al., 2010; Kuwata et al., 2011; Tritscher et al., 2011). Kuwata et al. (2011) observed that the O:C ratio dropped sometimes due to high TD temperatures, but argued that increases in the mass concentration were the main cause of the O:C ratio decreasing. Poulain et al. (2010) reported that the more oxygenated compounds were less volatile than the less oxygenated ones, which contradicts our results, but their conclusions were

based on changing the RH at which the SOA was formed, which could impact the SOA's response to heat treatment.

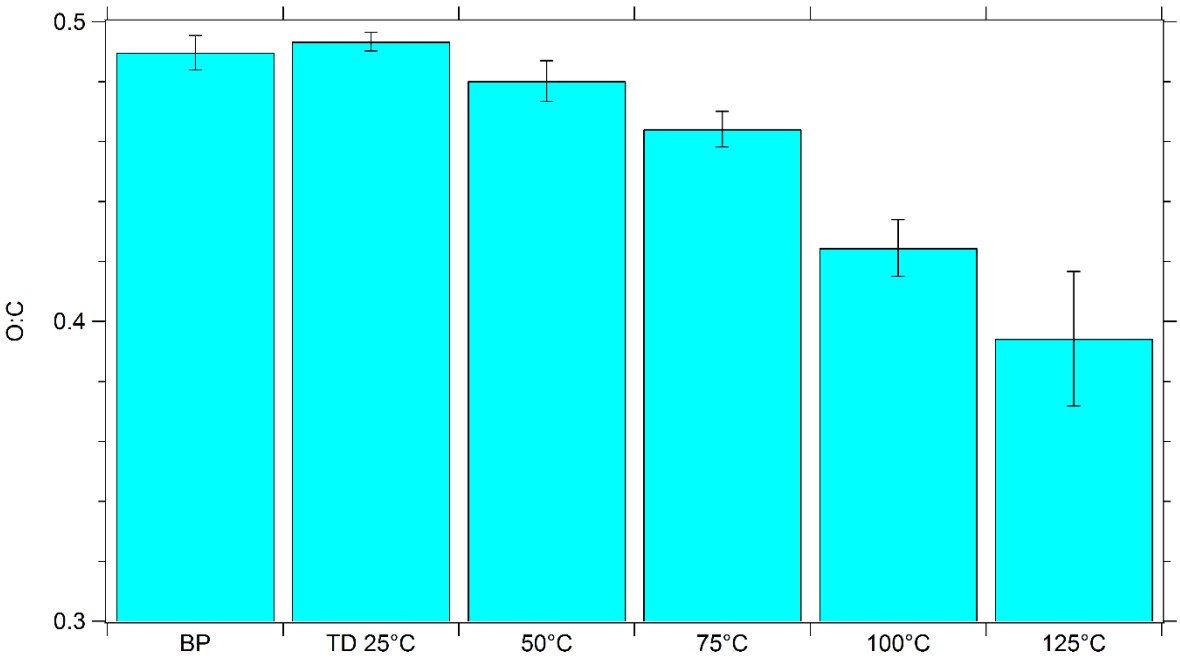

Figure 2.4. The average O:C ratio observed through the BP and several TD temperatures for Experiment 1. The error bars represent one standard deviation of the mean. The O:C ratios at a TD temperature of 50°C and greater were statistically smaller than the values at the BP and the TD at 25°C.

The SOA's hygroscopic activity was also measured at the same time. The measured activation diameter as a function of temperature for Experiment 1 is shown in Fig. 2.5a. The activation diameter of all the SOA remained fairly constant around 140 nm (0.2% supersaturation) during the experiment and as the temperature in the TD increased to 50°C. However, for even higher TD temperatures, the activation diameter increased, ending at 155 nm (0.2% supersaturation) for the least volatile 11% of the SOA. The activation diameters through the TD at temperatures of 75°C and greater were statistically larger than the activation diameter through either the BP or TD at 25°C (one-tailed *t*-test, $p < 0.0001$). This indicates that the least volatile

components of the α-pinene ozonolysis SOA also contained components that were not very hygroscopic. This is contradictory to the hypothesis of Jimenez et al. (2009), who proposed that the least volatile material is usually the most processed and therefore the most hygroscopic. However, the least volatile material in all our experiments had consistently the lowest O:C ratio and highest activation diameter, indicating a more complex relationship between hygroscopicity, oxidation level, and volatility in this system. There is however the possibility that chemical changes that occurred to the particles within the TD rendered them less CCN active.

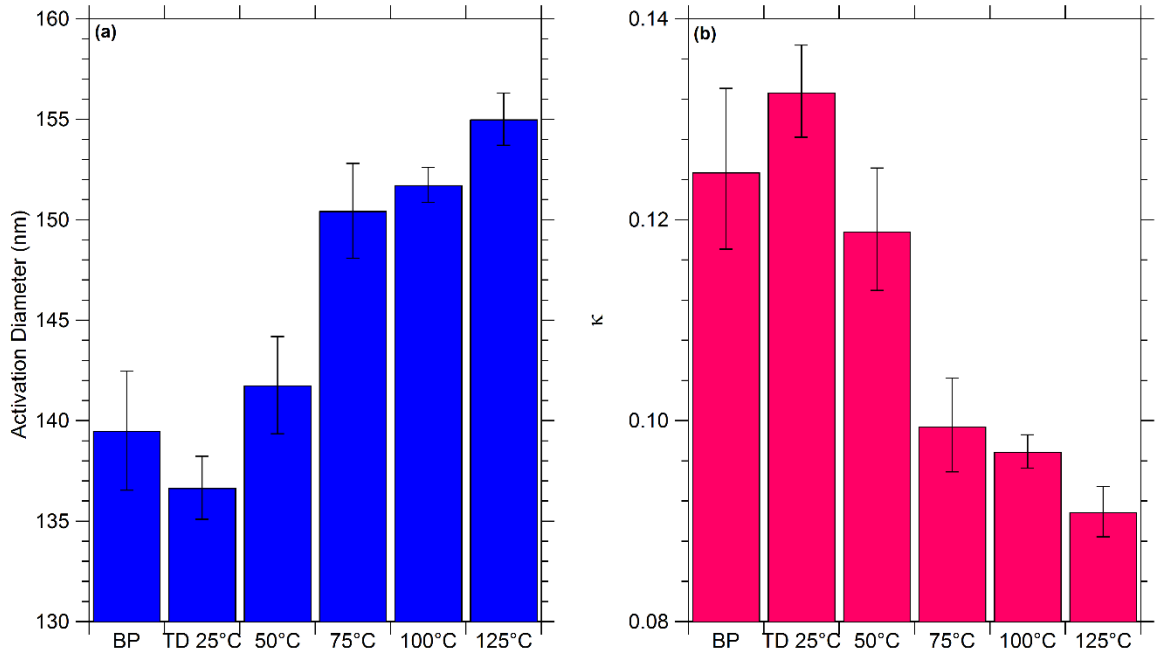

Figure 2.5. (a) The average activation diameter observed at 0.2% supersaturation in the CCNC for Experiment 1. The error bars represent one standard deviation of the mean. (b) The estimated κ values for Experiment 1. The error bars were obtained by estimating the κ at +/- one standard deviation of the average activation diameter measured. The values at TD temperatures of 75°C and greater were statistically different from the values at the BP and the TD at 25°C.

The estimated κ parameters as a function of TD temperature in Experiment 1 can be seen in Fig. 2.5b. Similar to the pattern observed with the activation diameters, the κ through the TD at

temperatures greater than or equal to 75°C were statistically lower than the κ through either the BP or TD at 25°C (one-tailed *t*-test, $p < 0.0001$), reiterating the notion that the least volatile SOA contained components that were less hygroscopic than the rest of the SOA. The κ's obtained in all experiments were similar to observed values for α-pinene ozonolysis SOA in other CCNC studies (Engelhart et al., 2008; Massoli et al., 2010; Frosch et al., 2011) and the decrease in hygroscopicity after heat treatment has also been reported by Kuwata et al. (2011).

Detailed results for Experiments 2, 3, and 4 can be found in Appendix A. They were all conducted with 50 ppb of α-pinene and around 500 ppb of ozone, generating around 40 μg m^{-3} of SOA. In general, the O:C ratios and κ's were slightly higher than those in Experiment 1. However, as with Experiment 1, these experiments also resulted in statistically lower O:C ratios and κ's through the TD at higher temperatures. The following section proposes and discusses a novel analysis method to further investigate this behavior.

2.6 Relating hygroscopicity and O:C with volatility

The above data can be used to estimate the SOA's hygroscopicity and oxidation level as a function of volatility. The compounds in a volatility bin, *i*, have an average O:C ratio, $[O:C]_i$, and hygroscopicity parameter, κ_i. The O:C ratio and κ distributions as a function of volatility can be determined utilizing the data obtained at each TD temperature by using the following equations:

$$[O:C]_{TD} = \sum_{i=1}^{n} x_{i,TD} [O:C]_i \quad (2.3)$$

$$\kappa_{TD} = \sum_{i=1}^{n} x_{i,TD} \kappa_i \quad (2.4)$$

where $[O:C]_{TD}$ and κ_{TD} are the measured O:C ratio and κ at a TD temperature, $x_{i,TD}$ is the SOA mass fraction in the i^{th} bin at the same temperature, and $[O:C]_i$ and κ_i are the unknown O:C ratio and κ for the i^{th} bin. The mass fraction for each bin as a function of TD temperature is estimated

by the TD model. An example for Experiment 1 is shown in Fig. 2.6. As expected, as the temperature in the TD increases, the more volatile components evaporate and the SOA is comprised of mostly low volatility compounds.

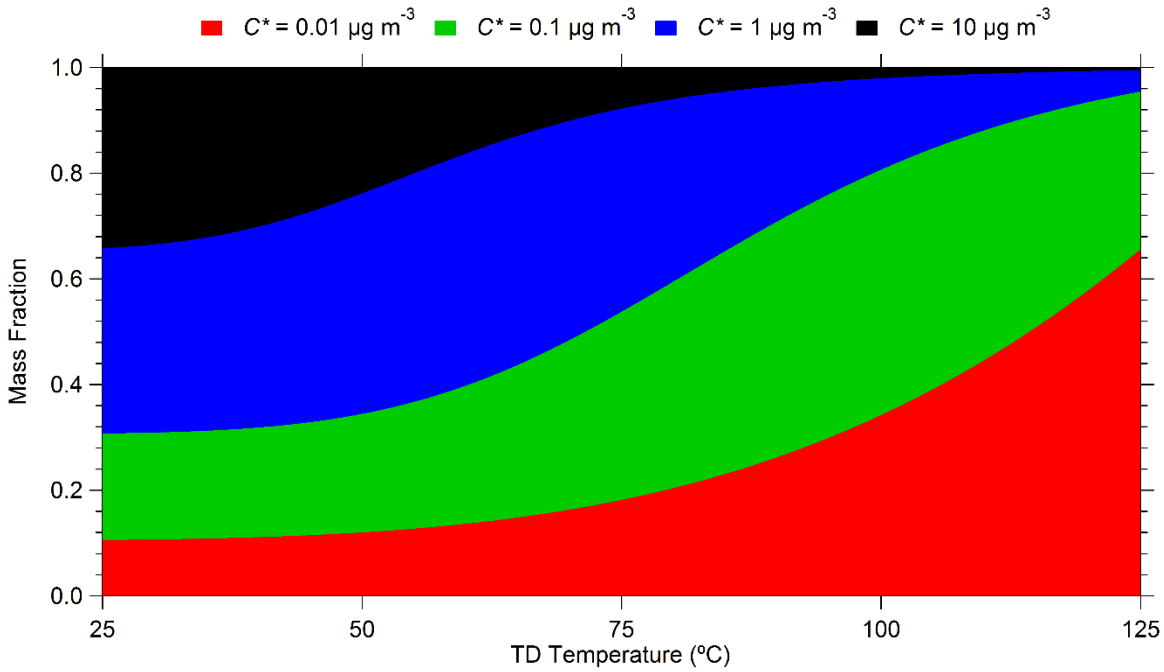

Figure 2.6. The estimated mass fractions for each volatility bin as a function of TD temperature for Experiment 1. Red represents the C^* = 0.01 µg m^{-3} bin, green the C^* = 0.1 µg m^{-3} bin, blue the C^* = 1 µg m^{-3} bin, and black the C^* = 10 µg m^{-3} bin.

For a future extension of the approach to ambient aerosols, the equations remain the same. The OA components could be separated into different groups using PMF with corresponding κ's, O:C ratios, and volatility distributions. This is similar to how Paciga et al. (2016) used PMF on ambient OA in Paris and generated volatility distributions for each factor.

Equation (2.3) assumes implicitly that the SOA in the various volatility bins has similar average number of carbon atoms per molecule and also similar average molecular weights. These are clearly zeroth order approximations and introduce corresponding uncertainties in the estimated O:C ratio for each bin. Equation (2.4) is based on the work of Petters and Kreidenweis (2007) and

assumes that the average density of the material in the various volatility bins is similar. These equations can be used to generate a system of equations for both the O:C ratios and κ's that can be solved separately.

First we focus on how to determine the O:C ratio distribution as a function of volatility, but the process to determine the κ distribution is exactly the same. Each measurement at a specific TD temperature results in one equation of the form of Eq. (2.3) with unknown O:C ratios for the various volatility bins. For example, for Experiment 1, we used the average O:C ratios from Fig. 2.4 and the mass fractions from Fig. 2.6 at each TD temperature to generate 5 equations with 4 unknowns. The combination of the results of all experiments led to 18 equations (5 from Experiment 1, 4 from Experiment 2, etc.) with 4 unknown O:C ratios ($[O:C]_{0.01}$, $[O:C]_{0.1}$, etc.). The optimum values of the O:C ratios were determined by minimizing the squared residual between the measured ($[O:C]_{TD}$) and predicted ($\sum_{i=1}^{n} x_{i,TD}\,[O:C]_i$) O:C ratios. Matlab's linear least squares solver, *lscov*, was used for this task.

The results for the O:C ratio distribution can be seen in Fig. 2.7a. The C^* = 0.01 μg m^{-3} bin had the lowest O:C ratio, while the C^* = 1 μg m^{-3} bin had the highest values. The C^* = 0.1 and 10 μg m^{-3} bins had nearly identical O:C ratios. These results suggest that, for this system and the conditions examined, the relationship between the O:C ratio and effective volatility was not monotonic.

The hygroscopicity parameter κ distribution was determined in exactly the same way and the results are depicted in Fig. 2.7b. The O:C ratios and corresponding κ's for each volatility bin were correlated extremely well (r^2 > 0.99, Fig. A.14), which has been reported in numerous studies (Rickards et al., 2013). The SOA in the C^* = 1 μg m^{-3} bin had the highest hygroscopicity while the most and least volatile components had lower κ values.

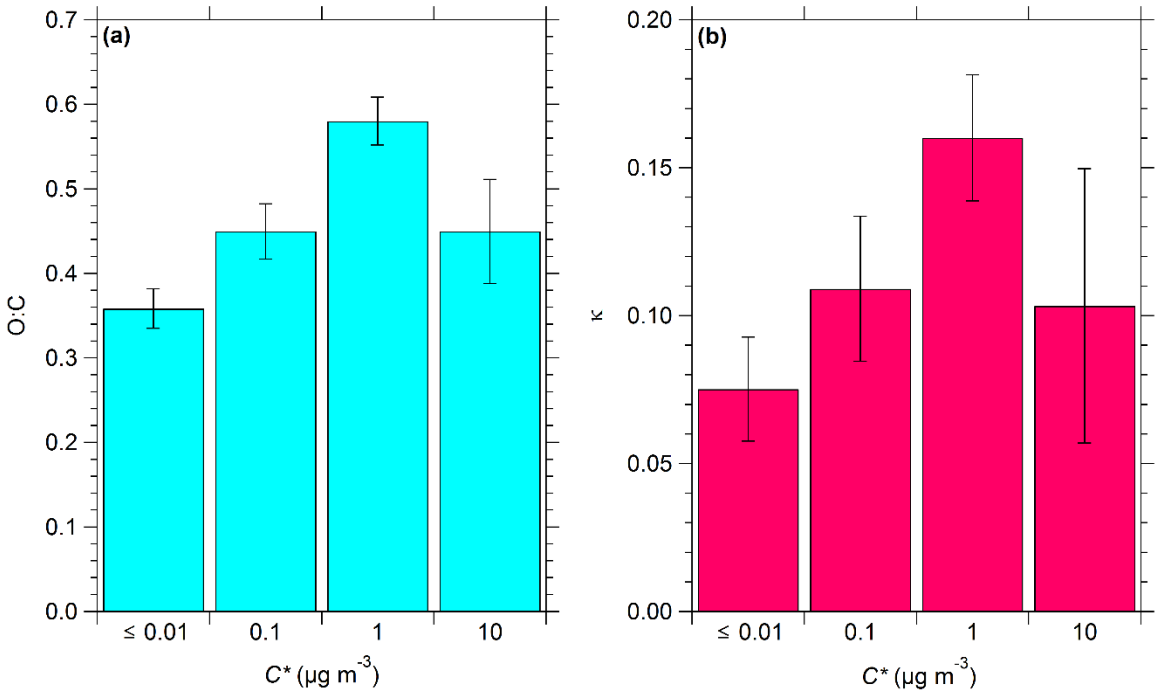

Figure 2.7. The (a) O:C ratio and (b) κ distributions for the volatility bins characterized in this study for α-pinene ozonolysis SOA. The error bars represent one standard deviation of the mean obtained from the least squares solver.

In order to determine the robustness of our solution, we compared the predicted O:C ratios and κ's at each TD temperature to the measured values for every experiment. For the predicted values, we used the distributions in Fig. 2.7, multiplied them by their corresponding mass fractions, and summed the products up at each TD temperature. The predicted versus measured O:C ratios and κ's can be seen in Figs. 2.8 and 2.9 respectively. The O:C ratio distribution appears to be a better predictor than the κ distribution because most of the predicted O:C ratios lie on the 1:1 line or very close to it, while the predicted κ's were more scattered. However, essentially all of the predicted values were very close to the measured ones and the remaining values were within one standard deviation of the measured values.

Figure 2.7 presents results that could, at least in principle, connect different, or even contradicting, results from previous studies. For example, Jimenez et al. (2009) proposed that

hygroscopicity and the O:C ratio increase as volatility decreases. However, Cerully et al. (2015) reported contradicting results that the more volatile components of ambient OA were more hygroscopic than the remaining material. The results presented here, albeit over a small range and only for α-pinene ozonolysis SOA, provide a context in which both conclusions can be true. As the volatility decreased from a C^* = 10 to 1 μg m^{-3}, the O:C ratio and κ increased (i.e. supporting the results of Jimenez et al. (2009)), but the O:C ratio and κ of the more volatile C^* = 1 μg m^{-3} bin were higher than those of the C^* = 0.01 and 0.1 μg m^{-3} bins (i.e. supporting the results of Cerully et al. (2015)). Therefore, the approach described in this study can provide a more comprehensive method to determine the relationship between OA hygroscopicity, oxidation level, and volatility.

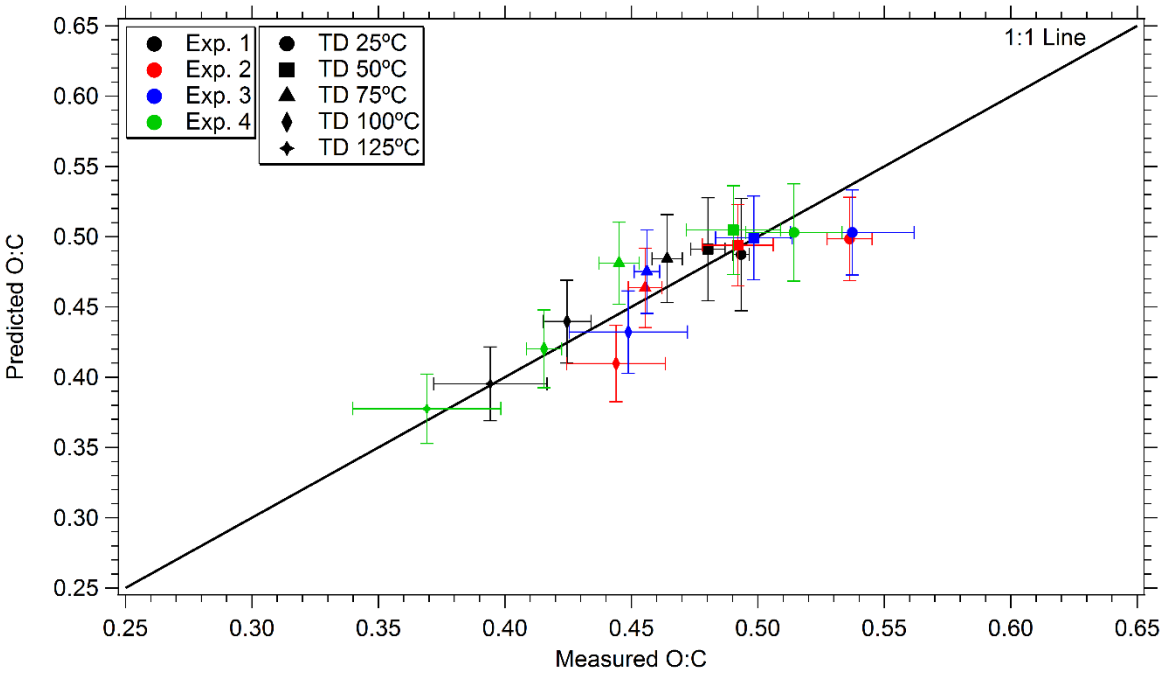

Figure 2.8. The predicted versus measured O:C ratios for all TD temperatures in all of the experiments. The color indicates the experiment number and the symbol indicates the TD temperature. The error bars for the predicted O:C ratios were obtained by predicting the O:C ratios using the O:C ratio distribution at +/- one standard deviation in Fig. 2.7a.

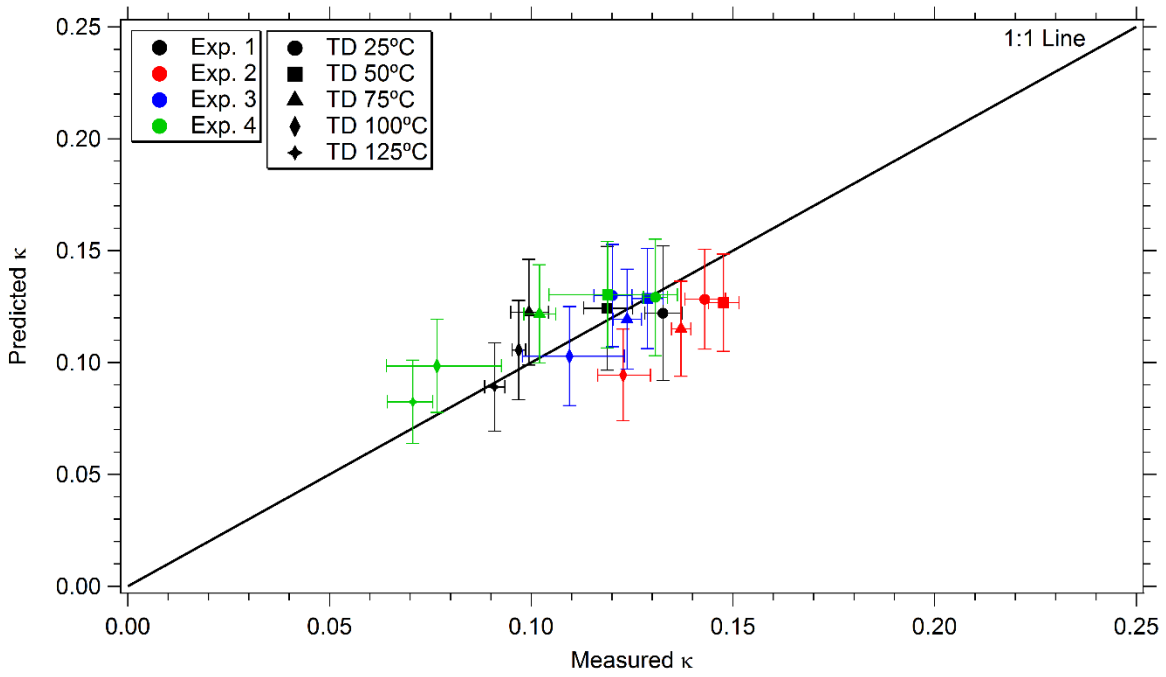

Figure 2.9. The predicted versus measured κ's for all TD temperatures in all of the experiments. The color indicates the experiment number and the symbol indicates the TD temperature. The error bars for the predicted κ's were obtained by predicting the κ's using the κ distribution at +/- one standard deviation in Fig. 2.7b.

2.6.1 Sensitivity analysis

As a test, we optimized the system of equations again, but this time we systematically eliminated one equation so that when we optimized the solution, we were only using 17 equations. After optimizing the system, we replaced the missing equation and removed another one. This test allowed us to determine if there was one measurement that significantly affected the results in Fig. 2.7. In all cases but one, the average values were nearly identical to the distributions from Fig. 2.7, demonstrating that one equation was not overly influencing the results. The only substantial deviation from Fig. 2.7 was observed for the C^* = 10 μg m^{-3} bin when the κ equation through the TD at 25°C for Experiment 1 was omitted. When the system was optimized without this equation, the κ for this bin decreased from 0.10 to 0.05. Since the mass fraction of the C^* = 10 μg m^{-3} bin

for Experiment 1 was almost double the next highest mass fraction in any measurement, it holds significantly more information, and therefore, weight, in the optimization process and impacts the solution for this bin. However, even if the κ for this bin changed when the corresponding measurement was omitted, the change is consistent with the large uncertainty bars for the κ of the $C^* = 10$ μg m^{-3} bin in Fig. 2.7. This exercise suggests that our results appear to be relatively robust.

As seen in Fig. 2.9, the κ distribution in Fig. 2.7 under predicts all of the measured κ's from Experiment 2. In order to investigate the cause of this discrepancy, we used Eq. (2.4) to determine the κ distribution just for Experiment 2. Since this experiment only had 4 TD temperatures (Fig. A.2), 4 equations could be written with 4 unknowns. However, when the system of equations was solved, the solution provided reasonable κ's for the three lowest bins, but produced a κ = -0.15 for the $C^* = 10$ μg m^{-3} bin. We hypothesized that the unreasonable value for the highest bin was due to the small mass fraction of the SOA in this bin at all temperatures (Fig. A.5). At 25°C, only 4% of the SOA had a $C^* = 10$ μg m^{-3} and those compounds completely evaporated as the temperature in the TD increased. Therefore, there was insufficient information to accurately estimate the properties of this bin for this experiment. To determine if this was true, we used Eq. (2.3) to solve for the O:C ratio distribution for Experiment 2. When we solved the system of equations, the solution again provided reasonable O:C ratios for the three lowest bins, but produced an O:C = 2.16 for the $C^* = 10$ μg m^{-3} bin. Since both solutions provided unreasonable values for the highest bin, we concluded that the method is unable to accurately estimate the properties of bins with very low concentrations (i.e. $x_i < 0.1$). However, when experiments with different concentrations were combined, as we did with Experiments 1–4 above, the method is able to determine reasonable estimates for the bins' properties.

To address the uncertainty introduced by the low concentration of material in the C^* = 10 μg m^{-3} bin for Experiment 2, we ignored the C^* = 10 μg m^{-3} bin and removed the κ equation at 25°C. This approach implicitly assumes that the material in the C^* = 10 μg m^{-3} bin has evaporated at 50°C, which is reasonable because the mass fraction for the bin is less than 2% at 50°C (Fig. A.5). This resulted in three equations with three unknown κ's. We solved the system of equations algebraically and the results for the κ distribution can be seen in Fig. 2.10. When compared to the κ distribution in Fig. 2.7b, the κ's for the C^* = 0.1 and 1 μg m^{-3} bins are the same within uncertainty (0.09 to 0.11 and 0.19 to 0.16 respectively), but the κ for the C^* = 0.01 μg m^{-3} bin is nearly twice that of the one in Fig 2.7b (0.14 to 0.08). This indicates that the SOA that had a C^* = 0.01 μg m^{-3} in Experiment 2 was more hygroscopic than indicated in Fig. 2.7b. To demonstrate this, we predicted the κ's for Experiment 2 again. In order to do this, we used the κ's for the three highest

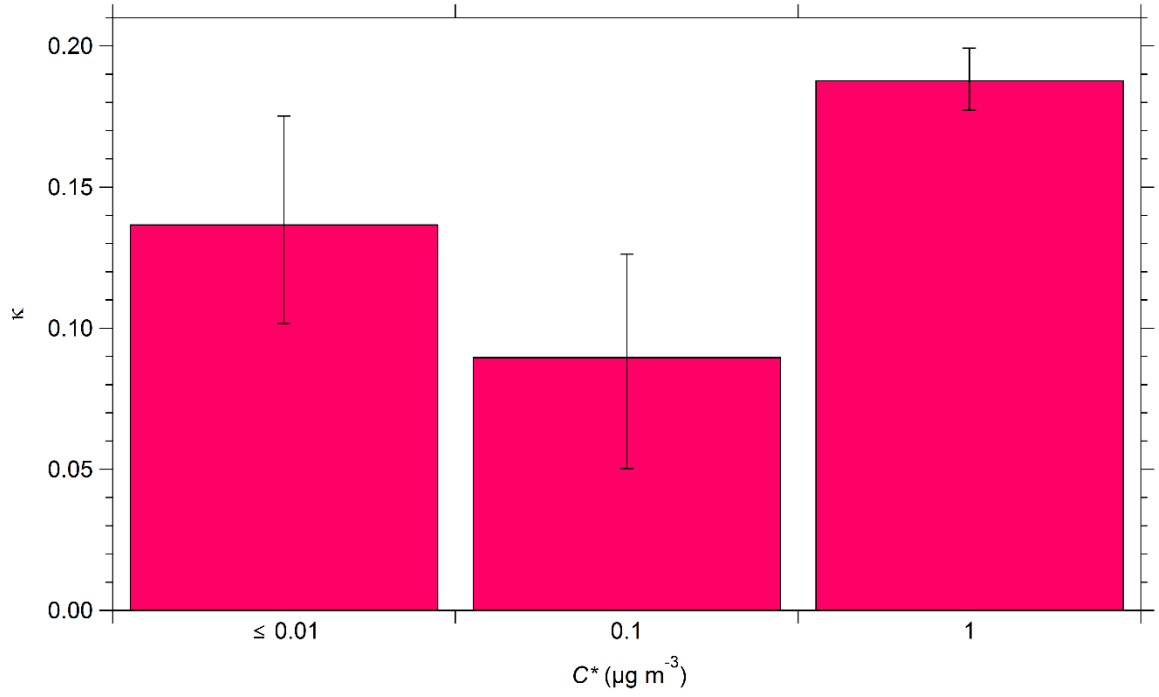

Figure 2.10. The κ distribution that resulted from solving Eq. (2.4) for TD temperatures greater than 50°C and the three lowest bins for Experiment 2. The error bars represent one standard deviation obtained by solving the equations at +/- one standard deviation of the measured κ.

bins from Fig. 2.7b, but we used the κ for the C^* = 0.01 μg m^{-3} bin estimated in Fig. 2.10. The results can be seen in Fig. A.15. With the larger κ for the C^* = 0.01 μg m^{-3} bin, the predicted κ's were nearly identical to the measured ones. This demonstrates the variability that can occur from experiment to experiment, but the analysis method developed here can examine experiments separately to determine the cause of the variability.

2.7 Conclusions

This study evaluates the feasibility of a novel measurement and analysis technique to quantify OA's hygroscopicity, O:C ratio, and volatility distribution. The experimental approach used a CCNC to study hygroscopicity, an AMS to determine the O:C ratio, and a TD to evaluate volatility. The experimental setup was tested with SOA generated from the ozonolysis of α-pinene. The results of these experiments revealed that the O:C ratio and κ decreased as the SOA passed through the TD at higher temperatures. This indicates that the lowest volatility material in this system contained components that had lower O:C ratios and κ_{CCN}'s. However, detailed characterization of the composition of the remaining compounds after the TD is required to quantify the contribution of chemical reactions to these observed changes.

An analysis technique to synthesize the data from this experimental setup was also developed. The results from this analysis confirmed that the SOA for this system had some low volatility material with a low O:C ratio and κ. It also showed that both low and high volatility compounds can have comparable oxidation levels and hygroscopicities.

This approach can be used to connect studies that were once thought to have contradicting results regarding the relationship between these three properties. Further chamber studies and ambient sampling are necessary in order to describe the relationship between OA hygroscopicity,

oxidation level, and volatility for multiple SOA systems, but also for ambient OA. This study was able to analyze a small portion of the 2D-VBS framework space, but this method can be utilized to help identify the relationship across the entire OA volatility axis. This approach also serves as an experimental branch to the theoretical framework proposed by Nakao (2017).

2.8 References

Alfarra, M. R., Paulsen, D., Gysel, M., Garforth, A. A., Dommen, J., Prévôt, A. S. H., Worsnop, D. R., Baltensperger, U., and Coe, H.: A mass spectrometric study of secondary organic aerosols formed from the photooxidation of anthropogenic and biogenic precursors in a reaction chamber, Atmos. Chem. Phys., 6, 5279–5293, doi: 10.5194/acpd-6-7747-2006, 2006.

An, W. J., Pathak, R. K., Lee, B. H., and Pandis, S. N.: Aerosol volatility measurement using an improved thermodenuder: Application to secondary organic aerosol, J. Aerosol Sci., 38, 305–314, doi: 10.1016/j.jaerosci.2006.12.002, 2007.

Bahreini, R., Keywood, M. D., Ng, N. L., Varutbangkul, V., Gao, S., Flagan, R. C., Seinfeld, J. H., Worsnop, D. R., and Jimenez, J. L.: Measurements of secondary organic aerosol from oxidation of cycloalkenes, terpenes, and m-xylene using an aerodyne aerosol mass spectrometer, Environ. Sci. Technol., 39, 5674–5688, doi: 10.1021/es048061a, 2005.

Brook, R. D., Rajagopalan, S., Pope, C. A., Brook, J. R., Bhatnagar, A., Diez-Roux, A. V., Holguin, F., Hong, Y., Luepker, R. V., Mittleman, M. A., Peters, A., Siscovick, D., Smith, S. C., Whitsel, L., and Kaufman, J. D.: Particulate matter air pollution and cardiovascular disease: An update to the scientific statement from the American Heart Association, Circulation, 121, 2331–2378, doi: 10.1161/CIR.0b013e3181dbece1, 2010.

Canagaratna, M. R., Jimenez, J. L., Kroll, J. H., Chen, Q., Kessler, S. H., Massoli, P., Hildebrandt Ruiz, L., Forner, E., Williams, L. R., Wilson, K. R., Surratt, J. D., Donahue, N. M., Jayne, J. T., and Worsnop, D. R.: Elemental ratio measurements of organic compounds using aerosol mass spectrometry: Characterization, improved calibration, and implications, Atmos. Chem. Phys., 15, 253–272, doi: 10.5194/acp-15-253-2015, 2015.

Cappa, C. D.: A model of aerosol evaporation kinetics in a thermodenuder, Atmos. Meas. Tech., 3, 579–592, doi: 10.5194/amt-3-579-2010, 2010.

Cappa, C. D., and Wilson, K. R.: Evolution of organic aerosol mass spectra upon heating: Implications for OA phase and partitioning behavior, Atmos. Chem. Phys., 11, 1895–1911, doi: 10.5194/acp-11-1895-2011, 2011.

Cerully, K. M., Bougiatioti, A., Hite Jr., J. R., Guo, H., Xu, L., Ng, N. L., Weber, R., and Nenes, A.: On the link between hygroscopicity, volatility, and oxidation state of ambient and water-

soluble aerosols in the southeastern United States, Atmos. Chem. Phys., 15, 8679–8694, doi: 10.5194/acp-15-8679-2015, 2015.

Clarke, A. D.: A thermo-optic technique for in situ analysis of size-resolved aerosol physicochemistry, Atmos. Environ., 25, 635–644, doi: 10.1016/0960-1686(91)90061-B, 1991.

Cruz, C. N., and Pandis, S. N.: A study of the ability of pure secondary organic aerosol to act as cloud condensation nuclei, Atmos. Environ., 31, 2205–2214, doi: 10.1016/S1352-2310(97)00054-X, 1997.

DeCarlo, P. F., Kimmel, J. R., Trimborn, A., Northway, M. J., Jayne, J. T., Aiken, A. C., Gonin, M., Fuhrer, K., Horvath, T., Docherty, K. S., Worsnop, D. R., Jimenez, J. L.: Field-deployable, high-resolution, time-of-flight aerosol mass spectrometer, Anal. Chem., 78, 8281–8289, doi: 10.1021/ac061249n, 2006.

Donahue, N. M., Robinson, A. L., Stanier, C. O., and Pandis, S. N.: Coupled partitioning, dilution, and chemical aging of semivolatile organics, Environ. Sci. Technol., 40, 2635–2643, doi: 10.1021/es052297c, 2006.

Donahue, N. M., Epstein, S. A., Pandis, S. N., and Robinson, A. L.: A two-dimensional volatility basis set: 1. Organic-aerosol mixing thermodynamics, Atmos. Chem. Phys., 11, 3303–3318, doi: 10.5194/acp-11-3303-2011, 2011.

Engelhart, G. J., Asa-Awuku, A., Nenes, A., and Pandis, S. N.: CCN activity and droplet growth kinetics of fresh and aged monoterpene secondary organic aerosol, Atmos. Chem. Phys., 8, 3937–3949, doi: 10.5194/acpd-8-95-2008, 2008.

Frosch, M., Bilde, M., DeCarlo, P. F., Jurányi, Z., Tritscher, T., Dommen, J., Donahue, N. M., Gysel, M., Weingartner, E., and Baltensperger, U.: Relating cloud condensation nuclei activity and oxidation level of α-pinene secondary organic aerosols, J. Geophys. Res., 116, D22212, doi: 10.1029/2011JD016401, 2011.

Good, N., Topping, D. O., Allan, J. D., Flynn, M., Fuentes, E., Irwin, M., Williams, P. I., Coe, H., and McFiggans, G.: Consistency between parameterisations of aerosol hygroscopicity and CCN activity during the RHaMBLe discovery cruise, Atmos. Chem. Phys., 10, 3189–3203, doi: 10.5194/acp-10-3189-2010, 2010.

Hildebrandt Ruiz, L., Paciga, A. L., Cerully, K. M., Nenes, A., Donahue, N. M., and Pandis, S. N.: Formation and aging of secondary organic aerosol from toluene: Changes in chemical composition, volatility, and hygroscopicity, Atmos. Chem. Phys., 15, 8301–8313, doi: 10.5194/acp-15-8301-2015, 2015.

Hong, J., Häkkinen, S. A. K., Paramonov, M., Äijälä, M., Hakala, J., Nieminen, T., Mikkilä, J., Prisle, N. L., Kulmala, M., Riipinen, I., Bilde, M., Kerminen, V.-M., and Petäjä, T.: Hygroscopicity, CCN and volatility properties of submicron atmospheric aerosol in a boreal forest environment during the summer of 2010, Atmos. Chem. Phys., 14, 4733–4748, doi: 10.5194/acp-14-4733-2014, 2014.

Huff Hartz, K. E., Rosenørn, T., Ferchak, S. R., Raymond, T. M., Bilde, M., Donahue, N. M., and Pandis, S. N.: Cloud condensation nuclei activation of monoterpene and sesquiterpene secondary organic aerosol, J. Geophys. Res., 110, D14208, doi: 10.1029/2004JD005754, 2005.

Huffman, J. A., Docherty, K. S., Mohr, C., Cubison, M. J., Ulbrich, I. M., Ziemann, P. J., Onasch, T. J., and Jimenez, J. L.: Chemically-resolved volatility measurements of organic aerosol from different sources, Environ. Sci. Technol., 43, 5351–5357, doi: 10.1021/es803539d, 2009.

IPCC: Summary for Policymakers, in: Climate Change 2013: The Physical Science Basis. Contribution of Working Group I to the Fifth Assessment Report of the Intergovernmental Panel on Climate Change, edited by: Stoker, T. F., Qin, D., Plattner, G.-K., Tignor, M., Allen, S. K., Boschung, J., Nauels, A., Xia, Y., and Midgley, P. M., Cambridge University Press, Cambridge, United Kingdom, and New York, NY, USA, doi: 10.1017/CBO9781107415324, 2013.

Jimenez, J. L., Canagaratna, M. R., Donahue, N. M., Prevot, A. S. H., Zhang, Q., Kroll, J. H., DeCarlo, P. F., Allan, J. D., Coe, H., Ng, N. L., Aiken, A. C., Docherty, K. S., Ulbrich, I. M., Grieshop, A. P., Robinson, A. L., Duplissy, J., Smith, J. D., Wilson, K. R., Lanz, V. A., Hueglin, C., Sun., Y. L., Tian, J., Laaksonen, A., Raatikainen, T., Rautiainen, J., Vaattovaara, P., Ehn, M., Kulmala, M., Tomlinson, J. M., Collins, D. R., Cubison, M. J., Dunlea, E., J., Huffman, J. A., Onasch, T. B., Alfarra, M. R., Williams, P. I., Bower, K., Kondo, Y., Schneider, J., Drewnick, F., Borrmann, S., Weimer, S., Demerjian, K., Salcedo, D., Cottrell, L., Griffin, R., Takami, A., Miyoshi, T., Hatakeyama, S., Shimono, A., Sun, J. Y, Zhang, Y. M., Dzepina, K., Kimmel, J. R., Sueper, D., Jayne, J. T., Herndon, S. C., Trimborn, A. M., Williams, L. R., Wood, E. C., Middlebrook, A. M., Kolb, C. E., Baltensperger, U., and Worsnop, D. R.: Evolution of organic aerosols in the atmosphere, Science, 326, 1525–1529, doi: 10.1126/science.1180353, 2009.

Jonsson, Å. M., Hallquist, M., and Saathoff, H.: Volatility of secondary organic aerosols from the ozone initiated oxidation of α-pinene and limonene, J. Aerosol Sci., 38, 843–852, doi: 10.1016/j.jaerosci.2007.06.008, 2007.

Karnezi, E., Riipinen, I., and Pandis, S. N.: Measuring the atmospheric organic aerosol volatility distribution: A theoretical analysis, Atmos. Meas. Tech., 7, 2953–2965, doi: 10.5194/amt-7-2953-2014, 2014.

King, S. M., Rosenoern, T., Shilling, J. E., Chen, Q., and Martin, S. T.: Cloud condensation nucleus activity of secondary organic aerosol particles mixed with sulfate, Geophys. Res. Lett., 34, L24806, doi: 10.1029/2007GL030390, 2007.

King, S. M., Rosenoern, T., Shilling, J. E., Chen, Q., and Martin, S. T.: Increased cloud activation potential of secondary organic aerosol for atmospheric mass loadings, Atmos. Chem. Phys., 9, 2959–2971, doi: 10.5194/acp-9-2959-2009, 2009.

Kostenidou, E., Pathak, R. K., and Pandis, S. N.: An algorithm for the calculation of secondary

organic aerosol density combining AMS and SMPS data, Aerosol Sci. Technol., 41, 1002–1010, doi: 10.1080/02786820701666270, 2007.

Kostenidou, E., Lee, B. H., Engelhart, G. J., Pierce, J. R., and Pandis, S. N.: Mass spectra deconvolution of low, medium, and high volatility biogenic secondary organic aerosol, Environ. Sci. Technol., 43, 4884–4889, doi: 10.1021/es803676g, 2009.

Kuwata, M., Chen, Q., and Martin, S. T.: Cloud condensation nuclei (CCN) activity and oxygen-to-carbon elemental ratios following thermodenuder treatment of organic particles grown by α-pinene ozonolysis, Phys. Chem. Chem. Phys., 13, 14571–14583, doi: 10.1039/c1cp20253g, 2011.

Lee, B. H., Pierce, J. R., Engelhart, G. J., and Pandis, S. N.: Volatility of secondary organic aerosol from the ozonolysis of monoterpenes, Atmos. Environ. 45, 2443–2452, doi: 10.1016/j.atmosenv.2011.02.004, 2011.

Massoli, P., Lambe, A. T., Ahern, A. T., Williams, L. R., Ehn, M., Mikkilä, J., Canagaratna, M. R., Brune, W. H., Onasch, T. B., Jayne, J. T., Petäjä, T., Kulmala, M., Laaksonen, A., Kolb, C. E., Davidovits, P., and Worsnop, D. R.: Relationship between aerosol oxidation level and hygroscopic properties of laboratory generated secondary organic aerosol (SOA) particles, Geophys. Res. Lett., 37, L24801, doi: 10.1029/2010GL045258, 2010.

Moore, R. H., Nenes, A., and Medina, J.: Scanning mobility CCN analysis—A method for fast measurements of size-resolved CCN distributions and activation kinetics, Aerosol Sci. Technol., 44, 861–871, doi: 10.1080/02786826.2010.498715, 2010.

Murphy, D. M., Cziczo, D. J., Froyd, K. D., Hudson, P. K., Matthew, B. M., Middlebrook, A. M., Peltier, R. E., Sullivan, A., Thomson, D. S., and Weber, R. J.: Single-particle mass spectrometry of tropospheric aerosol particles, J. Geophys. Res., 111, D23S32, doi: 10.1029/2006jd007340, 2006.

Nakao, S.: Why would apparent κ linearly change with O/C? Assessing the role of volatility, solubility, and surface activity of organic aerosols, Aerosol Sci. Technol., 51, 1377–1388, doi: 10.1080/02786826.2017.1352082, 2017.

Paciga, A., Karnezi, E., Kostenidou, E., Hildebrandt, L., Psichoudaki, M., Engelhart, G. J., Lee, B.-H., Crippa, M., Prévôt, A. S. H., Baltensperger, U., and Pandis, S. N.: Volatility of organic aerosol and its components in the megacity of Paris, Atmos. Chem. Phys., 16, 2013–2023, doi: 10.5194/acp-16-2013-2016, 2016.

Pathak, R. K., Stanier, C. O., Donahue, N. M., and Pandis, S. N.: Ozonolysis of α-pinene at atmospherically relevant concentrations: Temperature dependence of aerosol mass fractions (yields), J. Geophys. Res., 112, D03201, doi: 10.1029/2006JD007436, 2007.

Petters, M. D., and Kreidenweis, S. M.: A single parameter representation of hygroscopic growth and cloud condensation nucleus activity, Atmos. Chem. Phys., 7, 1961–1971, doi: 10.5194/acp-7-1961-2007, 2007.

Petters, M. D., Wex, H., Carrico, C. M., Hallbauer, E., Massling, A., McMeeking, G. R., Poulain, L., Wu, Z., and Stratmann, F.: Towards closing the gap between hygroscopic growth and activation for secondary organic aerosol – Part 2: Theoretical approaches, Atmos. Chem. Phys., 9, 3987–3997, doi: 10.5194/acp-9-3999-2009, 2009.

Pope, C. A.: What do epidemiologic findings tell us about health effects of environmental aerosols?, J. Aerosol Med., 13, 335–354, doi: 10.1089/jam.2000.13.335, 2000.

Poulain, L., Wu, Z., Petters, M. D., and Wex, H.: Towards closing the gap between hygroscopic growth and CCN activation for secondary organic aerosols – Part 3: Influence of the chemical composition on the hygroscopic properties of volatile fractions of aerosols, Atmos. Chem. Phys., 10, 3775–3785, doi: 10.5194/acp-10-3775-2010, 2010.

Prenni, A. J., Petters, M. D., Kreidenweis, S. M., DeMott, P. J., and Ziemann, P. J.: Cloud droplet activation of secondary organic aerosol, J. Geophys. Res., 112, D10223, doi: 10.1029/2006JD007963, 2007.

Rickards, A. M. J., Miles, R. E. H., Davies, J. F., Marshall, F. H., and Reid, J. P.: Measurements of the sensitivity of aerosol hygroscopicity and the κ parameter to the O/C ratio, J. Phys. Chem., 117, 14120–14131, doi: 10.1021/jp407991n, 2013.

Riipinen, I., Pierce, J. R., Donahue, N. M., and Pandis, S. N.: Equilibration time scales of organic aerosol inside thermodenuders: Evaporation kinetics versus thermodynamics, Atmos. Environ., 44, 597–607, doi: 10.1016/j.atmosenv.2009.11.022, 2010.

Roberts, G. C., and Nenes, A.: A continuous-flow streamwise thermal-gradient CCN chamber for atmospheric measurements, Aerosol Sci. Technol., 39, 206–221, doi: 10.1080/027868290913988, 2005.

Shilling, J. E., Chen, Q., and King, S. M.: Loading-dependent elemental composition of α-pinene SOA particles. Atmos. Chem. Phys., 9, 771–782, doi: 10.5194/acp-9-771-2009, 2009.

Song, C., Zaveri, R. A., Alexander, M. L., Thornton, J. A., Madronich, S., Ortega, J. V., Zelenyuk, A., Yu, X.-Y., Laskin, A., and Maughan, D. A.: Effect of hydrophobic primary organic aerosols on secondary organic aerosol formation from ozonolysis of α-pinene, Geophys. Res. Lett., 34, L20803, doi: 10.1029/2007GL030720, 2007.

Stanier, C. O., Pathak, R. K., and Pandis, S. N.: Measurements of the volatility of aerosols from α-pinene ozonolysis, Environ. Sci. Technol., 41, 2756–2763, doi: 10.1021/es0519280, 2007.

Tritscher, T., Dommen, J., Decarlo, P. F., Gysel, M., Barmet, P. B., Praplan, A. P., Weingartner, E., Prévôt, A. S. H., Riipinen, I., Donahue, N. M., and Baltensperger, U.: Volatility and hygroscopicity of aging secondary organic aerosol in a smog chamber, Atmos. Chem. Phys., 11, 11477–11496, doi: 10.5194/acp-11-11477-2011, 2011.

van Eeden, S. F., Yeung, A., Quinlam, K., and Hogg, J. C.: Systemic response to ambient particulate matter: Relevance to chronic obstructive pulmonary disease, Proc. Am. Thorac. Soc., 2, 61–67, doi: 10.1513/pats.200406-035MS, 2005.

VanReken, T. M., Ng, N. L., Flagan, R. C., and Seinfeld, J. H.: Cloud condensation nucleus activation properties of biogenic secondary organic aerosol, J. Geophys. Res., 110, D07206, doi: 10.1029/2004JD005465, 2005.

Wex, H., Petters, M. D., Carrico, C. M., Hallbauer, E., Massling, A., McMeeking, G. R., Poulain, L., Wu, Z., Kreidenweis, S. M., and Stratmann, F.: Towards closing the gap between hygroscopic growth and activation for secondary organic aerosol: Part 1 – Evidence from measurements, Atmos. Chem. Phys., 9, 3987–3997, doi: 10.5194/acpd-9-955-2009, 2009.

Zhang, Q., Jimenez, J. L., Canagaratna, M. R., Allan, J. D., Coe, H., Ulbrich, I., Alfarra, M. R., Takami, A., Middlebrook, A. M., Sun, Y. L., Dzepina, K., Dunlea, E., Docherty, K., DeCarlo, P. F., Salcedo, D., Onasch, T., Jayne, J. T., Miyoshi, T., Shimono, A., Hatakeyama, S., Takegawa, N., Kondo, Y., Schneider, J., Drewnick, F., Borrmann, S., Weimer, S., Demerjian, K., Williams, P., Bower, K., Bahreini, R., Cottrell, L., Griffin, R. J., Rautiainen, J., Sun, J. Y., Zhang, Y. M., and Worsnop, D. R.: Ubiquity and dominance of oxygenated species in organic aerosols in anthropogenically-influenced Northen Hemisphere midlatitudes, Geophys. Res. Lett., 34, L13801, doi: 10.1029/2007GL029979, 2007.

Chapter 3

Challenges in determining atmospheric organic aerosol volatility distributions using thermal evaporation techniques[2]

[2] Published as: Cain, K. P., Karnezi, E., and Pandis, S. N.: Challenges in determining atmospheric organic aerosol volatility distributions using thermal evaporation techniques, Aerosol Sci. Technol., doi: 10.1080/02786826.2020.1748172, 2020.

3.1 Abstract

Volatility is one of the most important physical properties of organic aerosol (OA), as it determines the partitioning of its components between the vapor and particulate phases. Despite their atmospheric importance, multicomponent OA volatility estimates remain quite uncertain.

This study combined thermodenuder (TD) and isothermal dilution measurements to characterize secondary OA (SOA) generated from the ozonolysis of α-pinene and cyclohexene. The SOA from both precursors evaporated similarly in the TD, but behaved quite differently when isothermally diluted by similar amounts. The α-pinene ozonolysis SOA evaporated by only 20% after 2 h of dilution by a factor of around 20, while 65% of the cyclohexene ozonolysis SOA evaporated at the same conditions.

The model of Karnezi, Riipinen, and Pandis (2014) was first used to estimate the volatility distributions by fitting only the evaporation in the TD. This approach resulted in similar volatility distributions for the two systems. Then, the model was used to fit both the evaporation in the TD and the dilution chamber. This technique estimated drastically different volatility distributions with the α-pinene ozonolysis SOA consisting of mostly low-volatility compounds and the cyclohexene ozonolysis SOA consisting of mostly semi-volatile compounds. In the next stage of analysis, the model was updated to account for vapor-phase wall-losses occurring in the dilution chamber. This approach resulted in slightly less volatile SOA and provided some information about the losses of vapors to the walls, but the results were fairly uncertain. These results show the necessity of combining thermal measurements with other techniques to accurately estimate OA volatility.

3.2 Introduction

Atmospheric aerosols have important adverse health effects (e.g., Di et al. 2017) and a significant but uncertain impact on the Earth's energy balance (IPCC 2013). Contributing to the uncertainty is the complexity of the composition of these aerosols; in many areas, the thousands of compounds constituting organic aerosol (OA) can represent anywhere from 20 to 90% of the submicron aerosol mass (Zhang et al. 2007). OA can either be emitted directly as particles, known as primary OA (POA), or produced by the condensation of products from the vapor-phase oxidation of volatile (VOCs), intermediate volatility (IVOCs), and semi-volatile (SVOCs) organic compounds, generating secondary OA (SOA) (Louvaris et al. 2017).

Volatility is one of the most important physical properties of OA because it determines the partitioning of organic compounds between the vapor and particle-phases. Vapor-to-particle partitioning is determined by a compound's effective saturation concentration, C_i^*, and the condensed-phase OA concentration, C_{OA} (Donahue et al. 2006). When C_{OA} is equal to C_i^*, 50% of compound i will exist in the particle phase and as C_{OA} increases, the fraction of higher volatility compounds (i.e., those with higher C_i^*) present in the particle phase increases. Due to the large range of saturation concentrations of atmospheric organic compounds, the one-dimensional volatility basis set (1D-VBS) has been proposed as a framework to describe the evolution of OA. The 1D-VBS utilizes logarithmically spaced bins based on an effective saturation concentration at 298 K (Donahue et al. 2006). Many previous studies have attempted to constrain OA volatility indirectly by heating (e.g., An et al. 2007) or diluting isothermally (e.g., Grieshop, Donahue, and Robinson 2007). Other studies have derived volatility information from SOA yield data (e.g., Odum et al. 1996). However, thermal evaporation techniques often estimate significantly lower

volatility than predicted by fitting yield data (Cappa and Jimenez 2010; Kolesar et al. 2015; Stanier, Pathak, and Pandis 2007).

A common instrument used in thermal evaporation studies is the thermodenuder (TD), a heated tube where volatile particle components evaporate followed by a cooling section with activated carbon to prevent vapor re-condensation. TDs are used to generate thermograms, particle mass fraction remaining (MFR) as a function of TD temperature. Thermograms are influenced by several parameters, including the OA concentration, residence time in the heating section, enthalpy of vaporization, and mass transfer resistances (Cappa 2010; Kuwata, Chen, and Martin 2011; Riipinen et al. 2010). Consequently, drawing conclusions from thermograms can be challenging.

In dilution-induced evaporation, the organic vapor concentrations are lowered and the evolution of the OA concentration is monitored over time (Grieshop, Donahue, and Robinson 2007; Grieshop et al. 2009; Hildemann, Cass, and Markowski 1989; Kolesar et al. 2015; Lipsky and Robinson 2006; Louvaris et al. 2017; Vaden et al. 2011). Some studies use a dilution sampler (Hildemann, Cass, and Markowski 1989; Lipsky and Robinson 2006) while others dilute the OA sample by moving it from one chamber to another (Louvaris et al. 2017; Vaden et al. 2011).

Grieshop et al. (2009) were the first to suggest the combination of TD and isothermal dilution measurements to better constrain OA volatility. In that study, the authors examined the volatility of POA from wood combustion and diesel engines through TD or isothermal dilution experiments. In the TD experiments, the POA evaporated readily at temperatures below 80°C. In the isothermal dilution experiments, clean air was injected into their chamber to reduce the POA concentration and there was substantial, but slow evaporation. The authors combined the results from these techniques to derive volatility distributions for the POA and concluded that the POA had semi-volatile components, but also some non-volatile material.

Karnezi, Riipinen, and Pandis (2014) established an algorithm for the combination of TD and isothermal dilution measurements, resulting in an optimum OA volatility distribution and its uncertainty. Louvaris et al. (2017) developed an experimental technique that combines TD and isothermal dilution measurements to determine volatility distributions. They observed that this technique resulted in a lower uncertainty of the estimated vaporization enthalpy and SVOC content for OA. Kolesar et al. (2015) rapidly diluted SOA from the ozonolysis of α-pinene and then passed the resulting particles through a TD, concluding that the volatility of these compounds was mostly independent of SOA concentration.

An important, yet still uncertain, process in chamber experiments is vapor-phase wall-losses. Recent studies have shown that organic vapors partition reversibly onto chamber walls, but the characteristic time scale measured for this process varies by up to three orders of magnitude (Krechmer et al. 2016; La et al. 2016; Loza et al. 2010; Matsunaga and Ziemann 2010; McVay, Cappa, and Seinfeld 2014; Nah et al. 2016; Shiraiwa et al. 2013; Ye et al. 2016; Yeh and Ziemann 2014, 2015; X. Zhang et al. 2014, 2015).

In this paper, we probe different experimental and data analysis techniques to estimate SOA volatility distributions, highlighting the challenges that arise when interpreting these data.

3.3 Methodology

3.3.1 Experimental setup

All experiments were conducted in the Carnegie Mellon University Air Quality Laboratory. The experimental setup is similar to that of Louvaris et al. (2017) and can be seen in Fig. 3.1. The smog chambers used in this study were Teflon (Welch Fluorocarbons) reactors. The main chamber was 10 m^3 and suspended in a temperature-controlled room (Pathak et al. 2007). The dilution chamber was 7 m^3 and suspended in the lab, protected from ambient UV light.

Dilution took place at approximately 25°C. Before each experiment, the main chamber was flushed overnight with purified air under UV illumination (GE, model 10526 and 10244) to remove any potential contaminants. The dilution chamber was also flushed with purified air for several days before an experiment. Purified air was generated by passing compressed air through a high-efficiency particulate air (HEPA) filter to remove any particles, an activated carbon filter to remove any vapors, and silica gel to maintain the relative humidity (RH) at less than 10%.

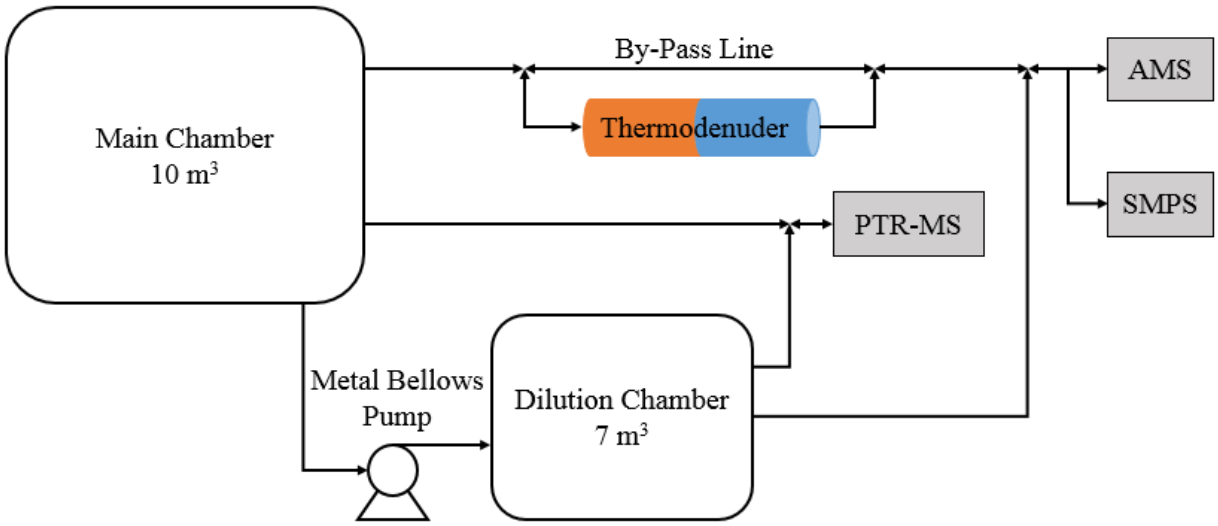

Figure 3.1. Experimental setup used in this study. Particles from the main chamber were characterized with a TD followed by an AMS and an SMPS. Aerosol was transferred from the main chamber to the dilution chamber via a metal bellows pump and then particles from the dilution chamber were sampled by the same AMS and SMPS. VOC concentrations were monitored in both chambers with a PTR-MS.

Particles were produced in the main chamber and characterized by passing through either a TD or by-pass line (BP) and then sampled by an Aerodyne high-resolution time-of-flight aerosol mass spectrometer (HR-ToF-AMS, hereafter AMS) and a scanning mobility particle sizer (SMPS, TSI, DMA model 3081, CPC model 3010/72/75). After initial characterization in the main chamber, aerosol from the main chamber was isothermally diluted by approximately a factor of 20 in the dilution chamber via a metal bellows pump (Baldor, model MB-302). The aerosol was

transferred only once at a flow rate of 70 L min^{-1} for less than 5 min. Particle losses in the transfer system were quantified by comparing size the distributions of ammonium sulfate aerosol transferred from the main to the dilution chamber (Fig. B.1). Volatile organic vapor losses for this pump have been characterized by Kaltsonoudis et al. (2019) and were found to vary from a few percent to not detectable.

Particle evolution over time in the dilution chamber was monitored by the same AMS and SMPS. After initial characterization in the dilution chamber, measurements from both chambers were alternated by three-way valves. VOC concentrations and the dilution ratio were measured with a proton transfer reaction mass spectrometer (PTR-MS, Ionicon Analytic). Isotopically-labelled butanol (n-butanol-d9, Cambridge Isotope Laboratories, 98%) was used as a dilution tracer and injected into the main chamber before particles were produced. In most experiments, the ozone concentration was measured in both chambers by an ozone monitor (Dasibi Environmental Corporation, model 1008-PC).

For the SOA experiments, once the dilution tracer was well-mixed in the chamber, either α-pinene (Sigma-Aldrich, ≥ 99%) or cyclohexene (Sigma-Aldrich, 99+%) was injected through a septum injector. Ozone was generated by an ozone generator (AZCO, model HTU-500ACPS) and injected into the main chamber after the VOC concentration stabilized. No OH scavenger was used in these experiments. The experimental conditions examined in this study are shown in Table 3.1. Mass concentrations were calculated assuming a density of 1.4 g cm^{-3} (Kostenidou, Pathak, and Pandis 2007). Experiments AP4, CH3, and CH4 were conducted without activated carbon in the cooling section of the TD for reasons discussed in Section 3.4.2.1.

In this study, the AMS used a flow rate of 0.1 L min^{-1} and an averaging time of 1 min in V-mode (DeCarlo et al. 2006). The SMPS used a sample flow rate of 1 L min^{-1} and a sheath flow

rate of 5 L min^{-1} with an upscan of 120 s and a downscan of 30 s. The PTR-MS sampled with a flow rate of 0.5 L min^{-1}. The TD from Cain and Pandis (2017) was used in these experiments and operated at temperatures from 25 to 150°C. Accounting for the flows downstream from the TD, the centerline residence time through the heating section at 25°C was 19 s.

Table 3.1. Description of the experimental conditions used in this study.

Exp.	VOC	VOC Concentration (ppb)	Ozone Concentration (ppb)	Main Chamber SOA Mass[a] (μg m^{-3})	Dilution Ratio
AP1	α-Pinene	75	330	131	16.8 ± 1.0
AP2	α-Pinene	75	N/A[b]	145	18.3 ± 1.3
AP3	α-Pinene	150	N/A[b]	375	19.0 ± 0.3
AP4[c]	α-Pinene	50	270	82	25.5 ± 1.0
CH1	Cyclohexene	400	750	236	15.5 ± 0.4
CH2	Cyclohexene	400	660	204	16.8 ± 0.6
CH3[c]	Cyclohexene	400	700	252	16.4 ± 0.6
CH4[c]	Cyclohexene	225	580	94	14.9 ± 0.5

[a]Mass calculated assuming a density of 1.4 g cm^{-3}.
[b]Ozone monitor data not available.
[c]Experiments conducted without activated carbon in the cooling section of the TD.

Following the suggestion of Wang et al. (2018), in order to account for particle wall-loss occurring in the dilution chamber, we injected a 5 g L^{-1} solution of ammonium sulfate (Sigma-Aldrich, ≥ 99%) into the dilution chamber at the end of our experiments (i.e., when the particle mass concentration was less than 2 μg m^{-3}) using an atomizer (TSI, model 3075). Before entering the chamber, the resulting droplets passed through a silica gel dryer to produce dry particles. After the mass concentration reached around 50 μg m^{-3}, we left the particles undisturbed for at least 4 h in order to determine the size-dependent particle wall-loss rate constant.

3.3.2 Data analysis

3.3.2.1 Dilution ratio

The dilution ratio was calculated by dividing the concentration of the isotopically-labelled butanol in the PTR-MS (*m*/*z* 66) in the main chamber by the concentration in the dilution chamber. We calculated the dilution ratio each time there was a switch from the main chamber to the dilution chamber and averaged them over the entire experiment.

3.3.2.2 Loss corrections

Size and temperature-dependent particle losses were corrected for in the TD in the same manner as in Cain and Pandis (2017). After correction for losses in the TD, we used the SMPS data from the main chamber to generate thermograms by dividing the TD mass concentration by an interpolated BP mass concentration using the BP measurements before and after the TD measurements.

Size-dependent particle wall-losses were also accounted for in the dilution chamber. We used the coagulation-corrected particle wall-loss rate constants derived from the model of Nah et al. (2017), using the data from the ammonium sulfate particle decay (Wang et al. 2018). Briefly, the model assumes that only two processes take place: particle wall-loss and coagulation. Using a given particle number size distribution at a specific time, the model predicts how the distribution would evolve at the next time step, assuming coagulation is the only process. Then, the model compares the measured size distribution at the next time step to the predicted one, attributes the differences to particle wall-loss, and calculates an instantaneous wall-loss rate constant for each size bin, *i*. The coagulation-corrected particle wall-loss rate constant, $k_{c,i}$, was determined by averaging the instantaneous wall-loss rate constants. The uncertainty of the coagulation-corrected particle wall-loss rate constant, $\delta_{k_{c,i}}$, was calculated by $\sigma_{k_{c,i}}/\sqrt{N}$, where $\sigma_{k_{c,i}}$ is the standard

deviation of k_c for a certain size bin, i, and N is the total number of time steps used. In order to minimize the uncertainty that results from calculating instantaneous wall-loss rate constants over small time steps, we averaged our SMPS scans over 10 min intervals (4 SMPS scans). Once the size-dependent particle wall-loss rate constant was determined, the SMPS number, volume, and mass concentrations at each size bin were corrected according to the method of Wang et al. (2018).

An example of the particle wall-loss rate constant as a function of size in the dilution chamber can be seen in Fig. B.2. All experiments had similar particle wall-loss rate constants. The particle wall-loss rates were kept low by using an ionizing fan on the dilution chamber (details on the fan and procedure can be found in Jorga et al. (2020)). The low particle loss rates make the experimental results less sensitive to the particle wall-loss corrections. However, these corrections are still important for the accurate determination of evaporation occurring due to the isothermal dilution.

To account for the uncertainty that results from correcting for particle wall-losses over several hours, we propagated the uncertainty of the wall-loss rate constants ($\delta_{k_{c,i}}$) into the corrected concentrations. The full derivation is available in Appendix B. The uncertainty in the number concentration at size bin i and time t, $\delta_{N_i}(t)$, can be calculated by:

$$\delta_{N_i}(t) = N_i(t) \cdot t \cdot \delta_{k_{c,i}} \tag{3.1}$$

where $N_i(t)$ is the corrected number concentration of size bin i at time t. The uncertainty in the total number concentration at time t, $\delta_N(t)$, is:

$$\delta_N(t) = \sqrt{\sum_i \delta_{N_i}(t)^2} \tag{3.2}$$

Similar equations can be derived for volume and mass concentrations. Those equations can be found in Appendix B.

After correction for wall-losses in the dilution chamber, we used the SMPS data to generate areograms, particle MFR as a function of time in the dilution chamber, by dividing the mass concentration at time *t* by the initial mass concentration in the dilution chamber at time t_0. To account for the uncertainty resulting from the wall-loss corrections in the areograms, we calculated the uncertainty of the MFR at time *t*, $\delta_{MFR}(t)$, by:

$$\delta_{MFR}(t) = MFR(t)\sqrt{\left(\frac{\delta_M(t)}{M(t)}\right)^2 + \left(\frac{\delta_{M_0}}{M_0}\right)^2} \tag{3.3}$$

where *MFR*(*t*) is the MFR at time *t*, $\delta_M(t)$ is the uncertainty of the mass concentration at time *t*, $M(t)$ is the mass concentration at time *t*, δ_{M_0} is the uncertainty of the initial mass concentration, and M_0 is the initial mass concentration.

3.3.2.3 Estimation of the volatility distributions

We used the dynamic mass transfer model of Riipinen et al. (2010) and the error minimization approach developed by Karnezi, Riipinen, and Pandis (2014) to estimate the SOA volatility distributions. Briefly, the mass flux of compound *i* from the vapor-phase to the particle-phase, I_i, is calculated by (Seinfeld and Pandis 2016):

$$I_i = \frac{2\pi d_p M_i \beta_{\mathrm{m}i} D_i}{RT}\left(p_i - p_i^0\right) \tag{3.4}$$

where d_p is the particle diameter, M_i is the molecular weight of compound *i*, D_i is the diffusion coefficient of compound *i* in the vapor-phase at temperature *T*, *R* is the universal gas constant, p_i and p_i^0 are the partial vapor pressures of *i* far away from the particle and at the particle surface, respectively, and β_{mi} is a correction factor for kinetic and transition regime effects (Fuchs and Sutugin 1970):

$$\beta_{\mathrm{m}i} = \frac{1+Kn_i}{1+\left(\frac{4}{3a_{\mathrm{m}i}}+0.377\right)Kn_i+\frac{4}{3a_{\mathrm{m}i}}Kn_i} \tag{3.5}$$

where Kn_i is the Knudsen number of compound *i* and a_{mi} is the mass accommodation coefficient of compound *i* on the particles. In this work, we assume a molecular weight of 200 g mol^{-1}, and a diffusion coefficient of 10^{-5} m^2 s^{-1} at 298 K.

The partial vapor pressure of compound *i* at the particle surface, p_i^0, is given by:

$$p_i^0 = x_{\mathrm{m}i}\frac{C_i^* RT}{M_i}\exp\left(\frac{4M_i\sigma}{RT_p\rho d_p}\right) \tag{3.6}$$

where x_{mi} is the mass fraction of compound *i* in the particle-phase, C_i^* represents the effective saturation concentration of compound *i* in the 1D-VBS (Donahue et al. 2006), σ is the surface tension (assumed to be 0.05 N m^{-1}), T_p is the particle temperature, and ρ is the particle density (assumed to be 1.4 g cm^{-3}).

The effective saturation concentration of compound *i* at any TD temperature, $C_i^*(T_{\mathrm{TD}})$, is estimated using the integrated form of the Clausius-Clapeyron equation:

$$C_i^*(T_{\mathrm{TD}}) = C_i^*(298\ \mathrm{K})\exp\left[\frac{\Delta H_{\mathrm{vap},i}}{R}\left(\frac{1}{298}-\frac{1}{T_{\mathrm{TD}}}\right)\right]\left(\frac{298}{T_{\mathrm{TD}}}\right) \tag{3.7}$$

where $\Delta H_{\mathrm{vap},i}$ is the enthalpy of vaporization of compound *i*.

The time-dependent evaporation of the SOA is simulated by solving the differential equations for total particle mass, m_p, and vapor-phase concentration of compound *i*, C_i, with the following equations:

$$\frac{\mathrm{d}m_{\mathrm{p}}}{\mathrm{d}t} = -\sum_{i=1}^{n} I_i \tag{3.8}$$

$$\frac{\mathrm{d}C_i}{\mathrm{d}t} = I_i \cdot N_{\mathrm{tot}} \tag{3.9}$$

where N_{tot} is the total number concentration of SOA particles.

In this work, the model uses as inputs the SOA mass concentration in the main chamber, the average particle size, and the dilution ratio. It also uses the geometry of the TD (lengths of the

heating and cooling sections and residence times in the heating and cooling sections) as inputs. While the model can simulate both the complete aerosol size distribution and the radial dependence of its concentration in the TD, in this study we are assuming a monodisperse aerosol population and also use the centerline residence time of the aerosol in the TD. These simplifications dramatically reduce the significant computational time of the model, introducing only minor errors (Riipinen et al. 2010).

The model can either assume that the SOA passes through the cooling section of the TD without any major changes in its concentration (e.g., experiments where the activated carbon was removed in the cooling section) or that the cooling section changes the SOA concentration by absorbing organic vapors and reducing the corresponding vapor-phase concentrations to zero (e.g., experiments that had activated carbon in the cooling section). Radial dependence is still neglected based on the findings of Saleh, Shihadeh, and Khlystov (2011) who showed that this simplification introduced only minor errors.

The volatility distribution, enthalpy of vaporization, and mass accommodation coefficient of the OA are used as fitting parameters. The optimization algorithm uses a brute force approach, trying all combinations of these fitting parameters (with user-selected intervals) to calculate an MFR (either in the TD or dilution chamber) from the ratio of the particle mass at $t = t_{res}$ (where t_{res} is the residence time in either the TD or dilution chamber) to the initial mass of the particles (either in the main or dilution chamber). The model then calculates a percent error, E_i:

$$E_i = \frac{100}{n}\sqrt{\sum_i^n \left(MFR_{i,\mathrm{sim}} - MFR_i\right)^2} \tag{3.10}$$

where n is the number of different temperatures in the TD or time steps in the dilution chamber, $MFR_{i,\mathrm{sim}}$ is the MFR for a certain combination of parameters for data point i (either a TD temperature or residence time in the dilution chamber), and MFR_i is the measured MFR. The model

uses the combinations with the lowest 1% of E_i to calculate a best estimate, $\bar{x}$ (where x can be the mass fraction of a volatility bin, enthalpy of vaporization, or logarithm of the mass accommodation coefficient) from the following equation:

$$\bar{x} = \frac{\sum_i^N \left[x_i \cdot \left(\frac{1}{E_i} \right) \right]}{\sum_i^N \left[\frac{1}{E_i} \right]} \tag{3.11}$$

where x_i is the best estimate of property i (the mass fraction of a volatility bin, the enthalpy of vaporization, or logarithm of the mass accommodation coefficient) and N is the number of combinations below the 1% threshold.

The model also calculates an uncertainty range for all three properties with the following equation:

$$\sigma = \sqrt{\frac{\sum_i^N \left[(x_i - \bar{x})^2 \cdot \left(\frac{1}{E_i} \right) \right]}{\sum_i^N \left[\frac{1}{E_i} \right]}} \tag{3.12}$$

3.4 Experimental results

3.4.1 System test with ammonium sulfate aerosol

To determine whether our system was working properly, we tested the experimental setup and analysis technique with ammonium sulfate particles because they should not evaporate in the TD at temperatures below approximately 125℃ or the dilution chamber. We injected a 5 g L^{-1} solution of ammonium sulfate (Sigma-Aldrich, ≥ 99%) into the main chamber using an atomizer (TSI, model 3075) and then followed the procedure outlined above to test the system.

After injection into the main chamber, the particles had a mean volume diameter of 263 nm and a mass concentration of 251 μg m^{-3}. The average dilution ratio for the experiment was 16.3 ± 0.5. After correcting for particle wall-losses, the initial mean volume diameter in the dilution

chamber was 243 nm. Furthermore, dividing the mass concentration in the main chamber by that of the wall-loss corrected mass concentration in the dilution chamber yielded a mass ratio of 27.5, which is nearly double that of the measured dilution ratio. However, after correcting for losses in the pump transfer (Fig. B.1), the initial mean volume diameter in the dilution chamber was 262 nm and the mass concentration was 16.4 μg m^{-3}, corresponding to a mass ratio of 15.3 between the two chambers.

The thermogram and areogram for this test can be seen in Fig. 3.2. No particle mass evaporated at TD temperatures below 125°C or after 5.5 h of dilution. As expected, nearly all of the mass evaporated in the TD at temperatures greater than 125°C. Since there was no evaporation in the TD or dilution chamber, we concluded that our system operates properly.

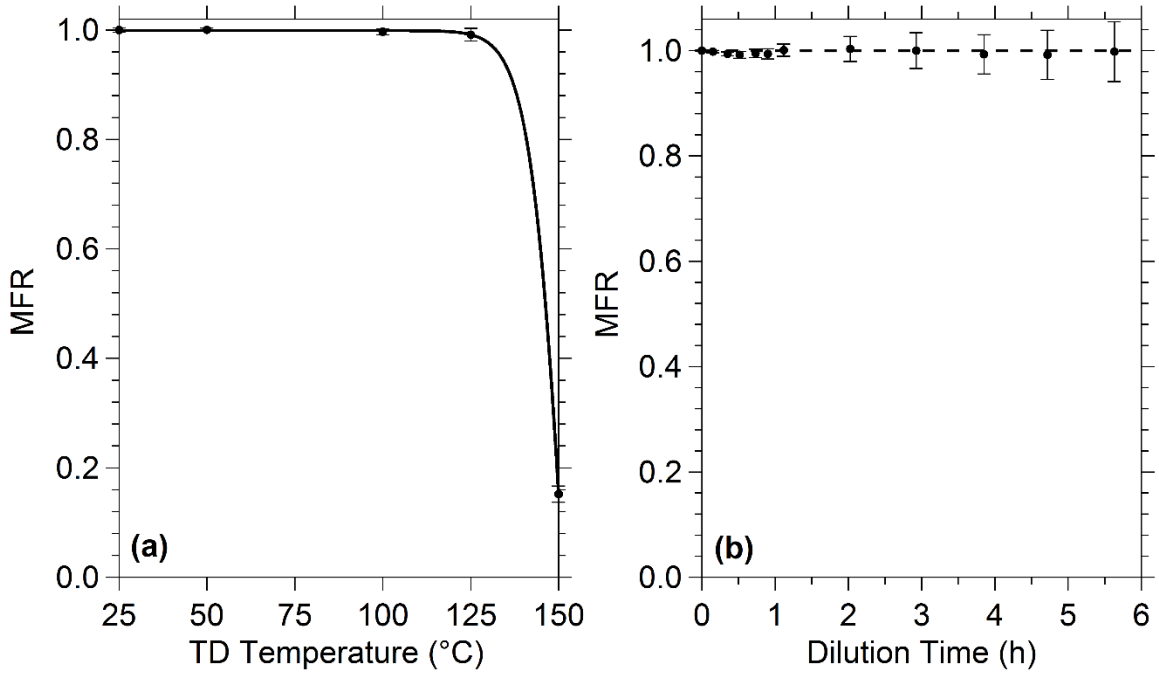

Figure 3.2. The (a) thermogram and (b) areogram for the ammonium sulfate particles. The error bars in the thermogram represent one standard deviation of the mean MFR, while the error bars in the areogram represent the uncertainty resulting from correcting for particle wall-losses.

3.4.2 SOA experiments

The experimental setup was then used to characterize SOA produced from the ozonolysis of α-pinene and cyclohexene. All of the experiments were conducted at fairly high SOA levels, ranging from 80–375 μg m^{-3}. These relatively high SOA concentrations allowed us to characterize higher volatility compounds that can initially be in the vapor-phase in the atmosphere, but easily partition into the particle-phase upon aging. Furthermore, the higher concentrations make it possible to dilute by a large factor and still be able to measure SOA evaporation in the dilution chamber.

3.4.2.1 TD results

The thermograms from all of the SOA experiments can be seen in Fig. 3.3. The SOA in these experiments, regardless of VOC precursor, evaporated similarly in the TD. There was some variability in the MFRs for TD temperatures between 50 and 100°C, but all of the thermograms merged together at higher TD temperatures. The temperature at which 50% of the SOA evaporated was around 90°C for the α-pinene experiments and 80°C for the cyclohexene experiments. Experiment AP4 was conducted at the lowest SOA concentration, which could explain why its MFR is higher than that in the other experiments. The increase in MFR could also have been caused by recondensation in the cooling section since Experiment AP4 did not have activated carbon, but this behavior was not observed in Experiments CH3 and CH4, where activated carbon was also removed from the cooling section. The thermograms in our study are consistent with the results of Kolesar et al. (2015) where the authors showed that thermograms from the ozonolysis of α-pinene were similar if the mass concentration was less than 300 μg m^{-3}.

The MFR at 25°C for Experiments CH1 and CH2 was around 0.93, indicating that SOA evaporation occurred in the TD at room temperature. These were cyclohexene experiments in

which activated carbon was used in the cooling section of the TD. Higher particle losses in the TD are also a potential explanation, but this is inconsistent with the results of all other experiments at room temperature, which were about 1 after correction. Saleh, Shihadeh, and Khlystov (2011) argued that activated carbon in the cooling section of TDs can remove vapor-phase compounds and cause more volatile particle components to evaporate. Therefore, we hypothesized that the cyclohexene ozonolysis SOA had some relatively volatile particle components that evaporated in response to the activated carbon section absorbing the vapor-phase compounds and thus, lowered the MFR at room temperature.

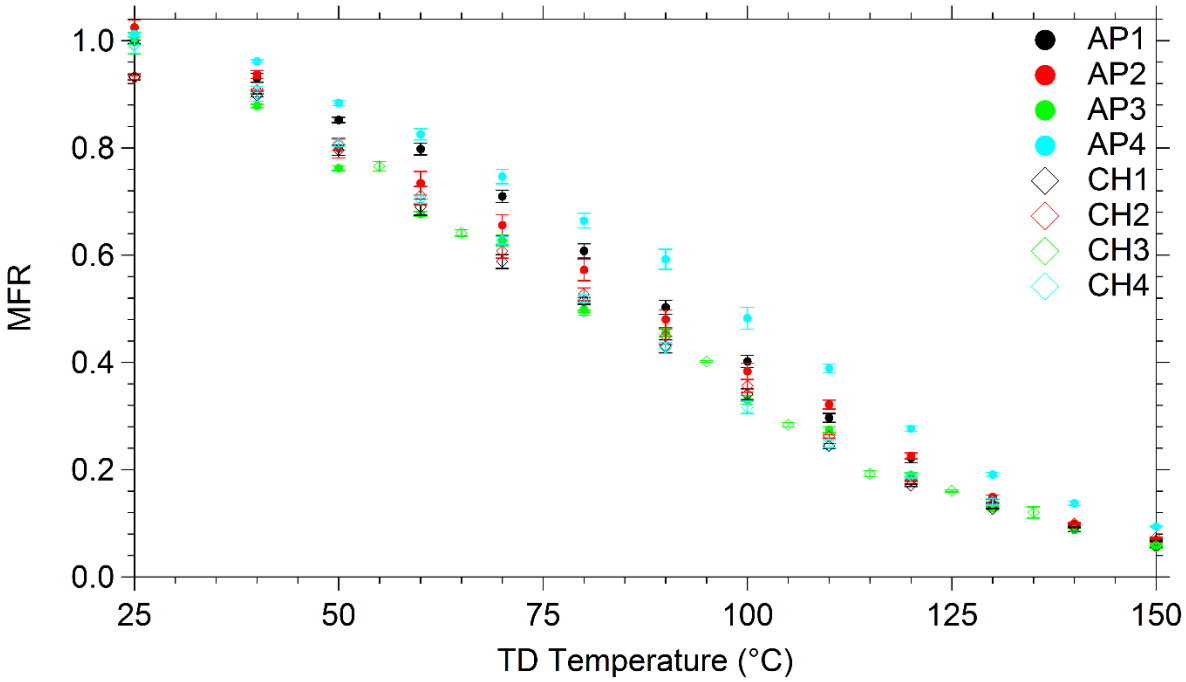

Figure 3.3. The thermograms for all of the SOA experiments. The error bars represent one standard deviation of the mean MFR.

To test this hypothesis, we ran three additional experiments without activated carbon in the cooling section of the TD, one with α-pinene ozonolysis SOA (Experiment AP4) and two with cyclohexene ozonolysis SOA (Experiments CH3 and CH4). The experimental procedure remained

exactly the same, except that we replaced the 2 ft of 1.5 in tubing that housed the activated carbon and replaced it with 5 ft of 0.25 in tubing and no activated carbon. The additional length of the cooling section was added to increase the residence time and allow the particles to return to room temperature before being sampled by the instruments. The smaller tubing was used to minimize re-condensation (Saleh, Shihadeh, and Khlystov 2011). As seen in Fig. 3.3, the MFRs for Experiments AP4, CH3, and CH4 at 25°C were about 1, indicating that the activated carbon was stripping volatile components from the cyclohexene ozonolysis SOA at least at room temperature in Experiments CH1 and CH2.

3.4.2.2 Dilution results

In order to verify that there was no evaporation occurring in the dilution chamber before the instruments sampled, we compared the dilution ratio and mean volume diameter after correcting for pump losses in the transfer from the main chamber to the dilution chamber. The results from this analysis can be seen in Table 3.2. For the α-pinene ozonolysis SOA, the corrected values were very close to the measured dilution ratio and mean volume diameter. This suggested

Table 3.2. Results from the analysis on the initial properties in the dilution chamber.

			Mean Volume Diameter (nm)	
Exp.	**Dilution Ratio**	**Main/Dilution Mass Ratio[a]**	**Main Chamber**	**Dilution Chamber[a]**
AP1	16.8	17.1	130	133
AP2	18.3	18.1	152	153
AP3	19.0	18.8	198	196
AP4	25.5	23.6	106	111
CH1	15.5	23.1	184	163
CH2	16.8	22.4	177	159
CH3	16.4	24.5	189	168
CH4	14.9	17.2	130	124

[a]After correction for pump losses.

that there was no evaporation of the α-pinene ozonolysis SOA during the few minutes required for the mixing of the dilution chamber and the first measurement. However, nearly all of the pump-loss corrected values for the cyclohexene ozonolysis SOA experiments differed significantly from the measured values. These differences were indicative of evaporation occurring before the instruments could sample. For example, in Experiment CH1 the pump corrected mass ratio between the main and dilution chambers was 23.6, but the dilution ratio was measured as 15.5, which implies that the initial SOA mass concentration in the dilution chamber was lower than expected. Furthermore, the initial mean volume diameter in the dilution chamber after correction for pump losses for Experiment CH1 was over 20 nm smaller than that in the main chamber, suggesting again that evaporation was occurring quickly.

To account for the rapid evaporation in the cyclohexene experiments, we determined the concentration that was present in the dilution chamber before evaporation started. To estimate this, we removed the particles lost in the pump from the average size distribution in the main chamber (Fig. B.1). Then, we divided this size distribution by the dilution ratio. We used the resulting concentration as the initial concentration in the dilution chamber for calculation of the areograms. We placed it one SMPS scan back in time (2.5 min) from the original initial concentration measured by the SMPS for the areograms. For example, in Experiment CH1, the original initial concentration in the dilution chamber measured by the SMPS was 6.9 μg m^{-3}. After performing the analysis described above, the initial concentration that we used was 10 μg m^{-3} and the second MFR in the areogram (2.5 min later) was 0.69.

The corrected (both for particle wall-losses and initial evaporation) areograms from all of the SOA experiments can be seen in Fig. 3.4. Since the initial concentration in the dilution chamber for the cyclohexene experiments depended on the correction of losses in the pump, we included

the corresponding uncertainty (Fig. B.1) in all cyclohexene areograms. Unlike the thermograms that were quite similar, the areograms from the two SOA systems were quite different. After 2 h of dilution, the α-pinene ozonolysis SOA evaporated by only 15–20%, while 45–65% of the cyclohexene ozonolysis SOA evaporated even though they were diluted by similar amounts and had similar mass concentrations. Interestingly, even after 2 h in the dilution chamber, the particle wall-loss corrected SOA concentrations continued to decrease for all experiments.

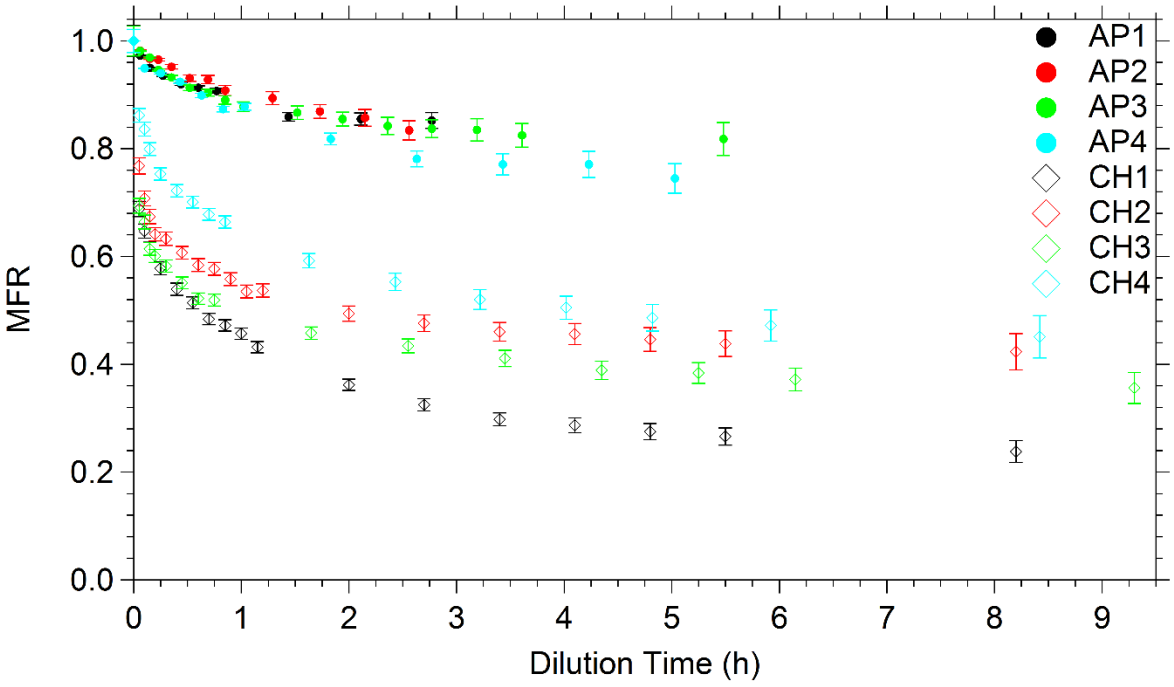

Figure 3.4. The areograms for all of the SOA experiments. The error bars represent the uncertainty resulting from correcting for particle wall-losses (and pump losses for the cyclohexene experiments).

All of the areograms after 2 h decreased at a rate of around 0.02% h^{-1} (or roughly 0.1 μg m^{-3} h^{-1}). It is expected that, after sometime, both SOA systems would stop evaporating and reach equilibrium, and, therefore, the areograms would level off. However, that was not the case for these experiments. There are a number of potential explanations for this behavior. First, there could be errors in our particle wall-loss correction, but we corrected the ammonium sulfate portion at the

end of our experiments, which we used to calculate the size-dependent particle wall-loss constant, and the corrected ammonium sulfate mass concentration in the dilution chamber reached a constant concentration (Fig. B.3), indicating that the particle wall-loss correction was accurate. Second, the time for these SOA systems to reach equilibrium could be longer than we measured, but we measured for over 9 h in selected experiments and the particles were still evaporating. Third, vapors could be continuously lost to the chamber walls, causing their particle-phase counterparts to evaporate. Therefore, we are hypothesizing that vapor-phase wall-losses were causing the SOA to continue to evaporate.

3.5 Modelling results

3.5.1 Estimating SOA volatility distributions using thermograms

The SOA thermograms were combined with the dynamic mass transfer model of Riipinen et al. (2010) and the error minimization approach developed by Karnezi, Riipinen, and Pandis (2014) to estimate the SOA volatility distributions. The estimated volatility distributions from Experiments AP1 and CH1 using only the TD data can be seen in Fig. 3.5. It should be noted that the lowest bin in the volatility distribution also includes compounds with even lower volatilities. According to these results, the α-pinene ozonolysis SOA in Experiment AP1 consisted of 51% low volatility compounds (LVOCs) and 49% SVOCs, while the cyclohexene ozonolysis SOA in Experiment CH1 consisted of 41% LVOCs and 59% SVOCs. These results imply that the SOA from these two experiments were comprised of compounds with similar volatility. The model also estimated enthalpies of vaporization, ΔH_{vap}, around 90 kJ mol^{-1} and accommodation coefficients of the order of 0.1 for both experiments. The model results for all experiments can be seen in Fig.

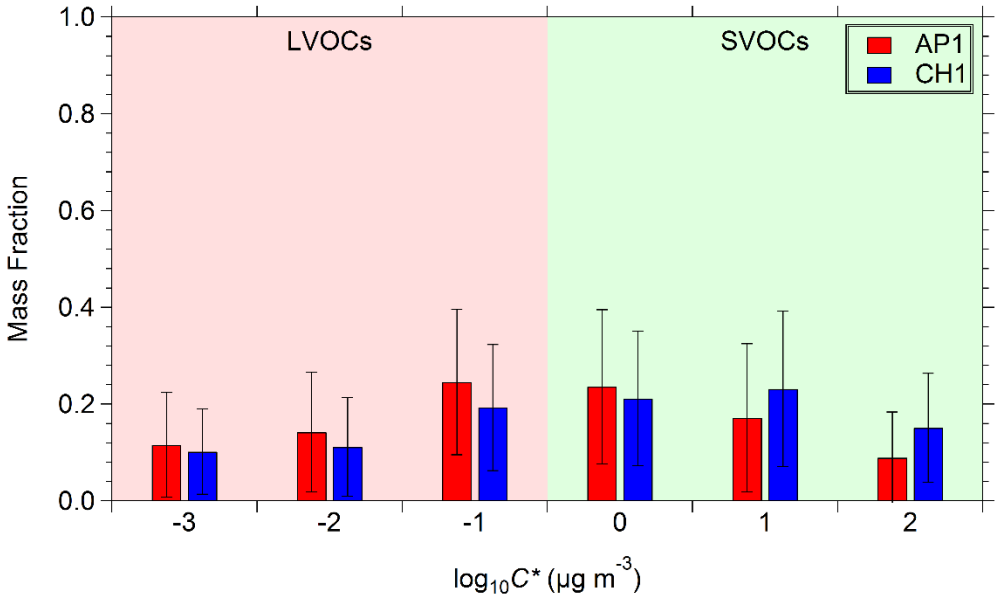

Figure 3.5. Estimated volatility distributions for Experiments AP1 (red bars) and CH1 (blue bars) using only the thermograms as inputs to the model. The error bars represent the uncertainty calculated by the model (Eq. 3.12). The LVOCs in the 1D-VBS framework are in the red shaded area, while the SVOCs are in the green shaded area.

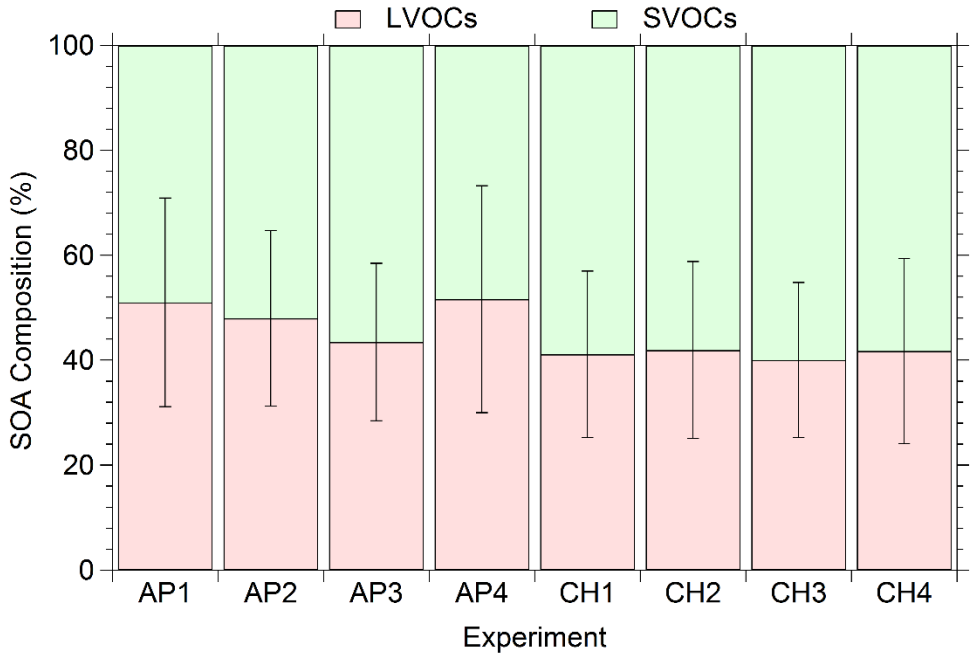

Figure 3.6. Estimated SOA composition for all SOA experiments along with their uncertainties (± 1 standard deviation) using only the TD data. The LVOCs are shown in red while the SVOCs are shown in green. Since there are only two classes of compounds, the uncertainty is the same for the SVOCs as it is for the LVOCs.

3.6, while estimates for the ΔH_{vap} and accommodation coefficient, can be seen in Table B.1. In general, the cyclohexene ozonolysis SOA was predicted to be comprised of slightly more SVOCs, but the large uncertainty makes it difficult to make any definite conclusions. However, these results do suggest that the SOA from the ozonolysis of α-pinene and cyclohexene were quite similar in volatility. The model fits to the thermograms for Experiments AP1 and CH1 can be seen in Fig. B.4. In general, the model was able to reproduce the thermograms from all experiments with deviations of a few percent or less.

3.5.2 Estimating SOA volatility distributions using thermograms and areograms

We again used the dynamic mass transfer model of Riipinen et al. (2010) and the error minimization approach developed by Karnezi, Riipinen, and Pandis (2014) to estimate the SOA volatility distributions, but this time, we used the model to fit an experiment's thermogram and areogram simultaneously. However, we discovered that, in this case, we obtained better fits to the thermograms and areograms when we expanded the range of volatility bins to 10^{-5} to 10^{3} μg m^{-3}. The reduction in error was consistent for all α-pinene experiments, but the behavior was more complex in the cyclohexene experiments, which are examined further in Section 3.5.3. Further expansion of the range of volatility bins did not result in any further decrease of the model error.

The volatility distributions for Experiments AP1 and CH1 using the new volatility range can be seen in Fig. 3.7. The addition of the areograms to the fitting process resulted in dramatic changes to the volatility distributions. According to these results, the α-pinene ozonolysis SOA in Experiment AP1 consisted of 13% extremely low volatility compounds (ELVOCs), 56% LVOCs, and 31% SVOCs and the cyclohexene ozonolysis SOA in Experiment CH1 was comprised of 16% LVOCs, 72% SVOCs, and 14% IVOCs. These results suggest that the α-pinene ozonolysis SOA

and cyclohexene ozonolysis SOA were no longer similar in volatility, with the α-pinene ozonolysis SOA being significantly less volatile than the cyclohexene ozonolysis SOA.

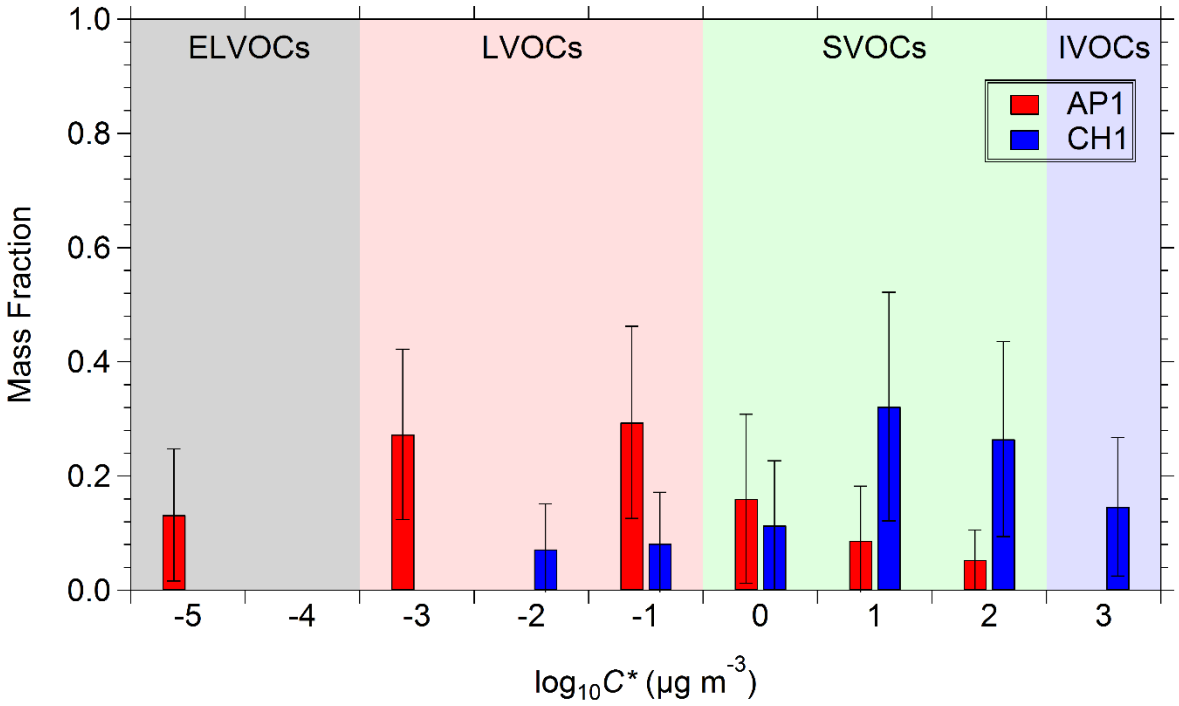

Figure 3.7. Estimated volatility distributions for Experiments AP1 (red bars) and CH1 (blue bars) using both the thermogram and areogram data. The error bars represent the uncertainty calculated by the model (Eq. 3.12). The ELVOCs in the 1D-VBS framework are in the grey shaded area, the LVOCs are in the red shaded area, the SVOCs are in the green shaded area, and the IVOCs are in the blue shaded area.

The model results from all experiments can be seen in Fig. 3.8, while estimates for the ΔH_{vap} and accommodation coefficient, can be seen in Table B.2. In general, after adding the areograms to the fitting process, the α-pinene ozonolysis SOA consisted of mostly LVOCs and lower volatility compounds with a ΔH_{vap} around 140 kJ mol^{-1} and accommodation coefficient around 0.07 while the cyclohexene ozonolysis SOA consisted of mostly SVOCs with a ΔH_{vap} around 80 kJ mol^{-1} and accommodation coefficient around 0.03. Experiments AP4 and CH4 were conducted at lower SOA concentrations where it is expected that the particle-phase would consist

of a higher fraction of lower volatility compounds than in the other six experiments. The model accurately predicted that the particles at 25°C for Experiments AP4 and CH4 would consist of more LVOCs and less SVOCs and IVOCs than the other experiments, indicating that more of the SVOCs and IVOCs remained in the vapor-phase.

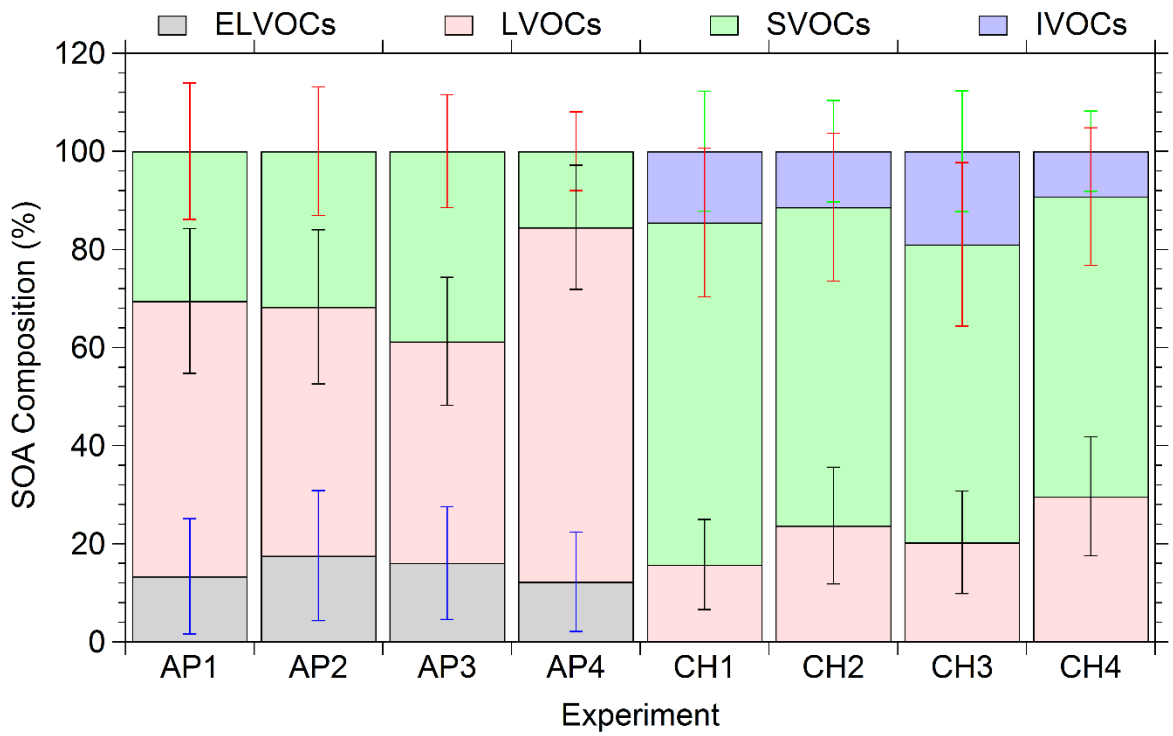

Figure 3.8. Estimated SOA composition for all SOA experiments with their uncertainties (± 1 standard deviation) using both the TD and dilution data. The ELVOCs are shown in grey, LVOCs in red, SVOCs in green, and IVOCs in blue. The uncertainties for the ELVOCs, LVOCs, SVOCs, and IVOCs are shown in blue, black, red, and green, respectively.

Interestingly, the addition of the dilution data to the analysis led to predictions of less volatile SOA from the ozonolysis of α-pinene, but more volatile SOA from the ozonolysis of cyclohexene. Louvaris et al. (2017) reported that the estimated volatility of cooking OA decreased when TD and dilution measurements were combined when compared to estimates from just TD measurements alone. The α-pinene ozonolysis SOA results reported here are consistent with those

results, but the cyclohexene ozonolysis SOA results reveal that the addition of the dilution measurements can also increase the estimated volatility. This is especially important in these two systems because without the dilution measurements, the volatility of the SOA from both precursors would appear to be quite similar.

3.5.3 Estimating SOA volatility distributions using thermograms and areograms accounting for vapor-phase wall-losses

In order to investigate the role of vapor-phase wall-losses in our experiments, we updated the model to account for vapor-phase wall-losses in the dilution chamber. Equation 3.9 for the dilution chamber was updated to account for vapor-phase wall-losses by adding a first order loss term:

$$\frac{\mathrm{d}C_i}{\mathrm{d}t} = I_i \cdot N_{\mathrm{tot}} - k_{v,w} \cdot C_i \tag{3.13}$$

where $k_{v,w}$ is the vapor-phase wall-loss constant. This approach assumes that all vapor-phase compounds are lost to the chamber walls irreversibly with the same rate constant. This differs from previous studies that model vapor-phase wall-losses as an equilibrium partitioning between the chamber walls and vapors (Krechmer et al. 2016; La et al. 2016; Matsunaga and Ziemann 2010; McVay, Cappa, and Seinfeld 2014; Nah et al. 2016; Yeh and Ziemann 2014, 2015), but is analogous to having a high equivalent mass of absorbing organic material on the chamber walls (Matsunaga and Ziemann 2010; X. Zhang et al. 2015). The one-way loss rate is consistent with our experimental results that showed relatively constant evaporation for several hours. In order to avoid having too many free parameters, as a first approximation, we used the model with the estimated ΔH_{vap} and accommodation coefficient for each experiment from Table B.2 and allowed it to estimate the volatility distribution and $k_{v,w}$.

The model fits to the thermogram and areogram from Experiments AP1 and CH1, either accounting for vapor-phase wall-losses or neglecting them, can be seen in Fig. 3.9. These results are representative of all experiments. For Experiment AP1, the model fits did not change significantly when either model was used. Both models predicted only models evaporation in the dilution chamber, with rapid evaporation for the first couple of minutes and then slow changes for the remainder of the experiment. For Experiment CH1, the thermogram fit improved slightly, but the areogram fit improved significantly when the model accounted for vapor-phase wall-losses. The model that did not account for vapor-phase wall-losses predicted that the cyclohexene ozonolysis SOA reached equilibrium in the dilution chamber after 1–2 h even though the particles

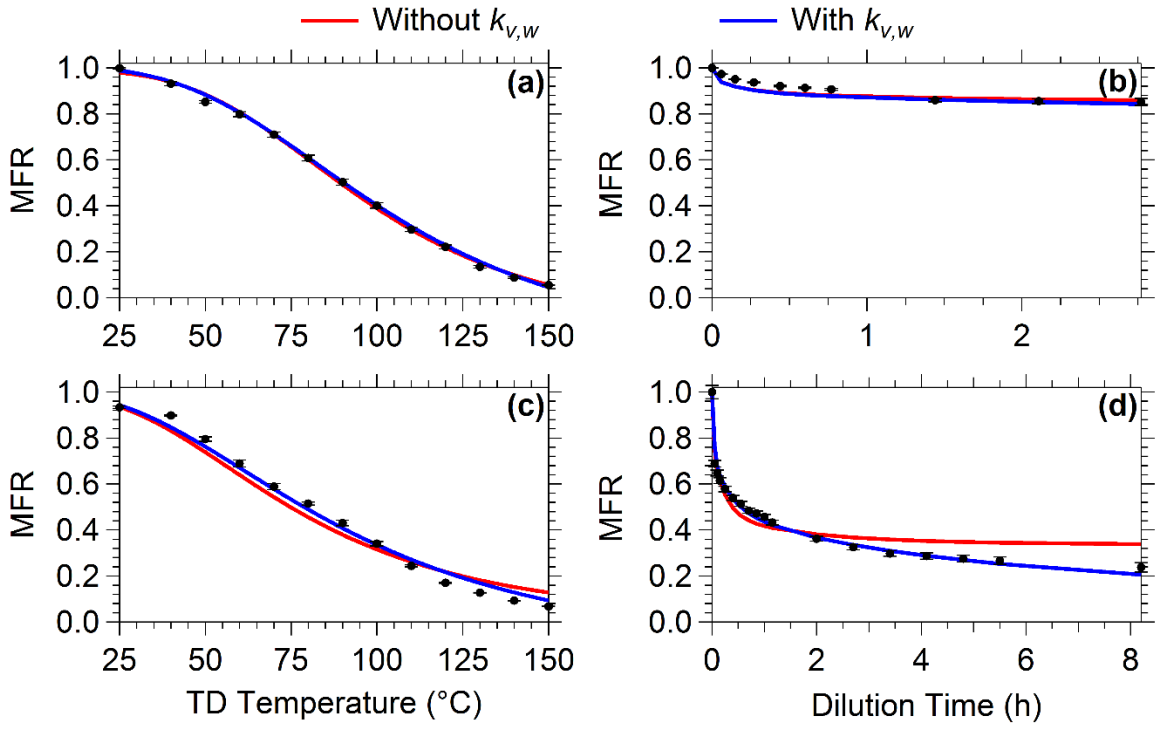

Figure 3.9. (a) Thermogram and (b) areogram for Experiment AP1. (c) Thermogram and (d) areogram for Experiment CH1. Black circles in (a) and (c) represent TD-loss corrected SMPS measurements with the error bars representing 1 standard deviation of the mean. Black circles in (b) and (d) represent particle wall-loss corrected SMPS measurements. The error bars in (b) and (d) represent the uncertainty resulting from correcting for particle wall-losses (and pump losses for (d)). The red line in each panel is the best fit from the model that does not account for vapor-phase wall-losses. The blue line in each panel is the best fit from the model that includes vapor-phase wall-losses.

continued to evaporate. For all cyclohexene experiments, the model that did not account for vapor-phase wall-losses reproduced the TD behavior, but could not reproduce the latter stages of the areograms, especially after 2 h. This behavior is consistent with slow evaporation after the first 2 h of dilution due to vapor-phase wall-losses. When the model incorporates vapor-phase wall-losses, the reduction in fractional error when the volatility range is expanded is consistent across all experiments.

The model estimated a vapor-phase wall-loss constant around 2 h^{-1} for most experiments (Table B.3), which implies that vapors were lost in the dilution chamber for these experiments on the time scale of about 30 min, but the uncertainty was significant. The vapor-phase wall-loss constants estimated in this work are similar to time scales measured for several different organic species (Krechmer et al. 2016; Matsunaga and Ziemann 2010; Ye et al. 2016; Yeh and Ziemann 2014, 2015).

The volatility distributions and SOA compositions comparing both versions of the model for Experiments AP1 and CH1 can be seen in Fig. 3.10. The remainder of the experiments' results, including estimates for $k_{v,w}$, can be seen in Table B.3. The addition of the vapor-phase wall-loss constant to the fitting process resulted in a shift of the volatility distributions to slightly lower volatilities. For example, in Experiment AP1, the SVOCs decreased from 31 to 23% and the LVOCs increased from 56 to 68% while the ELVOCs decreased slightly. These results suggest that the model that does not account for vapor-phase wall-losses tends to overestimate a little the SOA volatility because it attributes more of the evaporation in the dilution chamber to more volatile SOA components.

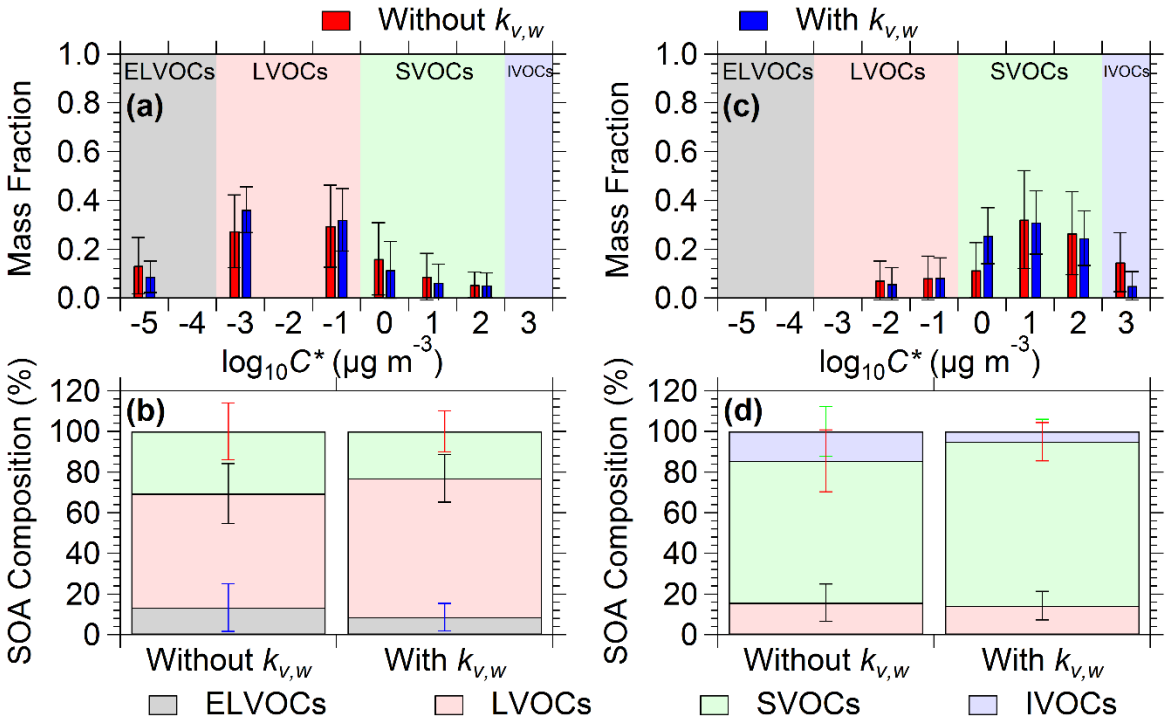

Figure 3.10. (a) Estimated volatility distributions from the model without (red) and with (blue) vapor wall-losses included for Experiment AP1. (b) Corresponding SOA composition of (a) along with their uncertainties (± 1 standard deviation). The ELVOCs are shown in grey, LVOCs in red, SVOCs in green, and IVOCs in blue. The uncertainties for the ELVOCs, LVOCs, SVOCs, and IVOCs are shown in blue, black, red, and green, respectively. (c) Estimated volatility distribution from the model without (red) and with (blue) vapor wall-losses included for Experiment CH1. (d) Corresponding SOA composition of (c) along with their uncertainties (± 1 standard deviation). The color scheme is the same as that in (a) and (b).

3.6 Potential effects of reactions and SOA phase state

SOA has been shown to often contain oligomers (Trump and Donahue 2014), which can dissociate at elevated temperatures in the TD or even during dilution. Our analysis assumes that particle-phase reactions are negligible. The ability of the model to explain both the thermogram and areogram with a single volatility distribution is encouraging, but it does not prove that no reactions are taking place. The PTR-MS measurements in the dilution chamber did not indicate the production of compounds that could be potential components of oligomers, but this is also not conclusive given the limitations of the PTR-MS used. Unfortunately, the AMS also provides

limited information about potential fragmentation of oligomers or other SOA components. These potential reactions in the system could be addressed experimentally in the future with high-resolution molecular composition measurements of both the particle and vapor-phases while using a TD or during isothermal dilution.

SOA phase state is another important property that could impact our results. The state of the SOA particles can range from liquid-like (minimal mass transfer resistances, e.g., Liu et al. 2019) to glassy solid (significant mass transfer resistances, e.g., Shiraiwa et al. 2017). Our experiments were conducted at low RH, which has been shown to decrease viscosity and, therefore, increase mass transfer resistances (Vaden et al. 2011; Wilson et al. 2015; Yli-Juuti et al. 2017; Y. Zhang et al. 2015). The model used in this work parameterizes all resistances to mass transfer between the vapor and particle-phases using an effective mass accommodation coefficient. Our analysis estimated a mass accommodation coefficient on the order of 0.1, suggesting the existence of relatively small limitations to mass transfer during evaporation. Karnezi, Riipinen, and Pandis (2014) noted that the small sensitivity of the mass transfer rate to near unity mass accommodation coefficients can result in lower estimates. Therefore, it is possible that our estimated mass accommodation coefficient is underestimated and closer to unity than the model suggests.

The SOA can be at different phase states at different temperatures in the TD. Currently, the model assumes that the mass accommodation coefficient is constant with temperature. It is possible that, at a certain TD temperature, the particle's phase state changes with removal of any resistances to mass transfer. To explore this possibility, we performed additional model simulations to examine how the thermograms in Experiments AP1 and CH1 would behave if there was a change in phase state at a TD temperature of 100°C. In order to accomplish this, we used

the volatility distributions from Fig. 3.7 and the ΔH_{vap} from Table B.2. The accommodation coefficient started at 0.0001, 0.001, 0.01, or 0.1 and was assumed to change to 1 at 100°C. The predicted thermograms for Experiments AP1 and CH1 can be seen in Fig. B.5 and B.6. In all cases, there was a sharp change in the thermograms at 100°C. This behavior was not observed in our experiments, so, even if a phase change occurs, the effect on the mass transfer is modest. Also, these results indicate that, at least for these systems, the accommodation coefficient does not change by more than one order of magnitude while passing through the TD.

3.7 Discussion and conclusions

This study combined TD and isothermal dilution measurements in order to better understand different techniques that estimate OA volatility distributions and their corresponding properties. Our experimental approach extends the work of Grieshop et al. (2009) by combining dilution and heating in the same set-up and applies it to SOA.

The experimental technique was tested with SOA from the ozonolysis of α-pinene and cyclohexene. The results from these experiments showed that the SOA from both systems evaporated similarly in the TD, but quite differently when diluted. The α-pinene ozonolysis SOA only evaporated 15–20% after 2 h of dilution, while 45–65% of the cyclohexene ozonolysis SOA evaporated in the same time even though they were diluted by similar amounts and had similar mass concentrations.

These two SOA systems highlight the difficulty in estimating OA volatility distributions using thermal evaporation techniques. When only a thermogram was used to estimate the volatility distributions, the α-pinene ozonolysis SOA appeared quite similar in volatility to the cyclohexene ozonolysis SOA. The addition of the areograms allowed the estimation of the volatility

distributions over a larger range and revealed that the α-pinene ozonolysis SOA was comprised of mostly LVOCs while the cyclohexene ozonolysis SOA was comprised of mostly SVOCs. However, the model struggled to fit the cyclohexene areograms because it predicted that the SOA reached equilibrium in the dilution chamber after a couple of hours even though the particles continued to evaporate. Incorporating vapor-phase wall-losses in the model allowed it to reproduce the areograms accurately and shifted the volatility distributions to lower values.

TD measurements alone can provide information about the full volatility distribution, but this information is coupled with the enthalpy of vaporization. There are several combinations of volatility distributions and enthalpy of vaporization values that fit the thermograms. On the other hand, isothermal dilution measurements remove the enthalpy of vaporization dependence, but they only provide direct information about SVOCs and higher volatility components. If isothermal dilution measurements are used alone, they only provide information about the sum of the LVOCs, ELVOCs, and lower volatility compounds without any details about their distribution. Karnezi, Riipinen, and Pandis (2014) showed that isothermal dilution measurements on their own result in worse volatility distribution estimates when compared to TD data being used alone. As shown in this study and Louvaris et al. (2017), combining TD and isothermal dilution measurements constrains not only the SVOCs, but also the enthalpy of vaporization. This study further reiterates the need to combine techniques, in this case TD and isothermal dilution measurements, in order to fully understand OA properties, such as volatility.

3.8 References

An, W. J., R. K. Pathak, B. H. Lee, and S. N. Pandis. 2007. Aerosol volatility measurement using an improved thermodenuder: Application to secondary organic aerosol. *J. Aerosol Sci.* 38: 305–14. doi: 10.1016/j.jaerosci.2006.12.002.

Cain, K. P., and S. N. Pandis. 2017. A technique for the measurement of organic aerosol

hygroscopicity, oxidation level, and volatility distributions. *Atmos. Meas. Tech.* 10: 4865–76. doi: 10.5194/amt-10-4865-2017.

Cappa, C. D. 2010. A model of aerosol evaporation kinetics in a thermodenuder. *Atmos. Meas. Tech.* 3: 579–92. doi: 10.5194/amt-3-579-2010.

Cappa, C. D., and J. L. Jimenez. 2010. Quantitative estimates of the volatility of ambient organic aerosol. *Atmos. Chem. Phys*. 10: 5409–24. doi: 10.5194/acp-10-5409-2010.

DeCarlo, P. F., J. R. Kimmel, A. Trimborn, M. J. Northway, J. T. Jayne, A. C. Aiken, M. Gonin, K. Fuhrer, T. Horvath, K. S. Docherty, et al. 2006. Field-deployable, high-resolution, time-of-flight aerosol mass spectrometer. *Anal. Chem.* 78: 8281–89. doi: 10.1021/ac061249n.

Di, Q., Y. Wang, A. Zanobetti, Y. Wang, P. Koutrakis, C. Choirat, F. Dominici, and J. D. Schwartz. 2017. Air pollution and mortality in the medicare population. *N. Engl. J. Med.* 376: 2513–22. doi: 10.1056/NEJMoa1702747.

Donahue, N. M., A. L. Robinson, C. O. Stanier, and S. N. Pandis. 2006. Coupled partitioning, dilution, and chemical aging of semivolatile organics. *Environ. Sci. Technol.* 40: 2635–43. doi: 10.1021/es052297c.

Fuchs, N. A., and A. G. Sutugin. 1970. *Highly Dispersed Aerosols*. Ann Arbor, MI. Ann Arbor Science Publishers.

Grieshop, A. P., N. M. Donahue, and A. L. Robinson. 2007. Is the gas-particle partitioning in alpha-pinene secondary organic aerosol reversible?. *Geophys. Res. Lett.* 34: L14810. doi: 10.1029/2007GL029987.

Grieshop, A. P., M. A. Miracolo, N. M. Donahue, and A. L. Robinson. 2009. Constraining the volatility distribution and gas-particle partitioning of combustion aerosols using isothermal dilution and thermodenuder measurements. *Envion. Sci. Technol.* 43: 4750–56. doi: 10.1021/es8032378.

Hildemann, L. M., G. R. Cass, and G. R. Markowski. 1989. A dilution stack sampler for collection of organic aerosol emissions: Design, characterization and field tests. *Aerosol Sci. Technol.* 10: 193–204. doi: 10.1080/02786828908959234.

IPCC. 2013. Summary for Policymakers. In T. F. Stoker, D. Qin, G.-K. Plattner, M. Tignore, S. K. Allen, J. Boschung, A. Nauels, Y. Xia, and P. M. Midgley (Eds.), *Climate Change 2013: The physical science basis. Contribution of Working Group I to the Fifth Assessment Report of the Intergovernmental Panel on Climate Change.* Cambridge. Cambridge University Press.

Jorga, S. D., C. Kaltsonoudis, A. Liangou, and S. N. Pandis. 2020. Measurement of formation rates of secondary aerosol in the ambient urban atmosphere using a dual smog chamber system. *Environ. Sci. Technol.* doi: 10.1021/acs.est.9b03479.

Kaltsonoudis, C., S. D. Jorga, E. Louvaris, K. Florou, and S. N. Pandis. 2019. A portable dual-smog-chamber system for atmospheric aerosol field studies. *Atmos. Meas. Tech.* 12: 2733–43. doi: 10.5194/amt-12-2733-2019.

Karnezi, E., I. Riipinen, and S. N. Pandis. 2014. Measuring the atmospheric organic aerosol volatility distribution: A theoretical analysis. *Atmos. Meas. Tech.* 7: 2953–65. doi: 10.5194/amt-7-2953-2014.

Kolesar, K. R., C. Chen, D. Johnson, and C. D. Cappa. 2015. The influences of mass loading and rapid dilution of secondary organic aerosol on particle volatility. *Atmos. Chem. Phys.* 15: 9327–43. doi: 10.5194/acp-15-9327-2015.

Kostenidou, E., R. K. Pathak, and S. N. Pandis. 2007. An algorithm for the calculation of secondary organic aerosol density combining AMS and SMPS data. *Aerosol Sci. Technol.* 41: 1002–10. doi: 10.1080/02786820701666270.

Krechmer, J. E., D. Pagonis, P. J. Ziemann, and J. L. Jimenez. 2016. Quantification of gas-wall partitioning in teflon environmental chambers using rapid bursts of low-volatility oxidized species generated in situ. *Environ. Sci. Technol.* 50: 5757–65. doi: 10.1021/acs.est.6b00606.

Kuwata, M., Q. Chen, and S. T. Martin. 2011. Cloud condensation nuclei (CCN) activity and oxygen-to-carbon elemental ratios following thermodenuder treatment of organic particles grown by α-pinene ozonolysis. *Phys. Chem. Chem. Phys.* 13: 14571–83. doi: 10.1039/c1cp20253g.

La, Y. S., M. Camredon, P. J. Ziemann, R. Valorso, A. Matsunaga, V. Lannuque, J. Lee-Taylor, A. Hodzic, S. Madronich, and B. Aumont. 2016. Impact of chamber wall loss of gaseous organic compounds on secondary organic aerosol formation: Explicit modeling of SOA formation from alkane and alkene oxidation. *Atmos. Chem. Phys.* 16: 1417–31. doi: 10.5194/acp-16-1417-2016.

Lipsky, E. M., and A. L. Robinson. 2006. Effects of dilution on fine particle mass and partitioning of semivolatile organics in diesel exhaust and wood smoke. *Environ. Sci. Technol.* 40: 155–62. doi: 10.1021/es050319p.

Liu, X., D. A. Day, J. E. Krechmer, W. Brown, Z. Peng, P. J. Ziemann, and J. L. Jimenez. 2019. Direct measurements of semi-volatile organic compound dynamics show near-unity mass accommodation coefficients for diverse aerosols. *Comm. Chem.* 2: 98. doi: 10.1038/s42004-019-0299-x.

Louvaris, E. E., E. Karnezi, E. Kostenidou, C. Kaltsonoudis, and S. N. Pandis. 2017. Estimation of the volatility distribution of organic aerosol combining thermodenuder and isothermal dilution measurements. *Atmos. Meas. Tech.* 10: 3909–18. doi: 10.5194/amt-10-3909-2017.

Loza, C. L., A. W. H. Chan, M. M. Galloway, F. N. Keutsch, R. C. Flagan, and J. H. Seinfeld. 2010. Characterization of vapor wall loss in laboratory chambers. *Environ. Sci. Technol.* 44:

5074–78. doi: 10.1021/es100727v.

Matsunaga, A., and P. J. Ziemann. 2010. Gas-wall partitioning of organic compounds in a teflon film chamber and potential effects on reaction product and aerosol yield measurements. *Aerosol Sci. Technol.* 44: 881–92. doi: 10.1080/02786826.2010.501044.

McVay, R. C., C. D. Cappa, and J. H. Seinfeld. 2014. Vapor–wall deposition in chambers: Theoretical considerations. *Environ. Sci. Technol.* 48: 10251–8. doi: 10.1021/es502170j.

Nah, T., R. C. McVay, X. Zhang, C. M. Boyd, J. H. Seinfeld, and N. L. Ng. 2016. Influence of seed aerosol surface area and oxidation rate on vapor wall deposition and SOA mass yields: A case study with α-pinene ozonolysis. *Atmos. Chem. Phys.* 16: 9361–79. doi: 10.5194/acp-16-9361-2016.

Nah, T., R. C. McVay, J. R. Pierce, J. H. Seinfeld, and N. L. Ng. 2017. Constraining uncertainties in particle-wall deposition correction during SOA formation in chamber experiments. *Atmos. Chem. Phys.* 17: 2297–310. doi: 10.5194/acp-17-2297-2017.

Odum, J. R., T. Hoffmann, F. Bowman, D. Collins, R. C. Flagan, and J. H. Seinfeld 1996. Gas/particle partitioning and secondary organic aerosol yields. *Environ. Sci. Technol.* 30: 2580–85. doi: 10.1021/es950943+.

Pathak, R. K., C. O. Stanier, N. M. Donahue, and S. N. Pandis. 2007. Ozonolysis of α-pinene at atmospherically relevant concentrations: Temperature dependence of aerosol mass fractions (yields). *J. Geophys. Res.* 112: D03201. doi: 10.1029/2006JD007436.

Riipinen, I., J. R. Pierce, N. M. Donahue, and S. N. Pandis. 2010. Equilibration time scales of organic aerosol inside thermodenuders: Evaporation kinetics versus thermodynamics. *Atmos. Environ.* 44: 597–607. doi: 10.1016/j.atmosenv.2009.11.022.

Saleh, R., A. Shihadeh, and A. Khlystov. 2011. On transport phenomena and equilibration time scales in thermodenuders. *Atmos. Meas. Tech.* 4: 571–81. doi: 10.5194/amt-4-571-2011.

Seinfeld, J. H., and S. N. Pandis. 2016. *Atmopsheric Chemistry and Physics.* 3rd ed. Hoboken, NJ. John Wiley & Sons, Inc.

Shiraiwa, M., L. D. Yee, K. A. Schilling, C. L. Loza, J. S. Craven, A. Zuend, P. J. Ziemann, and J. H. Seinfeld. 2013. Size distribution dynamics reveal particle-phase chemistry in organic aerosol formation. *Proc. Natl. Acad. Sci.* 110: 11746–50. doi: 10.1073/pnas.1307501110.

Shiraiwa, M., Y. Li, A. P. Tsimpidi, V. A. Karydis, T. Berkemeier, S. N. Pandis, J. Lelieveld, T. Koop, and U. Pöschl. 2017. Global distribution of particle phase state in atmospheric secondary organic aerosols. *Nat. Comm.* 8: 15002. doi: 10.1038/ncomms15002.

Stanier, C. O., R. K. Pathak, and S. N. Pandis. 2007. Measurements of the volatility of aerosols from α-pinene ozonolysis. *Environ. Sci. Technol.* 41: 2756–63. doi: 10.1021/es0519280.

Trump, E. R., and N. M. Donahue. 2014. Oligomer formation within secondary organic aerosols: Equilibrium and dynamic considerations. *Atmos. Chem. Phys.* 14: 3691–701. doi: 10.5194/acp-14-3691-2014.

Vaden, T. D., D. Imre, J. Beranek, M. Shrivastava, and A. Zelenyuk. 2011. Evaporation kinetics and phase of laboratory and ambient secondary organic aerosol. *Proc. Natl. Acad. Sci.* 108: 2190–95. doi: 10.1073/pnas.1013391108.

Wang, N., S. D. Jorga, J. R. Pierce, N. M. Donahue, and S. N. Pandis. 2018. Particle wall-loss correction methods in smog chamber experiments. *Atmos. Meas. Tech.* 11: 6577–88. doi: 10.5194/amt-11-6577-2018.

Wilson, J., D. Imre, J. Beránek, M. Shrivastava, and A. Zelenyuk. 2015. Evaporation kinetics of laboratory-generated secondary organic aerosols at elevated relative humidity. *Environ. Sci. Technol.* 49: 243–9. doi: 10.1021/es505331d.

Ye, P., X. Ding, J. Hakala, V. Hofbauer, E. S. Robinson, and N. M. Donahue. 2016. Vapor wall loss of semi-volatile organic compounds in a Teflon chamber. *Aerosol Sci. Technol.* 50: 822–34. doi: 10.1080/02786826.2016.1195905.

Yeh, G. K., and P. J. Ziemann. 2014. Alkyl nitrate formation from the reactions of C8-C14 n-Alkanes with OH radicals in the presence of NOx: Measured yields with essential corrections for gas-wall partitioning. *J. Phys. Chem.* 118: 8147–57 doi: 10.1021/jp500631v.

Yeh, G. K., and P. J. Ziemann. 2015. Gas-wall partitioning of oxygenated organic compounds: Measurements, structure-activity relationships, and correlation with gas chromatographic retention factor. *Aerosol Sci. Technol.* 49: 727–38. doi: 10.1080/02786826.2015.1068427.

Yli-Juuti, T., A. Pajunoja, O.-P. Tikkanen, A. Buchholz, C. Faiola, O. Väisänen, L. Hao, E. Kari, O. Peräkylä, O. Garmash, et al. 2017. Factors controlling the evaporation of secondary organic aerosol from α-pinene ozonolysis. *Geophys. Res. Lett.* 44: 2562–70. doi: 10.1002/2016GL072364.

Zhang, Q., J. L. Jimenez, M. R. Canagaratna, J. D. Allan, H. Coe, I. Ulbrich, M. R. Alfarra, A. Takami, A. M. Middlebrook, Y. L. Sun, et al. 2007. Ubiquity and dominance of oxygenated species in organic aerosols in anthropogenically-influenced Northern Hemisphere midlatitudes. *Geophys. Res. Lett.* 34: L13801. doi: 10.1029/2007GL029979.

Zhang, X., C. D. Cappa, S. H. Jathar, R. C. McVay, J. J. Ensberg, M. J. Kleeman, and J. H. Seinfeld. 2014. Influence of vapor wall loss in laboratory chambers on yields of secondary organic aerosol. *Proc. Natl. Acad. Sci.* 111: 5802–7. doi: 10.1073/pnas.1404727111.

Zhang, X., R. H. Schwantes, R. C. McVay, H. Lignell, M. M. Coggon, R. C. Flagan, and J. H. Seinfeld. 2015. Vapor wall deposition in Teflon chambers. *Atmos. Chem. Phys.* 15: 4197–214. doi: 10.5194/acp-15-4197-2015.

Zhang, Y., M. S. Sanchez, C. Douet, Y. Wang, A. P. Bateman, Z. Gong, M. Kuwata, L. Renbaum-Wolff, B. B. Sato, P. F. Liu, et al. 2015. Changing shapes and implied viscosities of suspended submicron particles. *Atmos. Chem. Phys.* 15: 7819–29. doi: 10.5194/acp-15-7819-2015.

Chapter 4

α-Pinene, limonene, and cyclohexene secondary organic aerosol hygroscopicity and oxidation level as a function of volatility

4.1 Abstract

The hygroscopicity and oxidation level of secondary organic aerosol (SOA) produced in an atmospheric simulation chamber were measured as a function of volatility. The improved technique combines thermodenuding, isothermal dilution, aerosol mass spectroscopy, and size-resolved cloud condensation nuclei measurements to separate the SOA by volatility and then measure its physical (hygroscopicity via the hygroscopicity parameter, κ) and chemical (oxidation level via the oxygen-to-carbon ratio, O:C) properties. The technique was applied to SOA from the ozonolysis of α-pinene, limonene, and cyclohexene. The O:C and κ of the α-pinene ozonolysis SOA decreased as volatility decreased. The semi-volatile (SVOCs) and the low volatility organic compounds (LVOCs) produced during limonene ozonolysis have similar O:C and κ values, but the corresponding extremely low volatility organic compounds (ELVOCs) have significantly lower oxygen content and hygroscopicity. The average O:C of the cyclohexene ozonolysis SOA increased, but the average κ decreased as volatility decreased. These results suggest that some organic aerosol (OA) systems have a more complex relationship between hygroscopicity, oxidation level, and volatility than originally thought. The two-dimensional volatility basis set (2D-VBS) framework can help in integrating these results and providing explanations of the measured hygroscopicity. Use of this technique with different OA systems, both laboratory and ambient, can supply parameters that can be incorporated in atmospheric chemical transport models.

4.2 Introduction

Organic aerosol (OA), a potentially large fraction of particulate matter (PM) depending on location (Zhang et al., 2007), is a complex mixture of organic compounds that continuously evolve

in the atmosphere. OA can be emitted directly in the particulate-phase, known as primary OA (POA), or produced by the condensation of compounds formed from the oxidation of vapor-phase precursors, known as secondary OA (SOA), (Kanakidou et al., 2005; Hallquist et al., 2009). The evolution of OA in the atmosphere is still poorly understood, largely due to the thousands of compounds that comprise it and the difficulty of elucidating their physical and chemical properties (Jimenez et al., 2009; Heald et al., 2010; Kroll et al., 2011; Ditto et al., 2018).

As OA progresses through time in the atmosphere, its composition changes due to evaporation/condensation, addition of fresh emissions, and particulate and vapor-phase reactions (Kroll et al., 2011; Donahue et al., 2013). Three crucial properties that affect the evolution and atmospheric fate of OA are hygroscopicity, oxidation level, and volatility. Hygroscopicity, often represented with the hygroscopicity parameter, κ (Petters and Kreidenweis, 2007), is a measure of a compound's ability to absorb water. Oxidation level, sometimes expressed as the oxygen-to-carbon ratio, O:C, or, more accurately, the average carbon oxidation state, OS_C (Kroll et al., 2011), is a surrogate for compositional changes of OA as it ages in the atmosphere. Volatility determines, to a large extent, a compound's partitioning between the particulate and vapor-phases. The one-dimensional volatility basis set (1D-VBS) was proposed as a framework to describe the volatility distribution of OA over several orders of magnitude (Donahue et al., 2006).

Many previous studies have attempted to relate two of these three properties for ambient and laboratory OA (Meyer et al., 2009; Massoli et al., 2010; Donahue et al., 2011; Frosch et al., 2011; Lambe et al., 2011; Rickards et al., 2013). A growing number of studies have attempted to relate all three properties, but the results are often inconclusive or a clear relationship between the studies cannot be established (Jimenez et al., 2009; Poulain et al., 2010; Kuwata et al., 2011; Tritscher et al., 2011; Hong et al., 2014; Cerully et al., 2015; Hildebrandt Ruiz et al., 2015; Cain

and Pandis, 2017; Alroe et al., 2018; Kostenidou et al., 2018). For example, Jimenez et al. (2009) proposed that, in general, the hygroscopicity and oxidation level of OA increase as volatility decreases. On the other hand, Cerully et al. (2015) observed similar oxidation levels for ambient OA components with significantly different volatility, but the hygroscopicity of the OA decreased with volatility. Nakao (2017) theoretically investigated the hygroscopicity and solubility of OA in the two-dimensional volatility basis set (2D-VBS, Donahue et al., 2011). This study estimated lines of constant κ in the 2D-VBS, which provided a plausible explanation for why the dependence of κ on O:C and volatility should not be simple. These examples and the results from several other studies (Poulain et al., 2010; Kuwata et al., 2011; Tritscher et al., 2011; Hong et al., 2014; Hildebrandt Ruiz et al., 2015; Cain and Pandis, 2017; Alroe et al., 2018; Kostenidou et al., 2018) indicate that the relationship between these three properties is complex and not well understood.

Cain and Pandis (2017) developed an experimental and analysis technique that quantitatively relates hygroscopicity and oxidation level to volatility. They utilized a thermodenuder (TD), a heated tube followed by a cooling section with activated carbon to absorb vapor-phase compounds, to evaporate SOA and characterize the remaining fraction's hygroscopicity and oxidation level. With this technique, the authors concluded that the least volatile components of α-pinene ozonolysis SOA had low O:C and κ values. However, the use of a TD as the only tool to probe the OA volatility introduced significant uncertainty and limited the results (Cain et al., 2020). In the present study, we use an improved approach to characterize the volatility distribution.

The composition and properties of the SOA resulting from the α-pinene and limonene ozonolysis have been studied extensively (e.g., Gao et al., 2004; Huff Hartz et al., 2005; Leungsakul et al., 2005; Varutbangkul et al., 2006; Heaton et al., 2007; Saathoff et al., 2009; Chen

and Hopke, 2010; Kundu et al., 2012; Watne et al., 2017; Witkowski and Gierczak, 2017; Yuan et al., 2017). Limonene has two double bonds (one endocyclic and one exocyclic), making it more reactive towards ozone and forming SOA with higher yields and O:C values than α-pinene ozonolysis SOA (Leungsakul et al., 2005; Heaton et al., 2007; Saathoff et al., 2009; Chen and Hopke, 2010). However, α-pinene and limonene ozonolysis SOA have similar hygroscopic properties (Huff Hartz et al., 2005; Varutbangkul et al., 2006; Yuan et al., 2017). SOA from the ozonolysis of cyclohexene has been studied primarily to understand the cycloalkene ozonolysis mechanism and reaction products (Kalberer et al., 2000; Keywood et al., 2004a; Keywood et al., 2004b; Gao et al., 2004; Bahreini et al., 2005; Rissanen et al., 2014; Hyttinen et al., 2017; Hansel et al., 2018), but a few studies have examined its hygroscopic properties (Varutbangkul et al., 2006; Warren et al., 2009). Both Varutbangkul et al. (2006) and Warren et al. (2009) used subsaturated conditions and observed diameter growth factors for cyclohexene ozonolysis SOA that were significantly higher than the growth factors of monoterpene ozonolysis SOA. The present study is the first, to the best of our knowledge, which examines the hygroscopic behavior of cyclohexene ozonolysis SOA under supersaturated conditions.

In this work, we extend the experimental technique of Cain and Pandis (2017) by adding isothermal dilution to the set of measurements. Cain et al. (2020) showed that this addition can better constrain the SOA volatility distribution. The resulting method is then applied to SOA from the ozonolysis of α-pinene, limonene, and cyclohexene to examine the relationship between hygroscopicity, oxidation level, and volatility in these systems.

4.3 Methodology

4.3.1 Experimental setup

All experiments were conducted in the Air Quality Laboratory at Carnegie Mellon University. The experimental setup is a combination of the setups from Cain and Pandis (2017) and Cain et al. (2020) and can be seen in Fig. 4.1. The two chambers used in this study were Teflon (Welch Fluorocarbons) reactors. The main chamber was a 10 m^3 reactor suspended in a temperature-controlled room (Pathak et al., 2007). The dilution chamber in this study was a 2.5 m^3 reactor suspended in a dark enclosure next to the main chamber. Isothermal dilution took place at approximately 25°C. Before each experiment, the main chamber was flushed overnight with purified air under UV illumination (GE, model 10526 and 10244) to remove any potential contaminants. The dilution chamber was also flushed with purified air for at least one day before each experiment. Purified air was generated by passing compressed air through a high-efficiency particulate air filter to remove any particles, an activated carbon filter to remove any vapors, and silica gel to maintain the relative humidity at less than 10%.

For all experiments, isotopically-labelled butanol (n-butanol-d9, Cambridge Isotope Laboratories, 98%) was used as a dilution tracer and was injected into the main chamber before particles were produced. Once the dilution tracer was well-mixed in the main chamber, either α-pinene (Sigma-Aldrich, ≥ 99%), limonene (Sigma-Aldrich, Analytical Standard), or cyclohexene (Sigma-Aldrich, 99+%) was injected through a heated septum injector. Ozone was generated by an ozone generator (AZCO, model HTU-500ACPS) and was injected into the main chamber after the precursor concentration stabilized. No OH scavenger was used in these experiments. The experimental conditions examined in this study are summarized in Table 4.1. Mass concentrations

were calculated from scanning mobility particle sizer (SMPS) measurements assuming a density of 1.4 g cm^{-3} (Bahreini et al., 2005; Kostenidou et al., 2007).

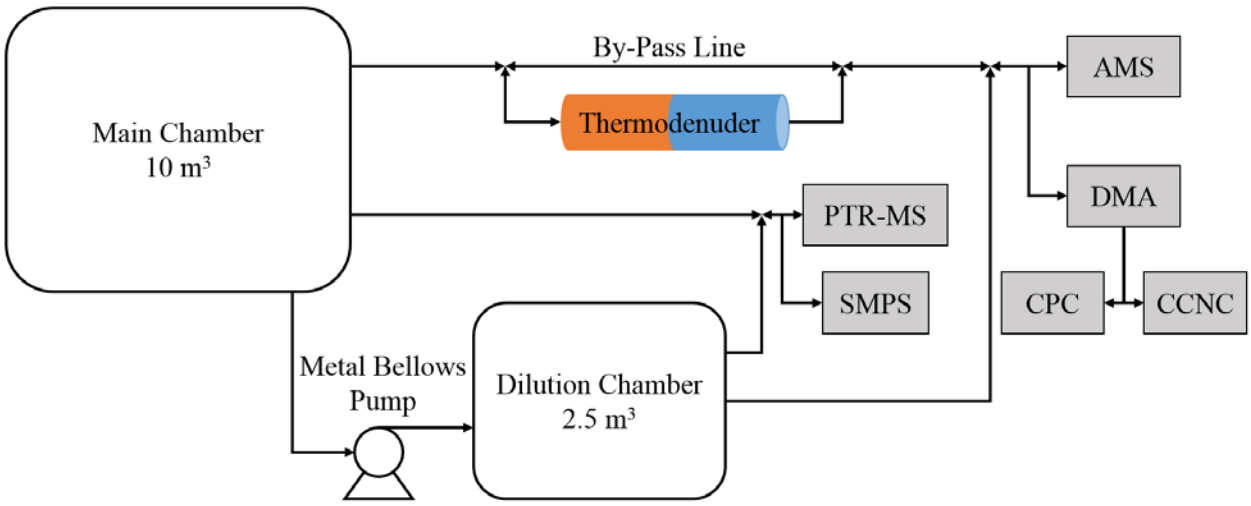

Figure 4.1. The experimental setup used in this study. Particles from the main chamber were characterized with a TD followed by an AMS and a DMA coupled with a CPC and CCNC. Particles were transferred from the main chamber to the dilution chamber via a metal bellows pump and then particles from the dilution chamber were sampled by the same equipment via a three-way valve. Also connected to both chambers via a three-way valve were a PTR-MS, ozone monitor, and SMPS.

Aerosol in the main chamber was characterized by passing through either a TD or by-pass line and then sampled by an Aerodyne high-resolution time-of-flight aerosol mass spectrometer (HR-ToF-AMS, hereafter AMS) and a differential mobility analyzer (DMA, TSI, model 3081) coupled with a condensation particle counter (CPC, TSI, model 3072) and a CCN counter (CCNC, Droplet Measurement Technologies) to allow for scanning mobility CCN analysis (SMCA, Moore et al., 2010). In this study, the AMS used a flow rate of 0.1 L min^{-1} and an averaging time of 1 min in V-mode (DeCarlo et al., 2006). The CPC and CCNC used flow rates of 0.3 and 0.5 L min^{-1} respectively. The sheath flow of the DMA was set to either 4 or 8 L min^{-1}, depending on the particle size distribution. The upscan of the DMA was set to 120 s and the downscan was set to 15 s. The TD from Cain and Pandis (2017) was used in these experiments with equally-spaced temperature

intervals from 25 to 150°C. The centerline residence time through the heating section of the TD at 25°C was 23 s.

Table 4.1. Description of the experimental conditions used in this study.

Exp.	Precursor	VOC (ppb)	Ozone (ppb)	Main Chamber SOA[a] (μg m^{-3})	CCNC SS[b] (%)	Dilution Ratio
AP1	α-Pinene	50	>500[c]	90	0.35	25.7 ± 1.0
AP2	α-Pinene	75	>500[c]	125	0.33	25.3 ± 1.1
AP3	α-Pinene	100	>500[c]	195	0.31	14.7 ± 0.8
AP4	α-Pinene	125	>500[c]	255	0.31	21.2 ± 1.2
LM1	Limonene	60	875	240	0.32	25.2 ± 1.5
LM2	Limonene	60	875	230	0.31	20.9 ± 1.4
LM3	Limonene	75	900	295	0.30	19.5 ± 0.7
CH1	Cyclohexene	150	600	45	0.09	9.1 ± 0.6
CH2	Cyclohexene	150	700	65	0.09	8.9 ± 0.6
CH3	Cyclohexene	175	750	80	0.08	11.2 ± 0.6
CH4	Cyclohexene	175	650	85	0.09	9.1 ± 0.6
CH5	Cyclohexene	200	650	105	0.08	8.2 ± 0.5

[a]SOA mass calculated from the SMPS measurements assuming a density of 1.4 g cm^{-3}.
[b]CCNC supersaturation was held constant during experiments to allow sufficient time for averaging.
[c]The exact value is uncertain due to problems with the ozone monitor.

After initial characterization in the main chamber, some of the aerosol from the main chamber was transferred to the dilution chamber via a metal bellows pump (Baldor, model MB-302) and characterized by the same instruments as the main chamber. The aerosol was transferred only once at a flow rate of 70 L min^{-1} for 45 to 130 s. Different transfer times were used to obtain different dilution ratios. Particle losses in the transfer system were quantified by Cain et al. (2020) and those losses were used for the corresponding corrections in this study. Volatile organic vapor losses for this transfer system were characterized by Kaltsonoudis et al. (2019) and were found to vary from a few percent to not detectable. After initial characterization in the dilution chamber, measurements from both chambers were alternated by three-way valves.

Also sampling from both chambers via a three-way valve were a proton transfer reaction mass spectrometer (PTR-MS, Ionicon Analytic) to monitor volatile organic compound (VOC) concentrations, an ozone monitor (Dasibi Environmental Corporation, model 1008-PC) to measure ozone concentrations, and an SMPS (TSI, DMA model 3081, CPC model 3075) to monitor particle size distributions and concentrations. The PTR-MS and ozone monitor sampled with flow rates of roughly 0.5 L min^{-1} and their data were averaged over 5 minute periods while the SMPS used a sample flow rate of 0.3 L min^{-1} and a sheath flow rate of 3 L min^{-1} with an upscan of 120 s and a downscan of 60 s.

We injected a 5 g L^{-1} solution of ammonium sulfate (Sigma-Aldrich, $\geq$ 99%) into the dilution chamber at the end of our experiments using an atomizer (TSI, model 3075) in order to quantify particle wall-losses occurring in the dilution chamber (Wang et al., 2018). Before entering the chamber, the resulting droplets passed through a silica gel dryer to produce dry particles. After the mass concentration stabilized, we left the particles undisturbed for several hours to determine the size-dependent particle wall-loss rate constant (Wang et al., 2018).

4.3.2 Data analysis

4.3.2.1 Dilution ratio

A dilution ratio was calculated by dividing the concentration of the isotopically-labelled butanol in the PTR-MS (*m*/*z* 66) in the main chamber by the concentration in the dilution chamber. We calculated the dilution ratio each time there was a switch from the main chamber to the dilution chamber and averaged them over the entire experiment.

4.3.2.2 Loss corrections

The TD data were corrected for size and temperature-dependent particle losses following the method in Cain and Pandis (2017). The corrected data were then used to generate thermograms,

particle mass fraction remaining (MFR) as a function of TD temperature, by dividing the TD mass concentration at a certain temperature by the average by-pass mass concentration.

Size-dependent particle wall-losses were also accounted for in the dilution chamber using the method outlined in Cain et al. (2020). Briefly, a size-dependent coagulation-corrected particle wall-loss rate constant was derived from the ammonium sulfate decay and used to correct the SMPS number, volume, and mass concentrations at each size bin (Wang et al., 2018). After correcting for particle wall-losses, we used the mass concentrations to generate areograms, MFR as a function of dilution time, by dividing the mass concentration at time *t* by the initial mass concentration in the dilution chamber at time t_0. As in Cain et al. (2020), we propagated the uncertainty that results from correcting for particle wall-losses over several hours.

For the cyclohexene ozonolysis SOA, we determined that the SOA was evaporating in the dilution chamber faster than the instruments could sample (Table D.1). Therefore, following the approach of Cain et al. (2020), we estimated the initial SOA concentration present in the dilution chamber by taking into account the particles lost in the transfer system and the dilution factor. This initial concentration was higher than the first measured value because non-negligible evaporation had already taken place. Since the initial concentration in the dilution chamber depends on the losses in the transfer system, we also propagated the uncertainty from the losses in the cyclohexene areograms.

4.3.2.3 Hygroscopicity

Activation curves, which express the fraction of particles that activate to become cloud droplets as a function of size at a water supersaturation, were produced with the coupled CPC and CCNC data following the SMCA method (Moore et al., 2010). The activation diameter, the diameter at which 50% of the particles activate, was calculated by fitting the activation curves with

a sigmodal function. The activation diameter, $d_{p,50}$, and CCNC supersaturation, s_c, were combined with κ-Köhler theory to determine the corresponding κ value (Petters and Kreidenweis, 2007):

$$\kappa = \frac{4A^3}{27 d_{p,50}^3 \ln^2 s_c} \quad (4.1)$$

where $A = 4\sigma_{s/a} M_w / RT\rho_w$, $\sigma_{s/a}$ is the surface tension of the solution/air interface, M_w is the molecular weight of water, R is the universal gas constant, T is the temperature, and ρ_w is the density of water. Unless stated otherwise, we used the surface tension of water (0.072 J m^{-2}) and a temperature of 25°C for our calculations.

The monoterpene ozonolysis SOA generated ~10^4 CCN cm^{-3} in the main chamber and, after dilution, there were still ~10^3 CCN cm^{-3} remaining. The cyclohexene ozonolysis SOA generated fewer particles (~10^3 CCN cm^{-3} in the main chamber) and, therefore, upon dilution there were only ~10^2 CCN cm^{-3}. After roughly an hour in the dilution chamber, evaporation and particle wall-losses decreased the CCN concentration to levels that made it difficult to calculate an average activation diameter. Therefore, we stopped calculating the activation diameters in the dilution chamber once the CCN concentration dropped below 50 cm^{-3}.

4.3.2.4 Oxygen content

The AMS data were analyzed in Igor Pro 6.22A (Wavemetrics) using "Squirrel" version 1.56D for unit mass resolution analysis and "Pika" version 1.15D for high resolution analysis. The O:C values reported here were calculated using the Canagaratna et al. (2015) method.

4.3.2.5 Estimation of the volatility distributions

We used the mass transfer model of Riipinen et al. (2010) and the error minimization approach developed by Karnezi et al. (2014) to estimate the SOA volatility distributions. Full details on the approach can be found in Cain et al. (2020) and Karnezi et al. (2014). Briefly, the

model uses as inputs the SOA mass concentration in the main chamber, the average particle size, dilution ratio, and the geometry of the TD (lengths of the heating and cooling sections and residence times in the heating and cooling sections). The volatility distribution in the 1D-VBS framework, enthalpy of vaporization, and mass accommodation coefficient of the SOA are used as fitting parameters. The optimization algorithm uses a brute force approach, trying all combinations of these fitting parameters (with user-selected intervals) to calculate an MFR (either in the TD or dilution chamber) from the ratio of the particle mass at $t = t_{res}$ (where t_{res} is the residence time in either the TD or dilution chamber) to the initial mass of the SOA (either in the main or dilution chamber) and compares it to the measured MFR. The model uses all combinations that fit the data with a user defined accuracy (1% in this study) to calculate a best estimate (and standard deviation) for the fitting parameters. In this work, we used volatility bins for all of the SOA ranging from 10^{-5} to 10^{3} μg m^{-3}. After the detailed 1-D VBS volatility distribution was estimated, we also grouped the results based on their effective saturation concentration, C^*, into four classes, intermediate volatility organic compounds (IVOCs, $C^* \geq 10^3$), semi-volatile organic compounds (SVOCs, $10^0 \leq C^* \leq 10^2$), low volatility organic compounds (LVOCs, $10^{-3} \leq C^* \leq 10^{-1}$), or extremely low volatility organic compounds (ELVOCs, $C^* \leq 10^{-4}$).

We also used another version of this model that accounts for vapor-phase wall-losses in the dilution chamber (Cain et al., 2020). This version adds another fitting parameter to the approach, but the estimated distributions were nearly identical to those neglecting these losses and are only discussed in Appendix D.

4.3.2.6 Determination of O:C and κ distributions as a function of volatility

We used the analysis technique developed in Cain and Pandis (2017) to determine O:C and κ distributions as a function of volatility bin for each experiment using the following equations:

$$[\mathrm{O{:}C}]_j = \sum_{i=1}^{n} x_{i,j}\,[\mathrm{O{:}C}]_i \quad (4.2)$$

$$\kappa_j = \sum_{i=1}^{n} x_{i,j}\kappa_i \quad (4.3)$$

where $[\mathrm{O{:}C}]_j$ and κ_j are the measured O:C and κ at a TD temperature or dilution residence time, $x_{i,j}$ is the SOA mass fraction in the i^{th} volatility bin (e.g., $C^* = 10^{-5}$ μg m^{-3}) at the same temperature or dilution time (estimated by the mass transfer model), and $[\mathrm{O{:}C}]_i$ and κ_i are the unknown O:C and κ for the i^{th} volatility bin.

This approach assumes that the SOA in the various volatility bins has similar average number of carbon atoms per molecule and also similar average molecular weights. It also assumes that the average density of the material in the various volatility bins is similar. The use of Eq. (4.3) is based on the assumption that the SOA has the same surface tension at activation even after evaporation of the more volatile material.

These equations were used to generate a system of equations for both the O:C and κ values that can be solved separately. Due to the number of TD and dilution measurements, each experiment resulted in an overdetermined problem (i.e., more equations than unknown parameters). Therefore, we used a linear least squares approach to minimize the difference between the measured and predicted O:C and κ values. Matlab's linear least squares solver, *lsqlin*, was used for this error minimization problem with a lower bound constraint of zero for both systems. For each SOA experiment, we averaged the O:C and κ values across the different volatility classes to reduce the uncertainty in the O:C and κ distributions. We then averaged these distributions over all experiments and used the standard deviation as a zeroth order metric for the uncertainty of our analysis.

4.4 System test with ammonium sulfate aerosol

We tested our system with ammonium sulfate aerosol to ensure that this complex experimental setup was working properly (Cain and Pandis, 2017; Cain et al., 2020). For this test, we injected a 1 g L^{-1} solution of ammonium sulfate (Sigma-Aldrich, $\geq$ 99%) into the main chamber using an atomizer (TSI, model 3075) followed by a silica gel dryer to produce dry particles. We then followed the procedure outlined in Sect. 4.3 to test the system. The thermogram, areogram, and activation diameter results for this experiment can be seen in Fig. D.4. There was no evaporation in either the TD (below temperatures of 125°C) or dilution chamber (after 5 h of dilution). In addition, the activation diameters at different TD temperatures and in the dilution chamber agreed with Köhler theory predictions using the surface tension of water at 25°C. Therefore, we concluded that our system was operating properly.

4.5 SOA results

The approach discussed in Sect. 4.3 was applied to SOA from the ozonolysis of α-pinene, limonene, and cyclohexene with the conditions specified in Table 4.1. All of the results can be found in Appendix D with results of a few representative experiments discussed in more detail in the subsequent sections.

4.5.1 α-Pinene ozonolysis SOA

The thermogram and areogram, along with fits from the mass transfer model, for Experiment AP1 are shown in Fig. 4.2. There was 5% of the SOA remaining after passing through the TD at 150°C, but only 12% of the SOA evaporated in the dilution chamber after being diluted by a factor of 25 for over 3 h. The model reproduced the measurements well with only small

deviations from the measured MFRs. The SOA in Experiment AP1 was comprised of, according to the model, 15% ELVOCs, 59% LVOCs, and 26% SVOCs (Fig. 4.2c).

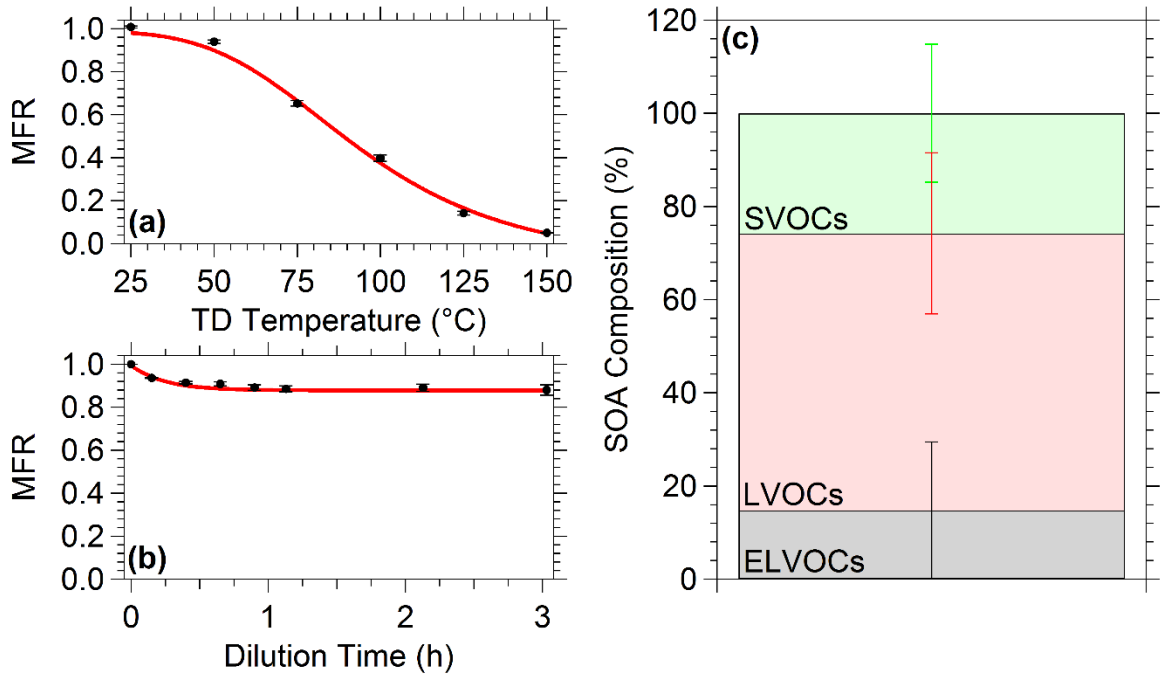

Figure 4.2. The (a) thermogram and (b) areogram for Experiment AP1 with fits from the model (red line). The error bars in (a) represent one standard deviation of the mean MFR while the error bars in (b) represent the uncertainty resulting from correcting for particle wall-losses. (c) SOA composition for Experiment AP1 along with their uncertainties (± one standard deviation) from the model. The ELVOCs are shown in grey, LVOCs in red, and SVOCs in green. The uncertainties for the ELVOCs, LVOCs, and SVOCs are shown in black, red, and green respectively.

The average O:C in the main chamber for the SOA in Experiment AP1 remained practically constant at 0.42 during this experiment. The average O:C of the SOA exiting the TD can be seen in Fig. 4.3a. The O:C remained around 0.42 until the temperature reached 125°C at which 85% of the SOA mass had evaporated and the O:C decreased to 0.40. At higher temperatures, the average O:C continued to decrease, reaching 0.33 at 150°C. At this temperature 5% of the SOA remained, suggesting that the least volatile fraction of the SOA in this experiment had, on average, an O:C of 0.33.

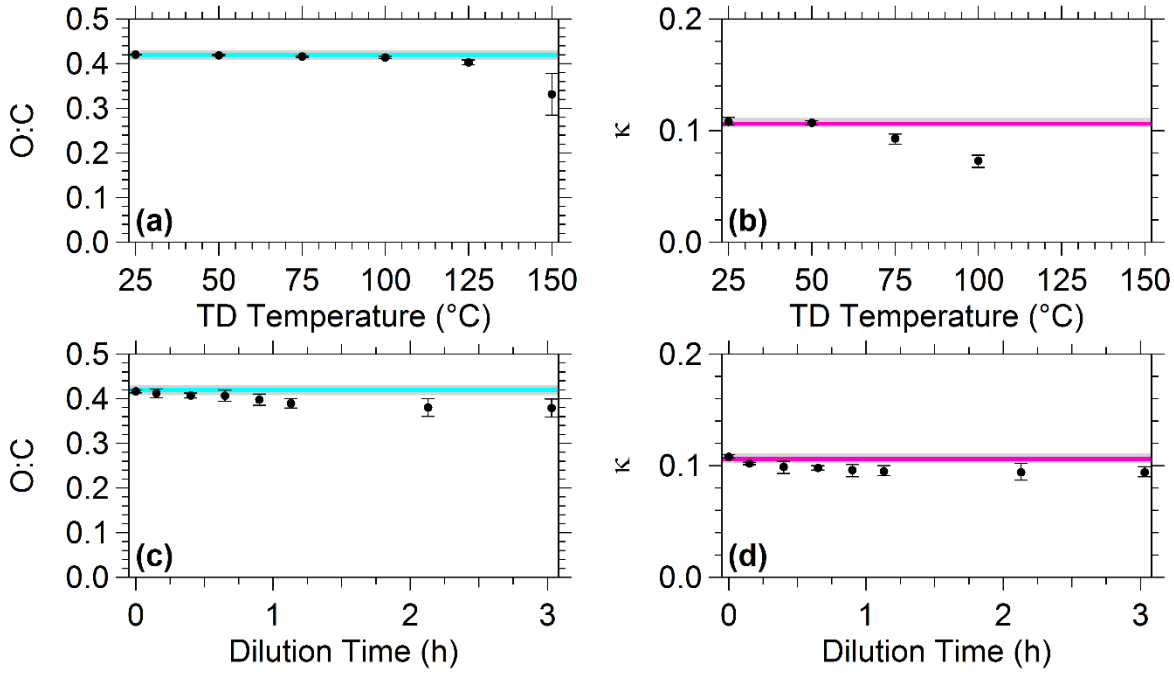

Figure 4.3. The (a) O:C and (b) κ as a function of TD temperature for Experiment AP1. The (c) O:C and (d) κ as a function of dilution time. The error bars represent one standard deviation of the mean O:C or κ. Also shown are the average O:C (blue line) and κ (magenta line) along with ± one standard deviation (grey area) of the mean measured in the main chamber during Experiment AP1.

The average κ of the SOA in this experiment remained constant at 0.11 in the main chamber. The average κ of the SOA exiting the TD was also 0.11 until the temperature reached 75°C (Fig. 4.3b). At this temperature, 35% of the SOA had evaporated and the average κ decreased to 0.09. At higher temperatures, as more of the SOA evaporated, the κ continued to decrease, reaching a value of 0.07 at 100°C. This κ corresponds to the least volatile 40% of the SOA. The 15% of the SOA remaining after evaporation at 125°C did not activate at a supersaturation of 0.35%, indicating that the least volatile SOA components had low hygroscopicity.

The average O:C and κ measured in the dilution chamber as a function of time for Experiment AP1 can also be seen in Fig. 4.3. The initial O:C and κ in the dilution chamber were

the same as the average values in the main chamber. However, both the average O:C and κ decreased slightly for the first hour and then remained relatively constant for the remainder of the experiment.

The remainder of the α-pinene experiments' results can be seen in Appendix D (Figs. D.6–D.11). Experiments AP3 and AP4 were conducted at higher SOA concentrations and, as a result, the SVOCs present in the particulate-phase increased to around 50% of the SOA in these experiments. In general, the SOA had average O:C values around 0.4 and average κ values around 0.1, both consistent with previous observations of α-pinene ozonolysis SOA (Engelhart et al., 2008; Huffman et al., 2009; Massoli et al., 2010; Cain and Pandis, 2017). The O:C and κ behavior in the TD and dilution chamber for the remaining experiments were similar to the results of Experiment AP1 discussed in the previous paragraphs.

The result of applying the method described in Sect. 4.3.2.6 to all of the α-pinene experiments can be seen in Fig. 4.4. The α-pinene ozonolysis SOA generated in this study contained SVOCs with an average O:C of 0.46 ± 0.03 and κ of 0.13 ± 0.02, LVOCs with an average O:C of 0.43 ± 0.02 and κ of 0.09 ± 0.02, and ELVOCs with an average O:C of 0.28 ± 0.08 and κ of 0.06 ± 0.02. Both the O:C and κ values of the LVOCs were statistically lower than those of the SVOCs (alpha = .05). Furthermore, both the O:C and κ values of the ELVOCs were statistically lower than those of the LVOCs (alpha = .05), indicating that the decrease of O:C and κ as volatility decreased was significant.

The O:C and κ distributions determined in this study are bulk averages for a given volatility class, but each volatility class is comprised of many compounds that vary in O:C and κ. The O:C distribution in Fig. 4.4 is consistent with recent results from a study that used a chemical ionization mass spectrometer (CIMS) equipped with a Filter Inlet for Gases and AEROsols (FIGAERO) to

characterize the composition of the particulate-phase from the ozonolysis of α-pinene at 25°C and observed that the O:C of the compounds identified decreased with volatility (Ye et al., 2019).

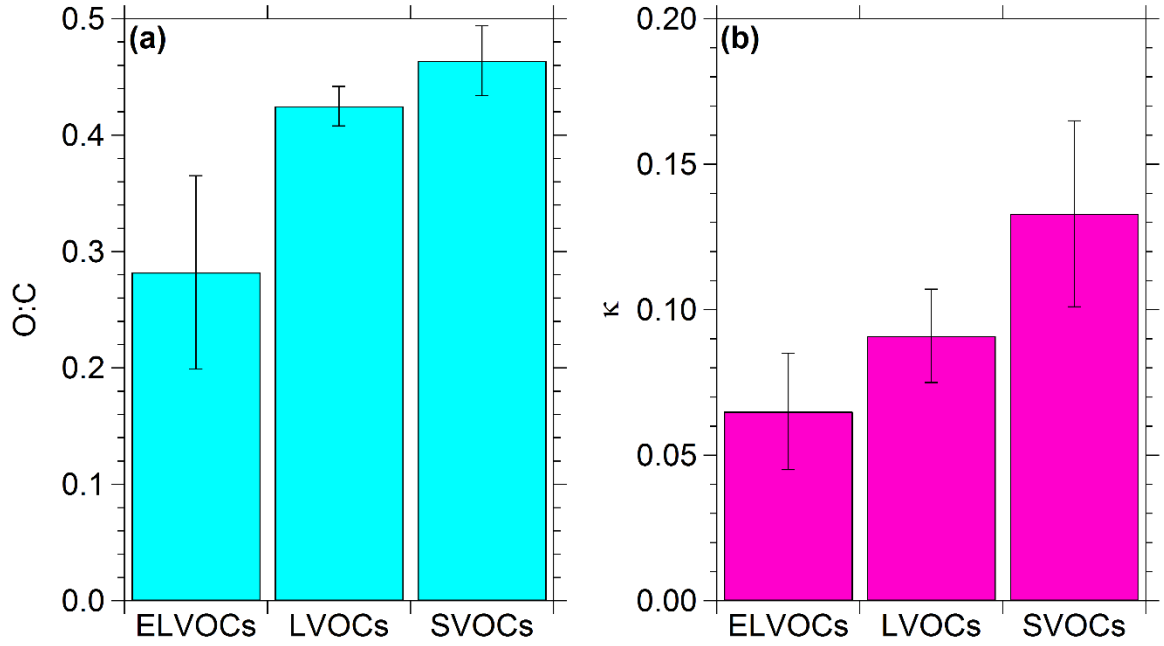

Figure 4.4. The (a) O:C and (b) κ distributions as a function of volatility for the α-pinene ozonolysis SOA examined in this study. The error bars were calculated from the standard deviation that results from determining O:C and κ distributions for each experiment and represent variability between experiments.

These distributions explain the O:C and κ behavior in the TD and dilution chamber. By 75°C in the TD, nearly all of the SVOCs had evaporated and the SOA was comprised of mostly LVOCs and ELVOCs (Fig. D.5), which had lower κ values than the SVOCs. As a result, the average κ measured through the TD decreased at this temperature. However, the average O:C through the TD at 75°C did not decrease significantly from the average O:C in the main chamber because the average O:C of the LVOCs was not that much lower than that of the SVOCs. Once the LVOCs started evaporating at higher temperatures, the average O:C through the TD decreased.

Similarly, according to the model, a small fraction of the SVOCs evaporated in the dilution chamber, which caused the O:C and κ in the dilution chamber to decrease slightly before stabilizing when the evaporation slowed.

4.5.2 Limonene ozonolysis SOA

The thermogram and areogram, along with fits from the model, for Experiment LM1 are shown in Fig. 4.5. In this experiment, 8% of the SOA remained after passing through the TD at 150°C and 20% of the SOA evaporated after being diluted by a factor of 25. The model reproduced the measured MFRs with deviations of only a few percent and estimated that the SOA was comprised of 9% ELVOCs, 49% LVOCs, and 42% SVOCs.

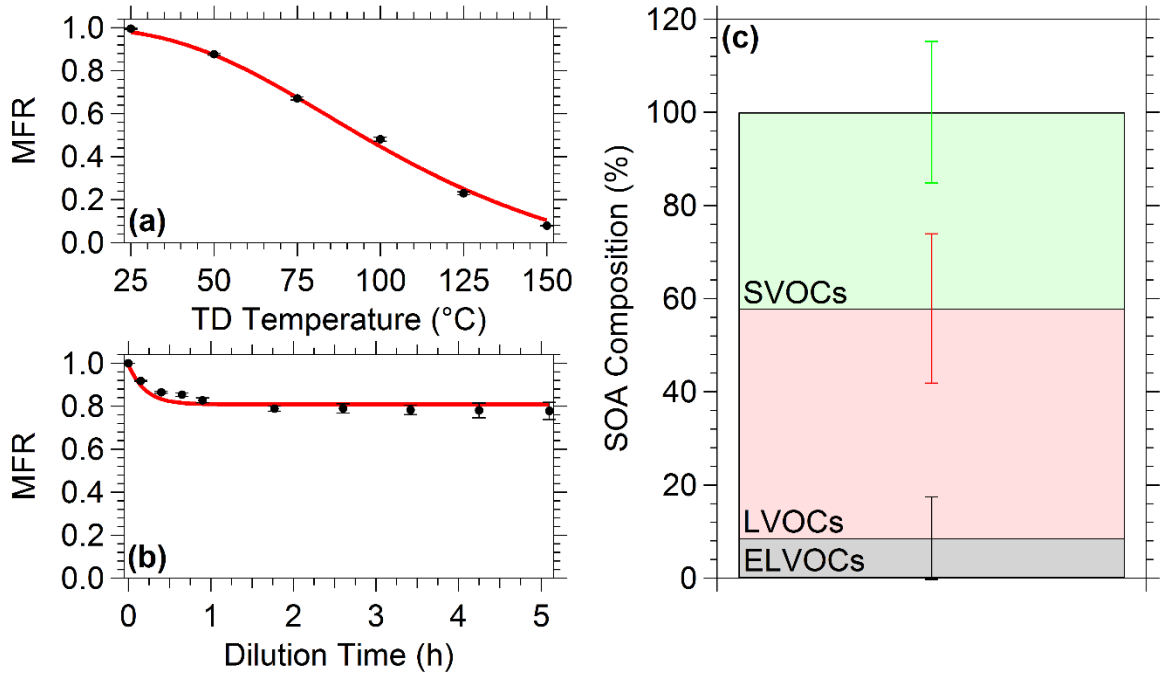

Figure 4.5. The (a) thermogram and (b) areogram for Experiment LM1 with fits from the model (red line). The error bars in (a) represent one standard deviation of the mean MFR while the error bars in (b) represent the uncertainty resulting from correcting for particle wall-losses. (c) SOA composition for Experiment LM1 along with their uncertainties (± one standard deviation) from the model. The ELVOCs are shown in grey, LVOCs in red, and SVOCs in green. The uncertainties for the ELVOCs, LVOCs, and SVOCs are shown in black, red, and green respectively.

The O:C of the SOA in the main chamber during Experiment LM1 remained stable at 0.46. The O:C of the SOA exiting the TD increased slightly at 50 and 75°C to 0.47 (Fig. 4.6a), indicating that the compounds that evaporated may have slightly lower O:C values than the remaining SOA. The O:C of the SOA decreased to 0.46 at 100°C and, as the temperature increased further, the average O:C of the SOA continued to decrease, reaching 0.39 at 150°C, indicating that the least volatile components had the lowest oxygen content.

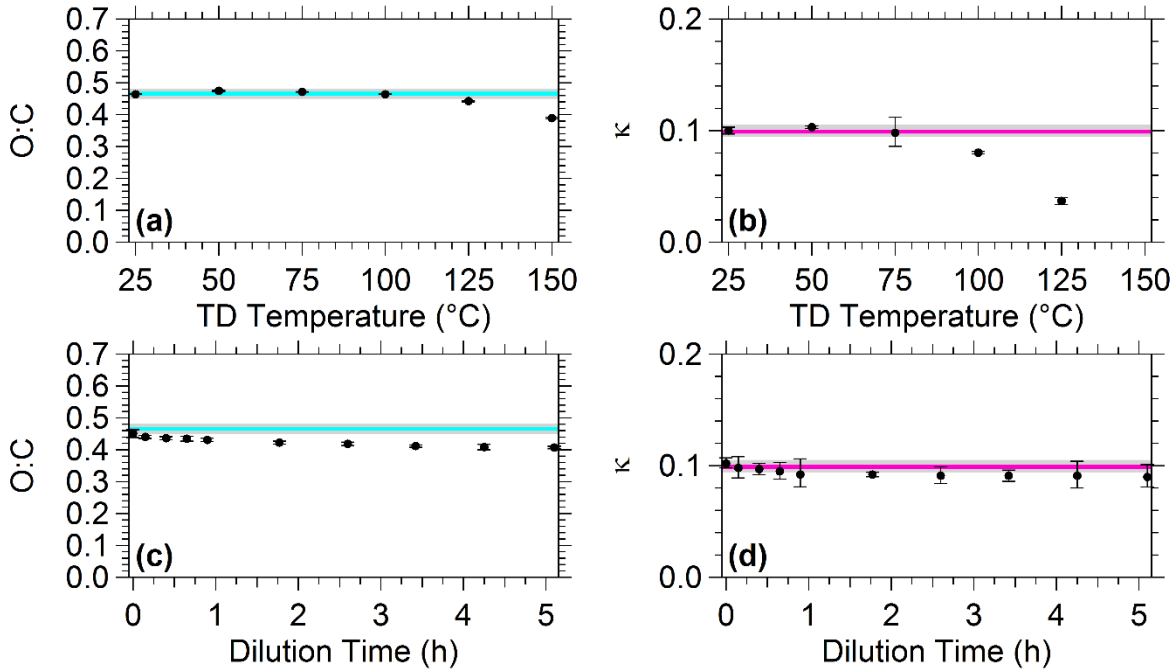

Figure 4.6. The average (a) O:C and (b) κ as a function of TD temperature for Experiment LM1. The average (c) O:C and (d) κ as a function of dilution time. The error bars represent one standard deviation of the mean O:C or κ. Also shown are the average O:C (blue line) and κ (magenta line) along with ± one standard deviation (grey area) of the mean measured in the main chamber during Experiment LM1.

The average κ for the SOA in the main chamber for this experiment was 0.10. The κ through the TD in this experiment remained around 0.10 until the temperature reached 75°C and then started decreasing, reaching 0.08 at 100°C when approximately 50% of the SOA had

evaporated (Fig. 4.6b). The remaining particles were still CCN active at 125°C, but their κ decreased even more to 0.04. After passing through the TD at 150°C, the remaining 8% of the SOA did not activate in the CCNC at a SS of 0.32%, indicating that the least volatile compounds in this experiment had low hygroscopicity.

The response of the O:C and κ to isothermal dilution for the SOA in Experiment LM1 can also be seen in Fig. 4.6. The O:C decreased slowly from the average value in the main chamber throughout the experiment, ending at 0.41 after 5 h of dilution. The κ did not change significantly from the average value in the main chamber. The small difference in the behavior of the O:C compared to that in the dilution chamber is noteworthy. The O:C of the SOA coming out of the TD at low temperatures remained constant or increased slightly, but the O:C in the dilution chamber decreased slightly. There are a number of potential explanations for this small discrepancy. The evaporation in the TD depends not only on the vapor pressure of the various SOA components at room temperature, but also on their enthalpy of vaporization. The evaporation in the dilution chamber is independent of the enthalpy of vaporization, so it is possible that there were differences in the compounds that evaporated in the two systems for the same amount of evaporated mass. This could also be due to experimental artifacts, including preferential losses of more oxidized semi-volatile SOA components in our transfer system to the dilution chamber or reactions in the TD. Even if this discrepancy is relatively small, it probably requires additional investigation with measurements of the molecular composition of both the particulate and vapor-phases in future work.

The results from Experiments LM2 and LM3 can be seen in Appendix D (Figs. D.13–D.16). The SOA from these experiments had similar composition to the SOA in Experiment LM1 and average O:C and κ values around 0.47 and 0.1 respectively. The behavior of the O:C and κ in

the TD and dilution chamber for these experiments were similar to the results from Experiment LM1.

The average O:C and κ distributions for the limonene ozonolysis SOA based on all experiments can be seen in Fig. 4.7. The limonene ozonolysis SOA generated in this study had SVOCs with an average O:C of 0.46 ± 0.11 and κ of 0.11 ± 0.02, LVOCs with an average O:C of 0.57 ± 0.08 and κ of 0.12 ± 0.02, and ELVOCs with an average O:C of 0.30 ± 0.09 and κ of 0.02 ± 0.02. The O:C and κ values of the LVOCs were not statistically different from those of the SVOCs (alpha = .05), but the O:C and κ values of the ELVOCs were statistically smaller than the values of both the SVOCs and LVOCs (alpha = .05).

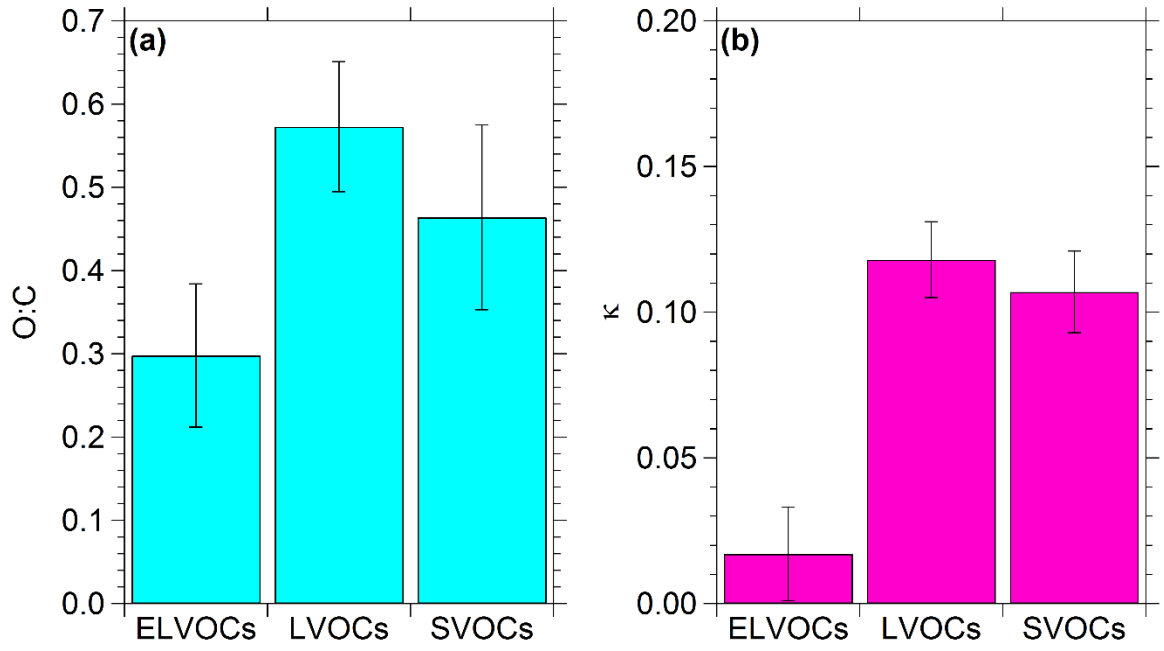

Figure 4.7. The (a) O:C and (b) κ distributions as a function of volatility for the limonene ozonolysis SOA examined in this study. The error bars were calculated from the standard deviation that results from determining O:C and κ distributions for each experiment and represent variability between experiments.

4.5.3 Cyclohexene ozonolysis SOA

The thermogram and areogram with fits from the model for Experiment CH1 can be seen in Fig. 4.8. The SOA in this experiment evaporated more at the same TD temperature than the SOA produced during the ozonolysis of the two monoterpenes. At 25°C, there was non-negligible evaporation as the MFR decreased to 0.93, which Cain et al. (2020) attributed to the activated carbon in the cooling section stripping the most volatile components from the particles. Furthermore, despite only being diluted by a factor of 9, 25% of the SOA evaporated in the dilution chamber, indicating that this SOA included a significant fraction of relatively volatile components.

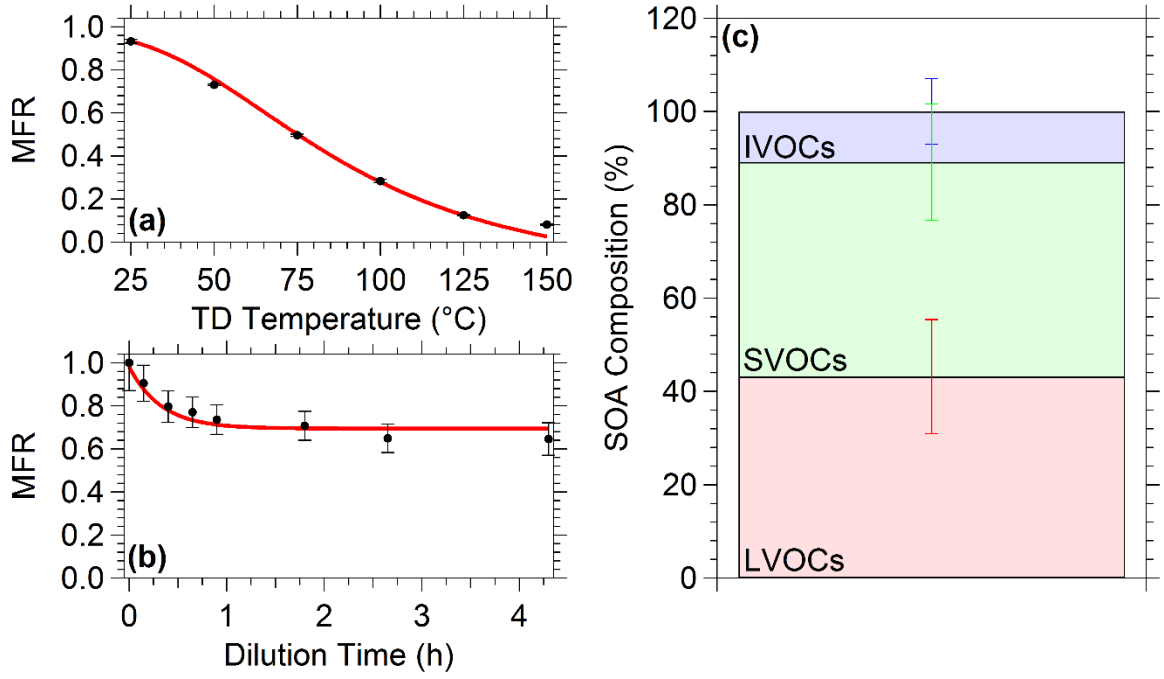

Figure 4.8. The (a) thermogram and (b) areogram for Experiment CH1 with fits from the model (red line). The error bars in (a) represent one standard deviation of the mean MFR while the error bars in (b) represent the uncertainty resulting from correcting for particle wall-losses and pump losses. (c) SOA composition for Experiment CH1 along with their uncertainties (± one standard deviation) from the model. The LVOCs are shown in red, SVOCs in green, and IVOCs in blue. The uncertainties for the LVOCs, SVOCs, and IVOCs are shown in red, green, and blue respectively.

The model estimated that the SOA in this experiment was more volatile than the monoterpene ozonolysis SOA with 11% IVOCs, 46% SVOCs, and 43% LVOCs. The IVOCs were responsible for, according to the model, the evaporation at room temperature in the TD and also for approximately half of the evaporation in the dilution chamber in all experiments.

The average O:C of the SOA in the main chamber for Experiment CH1 was constant around 0.55. The evaporation of the most volatile 7% of the SOA mass at 25°C led to an increase of the average O:C through the TD to 0.56 (Fig. 4.9a). This small amount of evaporated mass was almost exclusively IVOCs. The detectable increase in the O:C suggests that these IVOCs had lower O:C values than the less volatile SOA. The O:C remained at this slightly elevated value until the temperature reached 75°C, where 50% of the SOA mass had evaporated, and then it began to decrease, ending at 0.45 at 150°C.

Calculating the κ for this experiment using the surface tension of water resulted in an apparent κ of 0.85. This extremely high value strongly suggests the presence of surfactants in the system. Asa-Awuku et al. (2010) observed similar behavior for cycloheptene ozonolysis SOA and inferred a surface tension of 0.06 J m^{-2} for an aqueous solution of the SOA and ammonium sulfate. Given that only one methylene group separates cycloheptene from cyclohexene and that adding ammonium sulfate drives the surface tension of the droplets towards that of water (Asa-Awuku et al., 2010), we assumed a surface tension of 0.05 J m^{-2} for all of the cyclohexene ozonolysis SOA in this study. Using this surface tension resulted in an average κ of 0.28 for Experiment CH1, which is similar to the κ of 0.25 observed in Asa-Awuku et al. (2010) for cycloheptene ozonolysis SOA. It is also possible that some of the volatile products from this reaction may be partially dissolving in the droplets formed in the CCNC and thus, enhancing the CCN activity (Kroll et al., 2005; Donaldson and Vaida, 2006; Ervens and Volkamer, 2010; Sareen et al., 2013). If these

volatile compounds are indeed contributing to the observed CCN activity, then our estimate of a κ with a surface tension of 0.05 J m^{-2} may be too high and provides more of an upper bound on the SOA hygroscopicity.

The evaporation of the IVOCs caused by the activated carbon at 25°C led to a significant decrease in hygroscopicity with the κ dropping to 0.23 (Fig. 4.9b). The κ continued to decrease rapidly as temperature increased and the SOA did not activate at temperatures above 75°C. It is also possible that, since the activated carbon removes all vapor-phase compounds, if there was any vapor-phase dissolution, the enhanced CCN activity was removed. In any case, these results strongly suggest that the relatively more volatile products (IVOCs and maybe some VOCs) of the

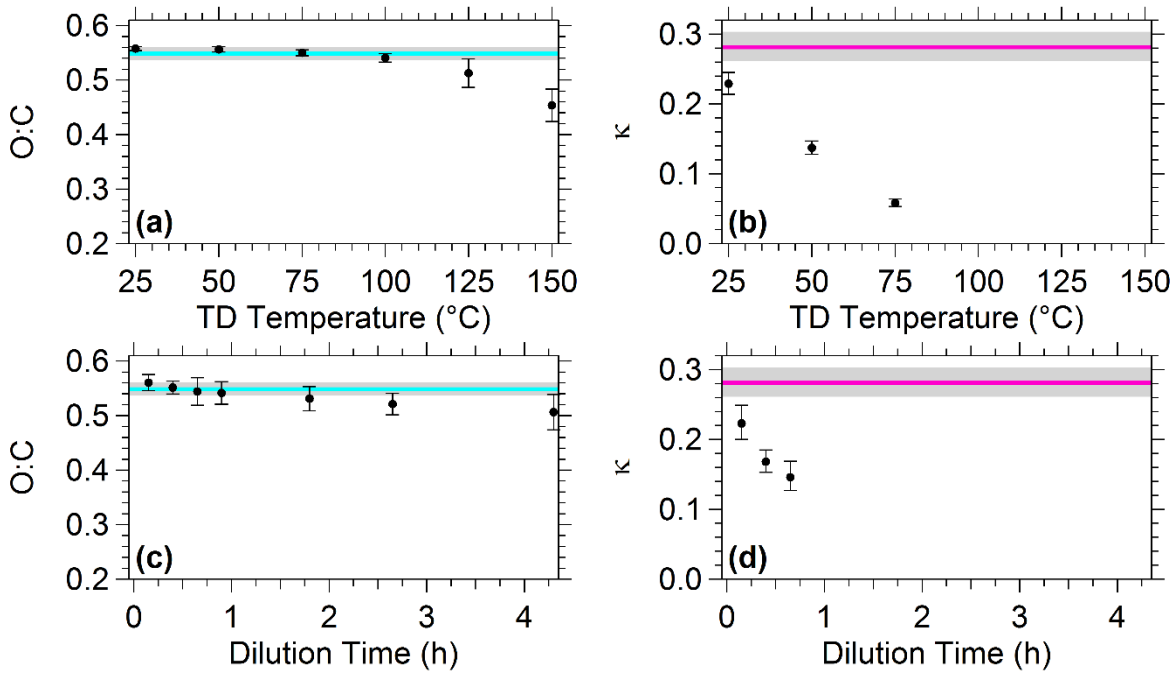

Figure 4.9. The average (a) O:C and (b) κ as a function of TD temperature for Experiment CH1. The average (c) O:C and (d) κ as a function of dilution time. The error bars represent one standard deviation of the mean O:C or κ. Also shown are the average O:C (blue line) and κ (magenta line) along with ± one standard deviation (grey area) of the mean measured in the main chamber during Experiment CH1.

cyclohexene ozonolysis reaction are responsible for a significant fraction of the observed high CCN activity.

The average O:C and κ measured in the dilution chamber as a function of time for Experiment CH1 can also be seen in Fig. 4.9. The initial O:C and κ in the dilution chamber could not be measured due to the evaporation occurring before the instruments could obtain the first sample. The comparison of the first measured O:C values in the dilution chamber (after the chamber equilibrated) with those in the main chamber suggest an increase of the O:C during this initial evaporation. This behavior is consistent with that observed in the TD. The κ decreased rapidly after dilution from the average value in the main chamber until the CCN concentration was too low to average. Given that the sample did not pass through activated carbon for these CCN measurements this behavior indicates that the IVOCs in the SOA were probably responsible for the high CCN activity.

The results from the four other cyclohexene ozonolysis SOA experiments can be found in Appendix D (Figs. D.18–D.25). The SOA in these experiments had an average O:C of 0.55 and κ values around and 0.3. The SOA in all of these experiments had similar behavior in the TD and dilution chamber to Experiment CH1.

In order to estimate the O:C and κ distributions, we used the average values from the main chamber for the O:C and κ at the TD temperature of 25°C and t = 0 h in the dilution chamber. The resulting O:C and κ distributions as a function of volatility for all experiments can be seen in Fig. 4.10. These results indicated that the cyclohexene ozonolysis SOA formed in this study was comprised of IVOCs with an average O:C of 0.33 ± 0.03 and κ of 0.80 ± 0.10, SVOCs with an average O:C of 0.57 ± 0.03 and κ of 0.36 ± 0.10, and LVOCs with an average O:C of 0.54 ± 0.02 and κ of 0.05 ± 0.01. The changes of the O:C and κ values as volatility decreased were statistically

significant (alpha = .05). The absolute values in the κ distribution are quite uncertain because we had to assume a surface tension, but the trend of decreasing hygroscopicity with volatility is quite robust.

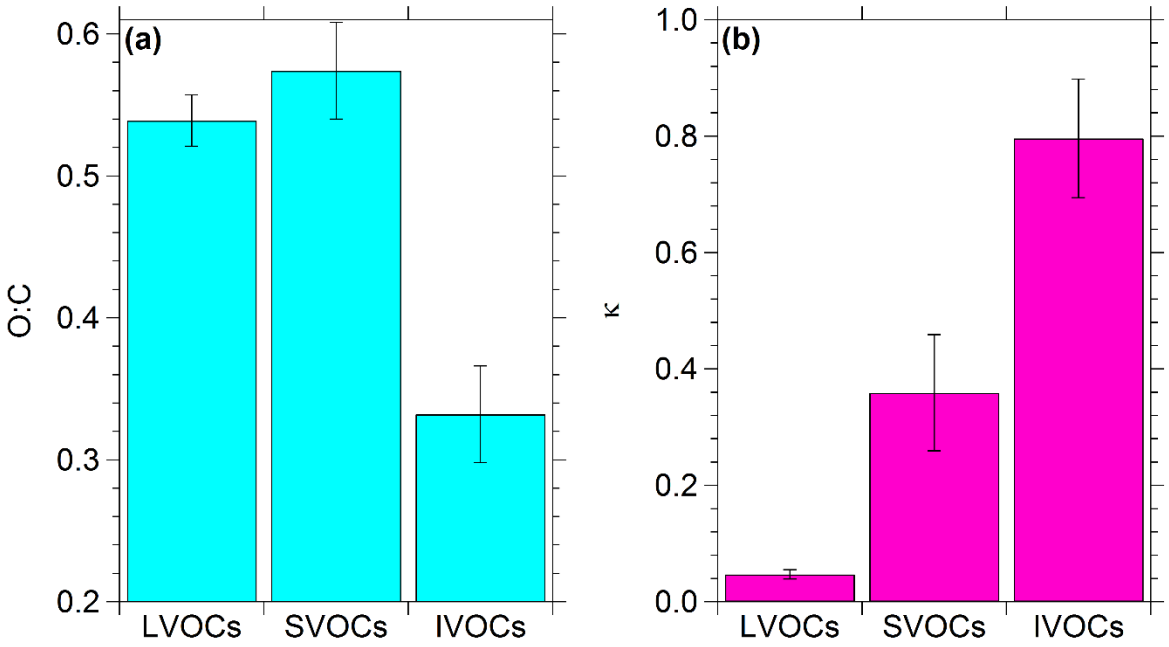

Figure 4.10. The (a) O:C and (b) κ distributions as a function of volatility for the cyclohexene ozonolysis SOA examined in this study. The error bars were calculated from the standard deviation that results from determining O:C and κ distributions for each experiment and represent variability between experiments.

The distributions in Fig. 4.10 quantitatively describe the O:C and κ behavior in the TD and dilution chamber. The small increase in O:C and significant decrease in κ of the SOA through the TD at 25°C can be attributed to the activated carbon stripping the IVOCs. Thus, increasing the average O:C and decreasing the average κ of the resulting SOA. The mass transfer model estimated that nearly all of SVOCs in Experiment CH1 evaporated at 100°C (Fig. D.17), which caused the decrease in the average O:C of the SOA exiting the TD. Similarly, the O:C in the dilution chamber

increased from the rapid evaporation of the IVOCs and then decreased slowly as the SVOCs with the highest O:C values evaporated.

4.6 2D-VBS synthesis

The distributions determined in this study can be implemented directly in the 2D-VBS framework (Fig. 4.11). The *x*-axis in this figure is the logarithm of the effective saturation concentration, *C**, and the *y*-axis is the O:C (Donahue et al., 2011). The 2D-VBS allows for a direct comparison with the κ predictions from Nakao (2017).

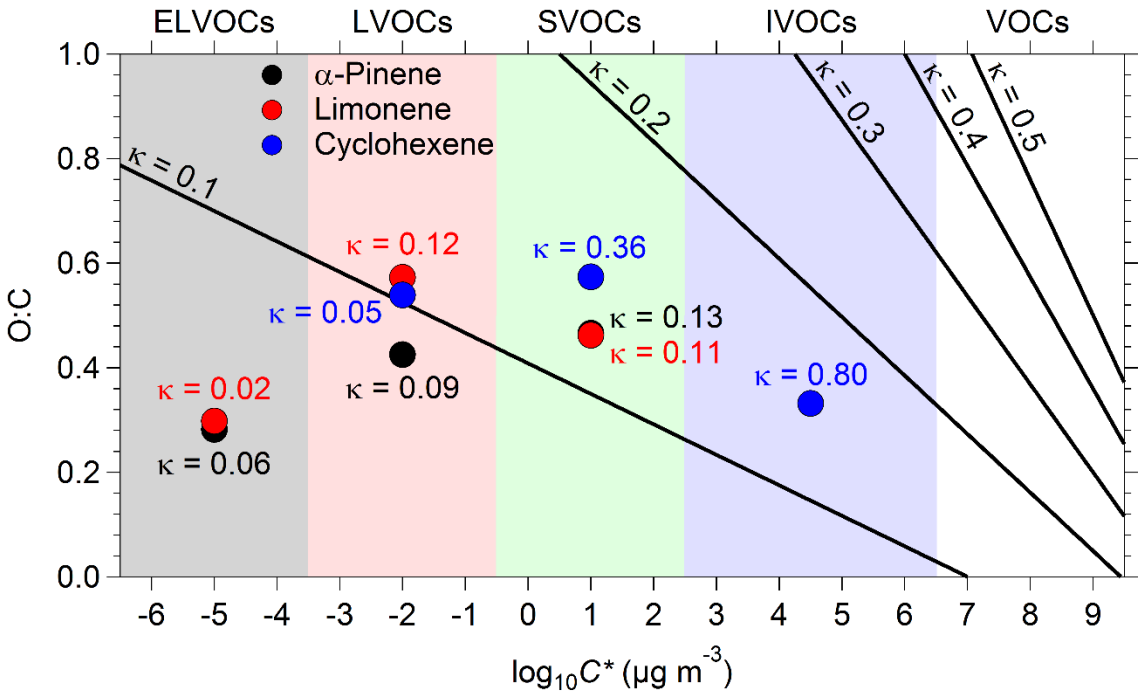

Figure 4.11. The O:C and κ distributions as a function of volatility for the α-pinene (black), limonene (red), and cyclohexene (blue) ozonolysis SOA. The data points represent the average O:C for a volatility class while the average κ is indicated in the figure. The distributions are presented in the 2D-VBS framework where the shaded regions indicate the ELVOCs, LVOCs, SVOCs, IVOCs, and VOCs according to their effective saturation concentration. Also shown are the lines of constant κ predicted by Nakao (2017).

The model predictions from Nakao (2017) are quite consistent with our distributions for the α-pinene and limonene SOA components. The SVOCs and LVOCs are quite consistent with the $\kappa = 0.1$ isoline and the corresponding predictions in this area of the 2D-VBS. For example, the LVOCs in the limonene ozonolysis SOA had a higher average O:C than the SVOCs, so conventional thinking would indicate that the LVOCs should be more hygroscopic (Jimenez et al., 2009). However, both our measurements and the κ distribution suggest that these compounds have similar hygroscopicity. This demonstrates that, at least in this system, the O:C can increase for less volatile components while the hygroscopicity remains constant. The ELVOCs for both systems are in the lower left corner of the 2D-VBS, agreeing with the predictions from Nakao (2017) that compounds in this area will have relatively low hygroscopicity.

The hygroscopicity results for the IVOCs and SVOCs for the cyclohexene ozonolysis SOA are not consistent with the predictions from Nakao (2017). The hygroscopicity of the LVOCs, considering the uncertainty in our assumed surface tension, is less inconsistent with the Nakao (2017) model. Our results suggest that improvements may be possible for the model in the areas of higher predicted hygroscopicity. However, these are the most uncertain estimates in our measurements, so the discrepancy may be a lot smaller than what Fig. 4.11 indicates. Studies in that area of the 2D-VBS would be quite helpful in determining if the behavior of the cyclohexene ozonolysis SOA is an outlier or if it is representative of the ambient SOA components in that region.

4.7 Benefit of isothermal dilution measurements

To demonstrate the benefit of adding isothermal dilution measurements to the technique, we repeated the analysis of our results without including the isothermal dilution measurements.

An example for the α-pinene ozonolysis SOA is shown in Fig. D.26. The first improvement is that the inclusion of the isothermal dilution measurements constraints the more volatile components of the system better, allowing for the estimation of the properties of the ELVOCs. Our ability to estimate the properties of these compounds in this study was due to a large extent to the availability of these additional measurements. The second benefit is the reduction of the uncertainties of the properties of the various volatility classes. The uncertainty in the distributions for the SVOCs and LVOCs was decreased by a factor of two with the addition of the dilution measurements. This comparison indicates that adding isothermal dilution measurements can be beneficial to understanding the relationship between hygroscopicity, oxidation level, and volatility of OA.

4.8 Discussion and conclusions

A technique that quantitatively relates hygroscopicity and oxidation level as a function of volatility was tested with SOA from the ozonolysis of α-pinene, limonene, and cyclohexene. The technique builds upon the approach of Cain and Pandis (2017), which separated SOA by volatility with a TD, by adding isothermal dilution measurements and observing the O:C and κ of the resulting SOA. The technique then determines O:C and κ distributions as a function of volatility that can be used to describe the SOA.

The O:C and κ distributions determined for the α-pinene ozonolysis SOA examined in this study indicated that the average O:C and κ decreased as volatility decreased. The average O:C and κ of the SVOCs and LVOCs of SOA from the ozonolysis of limonene were similar, but the ELVOCs had lower oxygen content and hygroscopicity.

The SVOCs and ELVOCs formed during the limonene ozonolysis had nearly identical O:C and κ values as the SVOCs and ELVOCs of the α-pinene ozonolysis SOA respectively. However,

the LVOCs of the limonene ozonolysis SOA had higher average O:C and κ values than the average values of the LVOCs from the α-pinene ozonolysis SOA. The increased O:C of the LVOCs could be a result of the second double bond in limonene and increased reactivity towards ozone. Both SOA systems had ELVOCs with the lowest O:C and κ values. The O:C distribution of the α-pinene ozonolysis SOA is consistent with recent results studying the composition of α-pinene ozonolysis SOA, which indicated that O:C decreased with volatility (Ye et al., 2019). The decrease in hygroscopicity with the ELVOCs could be explained by low solubility of the higher molecular weight products and is further supported by their lower O:C values.

The O:C and κ distributions of the cyclohexene ozonolysis SOA indicated that the relationship between these three properties can be more complex for some OA systems. The average O:C of this SOA increased as volatility decreased, but its average κ decreased as volatility decreased. Even though the absolute values in the κ distribution for this SOA are quite uncertain due to the presence of surfactants, these results suggest that even relatively volatile SOA components with small mass yields could, under some conditions, impact the CCN budget.

This work differs from Cain and Pandis (2017) due to the addition of the isothermal dilution measurements. The addition of the isothermal dilution measurements allows for the distributions to be extended over a larger range of volatility. Furthermore, the uncertainty of the distributions is reduced when isothermal dilution measurements are included due to the additional information about the more volatile OA components.

Complications that cannot be addressed in this work are the roles of reactions and possible oligomer decomposition at high TD temperatures and in the dilution chamber. Our analysis assumes that these complications are negligible, but without high-resolution molecular composition measurements of both the particulate and vapor-phases, we cannot definitively rule it

out. Complicating matters further are the possible changes in surface tension as the SOA evaporates. It is plausible that surface active components could evaporate at a low TD temperature or immediately in the dilution chamber, but our analysis assumes that the surface tension remains constant for all SOA as they evaporate.

More importantly, although not at atmospherically relevant concentrations, these results provide insights into SOA components. For example, most of the CCN activity of α-pinene ozonolysis SOA comes from SVOCs and LVOCs. In addition, the 2D-VBS framework can be used to integrate the results. Use of this technique with different OA systems, both laboratory and ambient, can supply parameters that can be incorporated in atmospheric chemical transport models.

4.9 References

Alroe, J., Cravigan, L. T., Mallet, M. D., Ristovski, Z. D., Miljevic, B., Osuagwu, C. G., & Johnson, G. R.: Determining the link between hygroscopicity and composition for semi-volatile aerosol species, Atmos. Meas. Tech., 11, 4361–4372, doi: 10.5194/amt-11-4361-2018, 2018.

Asa-Awuku, A., Nenes, A., Gao, S., Flagan, R. C., and Seinfeld, J. H.: Water-soluble SOA from alkene ozonolysis: Composition and droplet activation kinetics inferences from analysis of CCN activity, Atmos. Chem. Phys., 10, 1585–1597, doi: 10.5194/acp-10-1585-2010, 2010.

Bahreini, R., Keywood, M. D., Ng, N. L., Varutbangkul, V., Gao, S., Flagan, R. C., Seinfeld, J. H., Worsnop, D. R., and Jimenez, J. L.: Measurements of secondary organic aerosol from oxidation of cycloalkenes, terpenes, and m-xylene using an aerodyne aerosol mass spectrometer, Environ. Sci. Technol., 39, 5674–5688, doi: 10.1021/es048061a, 2005.

Cain, K. P., and Pandis, S. N.: A technique for the measurement of organic aerosol hygroscopicity, oxidation level, and volatility distributions, Atmos. Meas. Tech., 10, 4865–4876, doi: 10.5194/amt-10-4865-2017, 2017.

Cain, K. P., Karnezi, E., and Pandis, S. N.: Challenges in determining atmospheric organic aerosol volatility distributions using thermal evaporation techniques, Aerosol Sci. Technol., doi: 10.1080/02786826.2020.1748172, 2020.

Canagaratna, M. R., Jimenez, J. L., Kroll, J. H., Chen, Q., Kessler, S. H., Massoli, P., Hildebrandt

Ruiz, L., Forner, E., Williams, L. R., Wilson, K. R., Surratt, J. D., Donahue, N. M., Jayne, J. T., and Worsnop, D. R.: Elemental ratio measurements of organic compounds using aerosol mass spectrometry: Characterization, improved calibration, and implications, Atmos. Chem. Phys., 15, 253–272, doi: 10.5194/acp-15-253-2015, 2015.

Cerully, K. M., Bougiatioti, A., Hite Jr., J. R., Guo, H., Xu, L., Ng, N. L., Weber, R., and Nenes, A.: On the link between hygroscopicity, volatility, and oxidation state of ambient and water-soluble aerosols in the southeastern United States, Atmos. Chem. Phys., 15, 8679–8694, doi: 10.5194/acp-15-8679-2015, 2015.

Chen, X., and Hopke, P. K.: A chamber study of secondary organic aerosol formation by limonene ozonolysis, Indoor Air, 20, 320–328, doi: 10.1111/j.1600-0668.2010.00656.x, 2010.

DeCarlo, P. F., Kimmel, J. R., Trimborn, A., Northway, M. J., Jayne, J. T., Aiken, A. C., Gonin, M., Fuhrer, K., Horvath, T., Docherty, K. S., Worsnop, D. R., Jimenez, J. L.: Field-deployable, high-resolution, time-of-flight aerosol mass spectrometer, Anal. Chem., 78, 8281–8289, doi: 10.1021/ac061249n, 2006.

Ditto, J. C., Barnes, E. B., Khare, P., Takeuchi, M., Joo, T., Bui, A. A. T., Lee-Taylor, J., Eris, G., Chen, Y., Aumont, B., Jimenez, J. L., Ng, N. L., Griffin, R. J., and Gentner, D. R.: An omnipresent diversity and variability in the chemical composition of atmospheric functionalized organic aerosol, Comm. Chem., 1, 75, doi: 10.1038/s42004-018-0074-3, 2018.

Donahue, N. M., Robinson, A. L., Stanier, C. O., and Pandis, S. N.: Coupled partitioning, dilution, and chemical aging of semivolatile organics, Environ. Sci. Technol., 40, 2635–2643, doi: 10.1021/es052297c, 2006.

Donahue, N. M., Epstein, S. A., Pandis, S. N., and Robinson, A. L.: A two-dimensional volatility basis set: 1. Organic-aerosol mixing thermodynamics, Atmos. Chem. Phys., 11, 3303–3318, doi: 10.5194/acp-11-3303-2011, 2011.

Donahue, N. M., Chuang, W., Epstein, S. A., Kroll, J. H., Worsnop, D. R., Robinson, A. L., Adams, P. J., and Pandis, S. N.: Why do organic aerosols exist? Understanding aerosol lifetimes using the two-dimensional volatility basis set, Environ. Chem., 10, 151–157, doi: 10.1071/EN13022, 2013.

Donaldson, D. J., and Vaida, V.: The influence of organic films at the air-aqueous boundary on atmospheric processes, Chem. Rev., 106, 1445–1461, doi: 10.1021/cr040367c, 2006.

Ervens, B., and Volkamer, R.: Glyoxal processing by aerosol multiphase chemistry: Towards a kinetic modeling framework of secondary organic aerosol formation in aqueous particles, Atmos. Chem. Phys., 10, 8219–8244, doi: 10.5194/acp-10-8219-2010, 2010.

Frosch, M., Bilde, M., DeCarlo, P. F., Jurányi, Z., Tritscher, T., Dommen, J., Donahue, N. M., Gysel, M., Weingartner, E., and Baltensperger, U.: Relating cloud condensation nuclei activity and oxidation level of α-pinene secondary organic aerosols, J. Geophys. Res., 116,

D22212, doi: 10.1029/2011JD016401, 2011.

Gao, S., Keywood, M., Ng, N. L., Surratt, J., Varutbangkul, V., Bahreini, R., Flagan, R. C., and Seinfeld, J. H.: Low-molecular-weight and oligomeric components in secondary organic aerosol from the ozonolysis of cycloalkenes and α-pinene, J. Phys. Chem., 108, 10147 – 10164, doi: 10.1021/jp047466e, 2004.

Hallquist, M., Wenger, J. C., Baltensperger, U., Rudich, Y., Simpson, D., Claeys, M., Dommen, J., Donahue, N. M., George, C., Goldstein, A. H., Hamilton, J. F., Herrmann, H., Hoffmann, T., Iinuma, Y., Jang, M., Jenkin, M. E., Jimenez, J. L., Kiendler-Scharr, A., Maenhaut, W., McFiggans, G., Mentel, T. F., Monod, A., Prévôt, A. S. H., Seinfeld, J. H., Surratt, J. D., Szmigielski, R., and Wildt, J.: The formation, properties and impact of secondary organic aerosol: Current and emerging issues, Atmos. Chem. Phys., 9, 5155–5236, doi: 10.5194/acp-9-5155-2009, 2009.

Hansel, A., Scholz, W., Mentler, B., Fischer, L., and Berndt, T.: Detection of RO2 radicals and other products from cyclohexene ozonolysis with NH4+ and acetate chemical ionization mass spectrometry, Atmos. Environ., 186, 248–255, doi: 10.1016/j.atmosenv.2018.04.023, 2018.

Heald, C. L., Kroll, J. H., Jimenez, J. L., Docherty, K. S., Decarlo, P. F., Aiken, A. C., Chen, Q., Martin, S. T., Farmer, D. K., and Artaxo, P.: A simplified description of the evolution of organic aerosol composition in the atmosphere, Geophys. Res. Lett., 37, L08803, doi: 10.1029/2010GL042737, 2010.

Heaton, K. J., Dreyfus, M. A., Wang, S., and Johnston, M. V.: Oligomers in the early stage of biogenic secondary organic aerosol formation and growth, Environ. Sci. Technol., 41, 6129–6136, doi: 10.1021/es070314n, 2007.

Hildebrandt Ruiz, L., Paciga, A. L., Cerully, K. M., Nenes, A., Donahue, N. M., and Pandis, S. N.: Formation and aging of secondary organic aerosol from toluene: Changes in chemical composition, volatility, and hygroscopicity, Atmos. Chem. Phys., 15, 8301–8313, doi: 10.5194/acp-15-8301-2015, 2015.

Hong, J., Häkkinen, S. A. K., Paramonov, M., Äijälä, M., Hakala, J., Nieminen, T., Mikkilä, J., Prisle, N. L., Kulmala, M., Riipinen, I., Bilde, M., Kerminen, V.-M., and Petäjä, T.: Hygroscopicity, CCN and volatility properties of submicron atmospheric aerosol in a boreal forest environment during the summer of 2010, Atmos. Chem. Phys., 14, 4733–4748, doi: 10.5194/acp-14-4733-2014, 2014.

Huff Hartz, K. E., Rosenørn, T., Ferchak, S. R., Raymond, T. M., Bilde, M., Donahue, N. M., and Pandis, S. N.: Cloud condensation nuclei activation of monoterpene and sesquiterpene secondary organic aerosol, J. Geophys. Res., 110, D14208, doi: 10.1029/2004JD005754, 2005.

Huffman, J. A., Docherty, K. S., Mohr, C., Cubison, M. J., Ulbrich, I. M., Ziemann, P. J., Onasch, T. J., and Jimenez, J. L.: Chemically-resolved volatility measurements of organic aerosol

from different sources, Environ. Sci. Technol., 43, 5351–5357, doi: 10.1021/es803539d, 2009.

Hyttinen, N., Rissanen, M. P., and Kurtén, T.: Computational comparison of acetate and nitrate chemical ionization of highly oxidized cyclohexene ozonolysis intermediates and products, J. Phys. Chem., 121, 2172–2179, doi: 10.1021/acs.jpca.6b12654, 2017.

Jimenez, J. L., Canagaratna, M. R., Donahue, N. M., Prévôt, A. S. H., Zhang, Q., Kroll, J. H., DeCarlo, P. F., Allan, J. D., Coe, H., Ng, N. L., Aiken, A. C., Docherty, K. S., Ulbrich, I. M., Grieshop, A. P., Robinson, A. L., Duplissy, J., Smith, J. D., Wilson, K. R., Lanz, V. A., Hueglin, C., Sun., Y. L., Tian, J., Laaksonen, A., Raatikainen, T., Rautiainen, J., Vaattovaara, P., Ehn, M., Kulmala, M., Tomlinson, J. M., Collins, D. R., Cubison, M. J., Dunlea, E., J., Huffman, J. A., Onasch, T. B., Alfarra, M. R., Williams, P. I., Bower, K., Kondo, Y., Schneider, J., Drewnick, F., Borrmann, S., Weimer, S., Demerjian, K., Salcedo, D., Cottrell, L., Griffin, R., Takami, A., Miyoshi, T., Hatakeyama, S., Shimono, A., Sun, J. Y, Zhang, Y. M., Dzepina, K., Kimmel, J. R., Sueper, D., Jayne, J. T., Herndon, S. C., Trimborn, A. M., Williams, L. R., Wood, E. C., Middlebrook, A. M., Kolb, C. E., Baltensperger, U., and Worsnop, D. R.: Evolution of organic aerosols in the atmosphere, Science, 326, 1525–1529, doi: 10.1126/science.1180353, 2009.

Kalberer, M., Yu, J., Cocker, D. R., Flagan, R. C., and Seinfeld, J. H.: Aerosol formation in the cyclohexene-ozone system, Environ. Sci. Technol., 34, 4894–4901, doi: 10.1021/es001180f, 2000.

Kaltsonoudis, C., Jorga, S. D., Louvaris, E., Florou, K., & Pandis, S. N.: A portable dual-smog-chamber system for atmospheric aerosol field studies, Atmos. Meas. Tech., 12, 2733–2743, doi: 10.5194/amt-12-2733-2019, 2019.

Kanakidou, M., Seinfeld, J. H., Pandis, S. N., Barnes, I., Dentener, F. J., Facchini, M. C., Van Dingenen, R., Ervens, B., Nenes, A., Nielsen, C. J., Swietlicki, E., Putaud, J. P., Balkanski, Y., Fuzzi, S., Horth, J., Moortgat, G. K., Winterhalter, R., Myhre, C. E. L., Tsigaridis, K., Vignati, E., Stephanou, E. G., and Wilson, J.: Organic aerosol and global climate modelling: a review, Atmos. Chem. Phys., 5, 1053–1123, doi: 10.5194/acp-5-1053-2005, 2005.

Karnezi, E., Riipinen, I., and Pandis, S. N.: Measuring the atmospheric organic aerosol volatility distribution: A theoretical analysis, Atmos. Meas. Tech., 7, 2953–2965, doi: 10.5194/amt-7-2953-2014, 2014.

Keywood, M. D., Kroll, J. H., Varutbangkul, V., Bahreini, R., Flagan, R. C., and Seinfeld, J. H.: Secondary organic aerosol formation from cyclohexene ozonolysis: Effect of OH scavenger and the role of radical chemistry, Environ. Sci. Technol., 38, 3343–3350, doi: 10.1021/es049725j, 2004a.

Keywood, M. D., Varutbangkul, V., Bahreini, R., Flagan, R. C., and Seinfeld, J. H.: Secondary organic aerosol formation from the ozonolysis of cycloalkenes and related compounds, Environ. Sci. Technol., 38, 4157–4164, doi: 10.1021/es035363o, 2004b.

Kostenidou, E., Pathak, R. K., and Pandis, S. N.: An algorithm for the calculation of secondary organic aerosol density combining AMS and SMPS data, Aerosol Sci. Technol., 41, 1002–1010, doi: 10.1080/02786820701666270, 2007.

Kostenidou, E., Karnezi, E., Hite Jr., J. R., Bougiatioti, A., Cerully, K., Xu, L., Ng, N. L., Nenes, A., Pandis, S. N.: Organic aerosol in the summertime southeastern United States: Components and their link to volatility distribution, oxidation state and hygroscopicity, Atmos. Chem. Phys., 18, 5799–5819, doi: 10.5194/acp-18-5799-2018, 2018.

Kroll, J. H., Ng, N. L., Murphy, S. M., Varutbangkul, V., Flagan, R. C., and Seinfeld, J. H.: Chamber studies of secondary organic aerosol growth by reactive uptake of simple carbonyl compounds, J. Geophys. Res., D23207, doi: 10.1029/2005JD006004, 2005.

Kroll, J. H., Donahue, N. M., Jimenez, J. L., Kessler, S. H., Canagaratna, M. R., Wilson, K. R., Altieri, K. E., Mazzoleni, L. R., Wozniak, A. S., Bluhm, H., Mysak, E. R., Smith, J. D., Kolb, C. E., and Worsnop, D. R.: Carbon oxidation state as a metric for describing the chemistry of atmospheric organic aerosol, Nat. Chem., 3, 133–139, doi: 10.1038/nchem.948, 2011.

Kundu, S., Fisseha, R., Putman, A. L., Rahn, T. A., and Mazzoleni, L. R.: High molecular weight SOA formation during limonene ozonolysis: Insights from ultrahigh-resolution FT-ICR mass spectrometry characterization, Atmos. Chem. Phys., 12, 5523–5536, doi: 10.5194/acp-12-5523-2012, 2012.

Kuwata, M., Chen, Q., and Martin, S. T.: Cloud condensation nuclei (CCN) activity and oxygen-to-carbon elemental ratios following thermodenuder treatment of organic particles grown by α-pinene ozonolysis, Phys. Chem. Chem. Phys., 13, 14571–14583, doi: 10.1039/c1cp20253g, 2011.

Lambe, A. T., Onasch, T. B., Massoli, P., Croasdale, D. R., Wright, J. P., Ahern, A. T., Williams, L. R., Worsnop, D. R., Brune, W. H., and Davidovits, P.: Laboratory studies of the chemical composition and cloud condensation nuclei (CCN) activity of secondary organic aerosol (SOA) and oxidized primary organic aerosol (OPOA), Atmso. Chem. Phys., 11, 8913–8928, doi: 10.5194/acp-11-8913-2011, 2011.

Leungsakul, S., Jaoui, M., and Kamens, R. M.: Kinetic mechanism for predicting secondary organic aerosol formation from the reaction of d-limonene with ozone, Environ. Sci. Technol., 39, 9583–9594, doi: 10.1021/es0492687, 2005.

Louvaris, E. E., Karnezi, E., Kostenidou, E., Kaltsonoudis, C., and Pandis, S. N.: Estimation of the volatility distribution of organic aerosol combining thermodenuder and isothermal dilution measurements, Atmos. Meas. Tech., 10, 3909–3918, doi: 10.5194/amt-10-3909-2017, 2017.

Massoli, P., Lambe, A. T., Ahern, A. T., Williams, L. R., Ehn, M., Mikkilä, J., Canagaratna, M. R., Brune, W. H., Onasch, T. B., Jayne, J. T., Petäjä, T., Kulmala, M., Laaksonen, A., Kolb,

C. E., Davidovits, P., and Worsnop, D. R.: Relationship between aerosol oxidation level and hygroscopic properties of laboratory generated secondary organic aerosol (SOA) particles, Geophys. Res. Lett., 37, L24801, doi: 10.1029/2010GL045258, 2010.

Meyer, N. K., Duplissy, J., Gysel, M., Metzger, A., Dommen, J., Weingartner, E., Alfarra, M. R., Prévôt, A. S. H., Fletcher, C., Good, N., McFiggans, G., Jonsson, Å. M., Hallquist, M., Baltensperger, U., and Ristovski, Z. D.: Analysis of the hygroscopic and volatile properties of ammonium sulphate seeded and unseeded SOA particles, Atmos. Chem. Phys., 9, 721–732, doi: 10.5194/acp-9-721-2009, 2009.

Moore, R. H., Nenes, A., and Medina, J.: Scanning mobility CCN analysis—A method for fast measurements of size-resolved CCN distributions and activation kinetics, Aerosol Sci. Technol., 44, 861–871, doi: 10.1080/02786826.2010.498715, 2010.

Nakao, S.: Why would apparent κ linearly change with O/C? Assessing the role of volatility, solubility, and surface activity of organic aerosols, Aerosol Sci. Technol., 51, 1377–1388, doi: 10.1080/02786826.2017.1352082, 2017.

Pathak, R. K., Stanier, C. O., Donahue, N. M., and Pandis, S. N.: Ozonolysis of α-pinene at atmospherically relevant concentrations: Temperature dependence of aerosol mass fractions (yields), J. Geophys. Res., 112, D03201, doi: 10.1029/2006JD007436, 2007.

Petters, M. D., and Kreidenweis, S. M.: A single parameter representation of hygroscopic growth and cloud condensation nucleus activity, Atmos. Chem. Phys., 7, 1961–1971, doi: 10.5194/acp-7-1961-2007, 2007.

Poulain, L., Wu, Z., Petters, M. D., and Wex, H.: Towards closing the gap between hygroscopic growth and CCN activation for secondary organic aerosols – Part 3: Influence of the chemical composition on the hygroscopic properties of volatile fractions of aerosols, Atmos. Chem. Phys., 10, 3775–3785, doi: 10.5194/acp-10-3775-2010, 2010.

Rickards, A. M. J., Miles, R. E. H., Davies, J. F., Marshall, F. H., and Reid, J. P.: Measurements of the sensitivity of aerosol hygroscopicity and the κ parameter to the O/C ratio, J. Phys. Chem., 117, 14120–14131, doi: 10.1021/jp407991n, 2013.

Riipinen, I., Pierce, J. R., Donahue, N. M., and Pandis, S. N.: Equilibration time scales of organic aerosol inside thermodenuders: Evaporation kinetics versus thermodynamics, Atmos. Environ., 44, 597–607, doi: 10.1016/j.atmosenv.2009.11.022, 2010.

Rissanen, M. P., Kurtén, T., Sipilä, M., Thornton, J. A., Kangasluoma, J., Sarnela, N., Junninen, H., Jørgensen, S., Schallhart, S., Kajos, M. K., Taipale, R., Springer, M., Mentel, T. F., Ruuskanen, T., Petäjä, T., Worsnop, D. R., Kjaergaard, H. G., and Ehn, M.: The formation of highly oxidized multifunctional products in the ozonolysis of cyclohexene, J. Am. Chem. Soc., 136, 15596–15606, doi: 10.1021/ja507146s, 2014.

Saathoff, H., Naumann, K. H., Möhler, O., Jonsson, Å. M., Hallquist, M., Kiendler-Scharr, A.,

Mentel, T. F., Tillmann, R., and Schurath, U.: Temperature dependence of yields of secondary organic aerosols from the ozonolysis of α-pinene and limonene, Atmos. Chem. Phys., 9 1551–1577, doi: 10.5194/acp-9-1551-2009, 2009.

Sareen, N., Schwier, A. N., Lathem, T. L., Nenes, A., and McNeill, V. F.: Surfactants from the gas phase may promote cloud droplet formation, Proc. Natl. Acad. Sci., 110, 2723–2728, doi: 10.1073/pnas.1204838110, 2013.

Tritscher, T., Dommen, J., Decarlo, P. F., Gysel, M., Barmet, P. B., Praplan, A. P., Weingartner, E., Prévôt, A. S. H., Riipinen, I., Donahue, N. M., and Baltensperger, U.: Volatility and hygroscopicity of aging secondary organic aerosol in a smog chamber, Atmos. Chem. Phys., 11, 11477–11496, doi: 10.5194/acp-11-11477-2011, 2011.

Varutbangkul, V., Brechtel, F. J., Bahreini, R., Ng, N. L., Keywood, M. D., Kroll, J. H., Flagan, R. C., Seinfeld, J. H., and Goldstein, A. H.: Hygroscopicity of secondary organic aerosols formed by oxidation of cycloalkenes, monoterpenes, sesquiterpenes, and related compounds, Atmos. Chem. Phys., 6, 2367–2388, doi: 10.5194/acp-6-2367-2006, 2006.

Wang, N., Jorga, S., Pierce, J., Donahue, N., & Pandis, S.: Particle wall-loss correction methods in smog chamber experiments, Atmos. Meas. Tech., 11, 6577–6588, doi: 10.5194/amt-2018-175, 2018.

Warren, B., Malloy, Q. G. J., Yee, L. D., and Cocker, D. R.: Secondary organic aerosol formation from cyclohexene ozonolysis in the presence of water vapor and dissolved salts, Atmos. Environ., 43, 1789–1795, doi: 10.1016/j.atmosenv.2008.12.026, 2009.

Watne, Å. K., Westerlund, J., Hallquist, Å. M., Brune, W. H., and Hallquist, M.: Ozone and OH-induced oxidation of monoterpenes: Changes in the thermal properties of secondary organic aerosol (SOA), J. Aerosol Sci., 114, 31–41, doi: 10.1016/j.jaerosci.2017.08.011, 2017.

Witkowski, B., and Gierczak, T.: Characterization of the limonene oxidation products with liquid chromatography coupled to the tandem mass spectrometry, Atmos. Environ., 154, 297–307, doi: 10.1016/j.atmosenv.2017.02.005, 2017.

Ye, Q., Wang, M., Hofbauer, V., Stolzenburg, D., Chen, D., Schervish, M., Vogel, A., Mauldin, R. L., Baalbaki, R., Brilke, S., Dada, L., Dias, A., Duplissy, J., El Haddad, I., Finkenzeller, H., Fischer, L., He, X., Kim, C., Kürten, A., Lamkaddam, H., Mentler, B., Partoll, E., Petäjä, T., Rissanen, M., Schobesberger, S., Schuchmann, S., Simon, M., Yee Jun, T., Vazquez-Pufleau, M., Wagner, A. C., Wang, Y., Wu, Y., Xiao, M., Baltensperger, U., Curtius, J., Flagan, R., Kirkby, J., Kulmala, M., Volkamer, R., Winkler, P. M., Worsnop, D., and Donahue, N. M.: Molecular composition and volatility of nucleated particles from α-pinene xxidation between -50 °C and +25 °C, Environ. Sci. Technol., 53, 12357-12365, doi: 10.1021/acs.est.9b03265, 2019.

Yuan, C., Ma, Y., Diao, Y., Yao, L., Zhou, Y., Wang, X., and Zheng, J.: CCN activity of secondary aerosols from terpene ozonolysis under atmospheric relevant conditions, J. Geophys Res.,

122, 4654–4669, doi: 10.1002/2016JD026039, 2017.

Zhang, Q., Jimenez, J. L., Canagaratna, M. R., Allan, J. D., Coe, H., Ulbrich, I., Alfarra, M. R., Takami, A., Middlebrook, A. M., Sun, Y. L., Dzepina, K., Dunlea, E., Docherty, K., DeCarlo, P. F., Salcedo, D., Onasch, T., Jayne, J. T., Miyoshi, T., Shimono, A., Hatakeyama, S., Takegawa, N., Kondo, Y., Schneider, J., Drewnick, F., Borrmann, S., Weimer, S., Demerjian, K., Williams, P., Bower, K., Bahreini, R., Cottrell, L., Griffin, R. J., Rautiainen, J., Sun, J. Y., Zhang, Y. M., and Worsnop, D. R.: Ubiquity and dominance of oxygenated species in organic aerosols in anthropogenically-influenced Northern Hemisphere midlatitudes, Geophys. Res. Lett., 34, L13801, doi: 10.1029/2007GL029979, 2007.

Chapter 5

Summary and suggestions for future work

5.1 Summary

This work developed and tested three novel experimental techniques that characterize the hygroscopicity, oxidation level, and volatility of OA. The first technique utilized a TD with aerosol mass spectrometry and size-resolved CCN measurements to characterize the hygroscopicity and oxidation level of OA as a function of its volatility. The technique was tested with SOA from the ozonolysis of α-pinene and the results from these experiments indicated that the average O:C and κ of the SOA decreased as the temperature in the TD increased and more of the SOA evaporated. These results indicated that the lower volatility components of the SOA in this system were comprised of components that had lower O:C and κ values than the overall SOA.

The second technique combined TD and isothermal dilution measurements to improve the estimation of OA volatility distributions. The technique was tested with SOA from the ozonolysis of α-pinene and cyclohexene. The SOA from both systems evaporated similarly in the TD for the residence time used in these experiments, but quite differently when isothermally diluted. The α-pinene ozonolysis SOA only evaporated 15–20% after 2 h of dilution, while 45–65% of the cyclohexene ozonolysis SOA evaporated in the same time even though they were diluted by similar amounts and had similar mass concentrations.

This work highlighted the difficulty in estimating OA volatility distributions using thermal evaporation techniques. When the volatility distributions were estimated using only a thermogram, the two SOA systems were quite similar. The addition of the isothermal dilution measurements allowed the estimation of the volatility distributions over a larger range and revealed that the α-pinene ozonolysis SOA was comprised of mostly low-volatility components while the cyclohexene ozonolysis SOA was comprised of mostly semi-volatile components.

The mass transfer model used in this work was not able to reproduce the later stages of the evaporation of the cyclohexene ozonolysis SOA in the dilution chamber. The model predicted that the SOA achieved equilibrium in the dilution chamber after 2 h even though the particles continued to evaporate, most likely due to vapor-phase wall-losses. Incorporating vapor-phase wall-losses in the model allowed it to reproduce the areograms accurately and decreased the overall volatility of the SOA because it attributed more of the evaporation in the dilution chamber to more volatile components.

TD measurements alone can provide information about the full OA volatility distribution, but this information is coupled with the enthalpy of vaporization. There are several combinations of volatility distributions and enthalpy of vaporization values that fit the thermograms. On the other hand, isothermal dilution measurements remove the enthalpy of vaporization dependence, but they only provide direct information about SVOCs and higher volatility components. If isothermal dilution measurements are used alone, they only provide information about the sum of the LVOCs, ELVOCs, and lower volatility compounds without any details about their distribution. Combining TD and isothermal dilution measurements constrains not only the SVOCs, but also the enthalpy of vaporization. This technique further reiterates the need to combine techniques in order to fully understand OA properties.

The third technique combined the first two techniques and tested it with SOA from the ozonolysis of α-pinene, limonene, and cyclohexene to determine their O:C and κ distributions as a function of volatility. The O:C and κ distributions determined for the α-pinene ozonolysis SOA indicated that the average O:C and κ decreased as volatility decreased. The average O:C and κ of the SVOCs and LVOCs of SOA from the ozonolysis of limonene were similar, but the ELVOCs had lower oxygen content and hygroscopicity. The SVOCs and ELVOCs formed during the

limonene ozonolysis had nearly identical O:C and κ values as the SVOCs and ELVOCs of the α-pinene ozonolysis SOA respectively. However, the LVOCs of the limonene ozonolysis SOA had higher average O:C and κ values than the average values of the LVOCs from the α-pinene ozonolysis SOA. The O:C and κ distributions of the cyclohexene ozonolysis SOA indicated that the relationship between these three properties can be more complex for some OA systems. The average O:C of this SOA increased as volatility decreased, but its average κ decreased as volatility decreased. This technique differs from the first technique due to the addition of the isothermal dilution measurements from the second technique. The addition of the isothermal dilution measurements allows for the O:C and κ distributions to be extended over a larger range of volatility. Furthermore, the uncertainty of the distributions is reduced when isothermal dilution measurements are included due to the additional information about the more volatile OA components.

The techniques developed in this thesis provide insights into the links between OA hygroscopicity, oxidation level, and volatility. Use of these techniques with different OA systems, both laboratory and ambient, can supply parameters that can be incorporated in CTMs.

5.2 Suggestions for future work

The techniques developed in this work can be applied to ambient OA in different areas and thus allow the characterization of more complex chemical systems and the evaluation of chemical transport models that predict (or assume) the corresponding properties.

Some of the largest complications that were not addressed in this work are the roles of reactions and possible oligomer decomposition at high TD temperatures and in the dilution chamber. The analysis in this work assumed that these complications were negligible, but the

instrumentation used was not able to definitively rule it out. Therefore, future work should focus on compositional changes at a molecular level through the TD and dilution chamber. Removal of the activated carbon section of a TD and examining the molecular composition of both the particulate and vapor-phases would provide direct evidence of reactions or decomposition taking place. The use of a FIGAERO-CIMS or other soft ionization mass spectrometer is well-suited for this investigation and would provide much needed information for TD and dilution studies.

Appendices

Appendix A

Supplementary information for Chapter 2

A.1 TD loss fraction

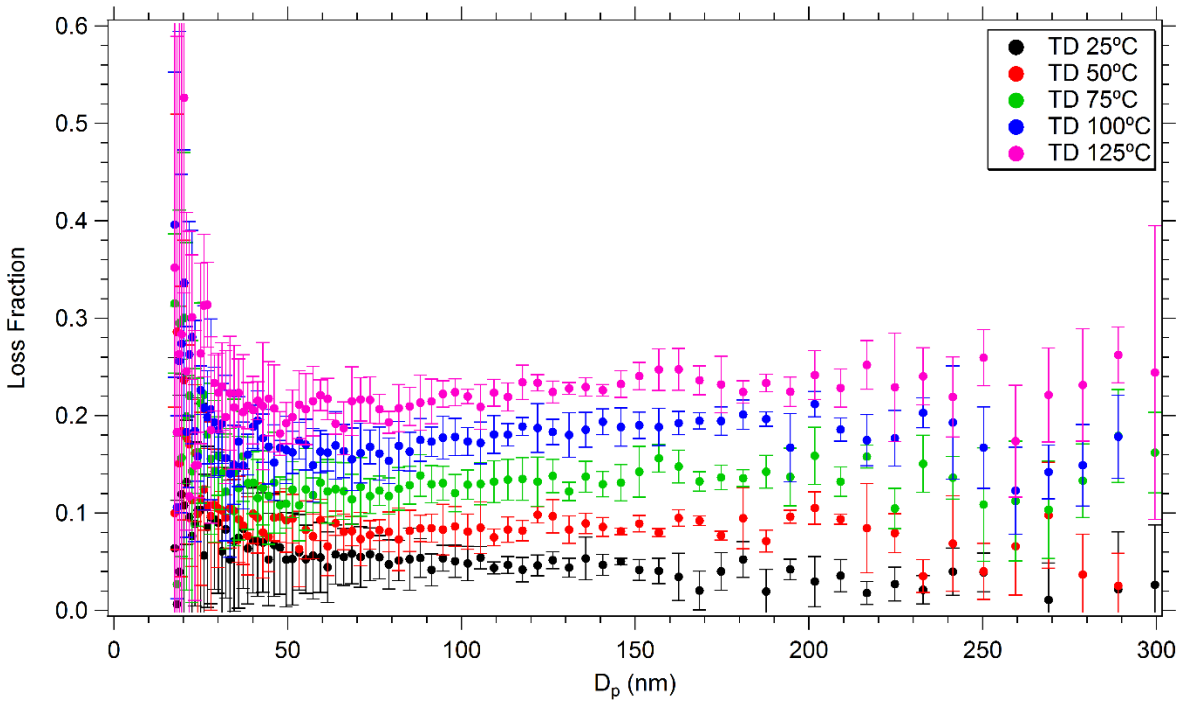

Figure A.1. Loss fraction in the TD as a function of particle size and temperature. The colors represent different TD temperatures. The error bars represent one standard deviation of the mean.

A.2 Results and analysis for Experiment 2

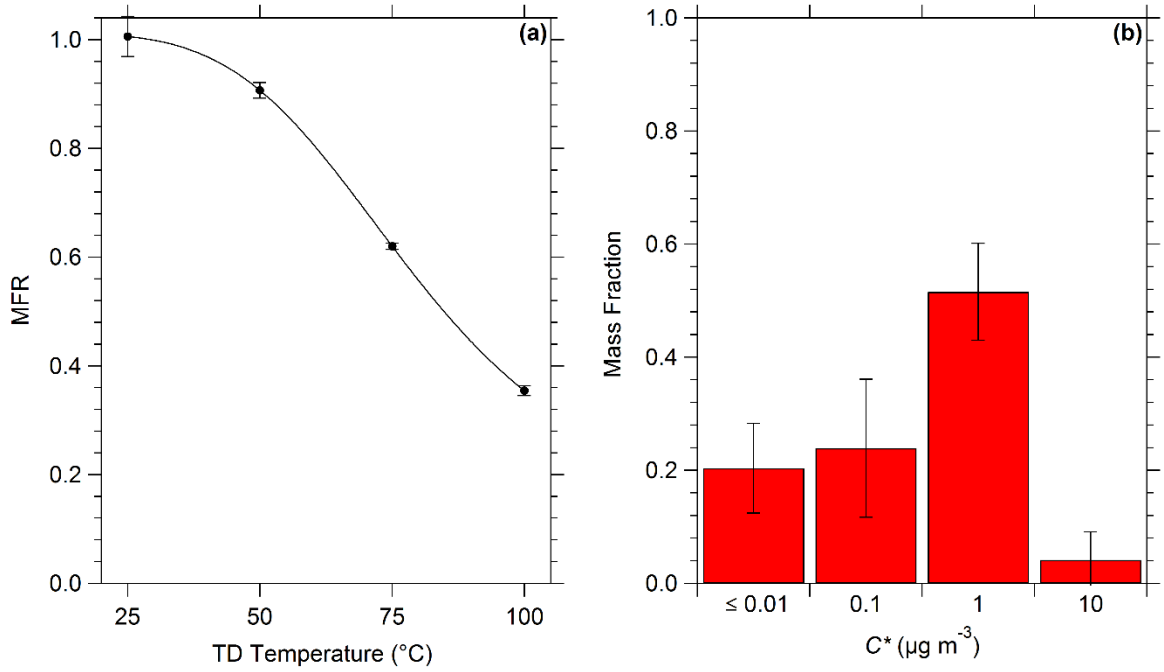

Figure A.2. (a) Thermogram, corrected for losses in the TD, for Experiment 2 with the fit from the TD model. The error bars represent one standard deviation of the mean. (b) SOA volatility distribution for Experiment 2 using the 1D-VBS framework. The error bars correspond to one standard deviation of the solution calculated by the model.

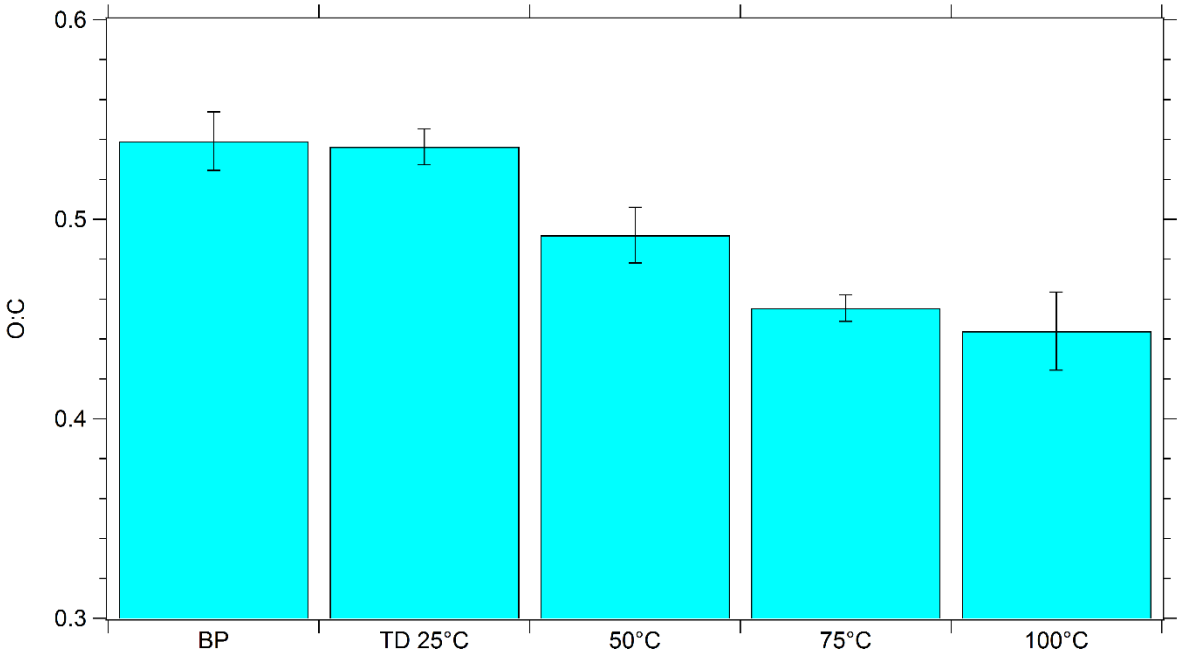

Figure A.3. The average O:C ratio observed through the BP and several TD temperatures for Experiment 2. The error bars represent one standard deviation of the mean. The O:C ratios at a TD temperature of 50°C and greater were statistically smaller than the values at the BP and the TD at 25°C.

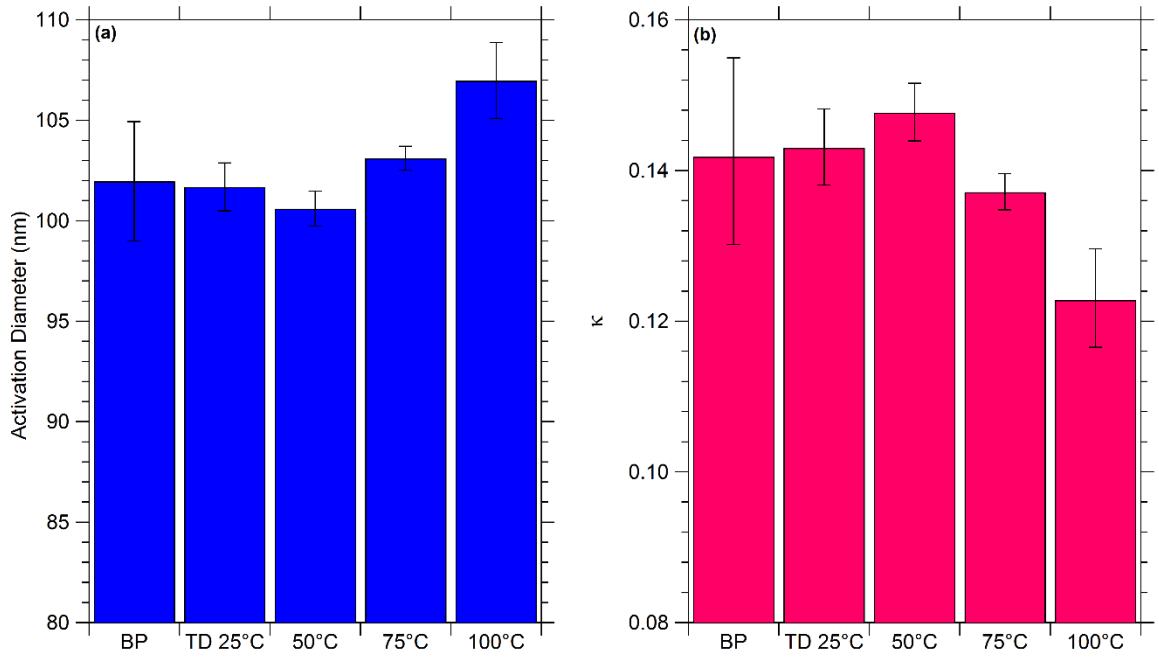

Figure A.4. (a) The average activation diameter observed at 0.3% supersaturation in the CCNC for Experiment 2. The error bars represent one standard deviation of the mean. (b) The estimated κ values for Experiment 2. The error bars were obtained by estimating the κ at +/- one standard deviation of the average activation diameter measured. The values at a TD temperature of 100°C was statistically different from the values at the BP and the TD at 25°C.

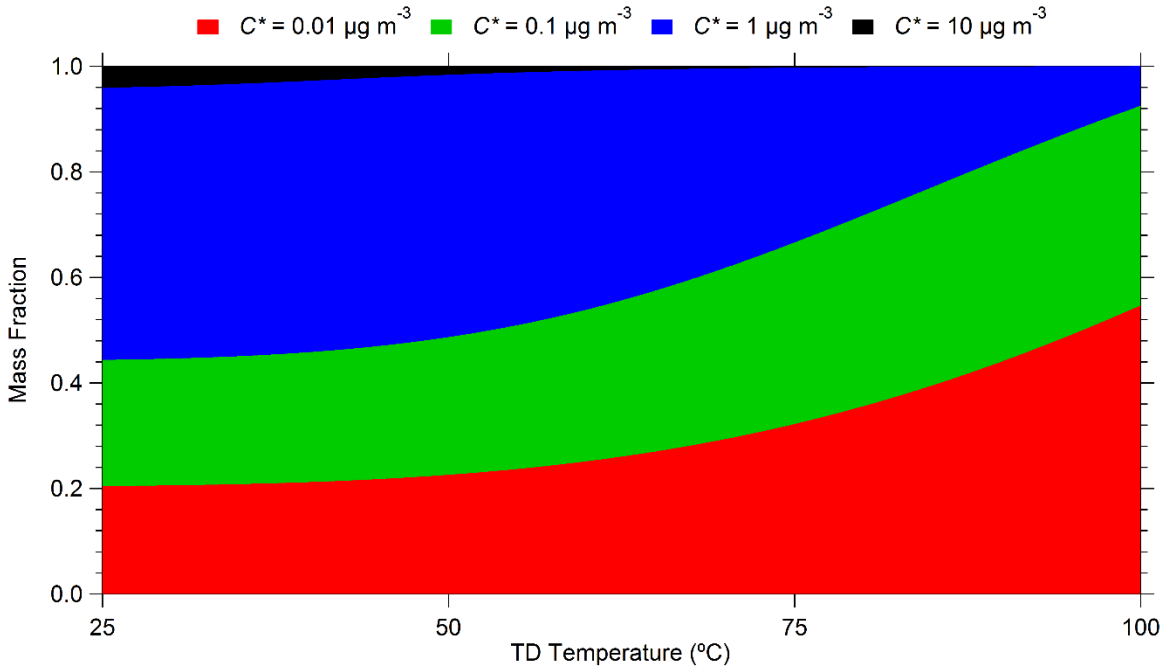

Figure A.5. The estimated mass fractions for each volatility bin as a function of TD temperature for Experiment 2. Red represents the C^* = 0.01 µg m^{-3} bin, green the C^* = 0.1 µg m^{-3} bin, blue the C^* = 1 µg m^{-3} bin, and black the C^* = 10 µg m^{-3} bin.

A.3 Results and analysis for Experiment 3

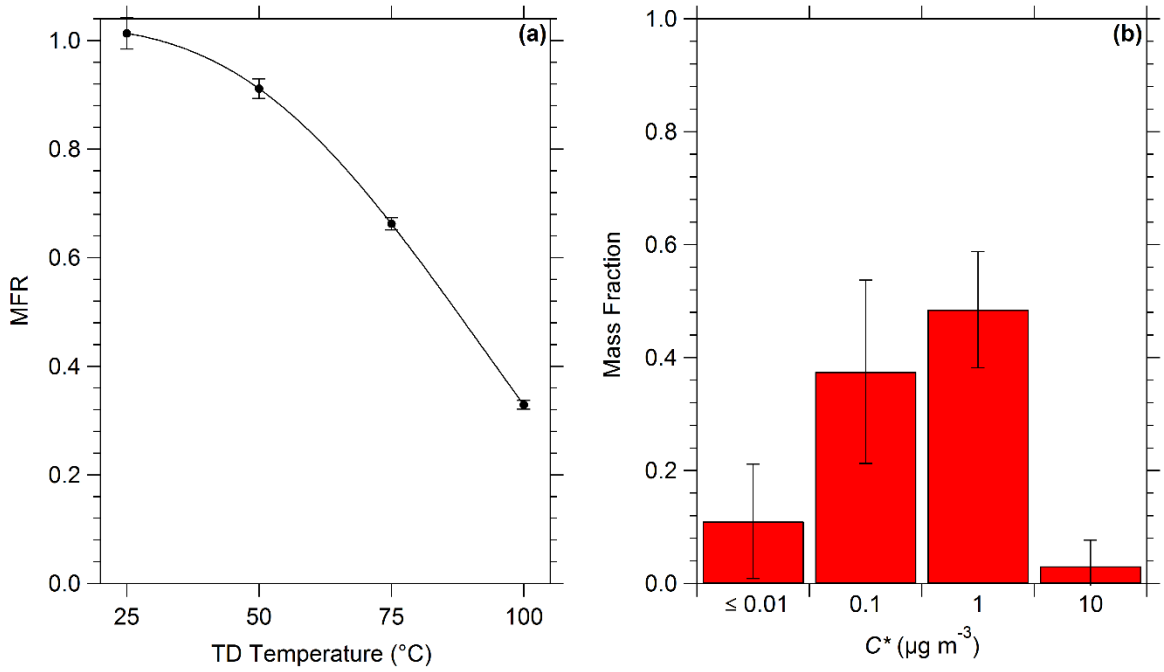

Figure A.6. (a) Thermogram, corrected for losses in the TD, for Experiment 3 with the fit from the TD model. The error bars represent one standard deviation of the mean. (b) SOA volatility distribution for Experiment 3 using the 1D-VBS framework. The error bars correspond to one standard deviation of the solution calculated by the model.

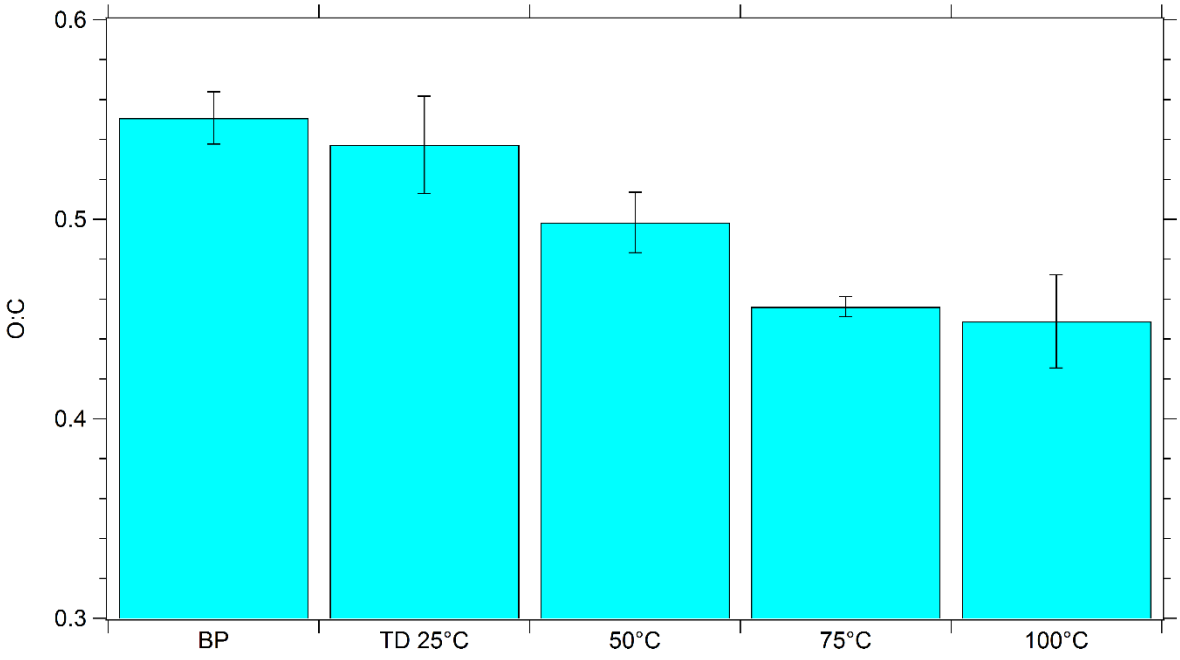

Figure A.7. The average O:C ratio observed through the BP and several TD temperatures for Experiment 3. The error bars represent one standard deviation of the mean. The O:C ratios at a TD temperature of 50°C and greater were statistically smaller than the values at the BP and the TD at 25°C.

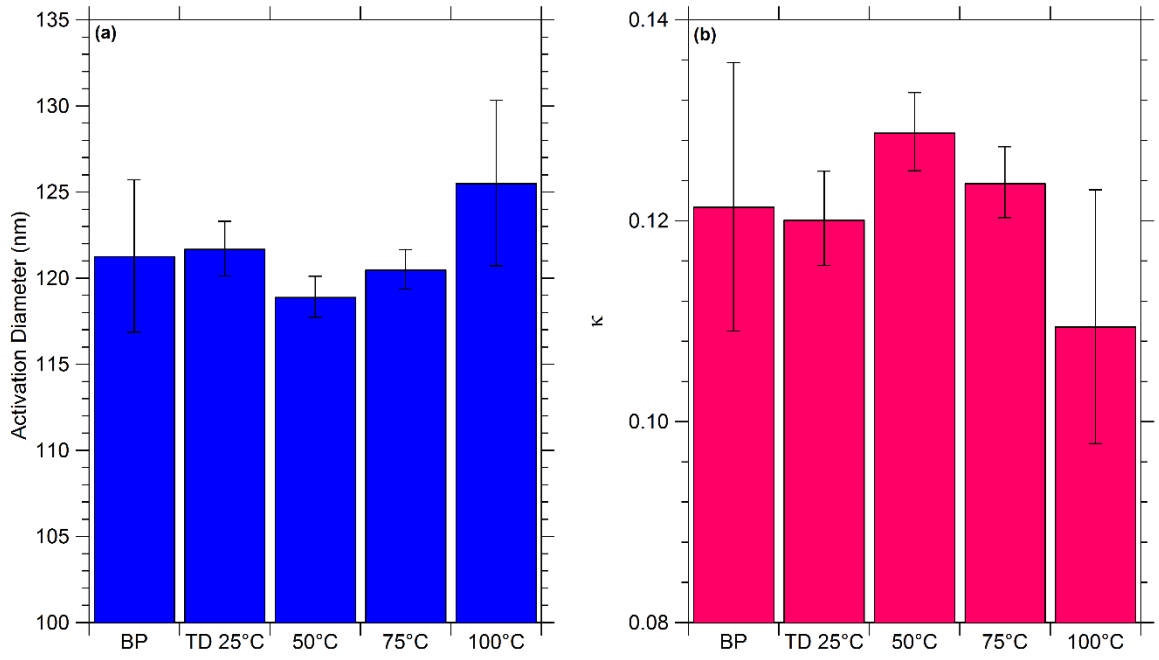

Figure A.8. (a) The average activation diameter observed at 0.25% supersaturation in the CCNC for Experiment 3. The error bars represent one standard deviation of the mean. (b) The estimated κ values for Experiment 3. The error bars were obtained by estimating the κ at +/- one standard deviation of the average activation diameter measured.

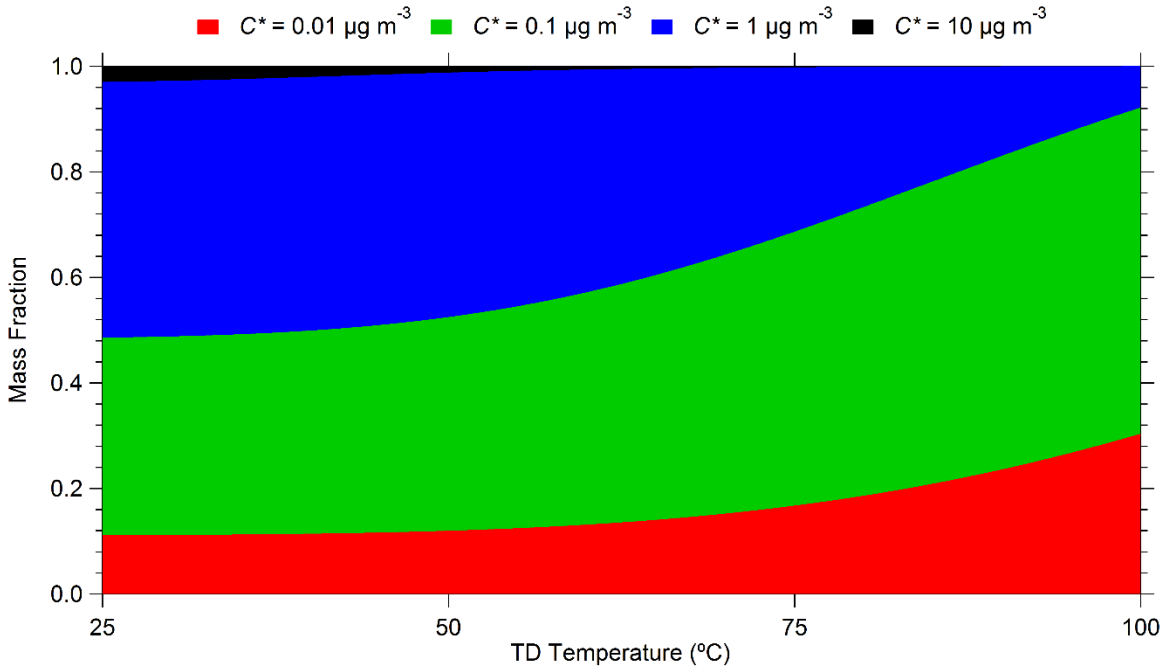

Figure A.9. The estimated mass fractions for each volatility bin as a function of TD temperature for Experiment 3. Red represents the C^* = 0.01 µg m^{-3} bin, green the C^* = 0.1 µg m^{-3} bin, blue the C^* = 1 µg m^{-3} bin, and black the C^* = 10 µg m^{-3} bin.

A.4 Results and analysis for Experiment 4

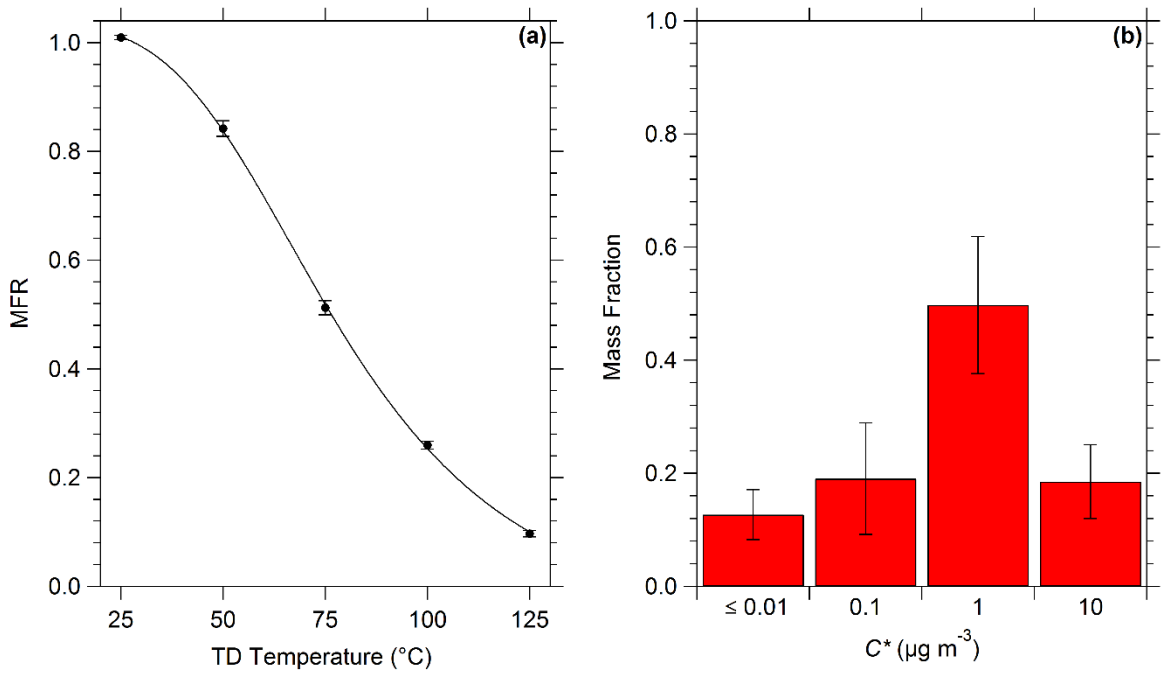

Figure A.10. (a) Thermogram, corrected for losses in the TD, for Experiment 4 with the fit from the TD model. The error bars represent one standard deviation of the mean. (b) SOA volatility distribution for Experiment 4 using the 1D-VBS framework. The error bars correspond to one standard deviation of the solution calculated by the model.

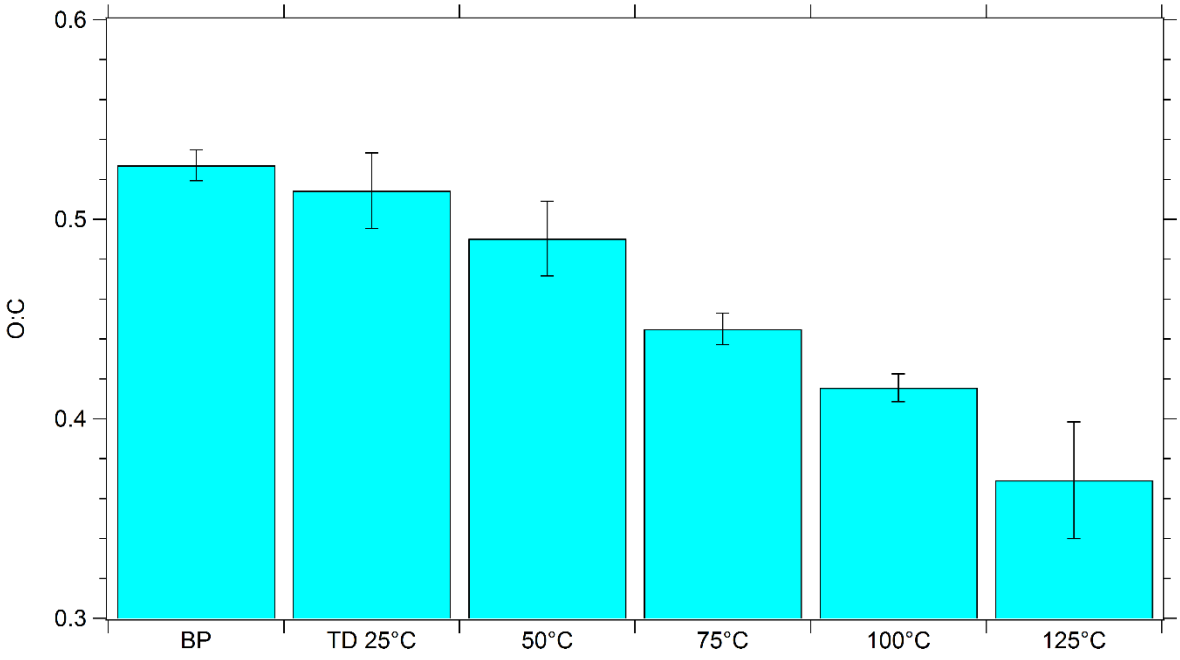

Figure A.11. The average O:C ratio observed through the BP and several TD temperatures for Experiment 4. The error bars represent one standard deviation of the mean. The O:C ratios at a TD temperature of 50°C and greater were statistically smaller than the values at the BP and the TD at 25°C.

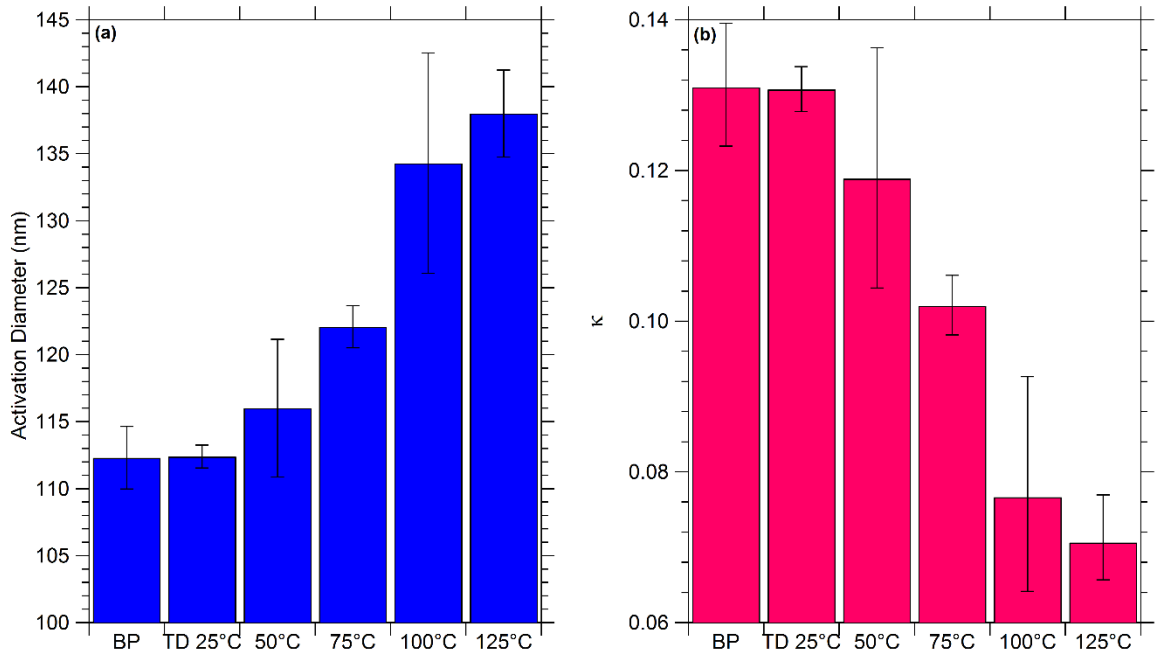

Figure A.12. (a) The average activation diameter observed at 0.27% supersaturation in the CCNC for Experiment 4. The error bars represent one standard deviation of the mean. (b) The estimated κ values for Experiment 4. The error bars were obtained by estimating the κ at +/- one standard deviation of the average activation diameter measured. The values at a TD temperature of 75°C and greater were statistically different from the values at the BP and the TD at 25°C. The SOA through the TD at 125°C did not have large enough particles to reach 50% activation, so the activation diameter was extrapolated from the particles that activated.

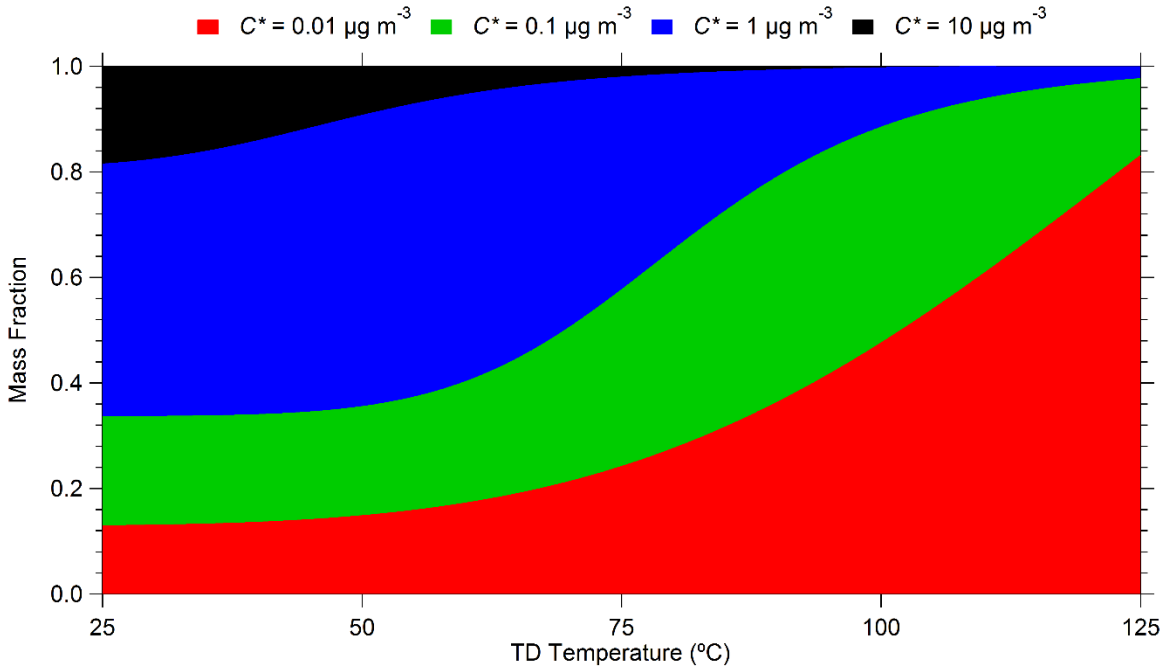

Figure A.13. The estimated mass fractions for each volatility bin as a function of TD temperature for Experiment 4. Red represents the C^* = 0.01 µg m^{-3} bin, green the C^* = 0.1 µg m^{-3} bin, blue the C^* = 1 µg m^{-3} bin, and black the C^* = 10 µg m^{-3} bin.

A.5 O:C and κ correlation

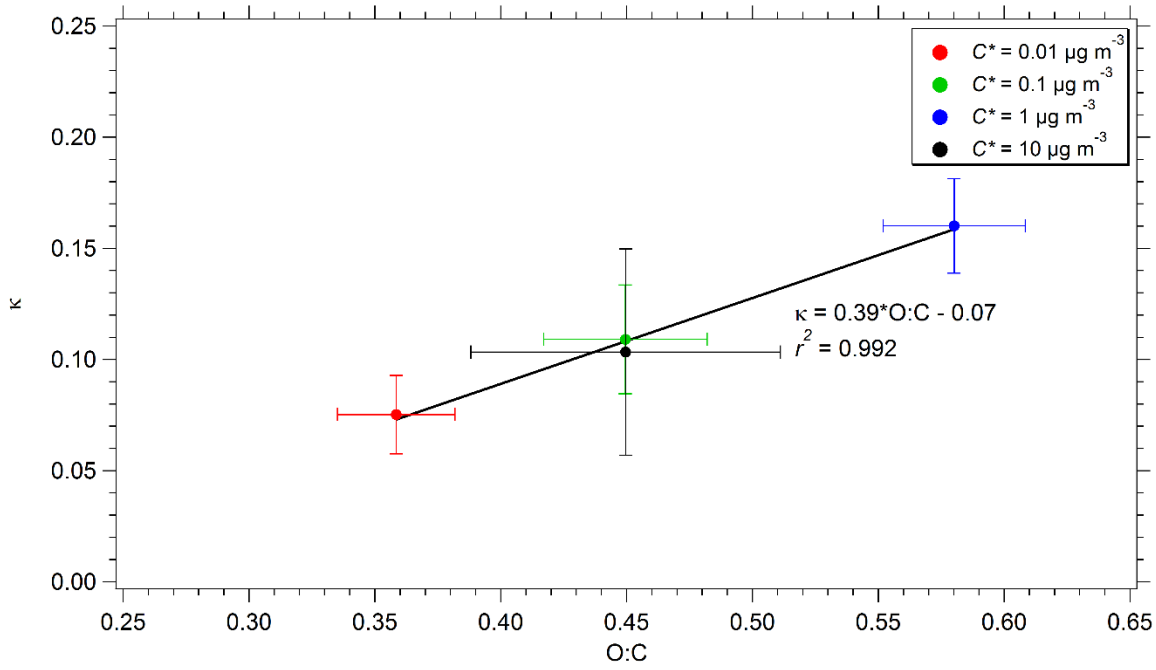

Figure A.14. The κ's plotted as a function of their corresponding O:C ratios for each volatility bin in Fig. 2.7. Red represents the C^* = 0.01 µg m^{-3} bin, green the C^* = 0.1 µg m^{-3} bin, blue the C^* = 1 µg m^{-3} bin, and black the C^* = 10 µg m^{-3} bin.

A.6 Predicted versus measured κ's for Experiment 2

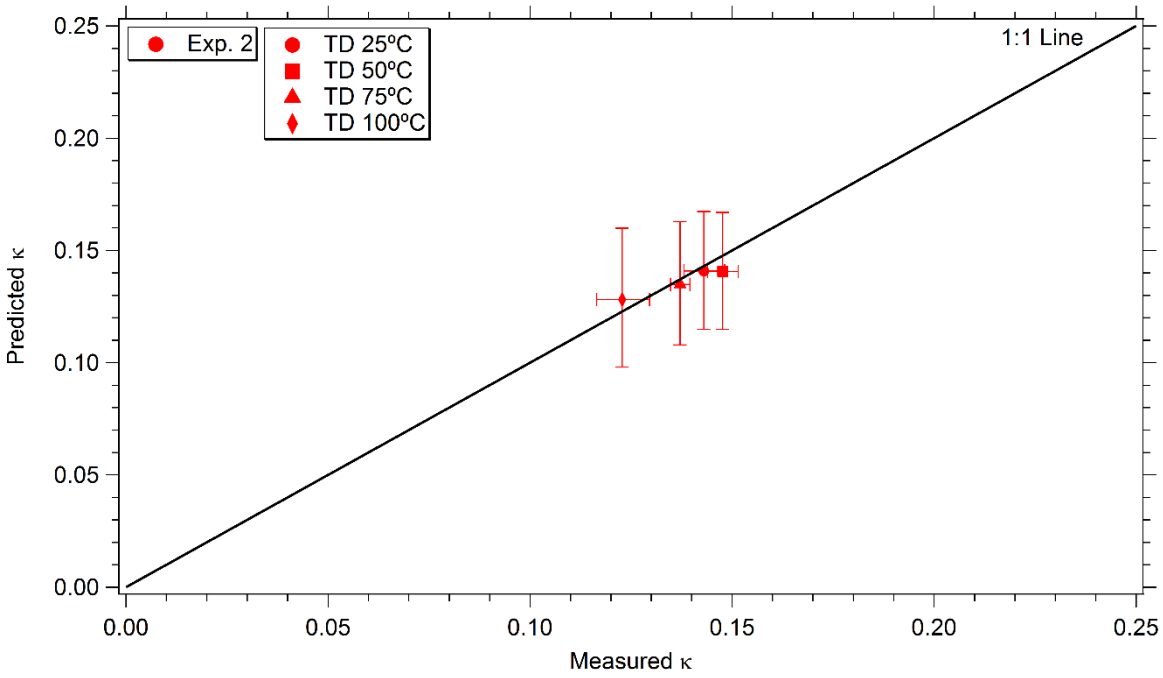

Figure A.15. The predicted versus measured κ's for Experiment 2 using the κ distribution in Fig. 2.7b for the three highest bins and the κ from the C^* = 0.01 μg m^{-3} bin in Fig. 2.10. The symbol indicates the TD temperature. The error bars for the predicted κ's were obtained by predicting the κ's using the κ distribution at +/- one standard deviation.

Appendix B

Supplementary information for Chapter 3

B1 Derivation of uncertainty introduced by particle wall-loss corrections

B1.1 Number

Particle wall-loss is a first order process and the decay of the number concentration at size bin *i* and time *t*, $N_i(t)$, can be described by:

$$\frac{dN_i(t)}{dt} = -k_{c,i}N_i(t) \tag{B.1}$$

where $k_{c,i}$ is the coagulation-corrected wall-loss rate constant at size bin *i*. Equation B.1 can be solved analytically to give an exponential decay for $N_i(t)$:

$$N_i(t) = N_{0,i}e^{-k_{c,i}\cdot t} \tag{B.2}$$

where $N_{0,i}$ is the initial number concentration at size bin *i*. The uncertainty in the number concentration at size bin *i* and time *t*, $\delta_{N_i}(t)$, was derived by the following equations:

$$\left|\delta_{N_i}(t)\right| = \delta\left(N_i(t)\right) = \delta\left(N_{0,i}e^{-k_{c,i}\cdot t}\right) \tag{B.3}$$

$$\left|\delta_{N_i}(t)\right| = N_{0,i}\left[\left(\frac{\partial}{\partial k_{c,i}}e^{-k_{c,i}\cdot t}\right)\delta_{k_{c,i}} + \left(\frac{\partial}{\partial t}e^{-k_{c,i}\cdot t}\right)\delta t\right] \tag{B.4}$$

$$\left|\delta_{N_i}(t)\right| = N_{0,i}e^{-k_{c,i}\cdot t}\cdot t\cdot\delta_{k_{c,i}} = \boldsymbol{N_i(t)\cdot t\cdot\delta_{k_{c,i}}} \tag{B.5}$$

The total number concentration at time *t*, $N(t)$, can be calculated by summing the number concentrations at all size bins:

$$N(t) = \sum_i N_i(t) \tag{B.6}$$

The uncertainty in the total number concentration at time *t*, $\delta_N(t)$, can be determined by:

$$\delta_N(t) = \delta\left(N(t)\right) = \sqrt{\sum_i \boldsymbol{\delta_{N_i}(t)^2}} \tag{B.7}$$

B1.2 Volume

Once the number concentration at size bin *i* and time *t* is corrected for wall-losses, the volume concentration at the same size bin and time, $V_i(t)$, can be determined:

$$V_i(t) = \frac{\pi d_{p,i}^3}{6} N_i(t) \tag{B.8}$$

where $d_{p,i}$ is the particle size at size bin *i*. The uncertainty in the volume concentration at size bin *i* and time *t*, $\delta_{V_i}(t)$, was derived by the following equations:

$$\left|\delta_{V_i}(t)\right| = \delta\left(V_i(t)\right) = \frac{\pi d_p^3}{6} \delta\left(N_i(t)\right) \tag{B.9}$$

$$\left|\delta_{V_i}(t)\right| = \frac{\pi d_p^3}{6} N_i(t) \cdot t \cdot \delta_{k_{c,i}} = \boldsymbol{V_i(t) \cdot t \cdot \delta_{k_{c,i}}} \tag{B.10}$$

Similar to the total number concentration, the total volume concentration at time *t*, $V(t)$, can be calculated by:

$$V(t) = \sum_i V_i(t) \tag{B.11}$$

and the uncertainty in the total volume concentration at time *t*, $\delta_V(t)$, can be determined by:

$$\delta_V(t) = \delta\left(V(t)\right) = \sqrt{\sum_i \boldsymbol{\delta_{V_i}(t)^2}} \tag{B.12}$$

B1.3 Mass

With the volume concentration known at size bin *i* and time *t*, the mass concentration at the same size bin and time, $M_i(t)$, is determined by:

$$M_i(t) = \rho V_i(t) \tag{B.13}$$

where ρ is the particle density. The uncertainty in the mass concentration at size bin *i* and time *t*, $\delta_{M_i}(t)$, was derived by the following equations:

$$\left|\delta_{M_i}(t)\right| = \delta\left(M_i(t)\right) = \rho\delta\left(V_i(t)\right) \tag{B.14}$$

$$\left|\delta_{M_i}(t)\right| = \rho V_i(t) \cdot t \cdot \delta_{k_{c,i}} = \boldsymbol{M_i(t) \cdot t \cdot \delta_{k_{c,i}}} \quad \text{(B.15)}$$

The total mass concentration at time *t*, *M*(*t*), can be calculated by:

$$M(t) = \sum_i M_i(t) \quad \text{(B.16)}$$

and the uncertainty in the total volume concentration at time *t*, $\delta_M(t)$, can be determined by:

$$\delta_M(t) = \delta\big(M(t)\big) = \sqrt{\sum_i \boldsymbol{\delta_{M_i}(t)^2}} \quad \text{(B.17)}$$

B1.4 Areogram MFR

The corrected MFR at time *t*, *MFR*(*t*), used in the areograms can be calculated by the following equation:

$$MFR(t) = \frac{M(t)}{M_0} \quad \text{(B.18)}$$

where *M*(*t*) and M_0 are the corrected mass concentration at time *t* and the initial mass concentration in the dilution chamber, respectively. Therefore, the uncertainty of the MFR at time *t*, $\delta_{MFR}(t)$, can be determined by:

$$\delta_{MFR}(t) = \boldsymbol{MFR(t)} \sqrt{\left(\frac{\boldsymbol{\delta_M(t)}}{\boldsymbol{M(t)}}\right)^2 + \left(\frac{\boldsymbol{\delta_{M_0}}}{\boldsymbol{M_0}}\right)^2} \quad \text{(B.19)}$$

where δ_{M_0} is the uncertainty of the initial mass concentration in the dilution chamber.

B1.5 Mean volume diameter

The corrected mean volume particle diameter at time *t*, $d_{p,v,mean}(t)$, can be calculated by:

$$d_{p,v,mean}(t) = \frac{\sum_i d_{p,i} \cdot V_i(t)}{V(t)} \quad \text{(B.20)}$$

Therefore, the uncertainty of the corrected mean volume particle diameter at time *t*, $\delta_{d_{p,v,mean}}(t)$, can be determined by:

$$\delta_{d_{p,v,mean}}(t) = \boldsymbol{d_{p,v,mean}(t)} \sqrt{\left(\frac{\sqrt{\sum_i \boldsymbol{d_{p,i}^2 \cdot \delta_{V_i}^2(t)}}}{\sum_i \boldsymbol{d_{p,i} \cdot V_i(t)}} \right)^{\mathbf{2}} + \left(\frac{\boldsymbol{\delta_V(t)}}{\boldsymbol{V(t)}} \right)^{\mathbf{2}}} \qquad \text{(B.21)}$$

B2 Particle losses in the pump used for the transfer to the dilution chamber

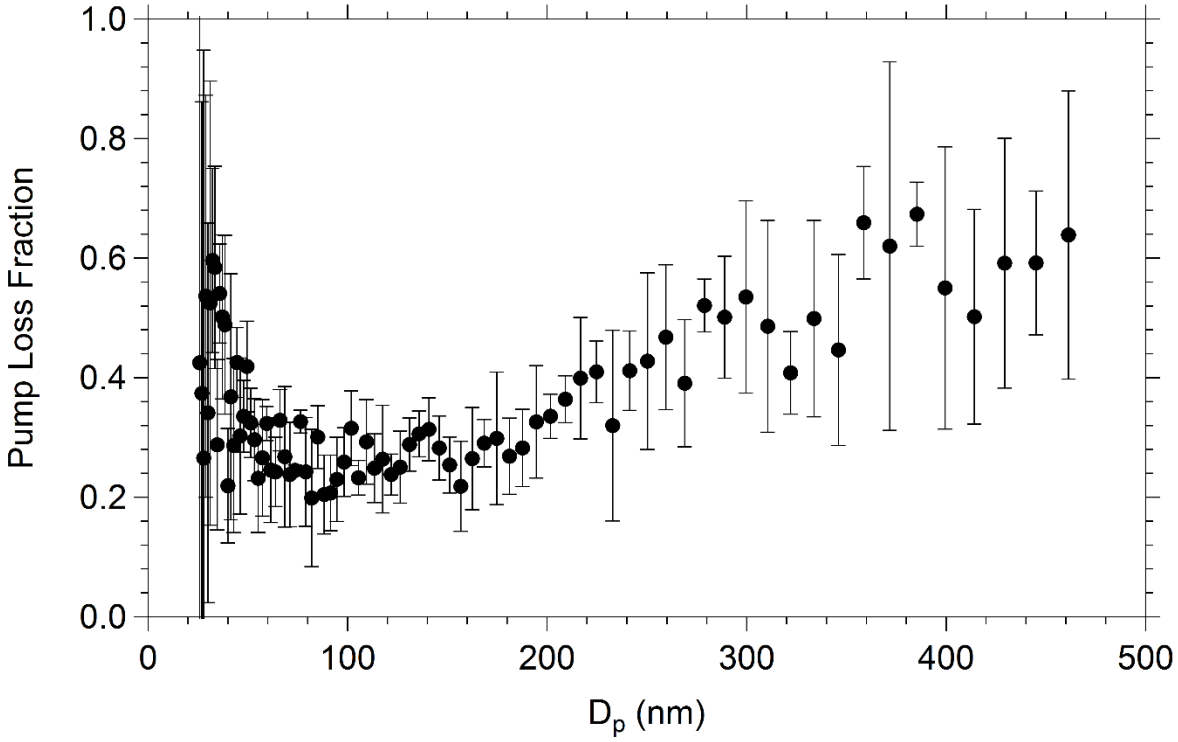

Figure B.1. Particle losses as a function of particle size due to transferring aerosol from the main chamber to the dilution chamber. The losses were measured by transferring ammonium sulfate particles from the main chamber to the dilution chamber and comparing the size distributions. The error bars represent one standard deviation of the mean.

B3 Coagulation-corrected particle wall-loss rate constant

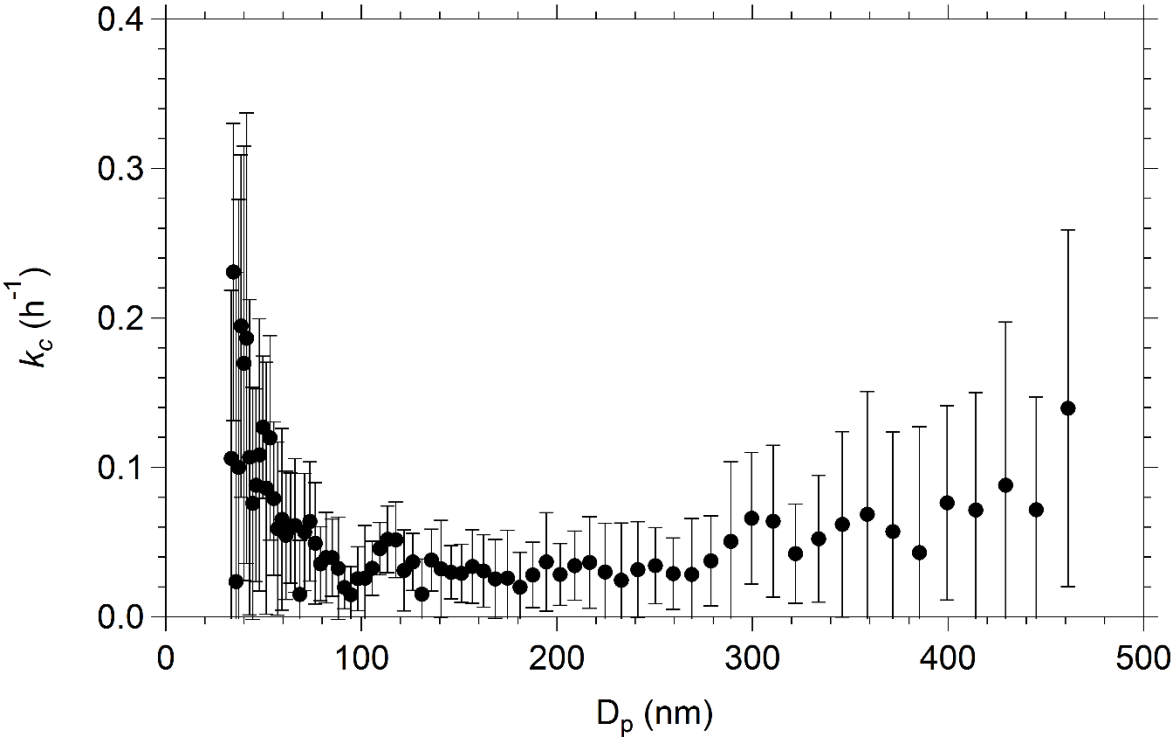

Figure B.2. An example of the coagulation-corrected particle wall-loss rate constants, k_c, as a function of particle diameter. The error bars represent the uncertainty of the rate constant, calculated by $\boldsymbol{\sigma_{k_{c,i}}}/\sqrt{\boldsymbol{N}}$, where $\boldsymbol{\sigma_{k_{c,i}}}$ is the standard deviation of k_c for a certain particle size, i, and N is the total number of time steps used.

B4 Particle wall-loss corrected ammonium sulfate mass concentration in dilution chamber

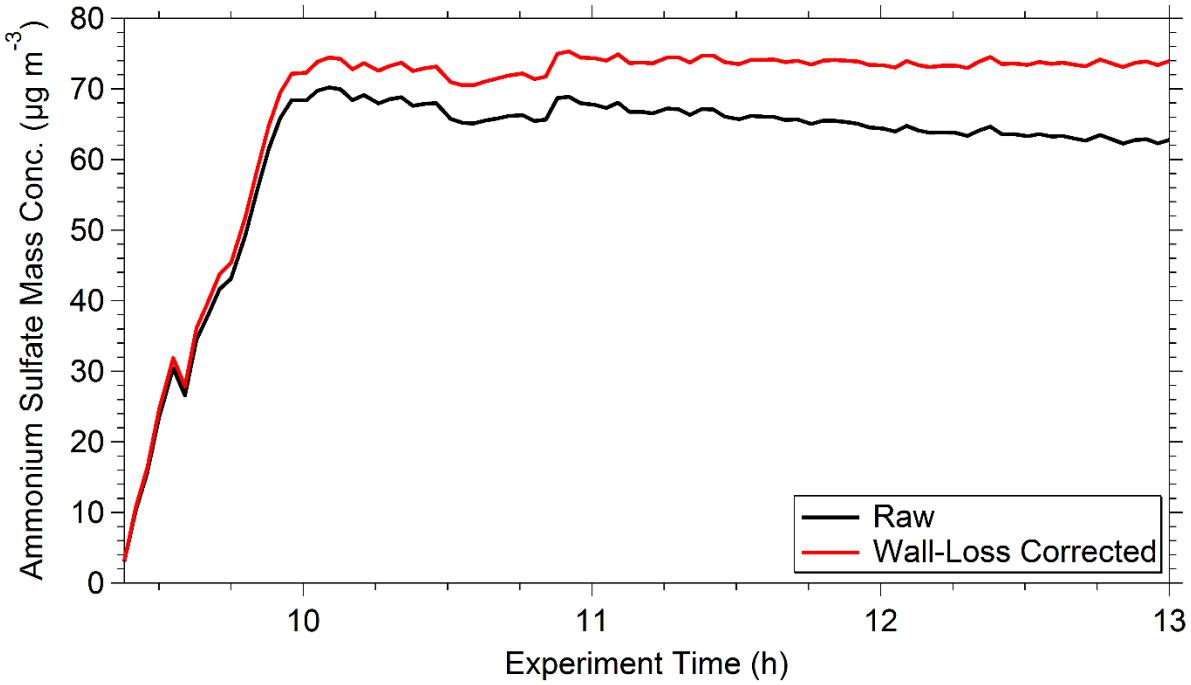

Figure B.3. The raw (black line) and particle wall-loss corrected (red line) ammonium sulfate mass concentration for Experiment AP1. The ammonium sulfate injection started in the dilution chamber around 9.5 h after the SOA experiment began.

B5 Estimating SOA volatility distributions using thermograms

Table B.1. The estimated SOA composition and corresponding properties from the model fitting only the thermograms.

	Experiment							
SOA Composition (%)	**AP1**	**AP2**	**AP3**	**AP4**	**CH1**	**CH2**	**CH3**	**CH4**
SVOCs	49 ± 20	52 ± 17	57 ± 15	48 ± 22	59 ± 16	58 ± 16	60 ± 14	58 ± 18
LVOCs	51 ± 20	48 ± 17	43 ± 15	52 ± 22	41 ± 16	42 ± 16	40 ± 14	42 ± 18
ΔH_{vap} (kJ mol^{-1})	93 ± 20	95 ± 19	95 ± 19	86 ± 21	91 ± 20	90 ± 20	93 ± 18	88 ± 21
Accomodation Coefficient[a]	0.09 (0.07-0.29)	0.10 (0.08-0.33)	0.17 (0.12-0.42)	0.08 (0.06-0.29)	0.15 (0.12-0.45)	0.15 (0.11-0.43)	0.15 (0.11-0.45)	0.14 (0.11-0.44)

[a]The values in parentheses represent the uncertainty range for the estimated accommodation coefficients.

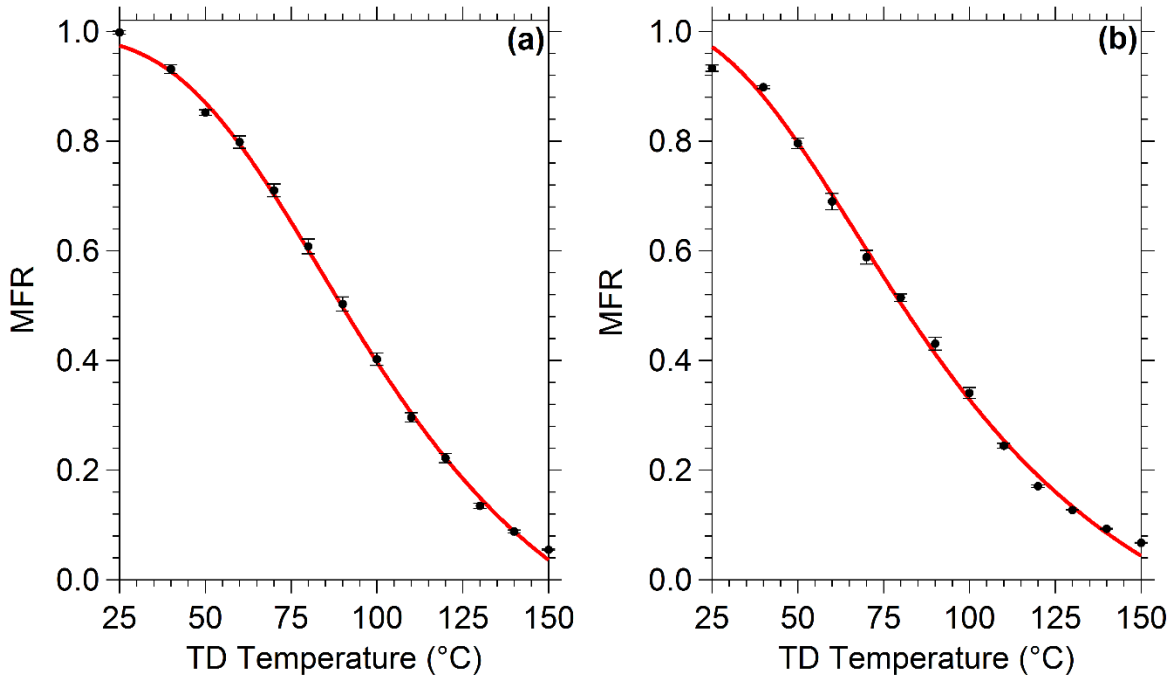

Figure B.4. The thermogram for Experiment (a) AP1 and (b) CH1. Black circles represent TD-loss corrected SMPS measurements with the error bars representing 1 standard deviation of the mean. The red line is the best fit from the model using only the thermogram as an input.

B6 Estimating SOA volatility distributions using thermograms and areograms

Table B.2. The estimated SOA composition and corresponding properties from the model fitting the thermograms and areograms simultaneously.

	Experiment							
SOA Composition (%)	**AP1**	**AP2**	**AP3**	**AP4**	**CH1**	**CH2**	**CH3**	**CH4**
IVOCs	N/A	N/A	N/A	N/A	14 ± 12	11 ± 10	19 ± 12	9 ± 8
SVOCs	31 ± 14	31 ± 13	39 ± 11	15 ± 8	72 ± 15	65 ± 15	61 ± 17	61 ± 14
LVOCs	56 ± 15	51 ± 16	45 ± 13	73 ± 13	16 ± 9	24 ± 12	20 ± 10	30 ± 12
ELVOCs	13 ± 12	18 ± 13	16 ± 12	12 ± 10	N/A	N/A	N/A	N/A
ΔH_{vap} (kJ mol^{-1})	129 ± 26	142 ± 26	146 ± 26	117 ± 22	68 ± 18	84 ± 15	82 ± 14	96 ± 14
Accomodation Coefficient[a]	0.08 (0.06-0.30)	0.07 (0.06-0.29)	0.10 (0.08-0.38)	0.04 (0.03-0.15)	0.03 (0.02-0.05)	0.03 (0.02-0.06)	0.03 (0.02-0.06)	0.02 (0.01-0.03)

[a]The values in parentheses represent the uncertainty range for the estimated accommodation coefficients.

B7 Estimating SOA volatility distributions using thermograms and areograms accounting for vapor-phase wall-losses

Table B.3. The estimated SOA composition and vapor-phase wall-loss constant for all experiments.

	Experiment							
SOA Composition (%)	**AP1**	**AP2**	**AP3**	**AP4**	**CH1**	**CH2**	**CH3**	**CH4**
IVOCs	N/A	N/A	N/A	N/A	5 ± 6	6 ± 5	18 ± 10	8 ± 7
SVOCs	23 ± 10	31 ± 11	35 ± 10	14 ± 5	81 ± 9	72 ± 9	62 ± 12	62 ± 10
LVOCs	68 ± 12	53 ± 11	49 ± 11	79 ± 9	14 ± 7	22 ± 7	20 ± 6	30 ± 8
ELVOCs	9 ± 7	16 ± 5	16 ± 5	7 ± 8	N/A	N/A	N/A	N/A
$k_{v,w}$ (h^{-1})	1.8 ± 3.0	1.5 ± 2.8	0.5 ± 1.0	2.3 ± 3.4	1.9 ± 2.8	1.8 ± 3.0	1.5 ± 2.7	1.7 ± 2.9

B8 SOA phase state change in TD at 100°C

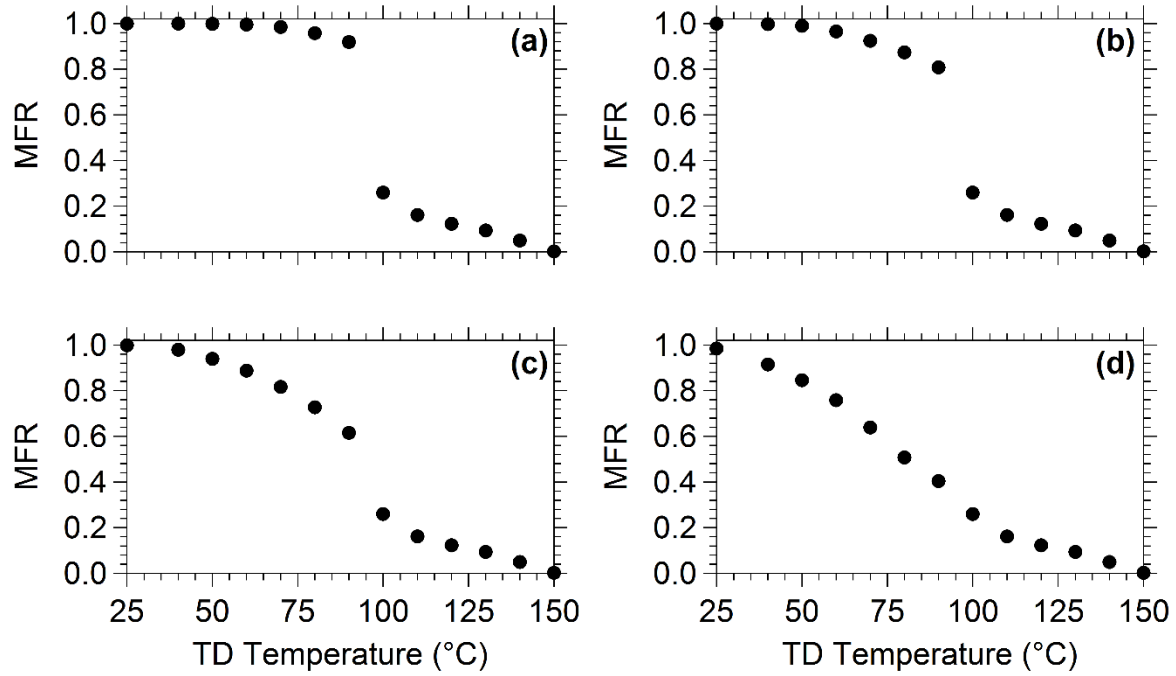

Figure B.5. Thermograms for Experiment AP1 assuming the volatility distribution from Fig. 3.7 and the ΔH_{vap} from Table B.2. The mass accommodation coefficient goes from (a) 0.0001, (b) 0.001, (c) 0.01, and (d) 0.1 to 1 at 100°C.

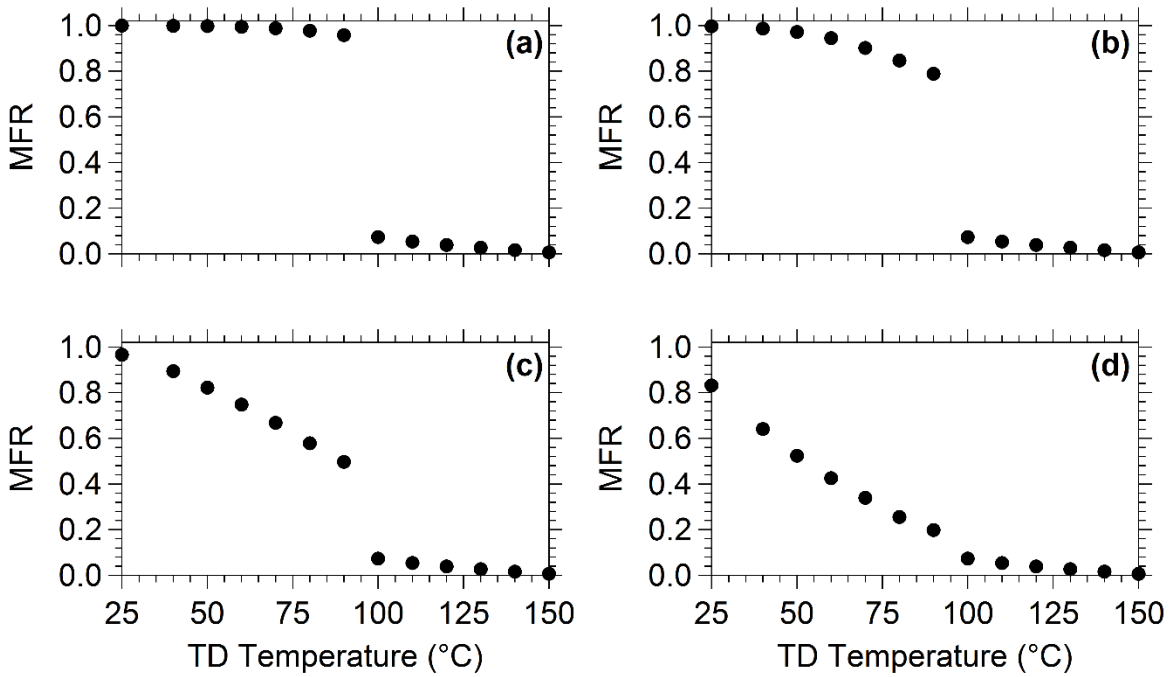

Figure B.6. Thermograms for Experiment CH1 assuming the volatility distribution from Fig. 3.7 and the ΔH_{vap} from Table B.2. The mass accommodation coefficient goes from (a) 0.0001, (b) 0.001, (c) 0.01, and (d) 0.1 to 1 at 100°C.

Appendix C

Elemental ratio behavior from SOA in Chapter 3

C.1 Elemental ratios

The average oxygen-to-carbon (O:C) ratio, hydrogen-to-carbon (H:C) ratio, and carbon oxidation state (OS_c, $OS_c \approx 2(O:C) - H:C$) in the main chamber for all experiments in Chapter 3 are shown in Table C.1. The SOA generated from the ozonolysis of cyclohexene had, on average, slightly higher O:C ratios, but similar H:C ratios to the α-pinene ozonolysis SOA, resulting in the cyclohexene SOA having a higher average carbon oxidation state.

The average O:C ratios, H:C ratios, and OS_c as a function of TD temperature for all experiments are shown in Figs. C.1–C.6. In the α-pinene experiments, the average O:C ratios remained fairly constant or decreased slightly upon heating until decreasing significantly around 120°C (Fig. C.1). The average H:C ratios in these experiments also remained fairly constant upon heating, but began decreasing rapidly around 70°C (Fig. C.2). Therefore, the average OS_c for the α-pinene experiments remained constant at low TD temperatures, but then increased slightly around 70°C due to the H:C ratios decreasing and then started decreasing again around 120°C when the O:C ratios started decreasing (Fig. C.3). In contrast, in the cyclohexene experiments, the average O:C ratios increased upon heating in the TD, reached a maximum around 70°C, and then decreased upon further heating (Fig. C.4). The average H:C ratios in these experiments decreased almost immediately upon heating (Fig. C.5), and, therefore, the average OS_c increased significantly upon heating, but reached a maximum around 110°C and started decreasing due to the O:C ratios decreasing (Fig. C.6).

Although the thermograms from the α-pinene and cyclohexene experiments appear quite similar, the elemental ratios of the particles behave differently in the TD. Through the TD at 70°C, the MFRs of all experiments were around 0.65. However, the elemental ratios for the α-pinene ozonolysis SOA remained fairly constant up to this temperature, but the average O:C ratios for the

cyclohexene ozonolysis SOA were increasing while the average H:C ratios were decreasing, indicating that what evaporated in the α-pinene experiments at these lower temperatures had similar composition, but the cyclohexene ozonolysis SOA components that evaporated were less oxidized (i.e. they had lower O:C ratios and higher H:C ratios, on average) than the remaining SOA. At higher TD temperatures, both SOA systems responded similarly with the elemental ratios decreasing upon heating, indicating that the least volatile compounds in both systems had lower O:C and H:C ratios than the average SOA in the main chamber. It is important to note that, at these higher temperatures, the average OS_c remained the same or was slightly lower than the average OS_c in the main chamber for the α-pinene ozonolysis SOA, but the average OS_c was higher than the average OS_c in the main chamber for the cyclohexene ozonolysis SOA in all experiments except for Experiment CH4, demonstrating that while the elemental ratios may behave similarly, the oxidation state of these particles can be quite different.

The average O:C ratios, H:C ratios, and OS_c as a function of time in the dilution chamber for all experiments are shown in Figs. C.7–C.12. The average O:C ratios in both systems remained fairly constant upon dilution, but then began decreasing as time progressed (Figs. C.7 and C.10). The average H:C ratios for the α-pinene ozonolysis SOA decreased immediately upon dilution, but then remained constant or decreased slightly at longer times while the average H:C ratios for the cyclohexene ozonolysis SOA decreased more gradually over time after dilution (Figs. C.8 and C.11). Finally, the average OS_c increased immediately, but then decreased at longer dilution times for the α-pinene ozonolysis SOA while the average OS_c increased gradually upon dilution and then remained constant for the remainder of the experiment for the cyclohexene ozonolysis SOA (Figs. C.9 and C.12).

Table C.1. The average O:C ratio, H:C ratio, and average OS_c in the main chamber for all experiments in Chapter 3.

Exp.	O:C	H:C	OS_c
AP1	0.44	1.61	-0.73
AP2	0.44	1.69	-0.81
AP3	0.43	1.71	-0.85
AP4	0.41	1.62	-0.80
CH1	0.45	1.67	-0.76
CH2	0.46	1.67	-0.74
CH3	0.47	1.62	-0.68
CH4	0.49	1.63	-0.65

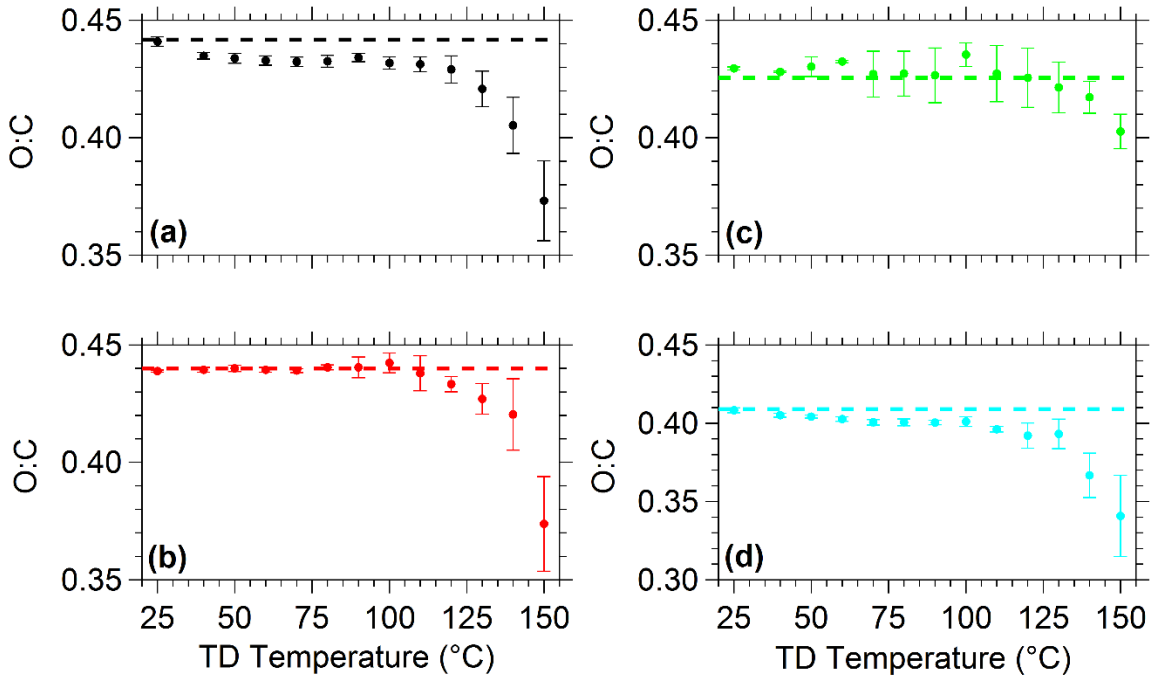

Figure C.1. Average O:C ratios through the TD for Experiment (a) AP1, (b) AP2, (c) AP3, and (d) AP4. The dotted line represents the average O:C ratio in the main chamber for the experiment. The error bars represent one standard deviation of the mean.

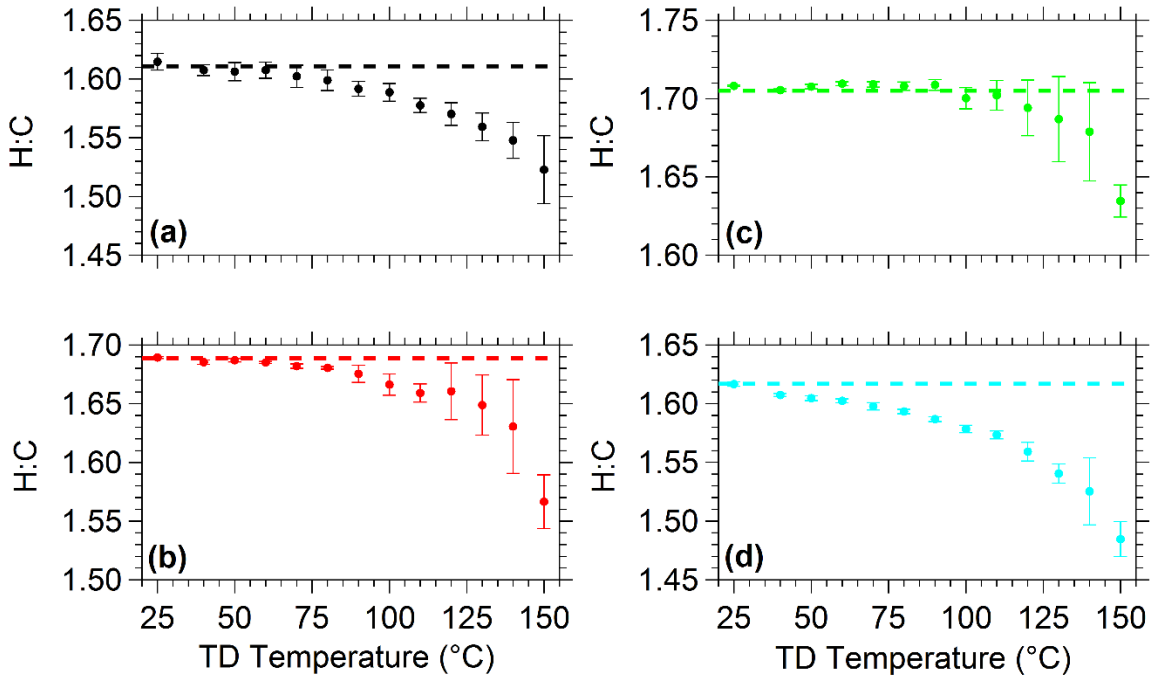

Figure C.2. Average H:C ratios through the TD for Experiment (a) AP1, (b) AP2, (c) AP3, and (d) AP4. The dotted line represents the average H:C ratio in the main chamber for the experiment. The error bars represent one standard deviation of the mean.

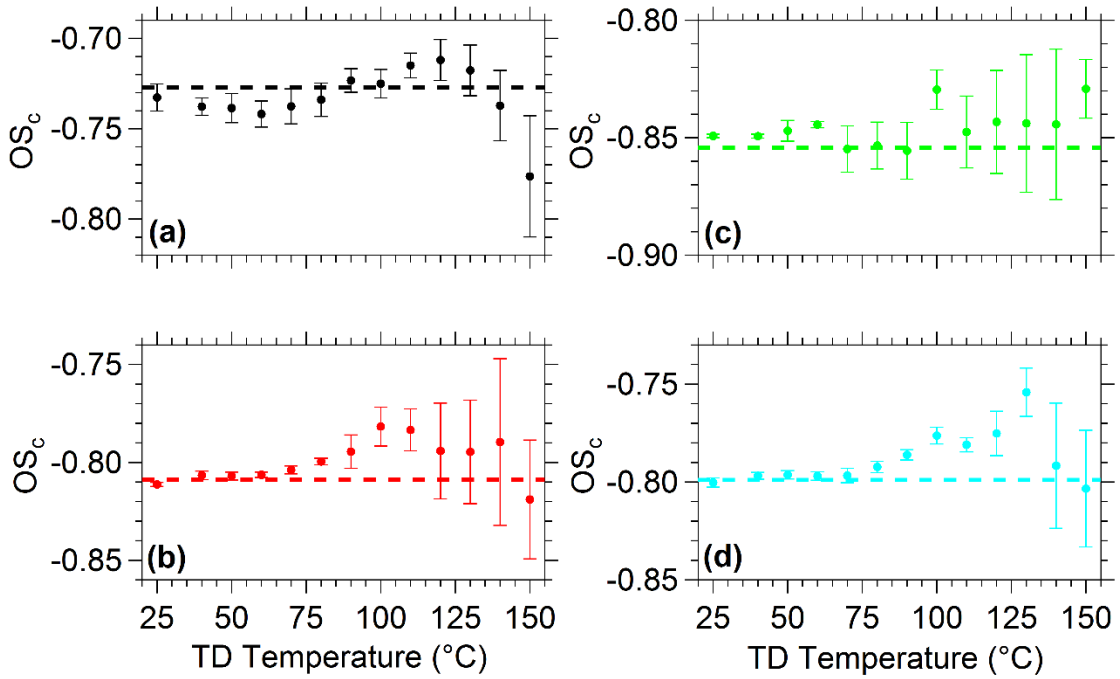

Figure C.3. The average OS_c through the TD for Experiment (a) AP1, (b) AP2, (c) AP3, and (d) AP4. The dotted line represents the average OS_c in the main chamber for the experiment. The error bars represent one standard deviation of the mean.

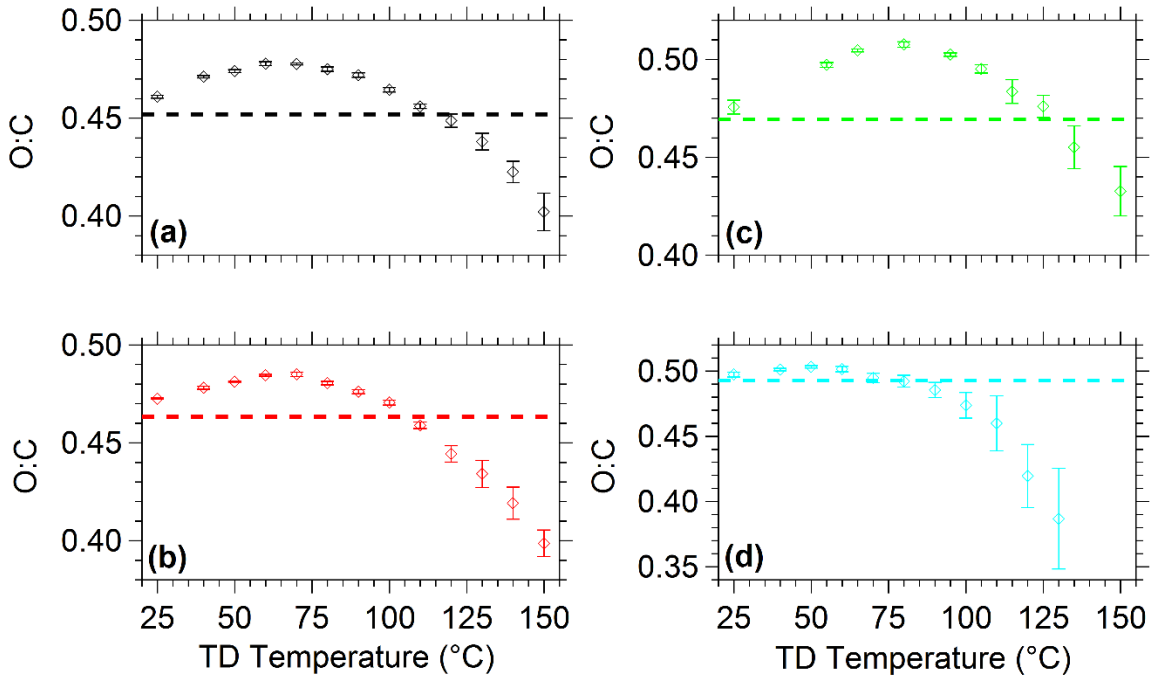

Figure C.4. Average O:C ratios through the TD for Experiment (a) CH1, (b) CH2, (c) CH3, and (d) CH4. The dotted line represents the average O:C ratio in the main chamber for the experiment. The error bars represent one standard deviation of the mean.

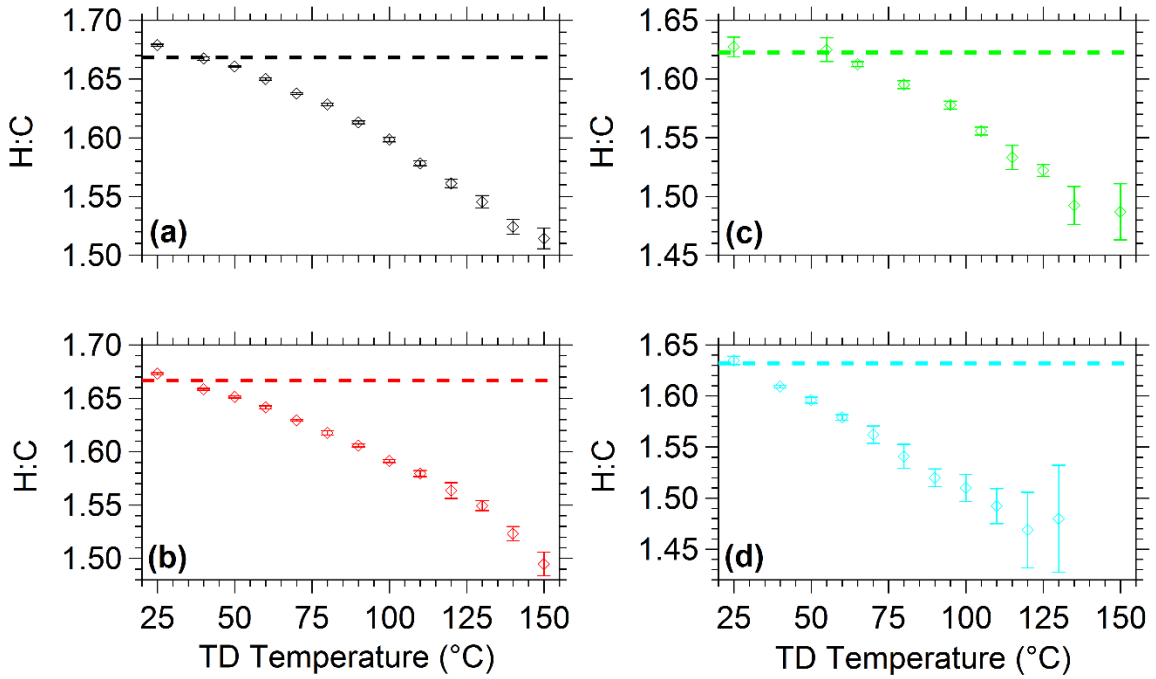

Figure C.5. Average H:C ratios through the TD for Experiment (a) CH1, (b) CH2, (c) CH3, and (d) CH4. The dotted line represents the average H:C ratio in the main chamber for the experiment. The error bars represent one standard deviation of the mean.

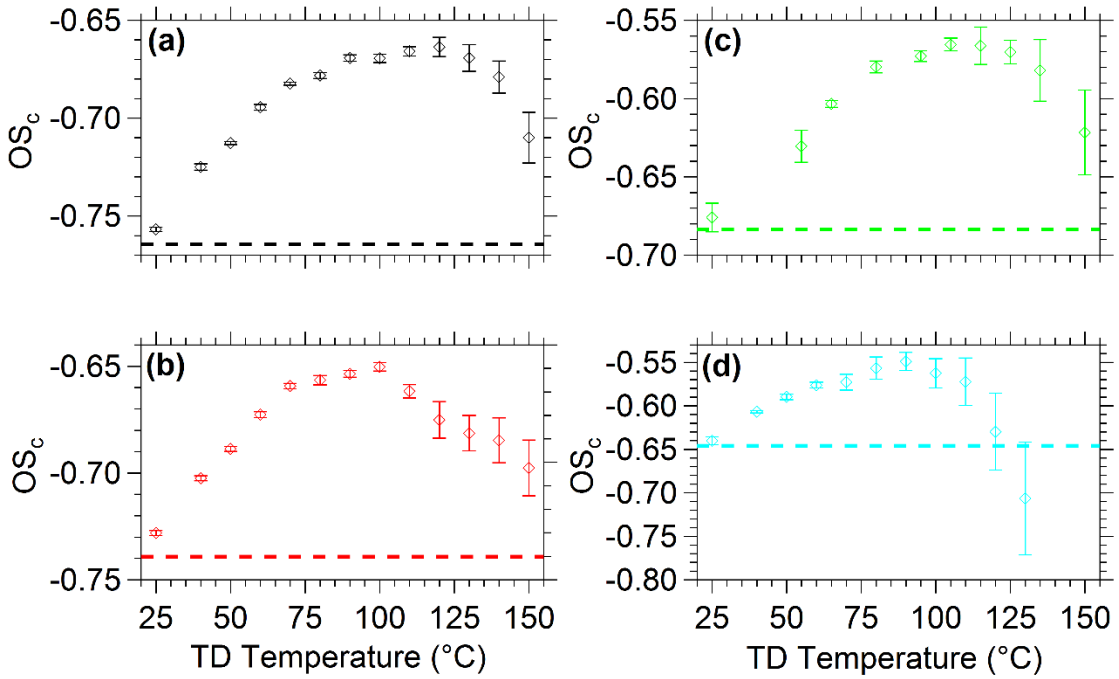

Figure C.6. The average OS_c through the TD for Experiment (a) CH1, (b) CH2, (c) CH3, and (d) CH4. The dotted line represents the average OS_c in the main chamber for the experiment. The error bars represent one standard deviation of the mean.

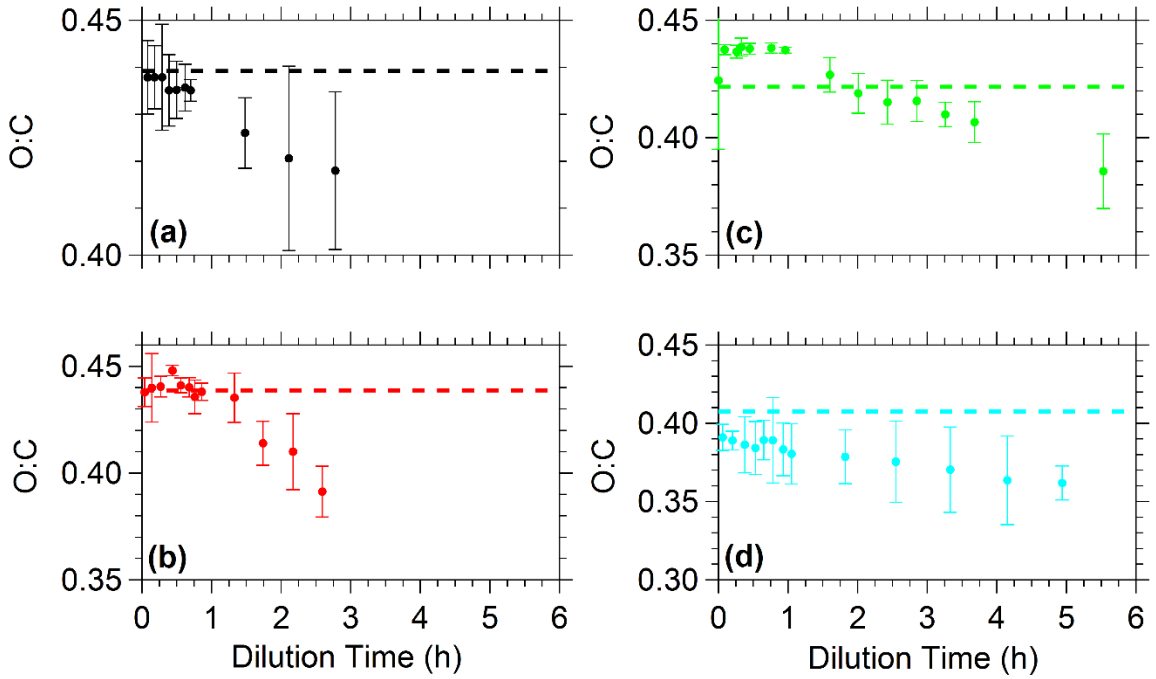

Figure C.7. Average O:C ratios in the dilution chamber for Experiment (a) AP1, (b) AP2, (c) AP3, and (d) AP4. The dotted line represents the average O:C ratio in the main chamber just before dilution. The error bars represent one standard deviation of the mean.

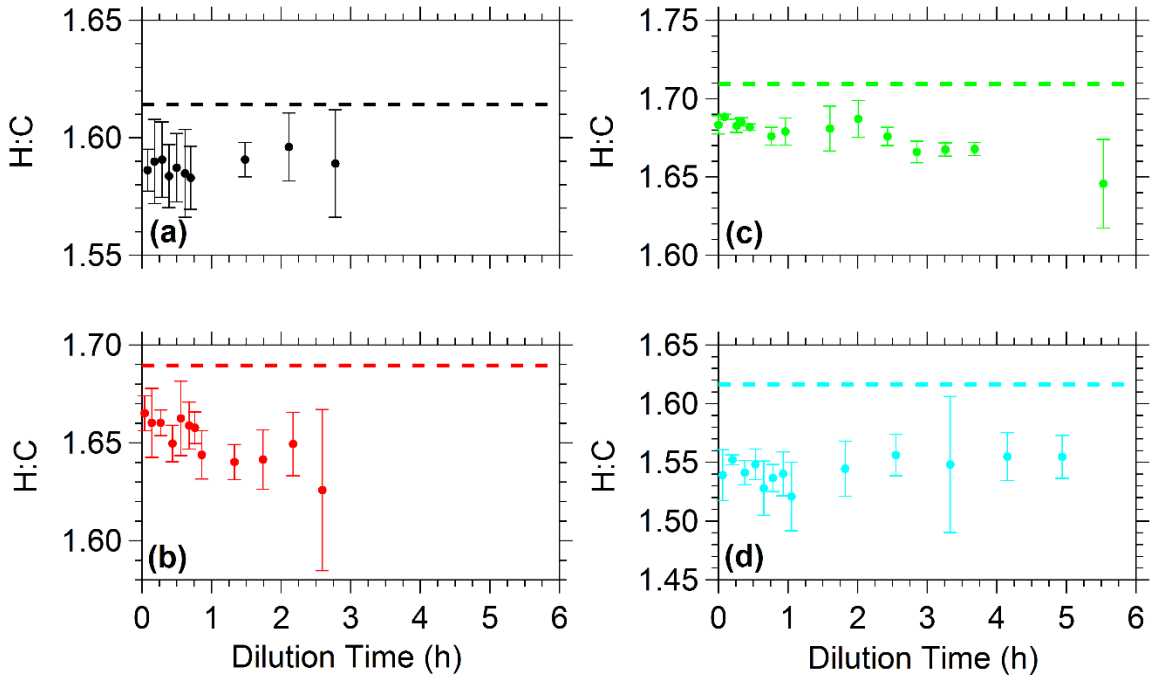

Figure C.8. Average H:C ratios in the dilution chamber for Experiment (a) AP1, (b) AP2, (c) AP3, and (d) AP4. The dotted line represents the average H:C ratio in the main chamber just before dilution. The error bars represent one standard deviation of the mean.

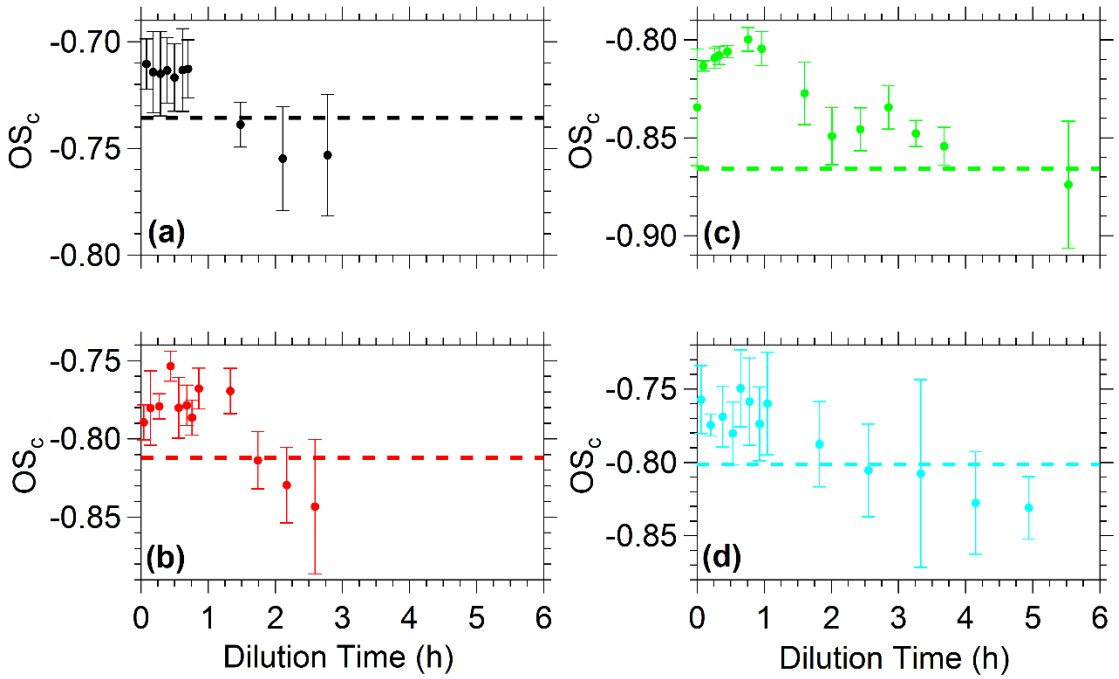

Figure C.9. The average OS_c in the dilution chamber for Experiment (a) AP1, (b) AP2, (c) AP3, and (d) AP4. The dotted line represents the average OS_c in the main chamber just before dilution. The error bars represent one standard deviation of the mean.

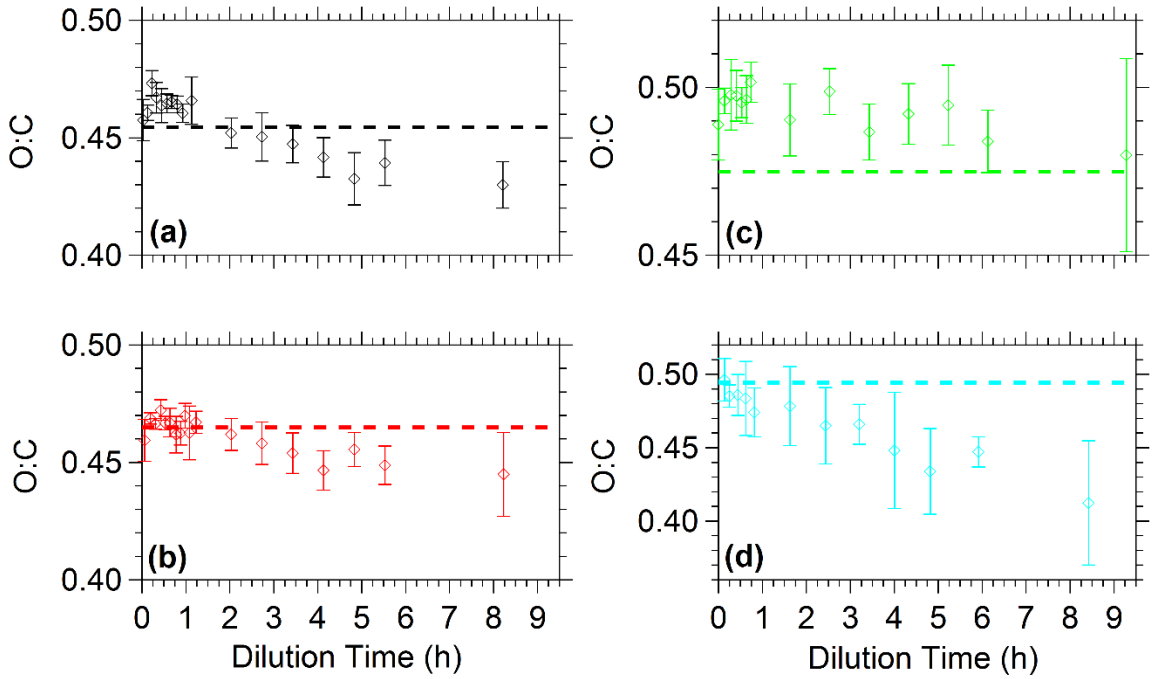

Figure C.10. Average O:C ratios in the dilution chamber for Experiment (a) CH1, (b) CH2, (c) CH3, and (d) CH4. The dotted line represents the average O:C ratio in the main chamber just before dilution. The error bars represent one standard deviation of the mean.

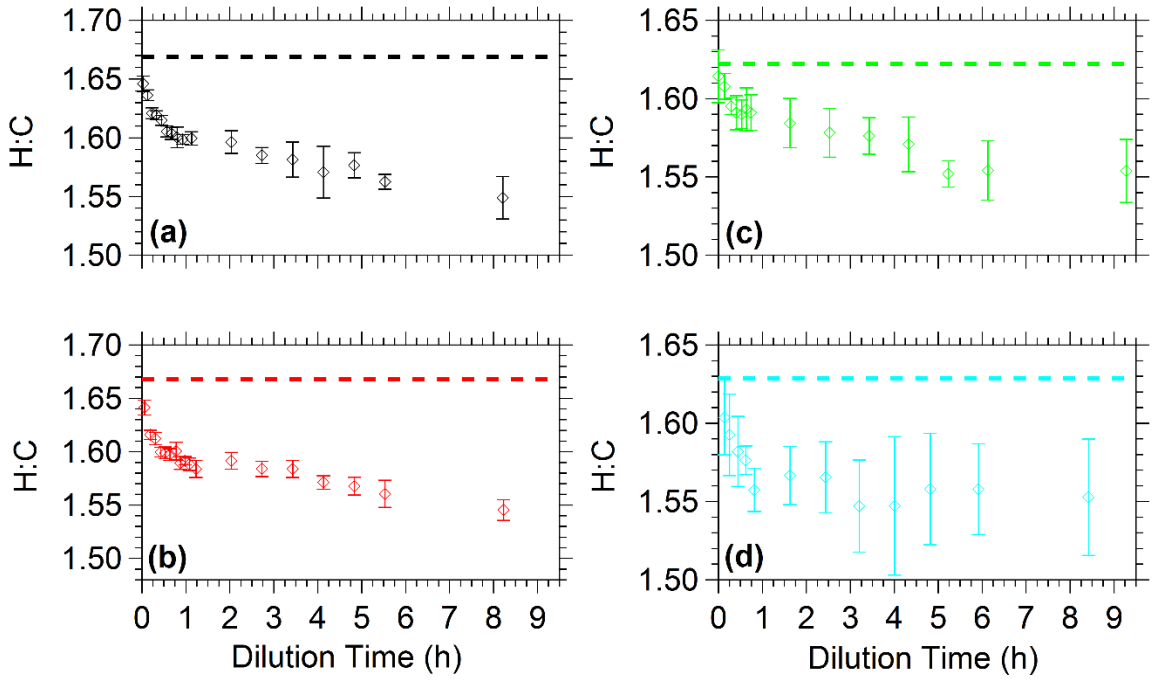

Figure C.11. Average H:C ratios in the dilution chamber for Experiment (a) CH1, (b) CH2, (c) CH3, and (d) CH4. The dotted line represents the average H:C ratio in the main chamber just before dilution. The error bars represent one standard deviation of the mean.

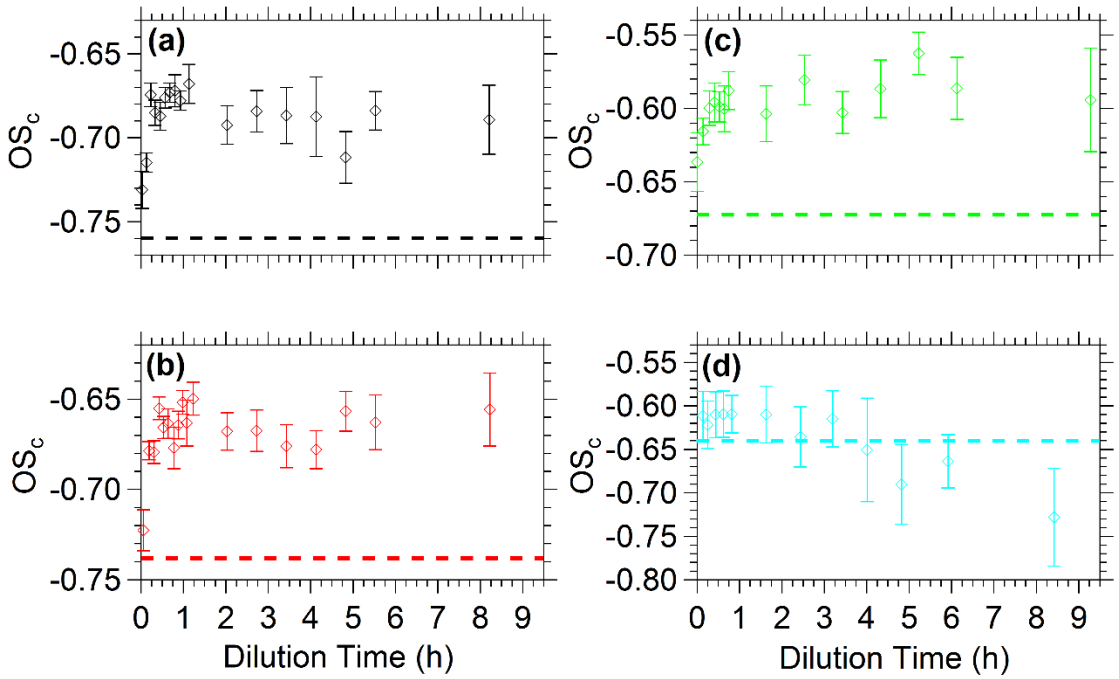

Figure C.12. The average OS_c in the dilution chamber for Experiment (a) CH1, (b) CH2, (c) CH3, and (d) CH4. The dotted line represents the average OS_c in the main chamber just before dilution. The error bars represent one standard deviation of the mean.

Appendix D

Supplementary information for Chapter 4

D1 Model results with and without vapor-phase wall-losses

Both versions of the model (with and without vapor-phase wall-losses) were able to reproduce the experimental results with only minor deviations. Examples from Experiments AP1, LM1, and CH1 showing the results from both models are shown in Figs. D.1, D.2, and D.3, respectively. The fits from both versions of the model were nearly identical with deviations of less than a few percent. In addition, the volatility distribution estimates were almost the same. As noted in Cain et al. (2020), the model that accounts for vapor wall-losses decreases the overall SOA volatility because it attributes more of the evaporation in the dilution chamber to more volatile SOA components. Furthermore, we minimized the time in the dilution chamber to avoid vapor wall-losses playing a major role. Therefore, we only used the results from the model that does not account for vapor-phase wall-losses for our analysis.

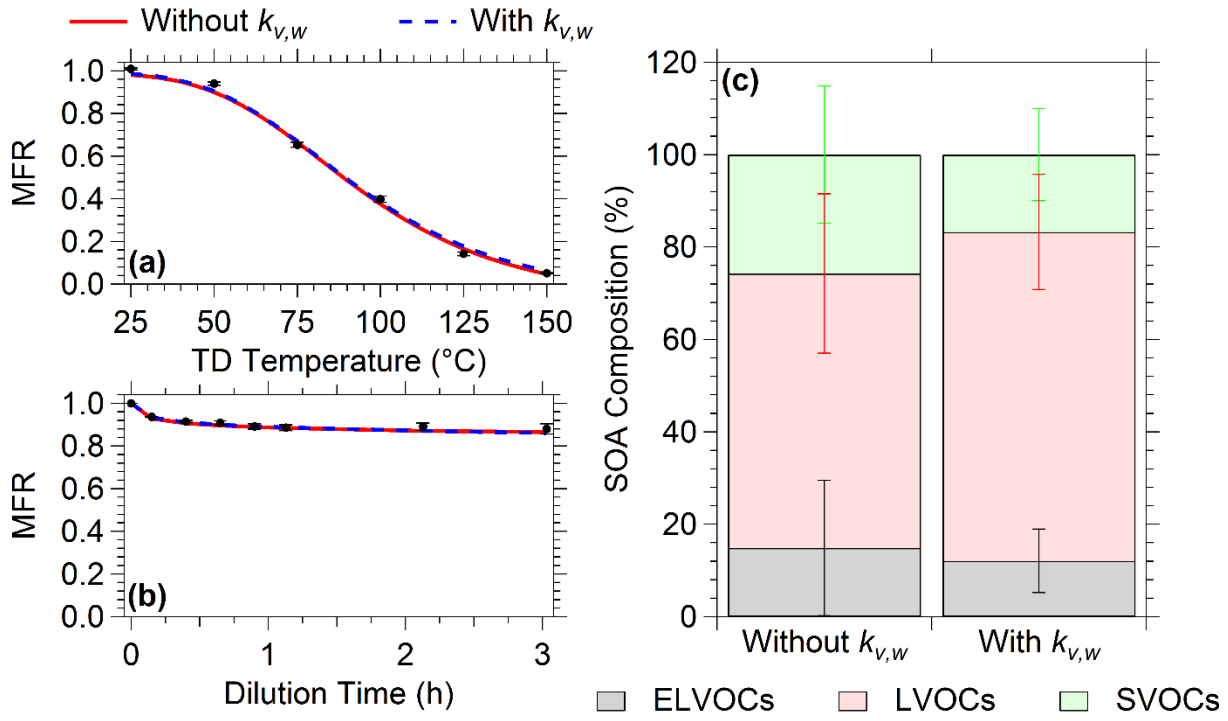

Figure D.1. The (a) thermogram and (b) areogram for Experiment AP1 with fits from the model with (blue dashed line) and without (red solid line) vapor wall-losses. The error bars in (a) represent one standard deviation of the mean MFR while the error bars in (b) represent the uncertainty resulting from correcting for particle wall-losses. (c) SOA composition for Experiment AP1 along with their uncertainties (± one standard deviation) from the model with and without vapor wall-losses. The ELVOCs are shown in grey, LVOCs in red, and SVOCs in green. The uncertainties for the ELVOCs, LVOCs, and SVOCs are shown in black, red, and green respectively.

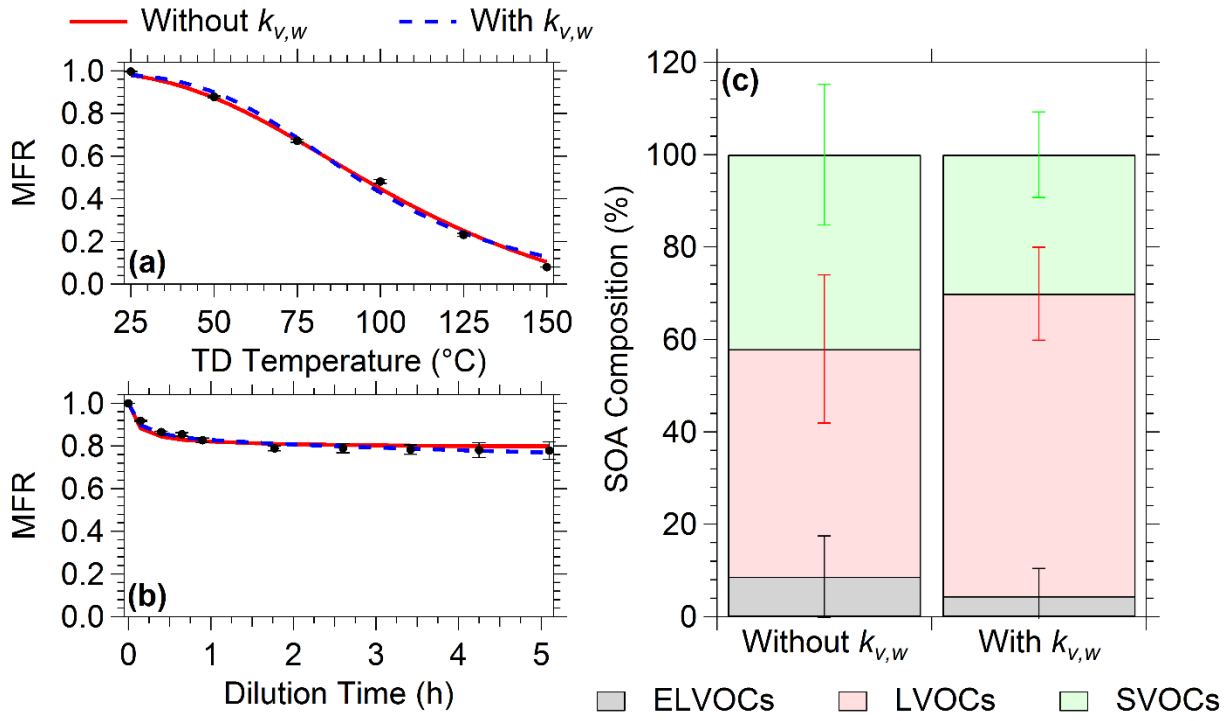

Figure D.2. The (a) thermogram and (b) areogram for Experiment LM1 with fits from the model with (blue dashed line) and without (red solid line) vapor wall-losses. The error bars in (a) represent one standard deviation of the mean MFR while the error bars in (b) represent the uncertainty resulting from correcting for particle wall-losses. (c) SOA composition for Experiment LM1 along with their uncertainties (± one standard deviation) from the model with and without vapor wall-losses. The ELVOCs are shown in grey, LVOCs in red, and SVOCs in green. The uncertainties for the ELVOCs, LVOCs, and SVOCs are shown in black, red, and green respectively.

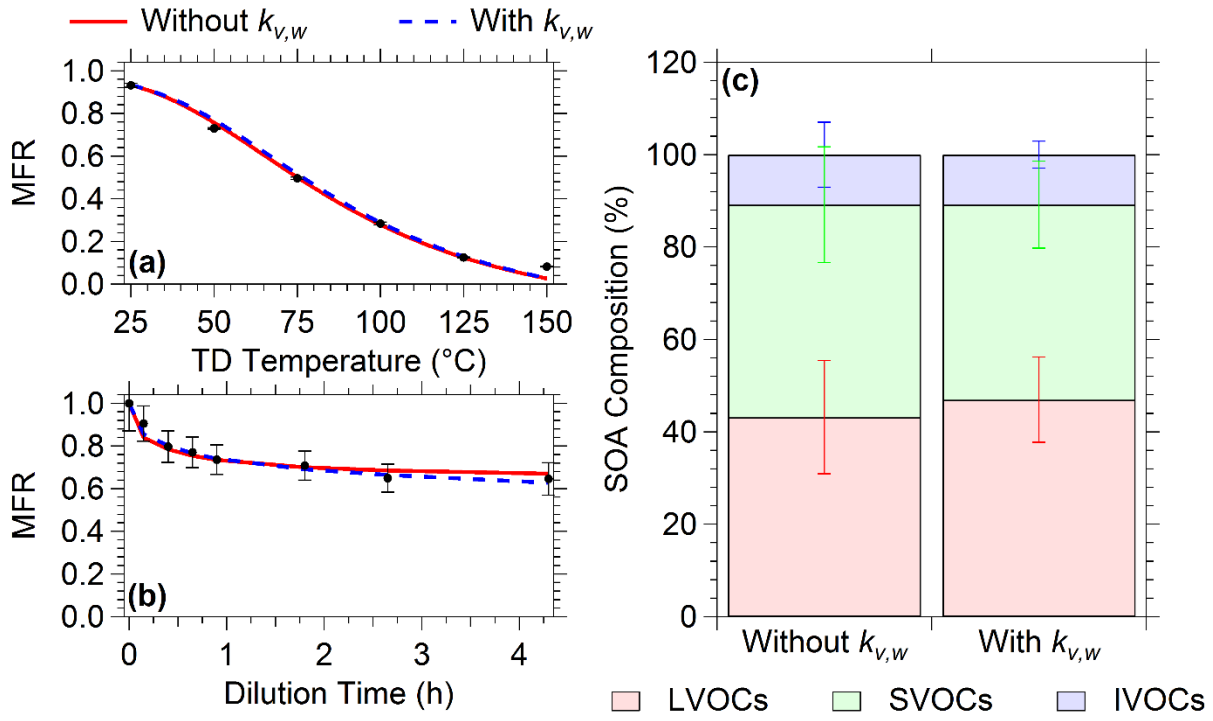

Figure D.3. The (a) thermogram and (b) areogram for Experiment CH1 with fits from the model with (blue dashed line) and without (red solid line) vapor wall-losses. The error bars in (a) represent one standard deviation of the mean MFR while the error bars in (b) represent the uncertainty resulting from correcting for particle wall-losses and pump losses. (c) SOA composition for Experiment CH1 along with their uncertainties (± one standard deviation) from the model with and without vapor wall-losses. The LVOCs are shown in red, SVOCs in green, and IVOCs in blue. The uncertainties for the LVOCs, SVOCs, and IVOCs are shown in red, green, and blue respectively.

D2 System test with ammonium sulfate

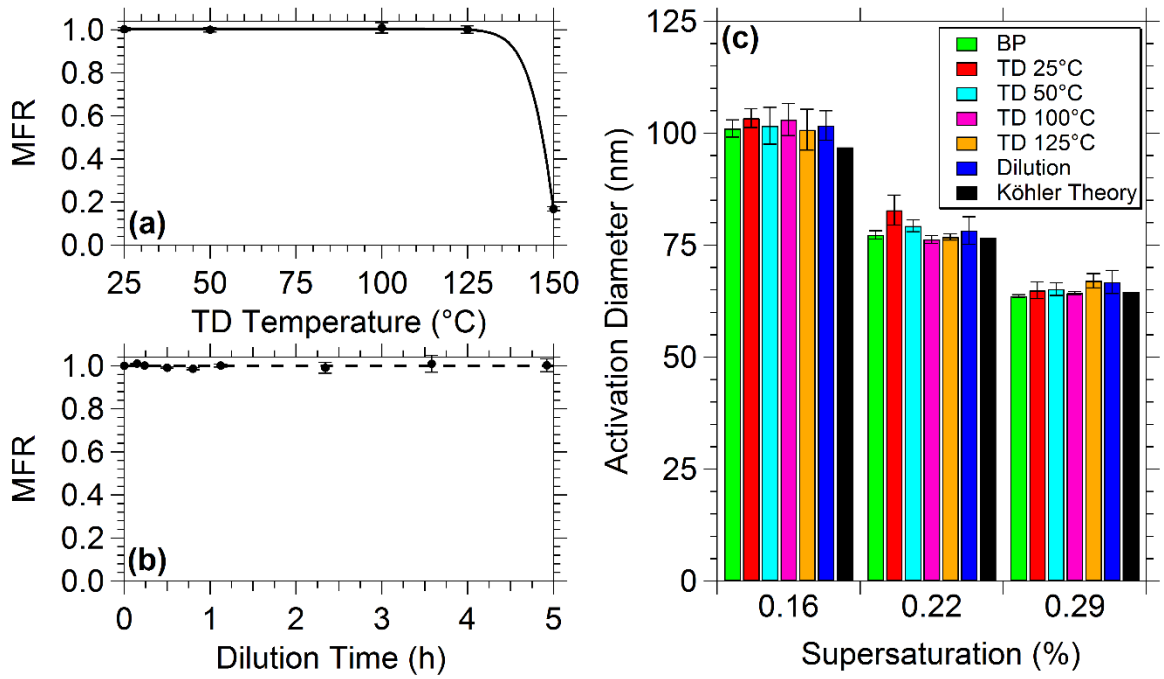

Figure D.4. The (a) thermogram and (b) areogram for the ammonium sulfate particles. The error bars in (a) represent one standard deviation of the mean MFR while the error bars in (b) represent the uncertainty that results from correcting for particle wall-losses. (c) The activation diameter measured at three CCNC supersaturations for the BP (green), four TD temperatures (red, light blue, magenta, and orange), dilution chamber (dark blue), and Köhler theory (black) for the ammonium sulfate particles. The error bars represent one standard deviation of the mean activation diameter. The Köhler theory bar was calculated assuming a surface tension of 0.072 J m^{-2} at 25°C.

D3 SOA experiments

D3.1 α-Pinene ozonolysis SOA

D3.1.1 Experiment AP1

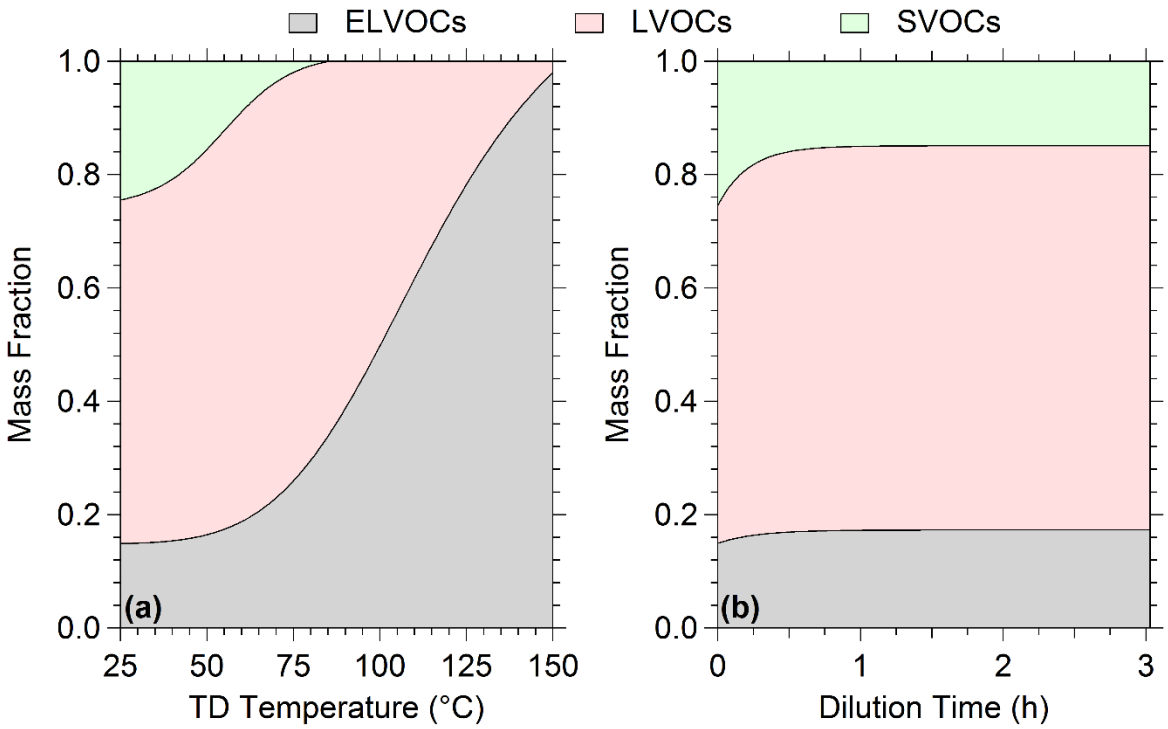

Figure D.5. The estimated mass fraction in the particulate-phase of Experiment AP1 for SVOCs (green), LVOCs (red), and ELVOCs (grey) as a function of (a) TD temperature and (b) dilution time.

D3.1.2 Experiment AP2

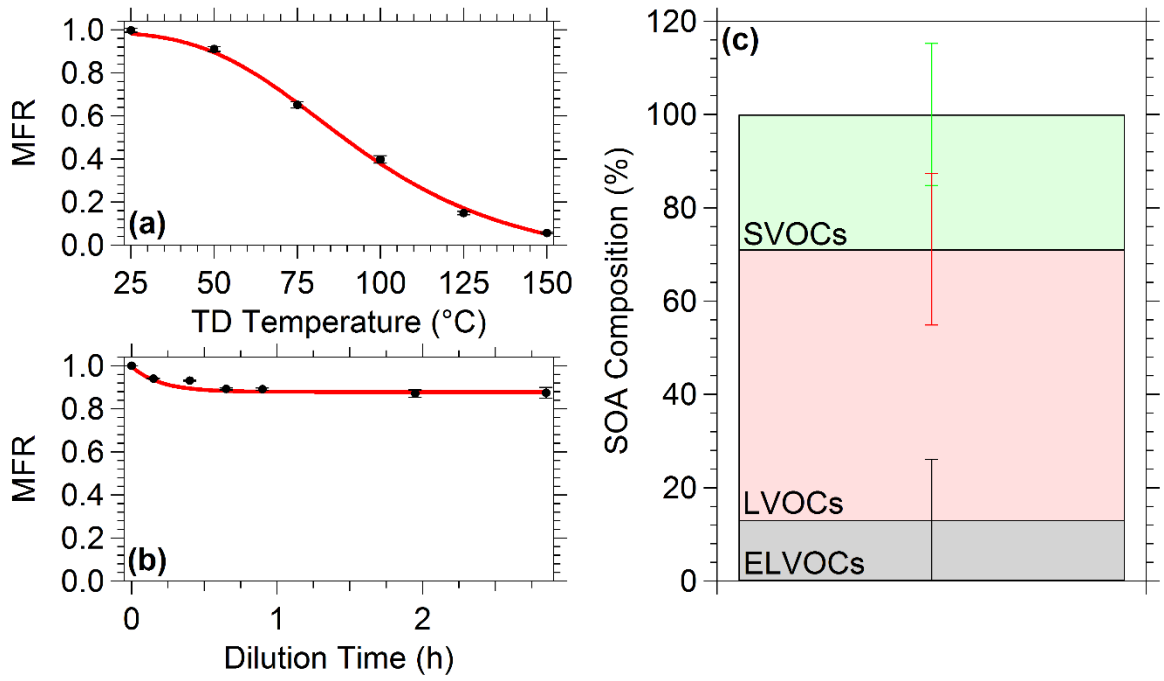

Figure D.6. The (a) thermogram and (b) areogram for Experiment AP2 with fits from the model (red line). The error bars in (a) represent one standard deviation of the mean MFR while the error bars in (b) represent the uncertainty resulting from correcting for particle wall-losses. (c) SOA composition for Experiment AP2 along with their uncertainties (± one standard deviation) from the model. The ELVOCs are shown in grey, LVOCs in red, and SVOCs in green. The uncertainties for the ELVOCs, LVOCs, and SVOCs are shown in black, red, and green respectively.

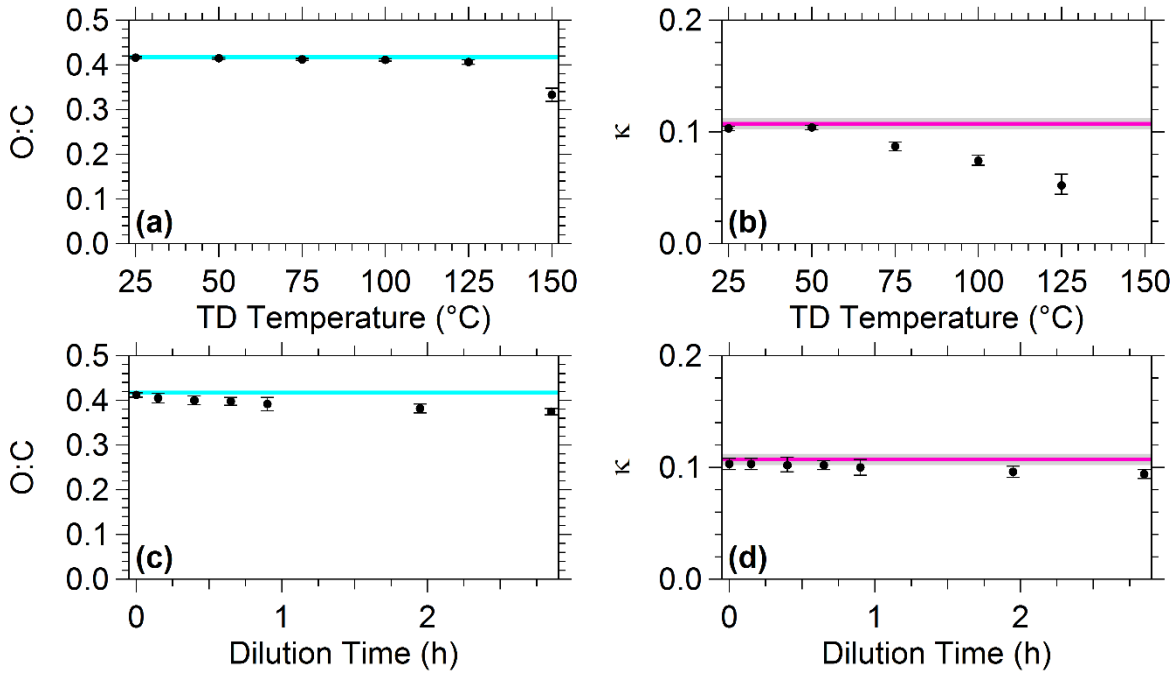

Figure D.7. The average (a) O:C and (b) κ as a function of TD temperature for Experiment AP2. The average (c) O:C and (d) κ as a function of dilution time. The error bars represent one standard deviation of the mean O:C or κ. Also shown are the average O:C (blue line) and κ (magenta line) along with ± one standard deviation (grey area) of the mean measured in the main chamber during Experiment AP2.

D3.1.3 Experiment AP3

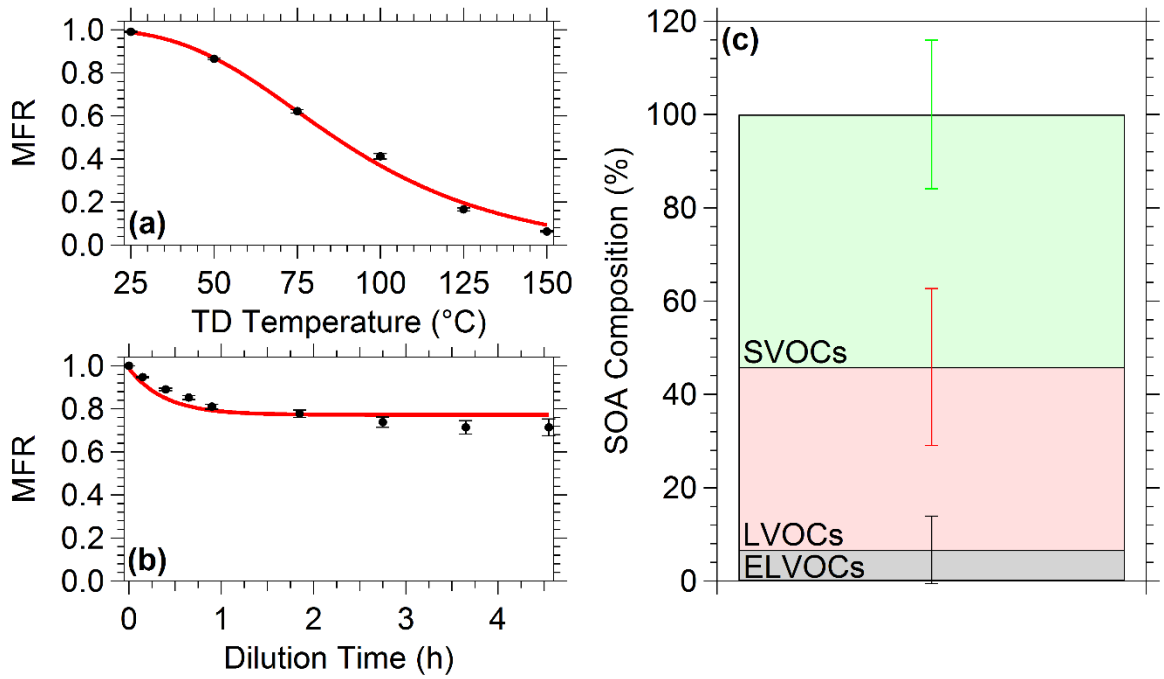

Figure D.8. The (a) thermogram and (b) areogram for Experiment AP3 with fits from the model (red line). The error bars in (a) represent one standard deviation of the mean MFR while the error bars in (b) represent the uncertainty resulting from correcting for particle wall-losses. (c) SOA composition for Experiment AP3 along with their uncertainties (± one standard deviation) from the model. The ELVOCs are shown in grey, LVOCs in red, and SVOCs in green. The uncertainties for the ELVOCs, LVOCs, and SVOCs are shown in black, red, and green respectively.

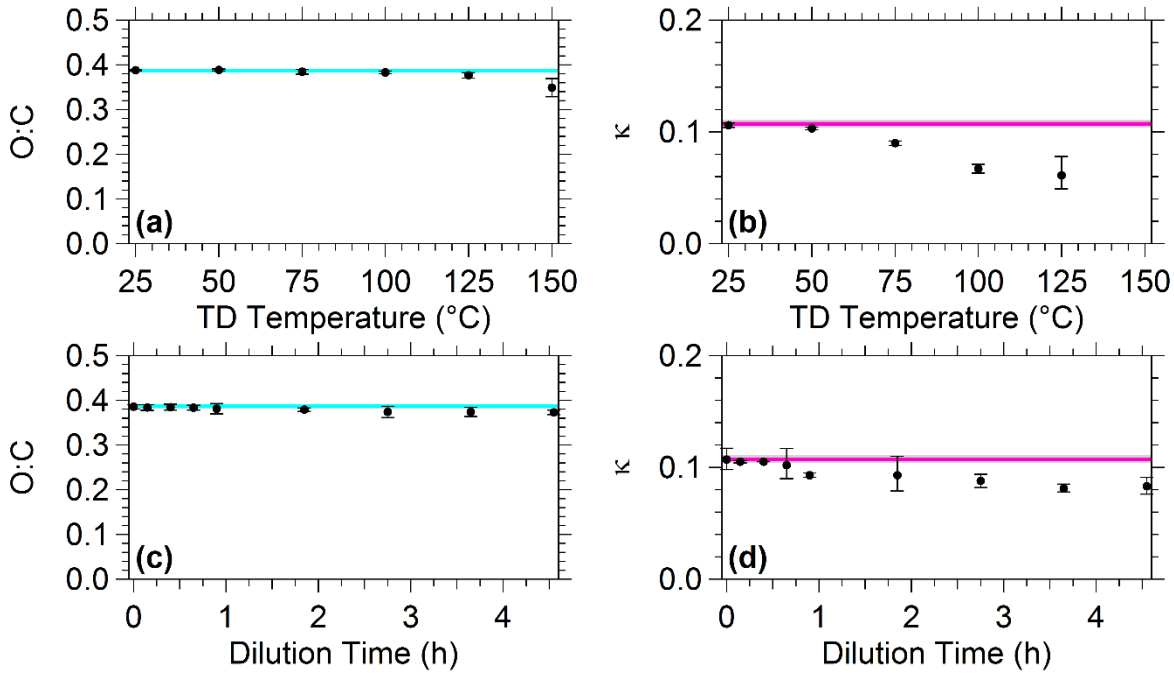

Figure D.9. The average (a) O:C and (b) κ as a function of TD temperature for Experiment AP3. The average (c) O:C and (d) κ as a function of dilution time. The error bars represent one standard deviation of the mean O:C or κ. Also shown are the average O:C (blue line) and κ (magenta line) along with ± one standard deviation (grey area) of the mean measured in the main chamber during Experiment AP3.

D3.1.4 Experiment AP4

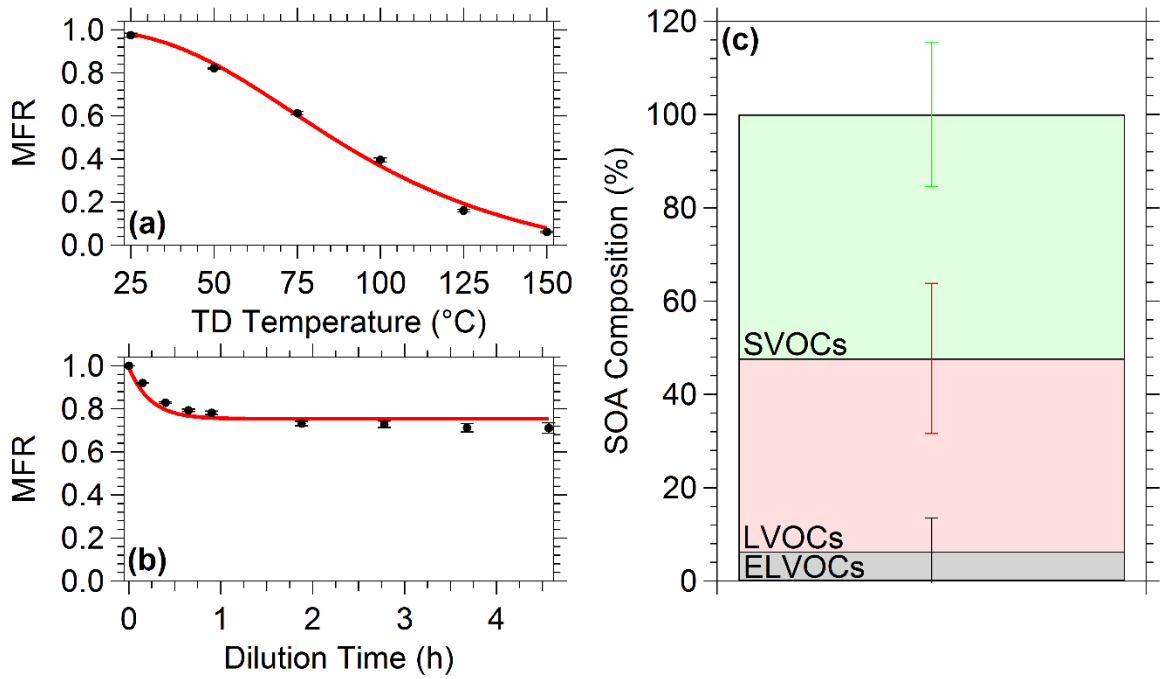

Figure D.10. The (a) thermogram and (b) areogram for Experiment AP4 with fits from the model (red line). The error bars in (a) represent one standard deviation of the mean MFR while the error bars in (b) represent the uncertainty resulting from correcting for particle wall-losses. (c) SOA composition for Experiment AP4 along with their uncertainties (± one standard deviation) from the model. The ELVOCs are shown in grey, LVOCs in red, and SVOCs in green. The uncertainties for the ELVOCs, LVOCs, and SVOCs are shown in black, red, and green respectively.

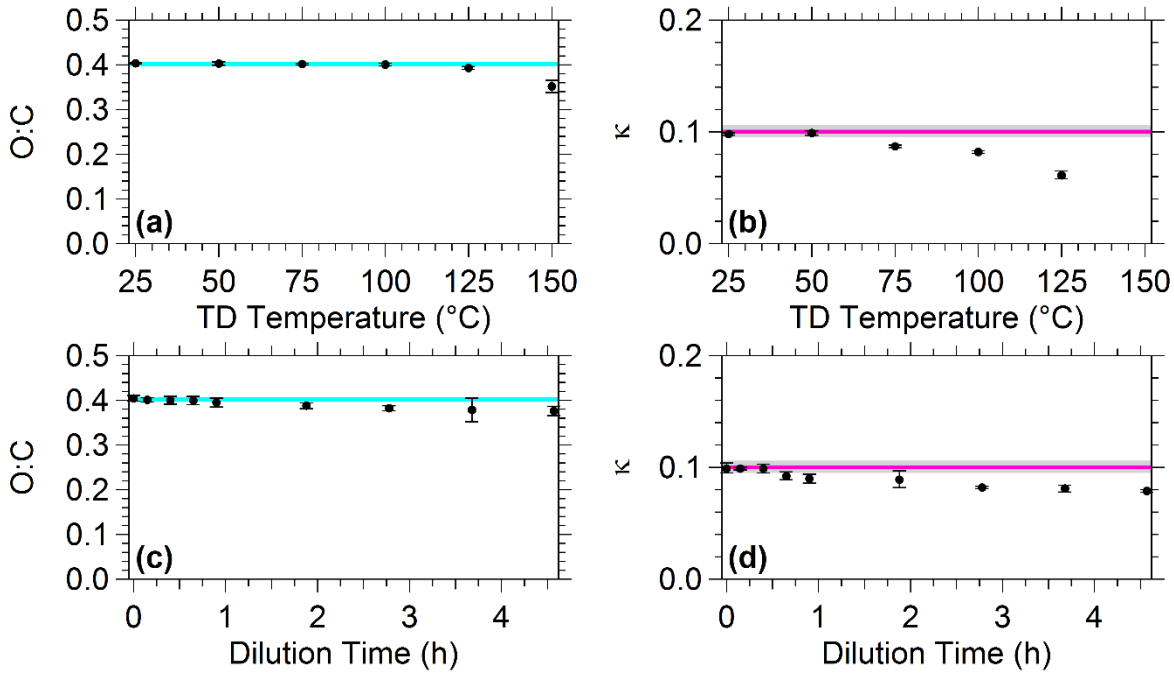

Figure D.11. The average (a) O:C and (b) κ as a function of TD temperature for Experiment AP4. The average (c) O:C and (d) κ as a function of dilution time. The error bars represent one standard deviation of the mean O:C or κ. Also shown are the average O:C (blue line) and κ (magenta line) along with ± one standard deviation (grey area) of the mean measured in the main chamber during Experiment AP4.

D3.2 Limonene ozonolysis SOA

D3.2.1 Experiment LM1

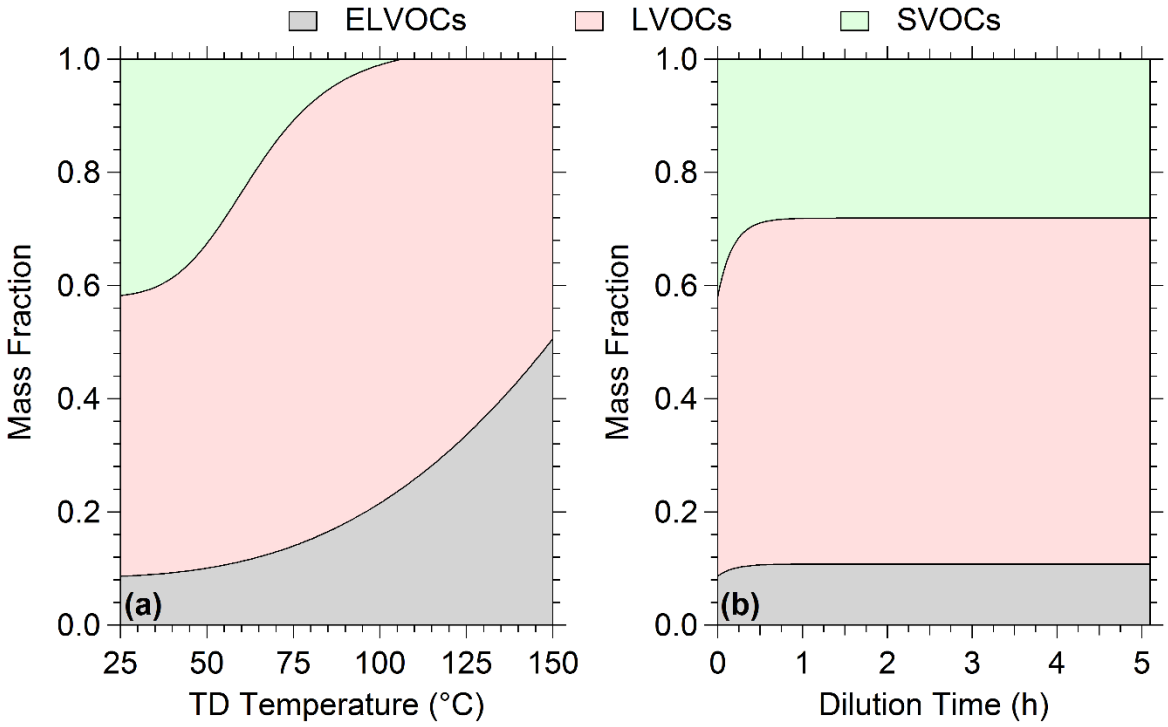

Figure D.12. The estimated mass fraction in the particulate-phase of Experiment LM1 for SVOCs (green), LVOCs (red), and ELVOCs (grey) as a function of (a) TD temperature and (b) dilution time.

D3.2.2 Experiment LM2

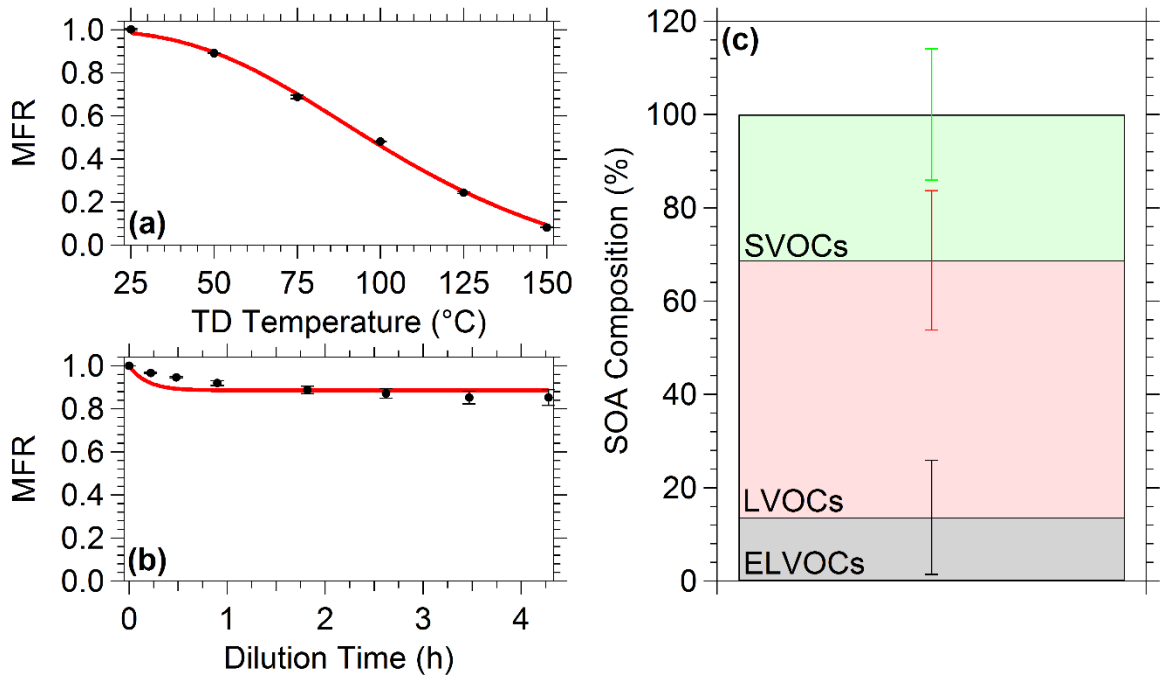

Figure D.13. The (a) thermogram and (b) areogram for Experiment LM2 with fits from the model (red line). The error bars in (a) represent one standard deviation of the mean MFR while the error bars in (b) represent the uncertainty resulting from correcting for particle wall-losses. (c) SOA composition for Experiment LM2 along with their uncertainties (± one standard deviation) from the model. The ELVOCs are shown in grey, LVOCs in red, and SVOCs in green. The uncertainties for the ELVOCs, LVOCs, and SVOCs are shown in black, red, and green respectively.

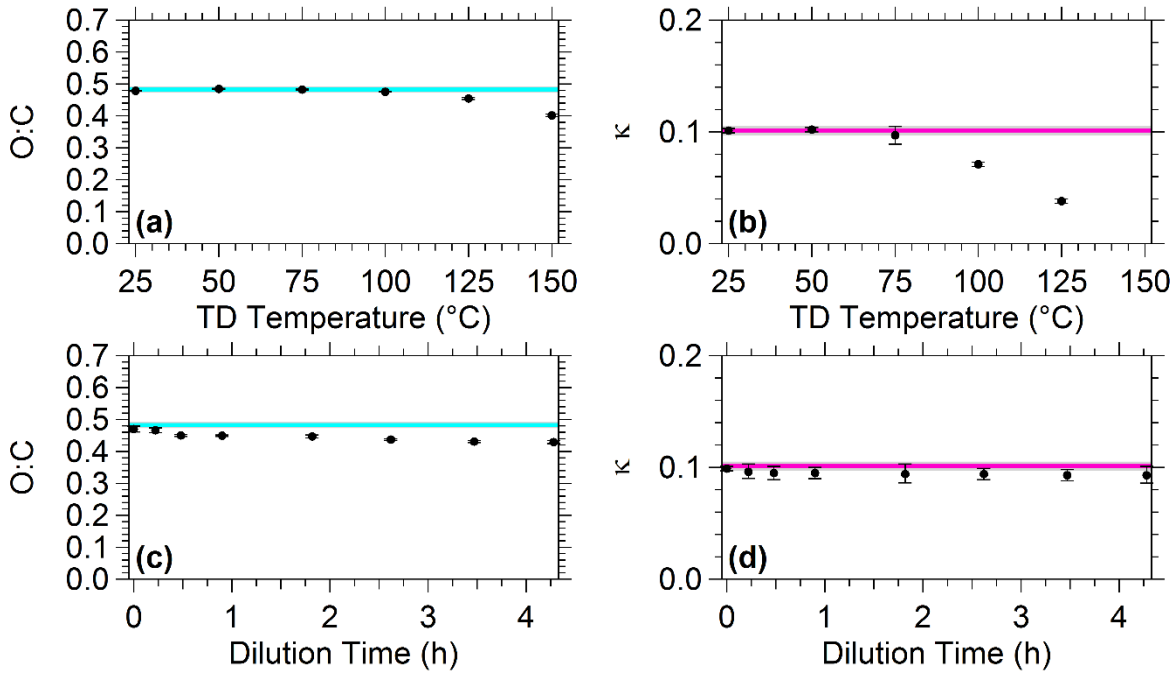

Figure D.14. The average (a) O:C and (b) κ as a function of TD temperature for Experiment LM2. The average (c) O:C and (d) κ as a function of dilution time. The error bars represent one standard deviation of the mean O:C or κ. Also shown are the average O:C (blue line) and κ (magenta line) along with ± one standard deviation (grey area) of the mean measured in the main chamber during Experiment LM2.

D3.2.3 Experiment LM3

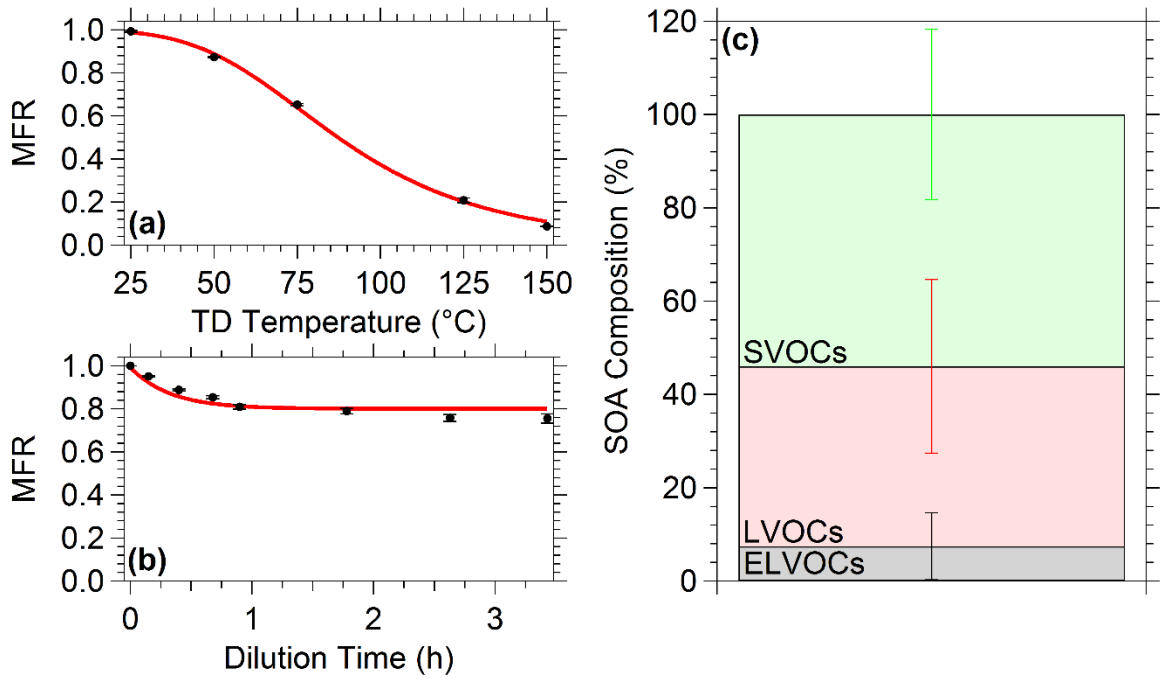

Figure D.15. The (a) thermogram and (b) areogram for Experiment LM3 with fits from the model (red line). The error bars in (a) represent one standard deviation of the mean MFR while the error bars in (b) represent the uncertainty resulting from correcting for particle wall-losses. (c) SOA composition for Experiment LM3 along with their uncertainties (± one standard deviation) from the model. The ELVOCs are shown in grey, LVOCs in red, and SVOCs in green. The uncertainties for the ELVOCs, LVOCs, and SVOCs are shown in black, red, and green respectively.

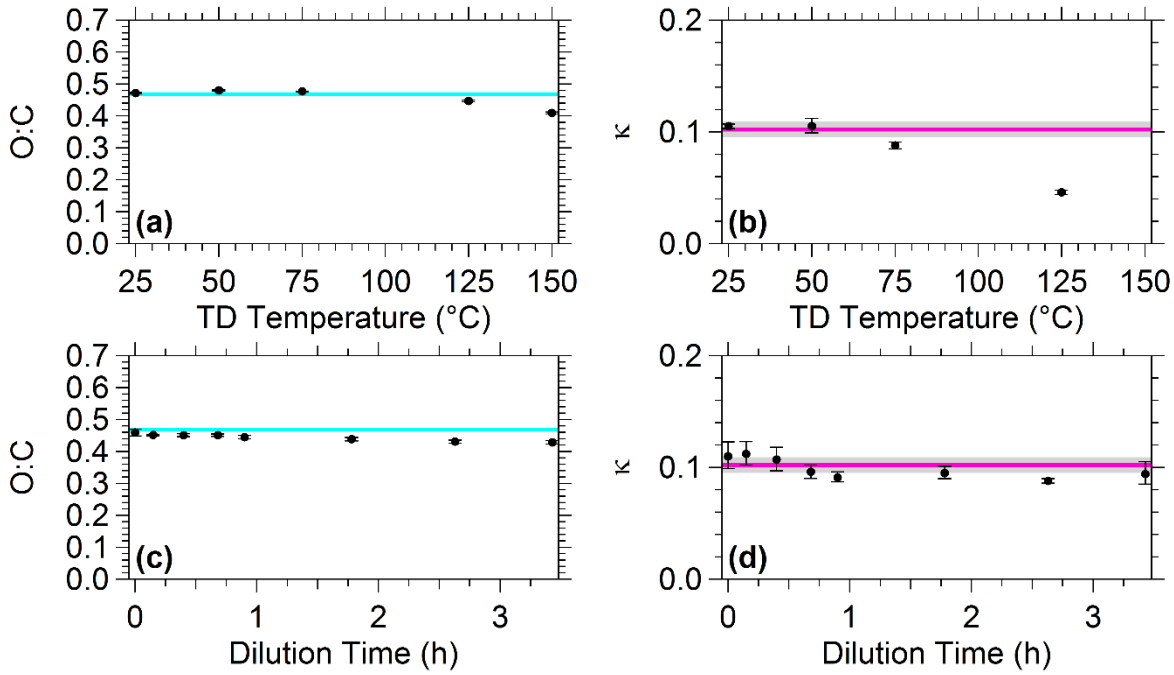

Figure D.16. The average (a) O:C and (b) κ as a function of TD temperature for Experiment LM3. The average (c) O:C and (d) κ as a function of dilution time. The error bars represent one standard deviation of the mean O:C or κ. Also shown are the average O:C (blue line) and κ (magenta line) along with ± one standard deviation (grey area) of the mean measured in the main chamber during Experiment LM3.

D3.3 Cyclohexene ozonolysis SOA

D3.3.1 Experiment CH1

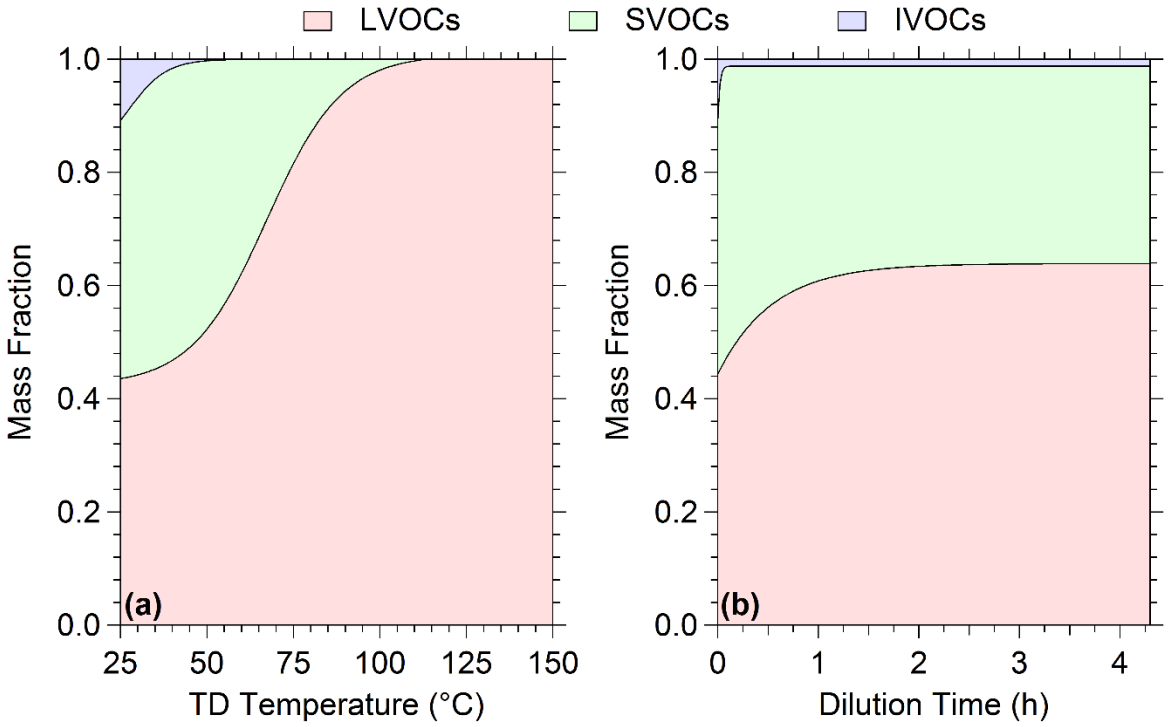

Figure D.17. The estimated mass fraction in the particulate-phase of Experiment CH1 for IVOCs (blue), SVOCs (green), and LVOCs (red) as a function of (a) TD temperature and (b) dilution time.

D3.3.2 Experiment CH2

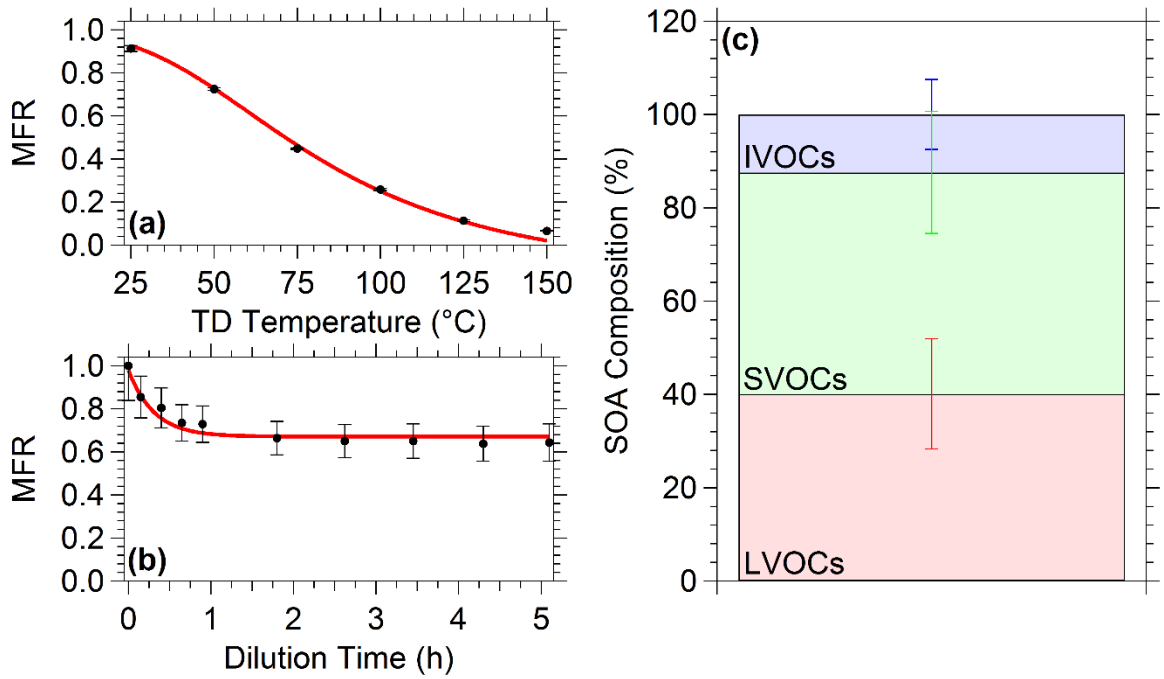

Figure D.18. The (a) thermogram and (b) areogram for Experiment CH2 with fits from the model (red line). The error bars in (a) represent one standard deviation of the mean MFR while the error bars in (b) represent the uncertainty resulting from correcting for particle wall-losses and pump losses. (c) SOA composition for Experiment CH2 along with their uncertainties (± one standard deviation) from the model. The LVOCs are shown in red, SVOCs in green, and IVOCs in blue. The uncertainties for the LVOCs, SVOCs, and IVOCs are shown in red, green, and blue respectively.

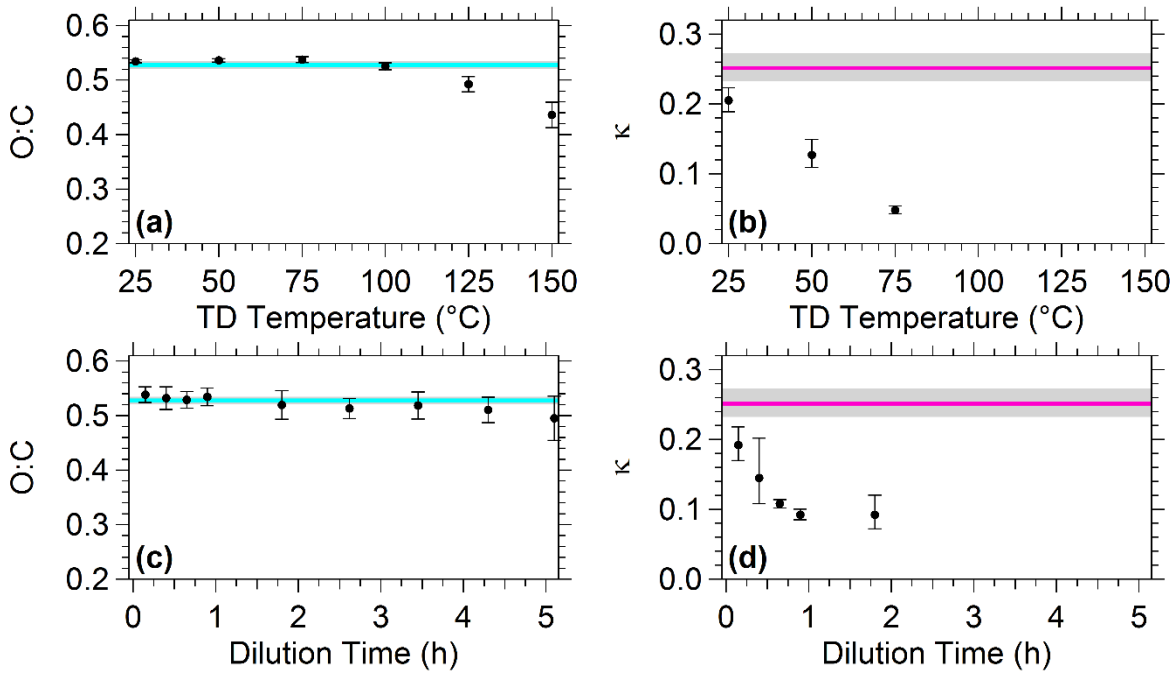

Figure D.19. The average (a) O:C and (b) κ as a function of TD temperature for Experiment CH2. The average (c) O:C and (d) κ as a function of dilution time. The error bars represent one standard deviation of the mean O:C or κ. Also shown are the average O:C (blue line) and κ (magenta line) along with ± one standard deviation (grey area) of the mean measured in the main chamber during Experiment CH2.

D3.3.3 Experiment CH3

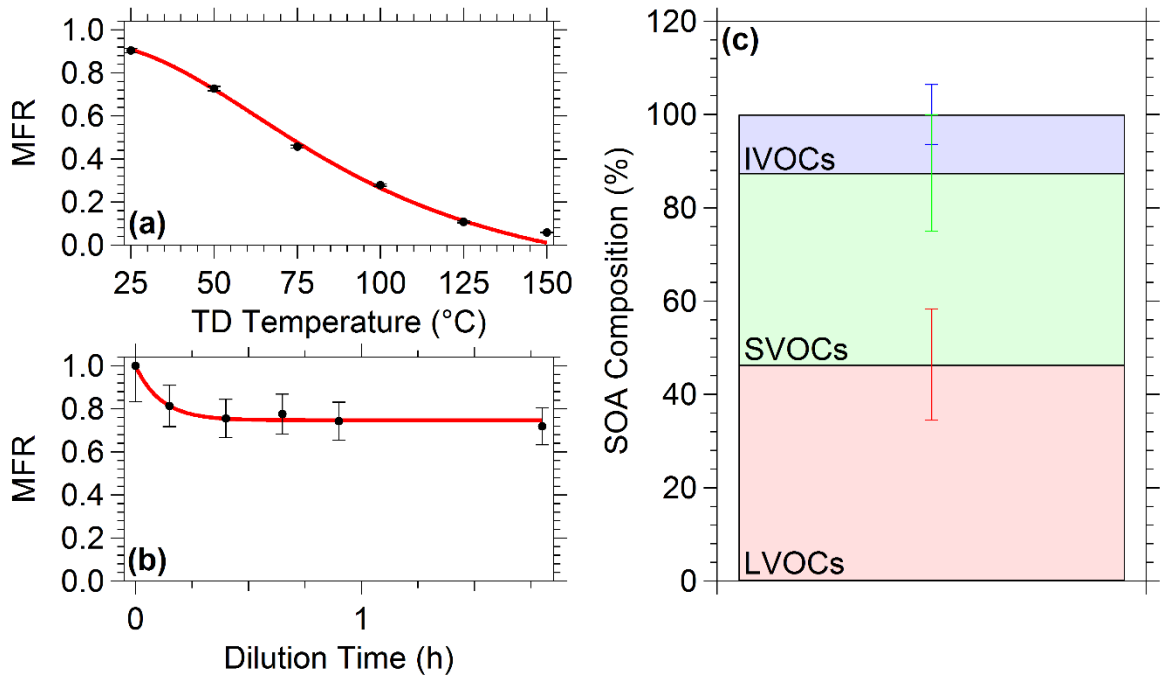

Figure D.20. The (a) thermogram and (b) areogram for Experiment CH3 with fits from the model (red line). The error bars in (a) represent one standard deviation of the mean MFR while the error bars in (b) represent the uncertainty resulting from correcting for particle wall-losses and pump losses. (c) SOA composition for Experiment CH3 along with their uncertainties (± one standard deviation) from the model. The LVOCs are shown in red, SVOCs in green, and IVOCs in blue. The uncertainties for the LVOCs, SVOCs, and IVOCs are shown in red, green, and blue respectively.

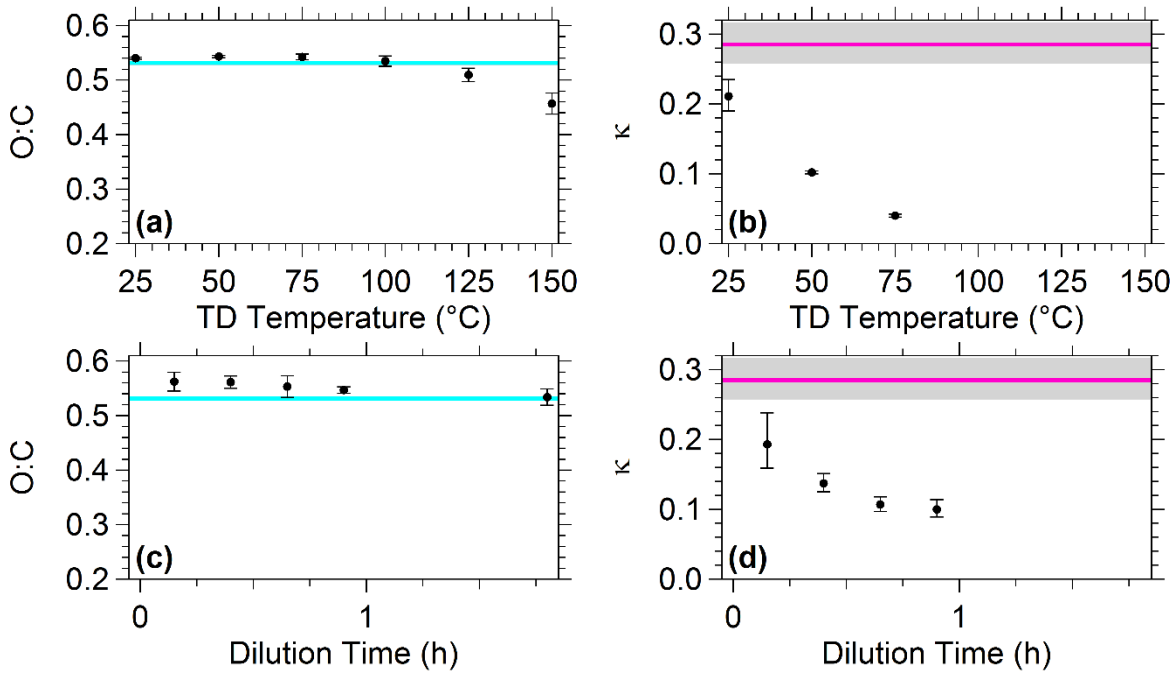

Figure D.21. The average (a) O:C and (b) κ as a function of TD temperature for Experiment CH3. The average (c) O:C and (d) κ as a function of dilution time. The error bars represent one standard deviation of the mean O:C or κ. Also shown are the average O:C (blue line) and κ (magenta line) along with ± one standard deviation (grey area) of the mean measured in the main chamber during Experiment CH3.

D3.3.4 Experiment CH4

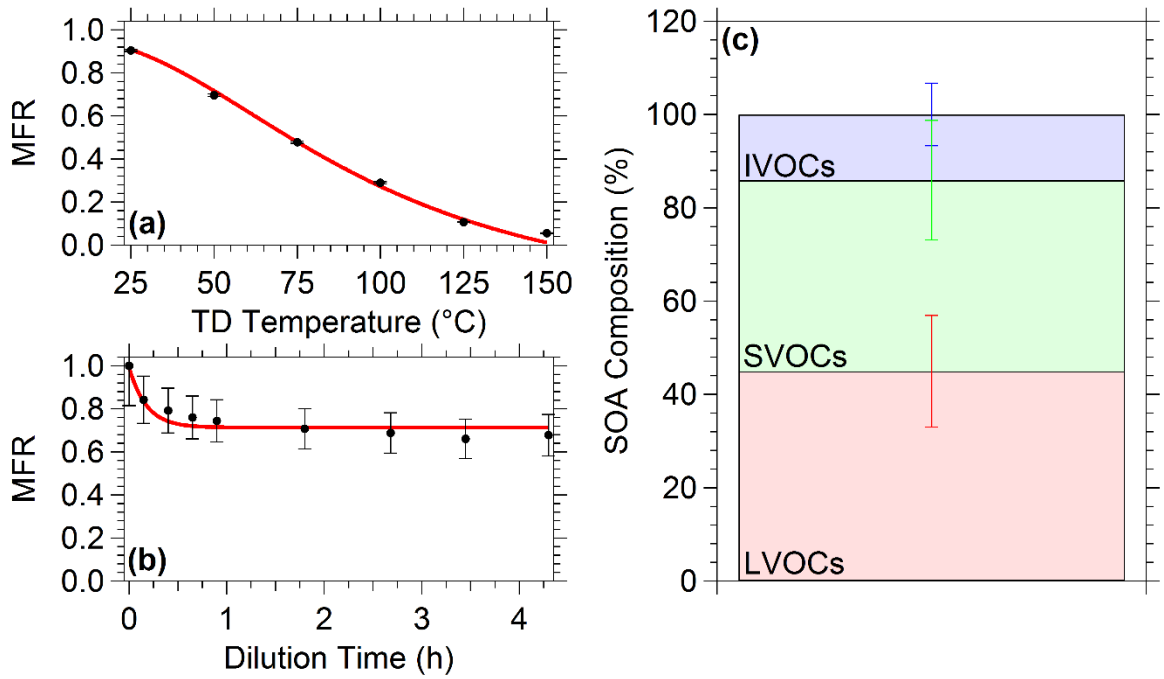

Figure D.22. The (a) thermogram and (b) areogram for Experiment CH4 with fits from the model (red line). The error bars in (a) represent one standard deviation of the mean MFR while the error bars in (b) represent the uncertainty resulting from correcting for particle wall-losses and pump losses. (c) SOA composition for Experiment CH4 along with their uncertainties (± one standard deviation) from the model. The LVOCs are shown in red, SVOCs in green, and IVOCs in blue. The uncertainties for the LVOCs, SVOCs, and IVOCs are shown in red, green, and blue respectively.

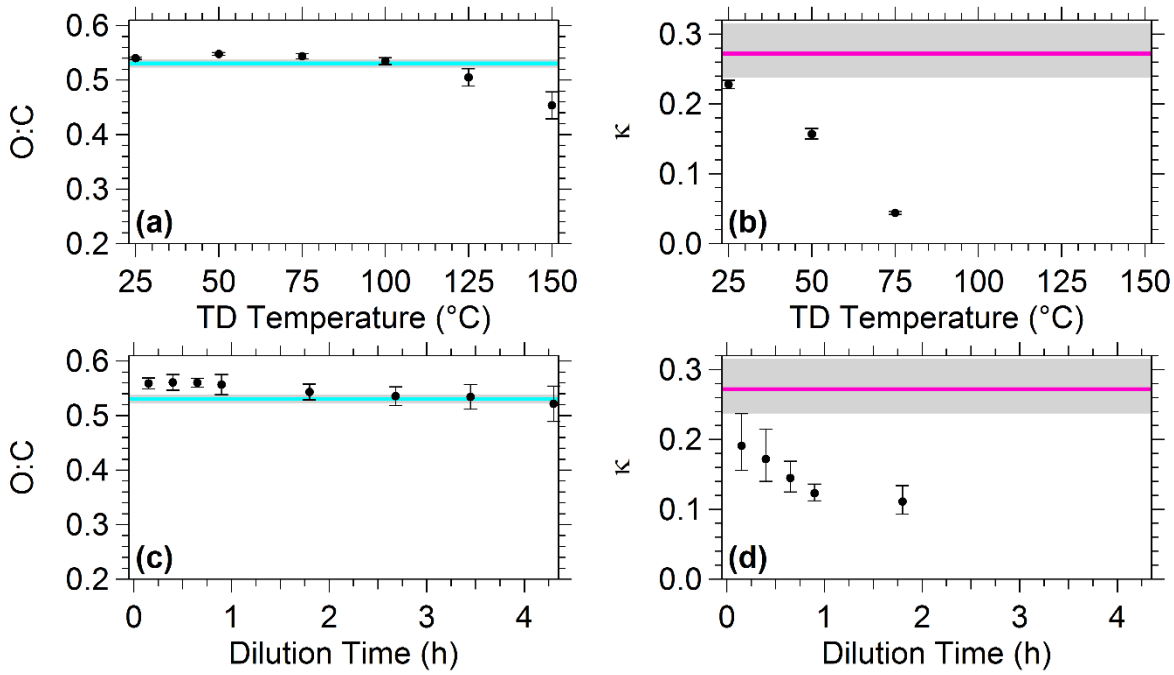

Figure D.23. The average (a) O:C and (b) κ as a function of TD temperature for Experiment CH4. The average (c) O:C and (d) κ as a function of dilution time. The error bars represent one standard deviation of the mean O:C or κ. Also shown are the average O:C (blue line) and κ (magenta line) along with ± one standard deviation (grey area) of the mean measured in the main chamber during Experiment CH4.

D3.3.5 Experiment CH5

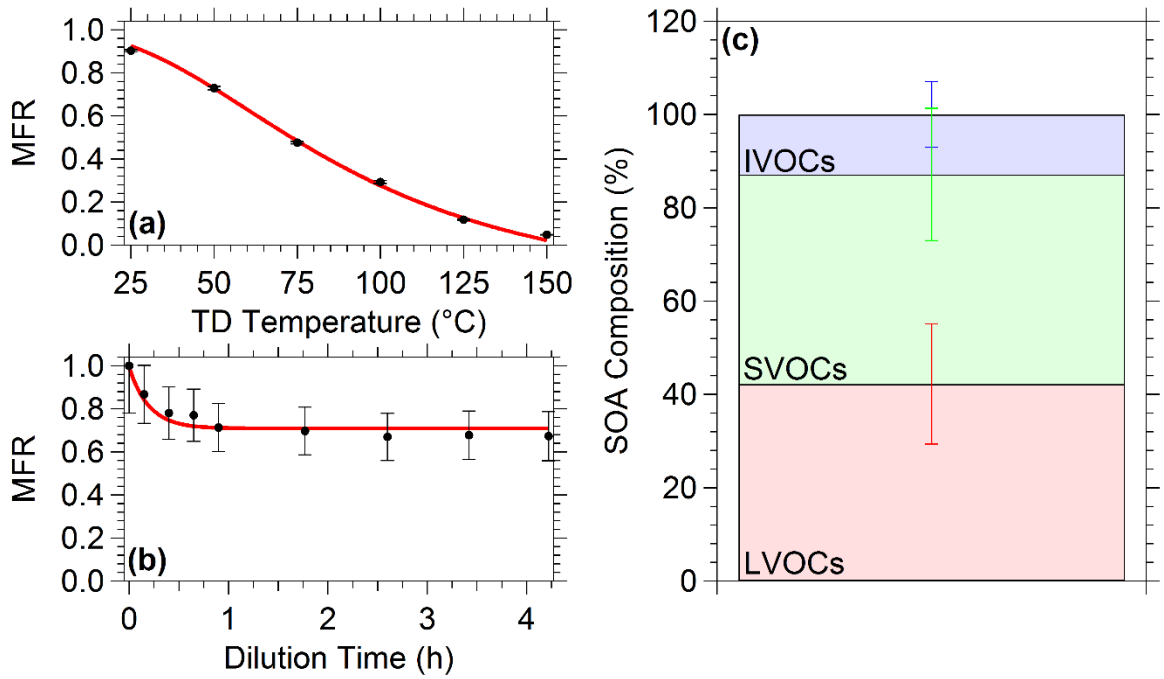

Figure D.24. The (a) thermogram and (b) areogram for Experiment CH5 with fits from the model (red line). The error bars in (a) represent one standard deviation of the mean MFR while the error bars in (b) represent the uncertainty resulting from correcting for particle wall-losses and pump losses. (c) SOA composition for Experiment CH5 along with their uncertainties (± one standard deviation) from the model. The LVOCs are shown in red, SVOCs in green, and IVOCs in blue. The uncertainties for the LVOCs, SVOCs, and IVOCs are shown in red, green, and blue respectively.

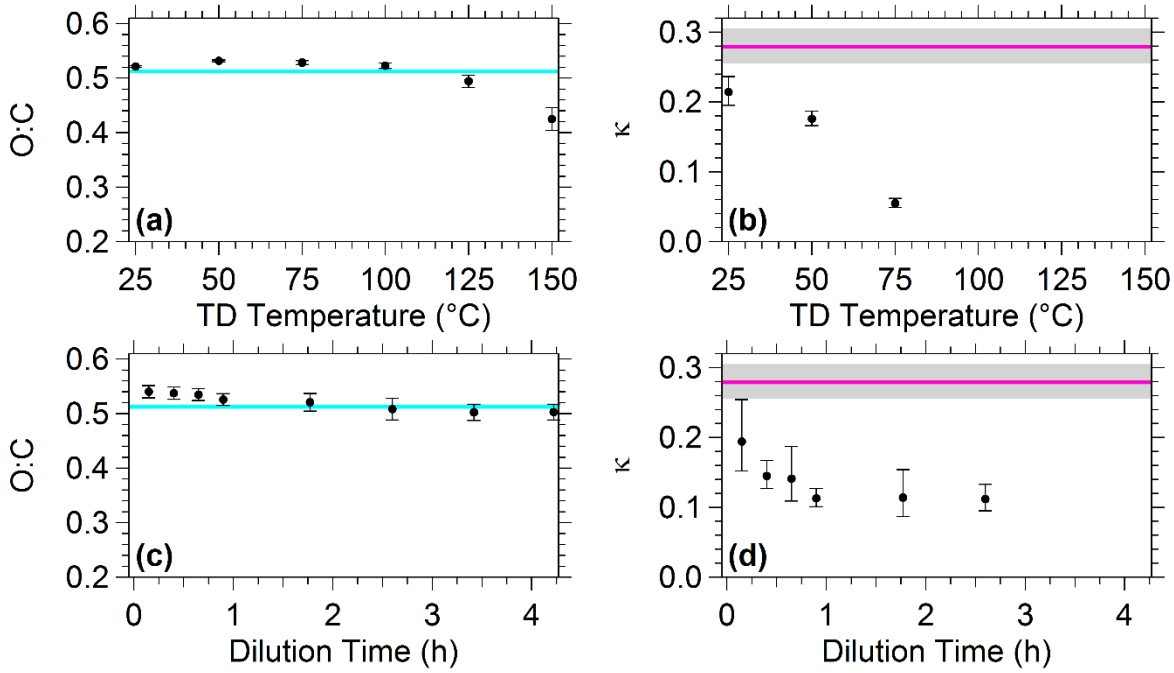

Figure D.25. The average (a) O:C and (b) κ as a function of TD temperature for Experiment CH5. The average (c) O:C and (d) κ as a function of dilution time. The error bars represent one standard deviation of the mean O:C or κ. Also shown are the average O:C (blue line) and κ (magenta line) along with ± one standard deviation (grey area) of the mean measured in the main chamber during Experiment CH5.

Table D.1. Results from the analysis on the initial properties in the dilution chamber.

			Mean Volume Diameter (nm)	
Exp.	**Dilution Ratio**	**Main/Dilution Mass Ratio[a]**	**Main Chamber**	**Dilution Chamber[a]**
CH1	9.13	10.42	240	226
CH2	8.85	10.14	273	259
CH3	11.22	13.69	262	249
CH4	9.00	11.11	276	260
CH5	8.24	9.13	307	282

[a]After correction for pump losses.

D4 Benefit of isothermal dilution measurements

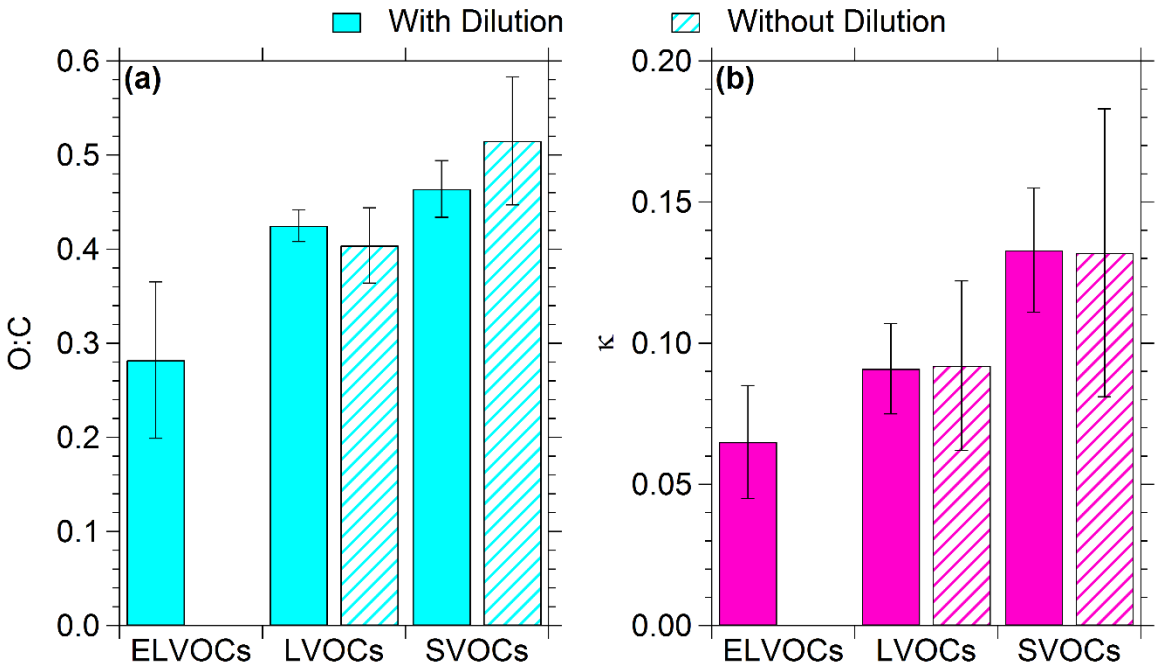

Figure D.26. The (a) O:C and (b) κ distributions as a function of volatility for the α-pinene ozonolysis SOA examined in this study with (solid bars) and without (patterned bars) dilution. The error bars were calculated from the standard deviation that results from determining O:C and κ distributions for each experiment and represent variability between experiments.

Appendix E

Hygroscopicity, oxidation level, and volatility measurements of fresh and aged biomass-burning aerosol

E1 Experimental section

E1.1 Experimental procedure

Smog chamber experiments were conducted in the Air Quality Laboratory (AQL) at Carnegie Mellon University to investigate the physiochemical properties of biomass-burning aerosol (BBA). All experiments were conducted in a 12 m^3 Teflon reactor (Welch Fluorocarbons). Full details on the experimental setup can be found in Jahl et al. (2020). Briefly, a small fuel sample (~0.5 kg) was ignited in the AQL's combustion room and the emissions during the burn were transferred to the smog chamber via two ejector dilutors (Dekati, DI-1000) in parallel. Sawgrass, cutgrass, and ponderosa pine were used as fuels. After the burn was completed, the fresh BBA were characterized with a suite of aerosol instrumentation for roughly 2 h. After characterization of the fresh emissions, the BBA were aged for 3–4 h using three different types of experiments to simulate atmospheric processing. The first type of experiment performed involved the injection of ozone into the smog chamber and aging in the dark. In the second set of experiments, nitrous acid (HONO) was injected and the UV lights were turned on, simulating photochemical aging with OH and other oxidants. Finally, a number of control experiments were performed in the dark without the introduction of any oxidants. The conditions for the 11 experiments examined in this study are summarized in Table E.1.

A differential mobility analyzer (DMA, TSI, model 3081) was coupled with a condensation particle counter (CPC, TSI, model 3072) and a cloud condensation nuclei (CCN) counter (CCNC, Droplet Measurement Technologies) to measure the CCN activity of the BBA. The CPC and CCNC used flow rates of 0.3 and 0.5 L min^{-1} respectively. The sheath flow of the DMA was set to 4 L min^{-1}, with an upscan of 120 s and downscan of 15 s. The CCNC used a variety of water supersaturations (SS) to characterize the aerosol, which are denoted in Table E.1.

Table E.1. Experimental conditions examined in this study.

Exp.	Fuel	CCNC SS (%)	Aging Scheme	Notes
1	Sawgrass 1	0.29, 0.49, 0.69	Control	
2	Sawgrass 2	0.29, 0.49, 0.69	Ozone	
3	Sawgrass 3	0.29, 0.49, 0.69	HONO + UV	TD before injection
4	Sawgrass 4	0.18	HONO + UV	Setup from Cain and Pandis (2017)
5	Cutgrass 1	0.29, 0.49, 0.69	Ozone	
6	Cutgrass 2	0.29, 0.49, 0.69	HONO + UV	TD before injection
7	Cutgrass 3	0.15	Ozone	Setup from Cain and Pandis (2017)
8	Cutgrass 4	0.18	HONO + UV	Setup from Cain and Pandis (2017)
9	Ponderosa Pine 1	0.29, 0.49, 0.69	Control	
10	Ponderosa Pine 2	0.30, 0.40, 0.50	HONO + UV	TD before injection
11	Ponderosa Pine 3	0.55	HONO + UV	Setup from Cain and Pandis (2017)

Experiments 3, 6, and 10 used the thermodenuder (TD) from Cain and Pandis (2017) to evaporate the more volatile fraction of the aerosol before injection into the smog chamber. In these experiments, the TD was set to 250°C and the centerline residence time was 1 s. Experiments 4, 7, 8, and 11 included the experimental setup from Cain and Pandis (2017), which utilizes a TD followed by an Aerodyne soot particle aerosol mass spectrometer (SP-AMS, hereafter AMS) and the DMA coupled with the CPC and CCNC, to characterize the hygroscopicity and oxidation level of the BBA as a function of volatility. In these experiments, the TD used temperatures ranging from 25 to 200°C and a centerline residence time of 23 s.

E1.2 Data analysis

The DMA coupled with the CPC and CCNC were used with the scanning mobility CCN analysis (SMCA) technique (Moore et al., 2010) to generate activation curves, which express the fraction of particles that activate to become cloud droplets as a function of size at a given SS, for every DMA scan. The activation diameter, the diameter at which 50% of the particles activate, was calculated by fitting the activation curves with a sigmodal function for each DMA scan. The

average activation diameter over several DMA scans, $d_{p,50}$, and CCNC SS, s_c, were combined with a parameterization of Köhler theory, referred to as κ-Köhler theory (Petters and Kreidenweis, 2007), to determine the apparent hygroscopicity parameter, κ_{app}, with the following equation:

$$\kappa_{\mathrm{app}} = \frac{4A^3}{27 d_{p,50}^3 \ln^2 s_c} \quad \text{(E.1)}$$

where $A = 4\sigma_{s/a} M_w / RT\rho_w$. $\sigma_{s/a}$ is the surface tension of the solution/air interface, M_w is the molecular weight of water, R is the universal gas constant, T is the temperature, and ρ_w is the density of water. For our calculations, we used the surface tension of water and a temperature of 25°C.

For the experiments with the setup from Cain and Pandis (2017), biomass-burning organic aerosol (BBOA) concentrations were determined from the AMS in V-mode with the laser off and an assumed collection efficiency of unity. The BBOA concentrations through the TD were used to generate thermograms, particle mass fraction remaining (MFR) as a function of TD temperature, by dividing the average BBOA mass concentration in the TD at a certain temperature by the average BBOA mass concentration in the chamber. The TD data were corrected for size and temperature-dependent particle losses following the method in Cain and Pandis (2017). The oxygen-to-carbon ratio (O:C) was also calculated for the BBOA from the AMS in V-mode with the laser off using the method from Canagaratna et al. (2015).

E2 Results and discussion

E2.1 Fresh BBA hygroscopicity

Fig. E.1 displays the average κ_{app} of the fresh and aged BBA for all SS and experiments. The κ_{app} and the corresponding SS for each experiment are shown in Table E.2. The κ_{app} of the

fresh aerosol ranged from 0.07 to 0.95. The κ_{app} of the fresh BBA from ponderosa pine was significantly lower and less variable than the κ_{app} of the fresh BBA from the sawgrass and cutgrass. The κ_{app} of the fresh BBA from ponderosa pine ranged from 0.07 to 0.10 whereas the κ_{app} of the fresh BBA from the grass experiments ranged from 0.21 to 0.95. This is consistent with previous studies examining BBA from evergreens and grasses (Petters et al., 2009; Engelhart et al., 2012), indicating that variations in CCN activity were largely due to the inorganic components of the BBA, which have significantly higher κ values than the organic components (Petters and Kreidenweis, 2007). The non-refractory fraction of the emitted aerosol from the burning of the grasses contained ~25% inorganic components, such as sulfate, nitrate, and chloride (Jahl et al., 2020). On the other hand, the BBA from ponderosa pine was mostly organic and black carbon with small fractions (< 5%) of inorganic components (Jahl et al., 2020). However, since the AMS only measures the non-refractory components of sub-micron particulate matter, more detailed composition information, especially for the refractory inorganic components, is required to determine κ values of the BBOA (Engelhart et al., 2012).

As seen in Fig. E.1, nearly all of the κ_{app} values above 0.6 were from the grass experiments where the TD removed the more volatile fraction from the BBA. In these experiments, the TD decreased the BBOA concentrations in the AMS to around 2 $\mu g\ m^{-3}$ and the BBA was comprised of mostly inorganic components and black carbon (Jahl et al., 2020). However, in Experiment 10, since the inorganic emissions from ponderosa pine were low, the remaining BBA after passing through the TD was not very hygroscopic and did not activate in the CCNC during the fresh characterization phase.

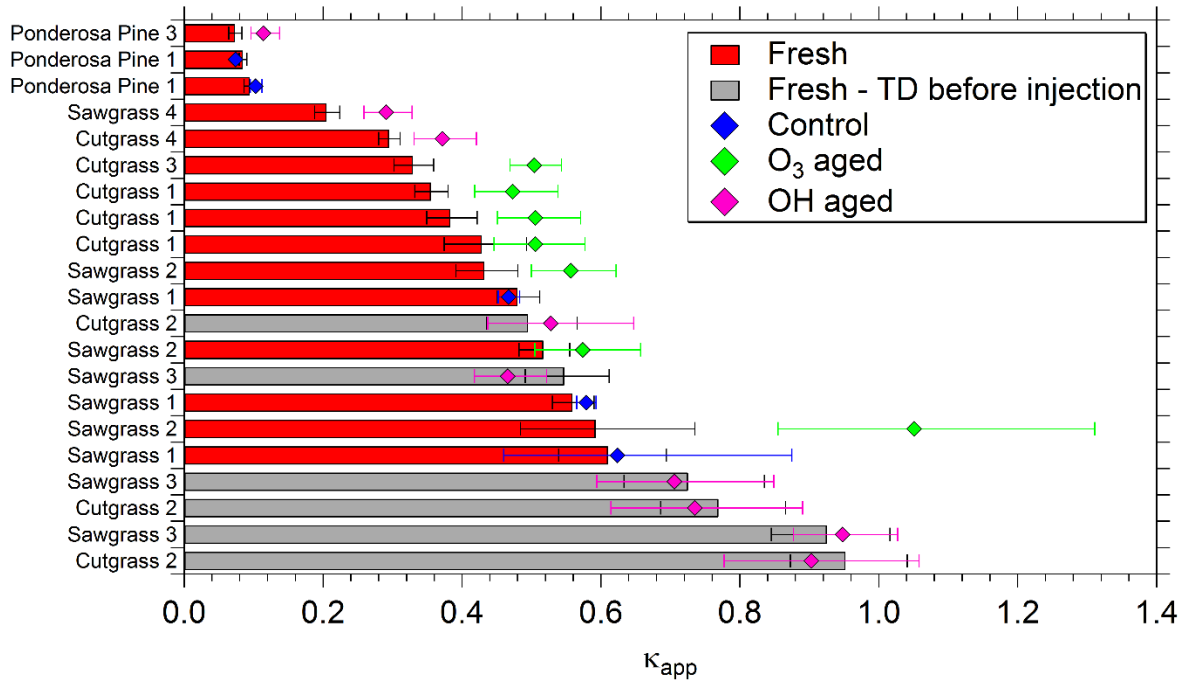

Figure E.1. The κ_{app} of the fresh (bars) and aged (diamonds) BBA from all experiments for all supersaturations (paired SS-κ_{app} values can be found in Table E.2). Grey bars indicate experiments in which the TD was used prior to injection in the chamber. Control experiments are represented by blue diamonds, ozone aging by green diamonds, and hydroxyl radical aging by magenta diamonds. Error bars represent one standard deviation of the average κ_{app}.

The fresh κ_{app} values at different SS in Table E.2 indicate that there were probably variations in composition as a function of size for the BBA because the κ_{app} values varied by SS. This was more pronounced in the grass experiments in which the TD removed the organic components (Experiments 3 and 6). For example, in Experiment 4, the fresh κ_{app} at a SS of 0.18% for sawgrass BBA was 0.21, but, in Experiment 1, the fresh κ_{app} at a SS of 0.69% was 0.61. The lower κ_{app} at the lower SS is indicative of more organic components at larger particle sizes, decreasing CCN activity, but this is not conclusive due to variations between burns. Likewise, when the TD removed the organic components of the BBA from the grasses prior to injection into the chamber, the fresh κ_{app} decreased as SS increased, indicating that there could have been a

higher concentration of inorganics at larger particle sizes, but, in experiments where the TD was not used, organics were also at these sizes and decreased the overall hygroscopicity considerably.

Table E.2. The average fresh and aged κ_{app} as a function of CCNC SS for each experiment.

Exp.	Fuel	CCNC SS (%)	Fresh κ_{app}	Aged κ_{app}	Aging Scheme	Notes
1	Sawgrass 1	0.29	0.56	0.58	Control	
		0.49	0.48	0.47		
		0.69	0.61	0.62		
2	Sawgrass 2	0.29	0.52	0.57	Ozone	
		0.49	0.43	0.56		
		0.69	0.59	1.05		
3	Sawgrass 3	0.29	0.93	0.95	HONO + UV	TD before injection
		0.49	0.72	0.71		
		0.69	0.55	0.47		
4	Sawgrass 4	0.18	0.21	0.29	HONO + UV	Setup from Cain and Pandis (2017)
5	Cutgrass 1	0.29	0.43	0.51	Ozone	
		0.49	0.38	0.51		
		0.69	0.35	0.47		
6	Cutgrass 2	0.29	0.95	0.90	HONO + UV	TD before injection
		0.49	0.77	0.73		
		0.69	0.50	0.53		
7	Cutgrass 3	0.15	0.33	0.50	Ozone	Setup from Cain and Pandis (2017)
8	Cutgrass 4	0.18	0.30	0.37	HONO + UV	Setup from Cain and Pandis (2017)
9	Ponderosa Pine 1	0.29	N/A[a]	N/A[a]	Control	
		0.49	0.09	0.07		
		0.69	0.10	0.10		
10	Ponderosa Pine 2	0.30	N/A[a]	N/A[b]	HONO + UV	TD before injection
		0.40	N/A[a]	N/A[b]		
		0.50	N/A[a]	N/A[b]		
11	Ponderosa Pine 3	0.55	0.07	0.11	HONO + UV	Setup from Cain and Pandis (2017)

[a]The BBA did not activate at this SS.
[b]The BBA began activating at the end of the experiment, but the activation diameter was changing with time.

E2.2 Aged BBA hygroscopicity

The average κ_{app} of the aged BBA depended on the aging scheme and whether the TD was used to remove volatile components prior to injection (Fig. E.1). In the control experiments with no oxidants added to chamber, the κ_{app}, after more than 6 h in the chamber, did not differ significantly from the initial value, with differences of less than 5%. Interestingly, Jahl et al. (2020) observed enhanced ice nucleating ability for the BBA in these experiments after 4–6 h and attributed it to evaporation of organic components over the course of the experiments, revealing more ice active sites. However, ice nucleating ability is largely dependent on the number of ice active sites in the BBA whereas CCN activity in these systems is largely driven by the inorganic components of the BBA. Therefore, a small decrease in the overall concentration of organic components has less of an impact on the CCN activity, but can greatly affect ice nucleation potential.

Upon oxidation (either by ozone or hydroxyl radical), the aged κ_{app} of the BBA increased when the TD was not used prior to injection. Both the dark and UV aging increased the oxidation level (measured by the O:C) of the BBA by over 70% (Jahl et al., 2020). Usually, as organic compounds become more oxidized, they become more water soluble, which explains the increased hygroscopicity observed after oxidation. When the TD was used prior to injection into the chamber, the aging of the BBA by the hydroxyl radical did not change the hygroscopicity from the fresh BBA, which was likely caused by there being little to no organic compounds to oxidize and, if they were oxidized, they contributed negligibly to the total volume. Interestingly, in Experiment 10, the fresh BBA from ponderosa pine did not activate at the SS used after using the TD prior to injection. However, after aging with the hydroxyl radical, the BBA began to activate and the activation diameter decreased as aging progressed (Fig. E.2), indicating that the small

organic fraction that did not volatilize in the TD for this experiment was not very hygroscopic, but, aging with the hydroxyl radical transformed the BBA into CCN active compounds.

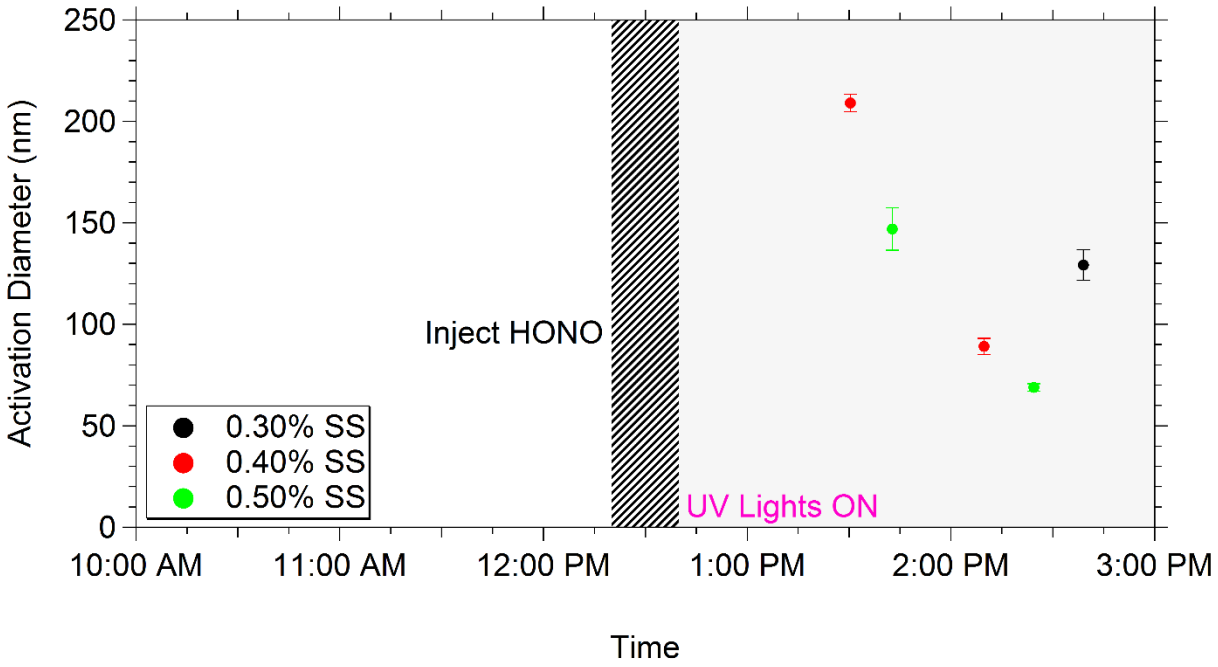

Figure E.2. The average activation diameter as a function of time in Experiment 10 for supersaturations of 0.3 (black), 0.4 (red), and 0.5% (green). Error bars represent one standard deviation of the average activation diameter. Addition of HONO for this experiment began at 12:20 and stopped at 12:40 when the UV lights were illuminated.

E2.3 Fresh and aged BBA hygroscopicity and oxidation level as a function of volatility

Experiments 4, 7, 8, and 11 used the experimental approach from Cain and Pandis (2017) to examine the hygroscopicity and oxidation level of BBA as a function of volatility. The thermograms for the fresh and aged aerosol for these experiments can be seen in Fig. E.3. The thermograms for the fresh aerosol were similar regardless of fuel. There was over 20% of the BBOA remaining after passing through the TD at 200°C, indicating the presence of low (LVOCs) or extremely low (ELVOCs) volatility organic compounds in the BBOA from these burns. The thermograms for the aged aerosol were similar for all experiments at temperatures below 100°C,

but there was more variation in the MFRs at higher temperatures. For example, the MFR at 200°C for Experiment 7 was 0.30 while the MFR for Experiment 8 was 0.52. The MFRs for all of the aged BBOA were higher than the fresh MFRs at all temperatures above 25°C, demonstrating that aging via ozone (Experiment 7) or the hydroxyl radical (Experiments 4, 8, and 11) generated less volatile compounds that were not present in the fresh BBOA. However, thermograms depend on several factors (e.g., the enthalpy of vaporization, particle size, residence time, and concentration), making conclusions based on thermograms alone difficult (Cappa, 2010; Riipinen et al., 2010; Cain et al., 2020).

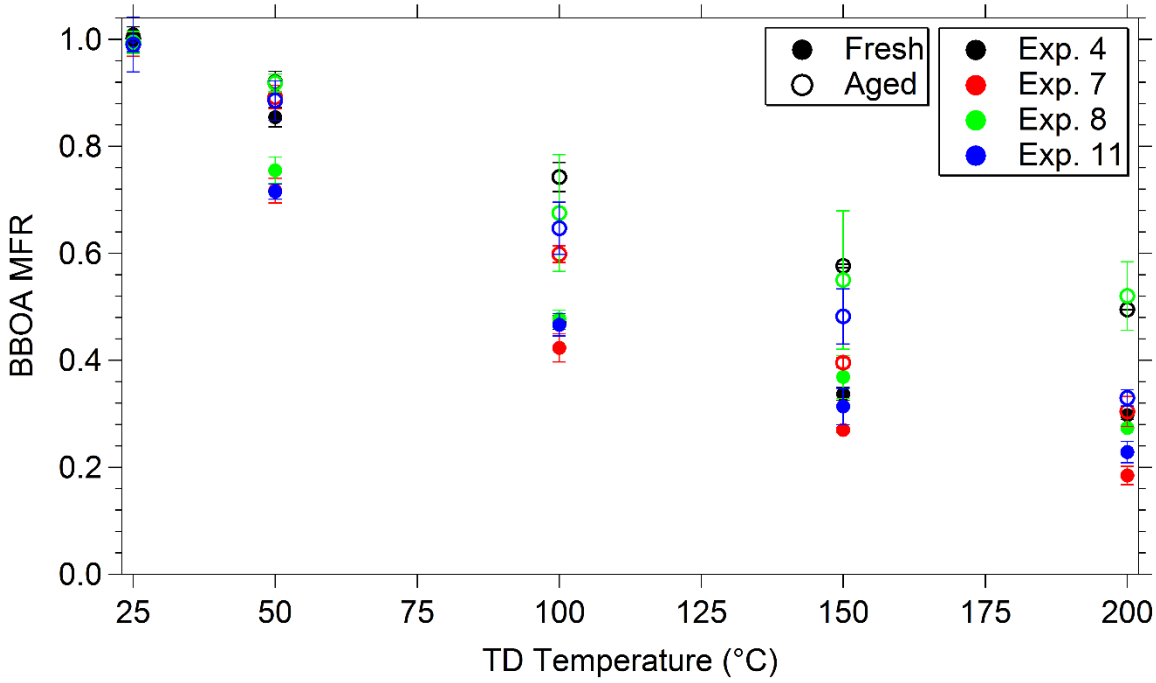

Figure E.3. Thermograms for the fresh (filled circles) and aged (open circles) BBOA in Experiments 4 (black), 7 (red), 8 (green), and 11 (blue). Error bars represent one standard deviation of the average MFR.

The average O:C and κ_{app} for both the fresh and aged BBA in Experiment 4 as a function of TD temperature can be seen in Fig. E.4. The average O:C for the fresh BBA in this experiment was 0.23 and the O:C remained around 0.23 in the TD until 100°C, where the O:C increased to

0.30 (Fig. E.4a). The average O:C continued to increase as the temperature in the TD increased, reaching a value of 0.51 at 200°C, indicating that the more volatile BBA components were less oxidized than the lower volatility components. According to the thermogram from Experiment 4 (Fig. E.3), 70% of the BBOA had evaporated at 200°C, indicating that the least volatile fraction had, on average, an O:C of 0.51.

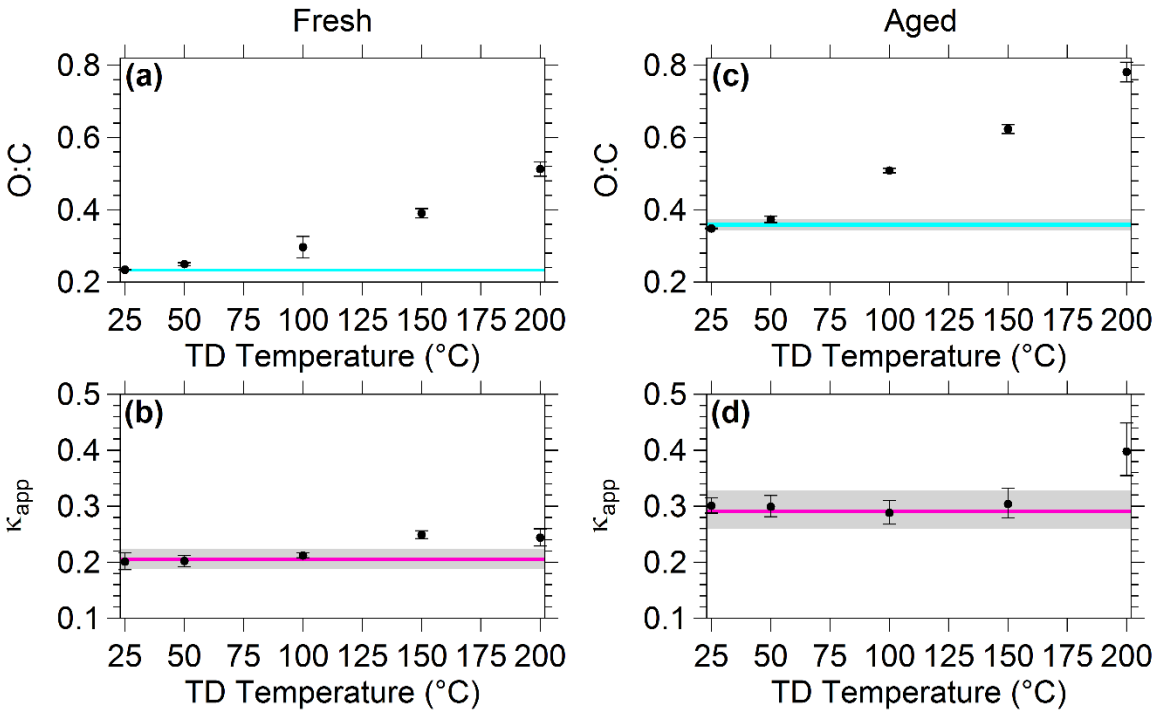

Figure E.4. The average (a) O:C and (b) κ_{app} of the fresh BBA in Experiment 4 as a function of TD temperature. The average O:C and κ_{app} of the aged BBA as a function of TD temperature are shown in (c) and (d) respectively. The error bars represent one standard deviation of the average O:C or κ_{app}. Also shown in each panel are the average O:C (blue line) and κ_{app} (magenta line) values along with ± one standard deviation (grey area) of the average value measured in the chamber for the fresh and aged BBA.

The average κ_{app} for the fresh BBA in Experiment 4 was 0.21 (Fig. E.4b). The average κ_{app} in this experiment remained at this value through the TD until the temperature reached 150°C, where the κ_{app} increased to 0.25. The κ_{app} remained at 0.25 when the temperature increased to 200°C. The increase in overall hygroscopicity at 150°C is indicative of the compounds that

evaporated having lower hygroscopicity, on average, than the remaining BBA. However, since there is no information about the refractory components of the BBA, this work can only make qualitative statements about the effect of evaporation of BBA components. Future work needs to focus on obtaining detailed composition measurements as a function of size in order to determine the impact of BBOA on overall hygroscopicity.

Aging by the hydroxyl radical in Experiment 4 increased the average O:C of the BBA to 0.36 (Fig. E.4c). Similar behavior was observed through the TD for the average O:C values of the aged BBA as for the fresh BBA, but the O:C values were higher due to oxidation. For example, at 150°C, the average O:C of the fresh BBA was 0.40, but, after aging, the average O:C at this temperature was 0.62, indicating that the less volatile components after aging were more oxidized.

Aging also increased the average κ_{app} of the BBA for this experiment to 0.29 (Fig. E.4d). The average κ_{app} through the TD remained around 0.29 until the temperature of the TD reached 200°C and the κ_{app} increased to 0.40. At this temperature, 50% of the aged BBOA had evaporated, indicating that the more volatile half of the BBA was CCN active, but had lower hygroscopicity than the less volatile fraction.

The average O:C and κ_{app} of the fresh and aged BBA from the other grass experiments observed using this technique (Experiments 7 and 8) can be seen in Figs. E.6 and E.7. Despite being from a different fuel (cutgrass as opposed to sawgrass), the fresh and aged BBA from Experiments 7 and 8 had similar results to Experiment 4. The absolute values vary from experiment to experiment due to variations in the burns, but, in all grass experiments, the less volatile components were more oxidized and more hygroscopic than the more volatile components.

The average O:C and κ_{app} of the fresh and aged BBA from Experiment 11 can be seen in Fig. E.5. The behavior of the fresh and aged BBA through the TD was similar to the other

experiments, but the BBA from ponderosa pine is almost exclusively organic (i.e., the average κ_{app} of the BBA is essentially κ_{org}). The average O:C for the fresh BBA in this experiment was 0.16, but the O:C increased to 0.18 at 50°C in the TD when only 28% of BBOA had evaporated (Fig. E.5a). The average O:C continued to increase as TD temperature increased, ending at 0.36 for the least volatile fraction of the BBA.

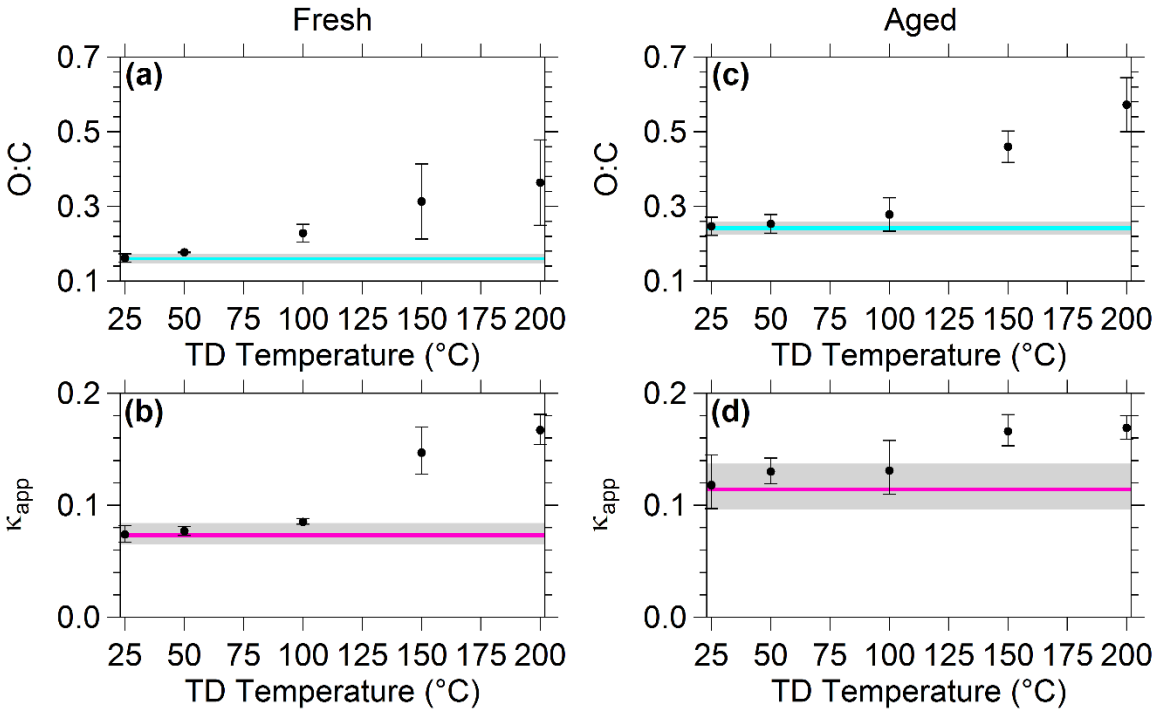

Figure E.5. The average (a) O:C and (b) κ_{app} of the fresh BBA in Experiment 11 as a function of TD temperature. The average O:C and κ_{app} of the aged BBA as a function of TD temperature are shown in (c) and (d) respectively. The error bars represent one standard deviation of the average O:C or κ_{app}. Also shown in each panel are the average O:C (blue line) and κ_{app} (magenta line) values along with ± one standard deviation (grey area) of the average value measured in the chamber for the fresh and aged BBA.

The average κ_{app} of the fresh BBA in Experiment 11 was 0.07 and the average κ_{app} remained at that value through the TD until the temperature reached 100°C, where the κ_{app} increased to 0.09 (Fig. E.5b). At this temperature, over 54% of the BBOA had evaporated,

indicating that the less volatile components were more hygroscopic than the more volatile components. The κ_{app} continued to increase as TD temperature increased, ending at 0.17 at 200°C.

Aging in this experiment increased the average O:C to 0.24 (Fig. E.5c) and the average κ_{app} to 0.11 (Fig. E.5d). The average O:C still increased with TD temperature, but the average values at all temperatures were higher than the values for the fresh BBA. The MFR at each temperature was higher as well (Fig. E.3), indicating that the BBA components became less volatile and more oxidized as a result of aging. Interestingly, the average κ_{app} through the TD at 150 and 200°C for the aged BBA were nearly identical to the values for the fresh BBA at those temperatures. These results indicate that, even though the less volatile compounds became more oxidized with aging, their hygroscopicity did not change significantly upon aging. Therefore, the increase in hygroscopicity for the aged BBA in this experiment is a result of the more volatile components becoming more hygroscopic, at least on average.

E3 Conclusions

Experiments were conducted in an atmospheric simulation chamber examining the hygroscopicity, oxidation level, and volatility of fresh and aged emissions of biomass-burning from sawgrass, cutgrass and ponderosa pine. All of the fresh BBA were CCN active at climate relevant SS, but the magnitude of the κ_{app} depended on the fuel used and SS, indicating size-dependent composition effects. The average κ_{app} of BBA from the grasses was significantly higher than the average κ_{app} of the BBA from ponderosa pine, largely due to the considerable amount of inorganic material present in the BBA from the grasses.

Chemical aging by ozone or the hydroxyl radical, increased the κ_{app} of the BBA in all experiments except where a TD removed the more volatile aerosol components and all

corresponding organic vapors before injection into the chamber. When no oxidant was added to the chamber, there was no observable change in the κ_{app} of the BBA.

The setup from Cain and Pandis (2017) was used in some experiments to examine the hygroscopicity and oxidation level of the BBA as a function of volatility. The least volatile organic components in all experiments were the most oxidized and most hygroscopic. However, more work is needed to determine the contribution of organics to the overall hygroscopicity of the BBA. Future work will focus on obtaining size-dependent composition measurements, especially for refractory BBA components, since these play an important role in cloud activation for emissions from biomass-burning.

E4 References

Cain, K. P., and Pandis, S. N.: A technique for the measurement of organic aerosol hygroscopicity, oxidation level, and volatility distributions, Atmos. Meas. Tech., 10, 4865–4876, doi: 10.5194/amt-10-4865-2017, 2017.

Cain, K. P., Karnezi, E., and Pandis, S. N.: Challenges in determining atmospheric organic aerosol volatility distributions using thermal evaporation techniques, Aerosol Sci. Technol., doi: 10.1080/02786826.2020.1748172, 2020.

Canagaratna, M. R., Jimenez, J. L., Kroll, J. H., Chen, Q., Kessler, S. H., Massoli, P., Hildebrandt Ruiz, L., Forner, E., Williams, L. R., Wilson, K. R., Surratt, J. D., Donahue, N. M., Jayne, J. T., and Worsnop, D. R.: Elemental ratio measurements of organic compounds using aerosol mass spectrometry: Characterization, improved calibration, and implications, Atmos. Chem. Phys., 15, 253–272, doi: 10.5194/acp-15-253-2015, 2015.

Cappa, C. D.: A model of aerosol evaporation kinetics in a thermodenuder, Atmos. Meas. Tech., 3, 579–592, doi: 10.5194/amt-3-579-2010, 2010.

Englehart, G. J., Hennigan, C. J., Miracolo, M. A., Robinson, A. L., and Pandis, S. N.: Cloud condensation nuclei activity of fresh primary and aged biomass burning aerosol, Atmos. Chem. Phys., 12, 7285–7293, doi: 12.5194/acp-12-7285-2012, 2012.

Jahl, L. G., Brubaker, T. A., Polen, M. J., Jahn, L. G., Cain, K. P., Bowers, B. B., Graves, S., Pandis, S. N., and Sullivan, R. C.: Atmospheric aging enhances the ice nucleation ability of biomass-burning aerosol, *in prep*.

Moore, R. H., Nenes, A., and Medina, J.: Scanning mobility CCN analysis—A method for fast measurements of size-resolved CCN distributions and activation kinetics, Aerosol Sci. Technol., 44, 861–871, doi: 10.1080/02786826.2010.498715, 2010.

Petters, M. D., and Kreidenweis, S. M.: A single parameter representation of hygroscopic growth and cloud condensation nucleus activity, Atmos. Chem. Phys., 7, 1961–1971, doi: 10.5194/acp-7-1961-2007, 2007.

Petters, M. D., Carrico, C. M., Kreidenweis, S. M., Prenni, A. J., DeMott, P. J., Collett, J. L., and Moosmuler, H.: Cloud condensation nucleation activity of biomass burning aerosol, J. Geophys. Res., 114, D22205, doi: 10.1029/2009JD012353, 2009.

Riipinen, I., Pierce, J. R., Donahue, N. M., and Pandis, S. N.: Equilibration time scales of organic aerosol inside thermodenuders: Evaporation kinetics versus thermodynamics, Atmos. Environ., 44, 597–607, doi: 10.1016/j.atmosenv.2009.11.022, 2010.

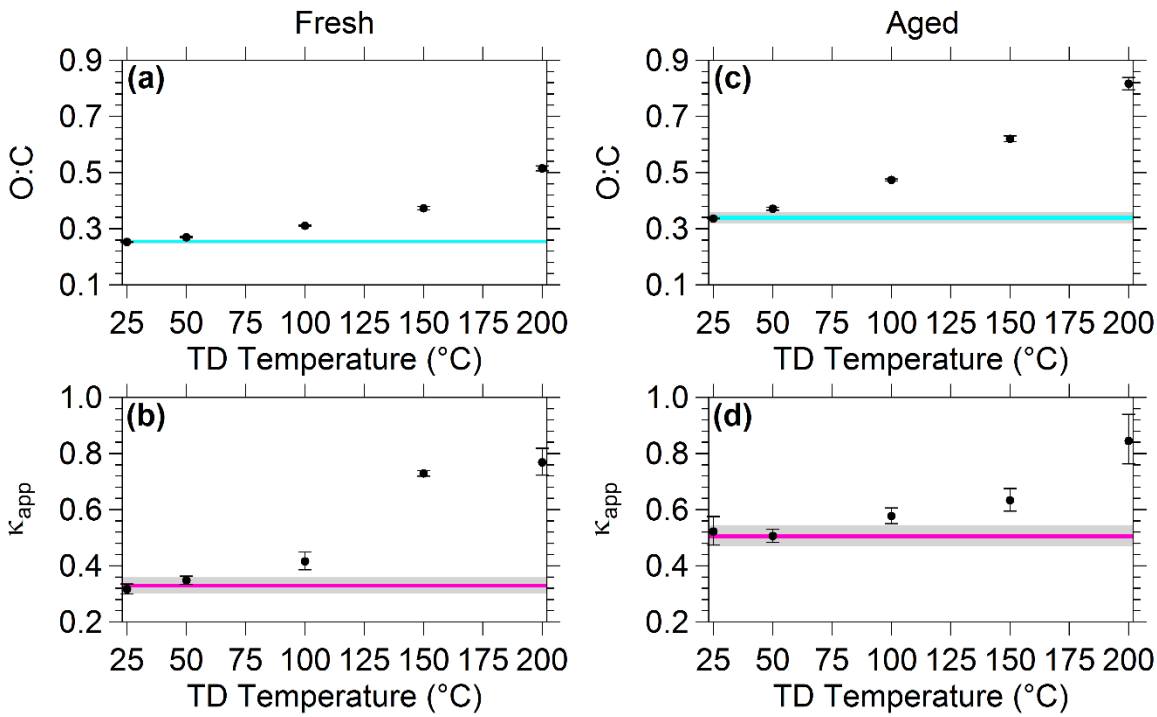

Figure E.6. The average (a) O:C and (b) κ_{app} of the fresh BBA in Experiment 7 as a function of TD temperature. The average O:C and κ_{app} of the aged BBA as a function of TD temperature are shown in (c) and (d) respectively. The error bars represent one standard deviation of the average O:C or κ_{app}. Also shown in each panel are the average O:C (blue line) and κ_{app} (magenta line) values along with ± one standard deviation (grey area) of the average value measured in the chamber for the fresh and aged BBA.

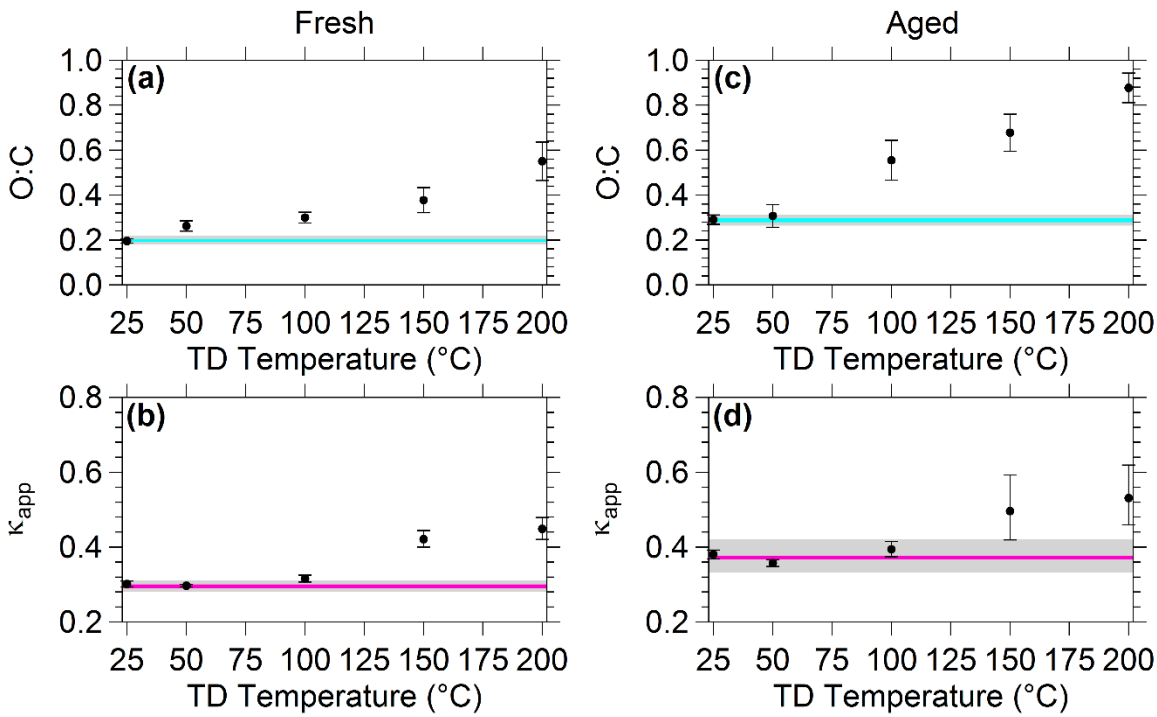

Figure E.7. The average (a) O:C and (b) κ_{app} of the fresh BBA in Experiment 8 as a function of TD temperature. The average O:C and κ_{app} of the aged BBA as a function of TD temperature are shown in (c) and (d) respectively. The error bars represent one standard deviation of the average O:C or κ_{app}. Also shown in each panel are the average O:C (blue line) and κ_{app} (magenta line) values along with ± one standard deviation (grey area) of the average value measured in the chamber for the fresh and aged BBA.